WEATHERING AND LANDSCAPE EVOLUTION RECORDED IN SUPERGENE JAROSITE, RED RIVER VALLEY, NORTHERN NEW MEXICO

By

Kimberly Ellen Samuels

Submitted in partial fulfillment of the requirements
for the Degree of Master of Science in Geochemistry at
New Mexico Institute of Mining and Technology

Earth and Environmental Science Department
Socorro, New Mexico
December, 2008

ABSTRACT

Field and experimental work on supergene jarosite from the Red River valley (RRV), northern New Mexico, indicate that alteration scar style erosion began up to 1.5 million years ago, possibly in response to downcutting in the Rio Grande rift. This study is composed of three parts: two sample preparation experiments conducted with the goal of improving methods to remove potassium-bearing silicate contaminants from jarosite and a synthesis of jarosite geochronology with stable isotope compositions in an effort to constrain the regional controls on alteration scar formation in the Red River valley.

The first experiment tested whether or not hydrofluoric acid (HF) can remove silicate contaminants without incongruently dissolving jarosite, preferentially removing potassium and argon. Four aliquots of pure Peña Blanca jarosite (PB) and four aliquots of 85% PB mixed with 15% Fish Canyon sanidine (FC-2) were crushed and treated with 40 mL of 25% HF for 0, 30, 240, and 480 minutes. Secondary electron images show that jarosite dissolves during HF treatment with jarosite grains becoming pitted and rounded with time in acid. K_2O concentration of PB jarosite treated for 480 minutes ranges from 7.32 to 9.43 weight percent, which overlaps with the K_2O concentration of untreated PB jarosite (7.93 to 9.43 weight percent), indicating that HF treatment does not preferentially remove potassium. Additionally, $^{40}Ar/^{39}Ar$ ages of both untreated and treated PB overlap with each other and

previously-dated aliquots of PB jarosite at the 95% confidence level, suggesting that HF treatment has no impact on jarosite's plateau age.

The plateau and integrated ages for the experimental mixture of PB and FC-2 overlapped with the reproducible age for pure PB jarosite. This mixture did not yield the integrated age of 12.35 Ma expected from the complete degassing of 9.6 Ma jarosite and 28.02 Ma feldspar. This overlap suggests that the sanidine did not degas when laser-heated between 1 and 16W with a defocused beam. Jarosite is heated to 10W or less, so sanidine contamination should not affect the apparent age of RRV jarosite. Back-scattered electron (BSE) images indicated that all FC-2 was removed from the mixture after 30 minutes of HF treatment.

The second experiment tested the effects of HF treatment on supergene jarosite from the RRV. Four samples that yielded age spectra with clear evidence of contamination with older phases when dated in 2006 were treated with HF for 30 minutes and re-dated. K_2O concentrations of HF-treated RRV jarosite overlapped with K_2O concentrations of untreated RRV jarosite, indicating that RRV jarosite did not lose potassium during acid treatment. BSE images show that HF-treated aliquots of RRV samples continue to be contaminated with quartz, sanidine, and clay, including illite and chlorite. Apparent age and radiogenic yield climb after the 6W step, which may indicate that clay is degassing in these steps. If a mixture of Quaternary or Pliocene jarosite and Miocene clay degassed completely, the expected integrated age of the mixture would be 7.5 to 11 Ma. The integrated ages of these samples is consistently less than 1 Ma, suggesting that young jarosite controls the apparent age of these samples. Large errors in apparent age may be attributed to low radiogenic yield.

ACKNOWLEDGEMENTS

Funding for this project was provided by several sources. I would like to thank the New Mexico Bureau of Geology and Mineral Resources for supporting me through the generous Kottlowski Fellowship for the past two years of my graduate work. Chevron Mining Inc. paid for $^{40}Ar/^{39}Ar$ and ^{14}C analyses. Other research funding was provided by the Geological Society of America and New Mexico Geological Society student research grant programs. The $^{40}Ar/^{39}Ar$ experiment presented in chapter three was conducted as a class project for the spring 2007 Practical Aspects of Mass Spectrometry class under the guidance of Matt Heizler and William McIntosh.

This work was presented at the Goldschmidt 2008 conference in Vancouver, Canada, which would not have been possible without generous travel grants provided by the New Mexico Institute of Mining and Technology Graduate Student Association and the Goldschmidt Conference. Student travel grants provided by the Goldschmidt Conference are supported by the National Science Foundation, European Association for Geochemistry, Geochemical Society, European Science Foundation, Mineralogical Association of Canada, Geochemical Society of Japan, Goldschmidt Conference Organizers, Geoscience BC.

Several people assisted me in the field and laboratory. I would like to thank Gabriel Graf and Ryan Crow for their help in sample collection. Gabriel Graf, Laura Rosales, Jesus Velador, and Matthew Earthman provided much needed assistance in the stable isotope lab. I would like to thank Nelia Dunbar and Lynn Heizler for assistance in the electron microprobe lab. It is no exaggeration to say that without Lisa Peters' assistance in the New Mexico Geochronology Research Lab, this study would not have been a success, and I am grateful for the time and effort she put into it.

I would like to thank my advisers, Dr. Andrew Campbell and Dr. Virgil Lueth for their guidance and insights. Dr. Phil Kyle assisted in editing the section on radiocarbon dating. I would also like to thank Dr. William McIntosh and Dr. Bruce Harrison for serving on my committee and providing me with much needed assistance in writing. Further writing assistance was provided by Dr. Nancy King. Ryan Crow's editing assistance improved this thesis tremendously.

Finally, I would like to thank the E&ES community at New Mexico Tech for sending cards, being flexible, visiting me in the hospital, and just generally helping me after my near-fatal cycling accident on February 10, 2007.

TABLE OF CONTENTS

LIST OF TABLES

LIST OF FIGURES

This thesis is accepted on behalf of the
Faculty of the Institute by the following committee:

Andrew Campbell
Advisor

Virgil W.

William C

Harrison

9/11/08
Date

I release this document to the New Mexico Institute of Mining and Technology.

Kimberly E. Samuels
Student's Signature

9/11/08
Date

1. OVERVIEW: JAROSITE IN LANDSCAPE EVOLUTION STUDIES

Supergene jarosite, a pyrite weathering product, can be used to determine the timing of weathering and to reconstruct weathering fluid compositions. Jarosite forms during both hydrothermal alteration and as a weathering product. When it forms as a weathering product, its fine grain size makes it difficult to separate from older phases, presenting an added challenge for analytical work.

This project included two experiments designed to improve sample preparation techniques with the goal of obtaining more accurate stable isotope and argon geochronology data. Jarosite prepared according to refined procedures was subsequently used to examine the Quaternary landscape development of the Red River valley (RRV), northern New Mexico. RRV jarosite is the ideal material for testing improved ^{40}Ar/^{39}Ar sample preparation techniques because the ages of potential contaminants have been established by previous workers.

This thesis is divided into three main sections: chapters two, three, and four. Chapters two and three describe experiments designed to improve supergene jarosite dating techniques. Chapter four describes the application of these experiments to landscape evolution in the Red River valley. This chapter (chapter one) provides background information about jarosite chemistry and the mineral's potential role in landscape evolution studies. The final chapter (chapter five) suggests further research projects related to jarosite geochronology and RRV landscape evolution.

1.1. Weathering geochronology

Climate and tectonics shape landscapes. One approach to evaluating which of these factors exerts a greater influence on landscape evolution in a given region, relies on constraining the timing of weathering and the compositions of weathering fluids. Geomorphologists employ a number of techniques to determine weathering and erosion rates (Table 1-1).

Table 1-1. Geochronology methods applicable to Quaternary deposits modified from Rosholt et al., 1991.

Sidereal	Isotopic/ Radiogenic	chemical/ biochemical	geomorphic	Correlation
Historical records	^{14}C*	Amino acid racemization	soil profile development	Stratigraphy
dendrochronology	$^{40}Ar/^{39}Ar$ (and K/Ar)*	obsidian hydration	rock/ mineral weathering	Tephrochronology
varve chronology	fission track	tephra hydration	rock varnish	Paleomagnetism
	U-trend	Lichenometry	progressive landform modification	fossils and artifacts
	Thermoluminescence	soil chemistry	rate of deposition	stable isotopes*
	electron-spin resonance		rate of deformation	astronomical correlation
	^{210}Pb		geomorphic position	tectites microtectites
	other cosmogenic isotopes (e.g. ^{36}Cl)			

* Methods used in this thesis.

I focused on $^{40}Ar/^{39}Ar$ geochronology of jarosite and ^{14}C dating of organic material to determine the timing of alteration scar formation and used stable isotope geochemistry to reconstruct weathering fluid compositions. Radiocarbon has a short half-life ($t_{1/2} = 5730$ years), which limits its application to Quaternary deposits less than 50,000 years old (Rosholt et al., 1991). Organic material trapped in ferricretes and debris flows formed in the last 50,000 years can be dated via this method, and those ages can be used to determine the timing of late Pleistocene to Holocene debris flow activity and accumulation rates for active ferricretes.

Establishing the longer histories of RRV scars depends on longer-lived radionuclides. I used $^{40}Ar/^{39}Ar$ geochronology of potassium-bearing weathering minerals to establish the timing of alteration scar initiation and development. Both jarosite and cryptomelane, a potassium-bearing manganese oxide, are present in RRV alteration scars. I attempted to date cryptomelane, but the apparent ages were geologically meaningless (see Appendix A). Jarosite geochronology results are described in chapters three, four, and Appendix B.

1.2. Jarosite Chemistry

Jarosite is an alunite-group mineral with the general formula $AB_3(XO_4)_2(OH)_6$ (Papike et al., 2006). The jarosite structure can incorporate a number of elements. The A-site holds cations in 12-fold coordination; B is an octahedral site; the X site is tetrahedral. The A-site can contain monovalent (e.g. K^+, Na^+, Rb^+, H_3O^+), divalent (e.g. Ca^{2+}, Pb^{2+}, Ba^{2+}, Sr^{2+}), and trivalent (esp. REE) cations (Papike et al., 2006 and Smith et al., 2006). The B-site can hold divalent or trivalent cations, but generally contains Fe^{3+}or Al^{3+}. Divalent substitutions in this site include Pb^{2+}, Zn^{2+}, and Mg^{2+} (Papike et al., 2006). X, the tetrahedral site, can contain S, P, As or Sb (Papike et al., 2006). Although several elements can substitute into each site, jarosite's idealized formula is $KFe_3(SO_4)_2(OH)_6$. There is complete solid solution between jarosite and natrojarosite [$NaFe_3(SO_4)_2(OH)_6$] at high temperatures (Stoffregen et al., 2000), but in supergene environments, there is an apparent miscibility gap (Figure 1-1; Papike et al., 2007).

Supergene jarosite can precipitate directly from solution through the reaction: $A^+_{(aq)} + 3B^{3+}_{(aq)} + 2XO_4^{2-}_{(aq)} + 6\ OH^-_{(aq)} \leftrightarrow AB_3(XO_4)_2(OH)_{6(s)}$. It can also form from the oxidation and potassium metasomatism of pyrite: $12FeS_{2(s)} + 4K^+_{(aq)} + 30H_2O_{(l)} + 45O_{2(aq)} \leftrightarrow$

$4KFe_3(SO_4)_2(OH)_{6(jrs)} + 16SO_4{}^{2-}{}_{(aq)} + 36H^+{}_{(aq)}$ (Vasconcelos and Conroy, 2003). When jarosite forms via the second reaction it exhibits replacement textures, which were not observed in RRV jarosite. RRV jarosite, therefore, predominantly precipitates from ions in solution.

Since RRV jarosite forms during weathering, stable isotope ratios of sulfur, hydrogen, sulfate oxygen, and hydroxyl oxygen preserve primary weathering solution compositions (Arehart and O'Neil, 1993; Rye and Stoffregen, 1995). Meteoric water is the sole source of hydrogen in all cases, so D/H ratios generally preserve meteoric water compositions. Temperature exerts the greatest control over D/H ratios of meteoric water with secondary effects from altitude, latitude, and distance inland, so alunite-group hydrogen isotopes can be used as a paleoclimate proxy (Arehart and O'Neil, 1993). H_3O^+ hydrogen in the A-site exchanges more readily with meteoric water than OH-site water (Alpers et al., 1992), but A-site hydrogen represents less than 0.2% percentage of all hydrogen in average RRV jarosite, so the δD signal is dominated by the OH-site hydrogen.

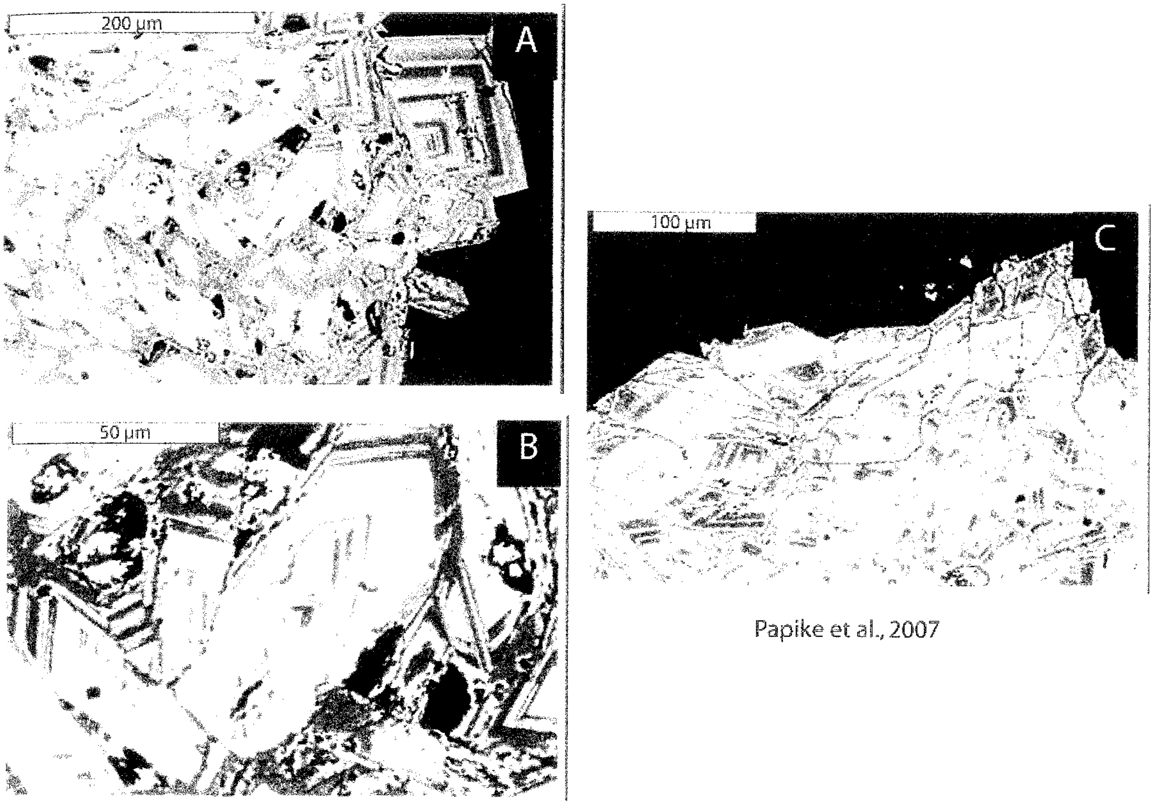

Papike et al., 2007

Figure 1-1. BSE and false-color BSE images of supergene jarosite from Apex Mine, AZ (a and b) and Gold Hill, UT (c) from Papike et al., 2007. These images show prominent oscillatory Na-K zoning. In the BSE image, brighter areas are more potassic and darker areas are more sodic. In the false-color images, redder areas are more sodic.

1.3. Potential problems in ^{40}Ar/^{39}Ar geochronology

Jarosite has a high concentration of potassium, which makes it datable by the ^{40}Ar/^{39}Ar method. Radioactive ^{40}K decays to ^{40}Ar, providing the basis for both conventional K/Ar and ^{40}Ar/^{39}Ar geochronology. In the ^{40}Ar/^{39}Ar method, a percentage of ^{39}K is converted to ^{39}Ar in a nuclear reactor. The irradiation process makes it possible to measure parent and daughter isotopes simultaneously as a ratio. The ^{40}K/^{39}K ratio is known and assumed to be fixed throughout geologic time, so ^{39}Ar serves as a proxy for the parent isotope in age calculations (McDougall and Harrison, 1988). ^{40}Ar/^{39}Ar measurements are more precise than conventional K/Ar, and measuring an isotopic ratio allows dating of smaller samples, increasing the applicability of ^{40}Ar/^{39}Ar to fine-grained weathering products. The ^{40}Ar/^{39}Ar method provides a means for evaluating the effects of contamination, excess argon, or argon loss on sample age. K/Ar techniques do not permit evaluation of these potential problems in dating weathering products.

1.3.1. Closed system behavior

A mineral must meet certain criteria before it can be dated. Minerals that dissolve or readily exchange potassium with meteoric water cannot be dated by the $^{40}Ar/^{39}Ar$ method because they do not act as a closed system with respect to the parent isotope. Jarosite's stability under surficial conditions has been subject to debate.

Vasconcelos (1999) found that jarosite has a small solubility product (K_{sp}), suggesting that it is stable in meteoric water: $K_{sp(jarosite)} = 10^{-93.21}$, $K_{sp(natrojarosite)} = 10^{-89.28}$, $K_{sp(hydronium\ jarosite)} = 10^{-75.39}$. Alkali exchange, rather than dissolution, controls K-loss from all forms of jarosite. Vasconcelos (1999) determined that the activation energy for alkali exchange between alunite-group minerals and water is 156.5 ± 6.3 kJ mol^{-1}, which is comparable to the activation energy for exchange reactions between alkali feldspar and water. The high activation energy indicates that K-exchange between jarosite and water is negligible.

Elwood Madden et al. (2008), however, question jarosite's stability based on dissolution experiments on both potassium jarosite and natrojarosite in pure water. These researchers concluded that potassium jarosite incongruently dissolves in pure water (pH = 6) and that jarosite should persist in the field for only 2 to 10,000 years in saturated conditions. Elwood Madden stated in her 2008 presentation at the V.M. Goldschmidt Conference that she plans to conduct further experiments on jarosite dissolution under different pH conditions.

Despite Elwood Madden et al.'s conclusions, jarosite has been shown to persist in the field for 9.5 Ma (Lueth et al., 2005). Additionally, ferricretes and veins that preserve RRV jarosite are not water-saturated at all. The key to jarosite preservation over geologic time may be isolation from dilute, high-pH solutions. This thesis research was conducted with the assumption that jarosite is stable for long periods of time in the low pH, unsaturated conditions present in alteration scars.

1.3.2. ^{39}Ar Recoil

^{39}Ar recoil is another factor that determines whether or not a mineral will yield a reliable ^{40}Ar/^{39}Ar date. ^{39}Ar recoils approximately 100 nm during formation in a reactor. Recoil can remove ^{39}Ar from or redistribute it throughout a sample. Although recoil loss has no effect on the apparent age of large grains or those with a homogenous distribution of potassium, it can increase the apparent age of small grains and disturb the age spectra of samples with fine-scale intergrowths of K-rich and K-poor phases (see esp. Smith et al., 1993; Villa, 1997; Lo and Onstott, 1989).

Supergene jarosite is fine-grained, so there is some debate about the potential effects of recoil loss or redistribution on age determinations. Vasconcelos (1999) documents recoil as a problem in his review paper, but he concluded that recoil had not compromised the quality of his earlier efforts to date weathering profiles (Vasconcelos et al., 1994). The New Mexico Geochronology Research Laboratory (NMGRL) has conducted encapsulation experiments on fine-grained alunite and determined that recoil loss in alunite ranges from 1.8% to 4.5%. Recoil loss disturbed the age spectra, but had no effect on the plateau ages of these samples (Polyak et al., 2006). Based on NMGRL's results and the mineralogical similarities between alunite and jarosite, jarosite samples analyzed for this thesis were not encapsulated prior to irradiation.

1.4. Contamination

RRV jarosite precipitates on the surface of rocks or in small veins and vugs, and is intermixed with older, hydrothermal illite. This spatial link to older, primary minerals results in mineral separates that are contaminated with older, fine-grained, K-bearing minerals, specifically potassium feldspar and illite. Although Meyer and Leonardson (1990) assumed that alteration scar clay formed under weathering conditions, Graf (2008) determined that RRV clay is hypogene in origin. Research by Lipman et al. (1986), Czamanske et al. (1990), Lueth et al. (2006), Tappa et al. (2008), and Zimmerer (2008) has determined that volcanism, plutonism, and hydrothermal alteration occurred during the Oligocene and Miocene. Therefore, any silicate contaminant formed during the early Tertiary and is significantly older than supergene jarosite. These fine-grained contaminants increase the apparent age of the sample, and the apparent age of high-wattage steps can reach the age of alteration in the area (Figure 1-2; Lueth and Campbell, 2006).

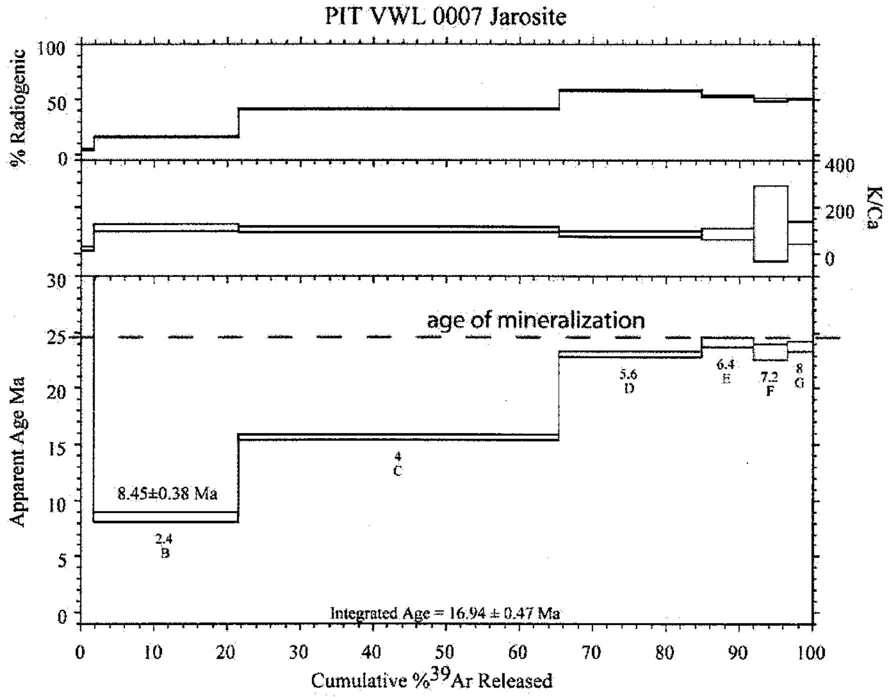

Modified from Lueth et al., 2006

Figure 1-2. Untreated RRV jarosite yields old apparent ages. Apparent age in untreated PIT VWL 0007 approached the age of mineralization (24.86 ± 0.15 Ma), suggesting that this sample is contaminated with hypogene, K-bearing phases.

Hydrofluoric acid (HF) dissolves silicates and has the potential to remove the K-bearing contaminants, but there is some debate over whether HF incongruently dissolves jarosite. HF has been used to remove clay from jarosite for stable isotope studies (see especially Arehart and O'Neil, 1993; Wasserman et al., 1992), but there have been no systematic experiments to evaluate the effects of HF on jarosite δD values.

Vasconcelos (1999) warns against using HF to chemically separate fine-grained, supergene alunite-group minerals from clay and other K-bearing, silicate contaminants because he believes that HF treatment leads to K and Ar loss. This is supported by Smith et al. (2006) who found that, although K_{sp} is very small within the pH range of most natural waters, synthetic jarosite dissolves incongruently at pH 2 and 8, preferentially losing K^+ and SO_4^{2-}. K and/ or Ar loss would make it impossible to accurately date HF-treated jarosite samples.

Other researchers have successfully dated HF-treated jarosite and alunite. Polyak et al. (1998 and 2006) used HF to separate fine-grained alunite from clay in order to date the timing of cave formation. Lueth et al. (2006) found that HF-treated jarosite yielded flatter age spectra than untreated aliquots of the same sample (Figure 1-3). None of these studies has critically evaluated the effects of HF on mineral composition and age determinations.

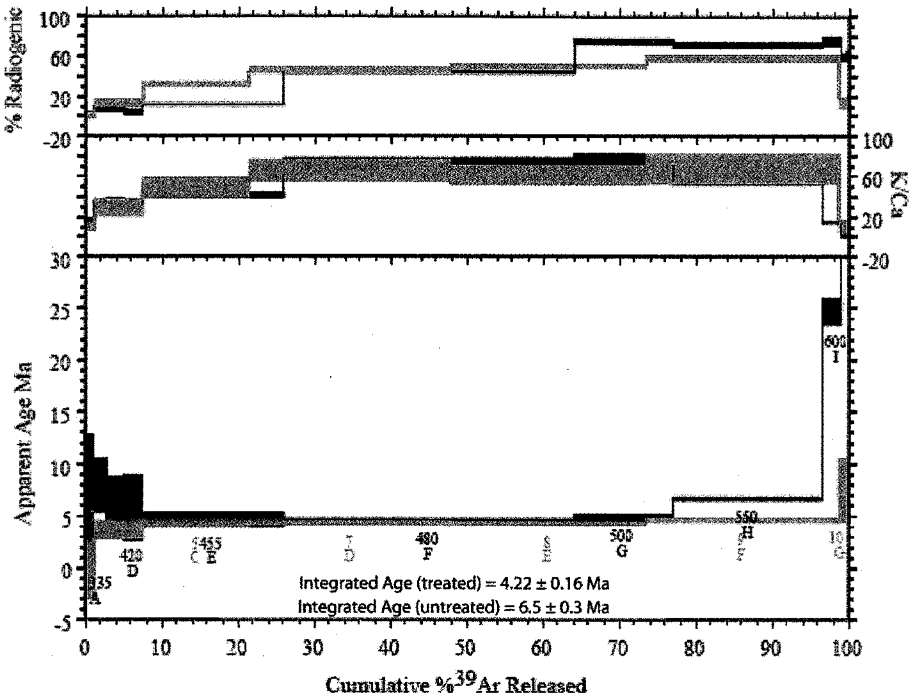

Lueth and Campbell, 2006

Figure 1-3. Untreated and HF-treated RRV jarosite. The untreated aliquot (black) yielded a disturbed age spectrum. 10 minutes of HF treatment (gray) yielded a flat spectrum with a plateau age of ca. 5 Ma.

In order to evaluate whether or not HF can be used to dissolve silicate contaminants from jarosite samples without rendering the jarosite undatable, I conducted a systematic experiment on the effects of HF on pure, hypogene jarosite from Peña Blanca, Mexico. Peña Blanca jarosite is well-characterized, having been dated by Lueth et al. (2005) and characterized chemically by Papike et al. (2007). Chapter two of this thesis provides detailed results of this experiment and a discussion of the implications of these results for supergene jarosite sample preparation methods. I then applied the sample preparation methods to previously-dated RRV jarosite. Chapter three provides detailed results of $^{40}Ar/^{39}Ar$ age determinations on untreated and treated RRV supergene jarosite.

1.5. Using jarosite to study landscape evolution

Improving the accuracy of supergene jarosite ages increases the mineral's applicability to landscape evolution studies. Jarosite ages record the timing of mineral precipitation, which are interpreted in this thesis as a temporal record of alteration scar formation. Hydrothermal mineralization in the RRV led to sulfide formation several kilometers beneath the surface (Figure 1-4a). Uplift along the Sangre de Cristo fault led to erosion of the Amalia tuff that overlay the hydrothermally-altered rocks, exposing these pyrite-rich rocks to surface and vadose zone conditions. Under these surficial conditions, pyrite oxidizes according to the following reactions (Seal, 2003):

$$FeS_{2(py)} + 7/2O_2 + H_2O \rightarrow Fe^{2+} + 2SO_4^{2-} + 2H^+ (1)$$

$$FeS_{2(py)} + 14Fe^{3+} + 8H_2O \rightarrow 15Fe^{2+} + 2SO_4^{2-} + 16H^+ (2)$$

These oxidizing reactions create both the acidic conditions and the sulfate in solution necessary for supergene jarosite formation in the vadose zone (Figure 1-4b). Although new silicates do not form, the acidic conditions dissolve silicates (Nordstrom et al., 2005), putting potassium into solution (Figure 1-4c). Jarosite precipitates when the fluid is saturated with its components (Figure 1-4d). The process described above continues as erosion of hydrothermally-altered rock exposes more pyrite to surficial conditions, leading to the precipitation of more jarosite.

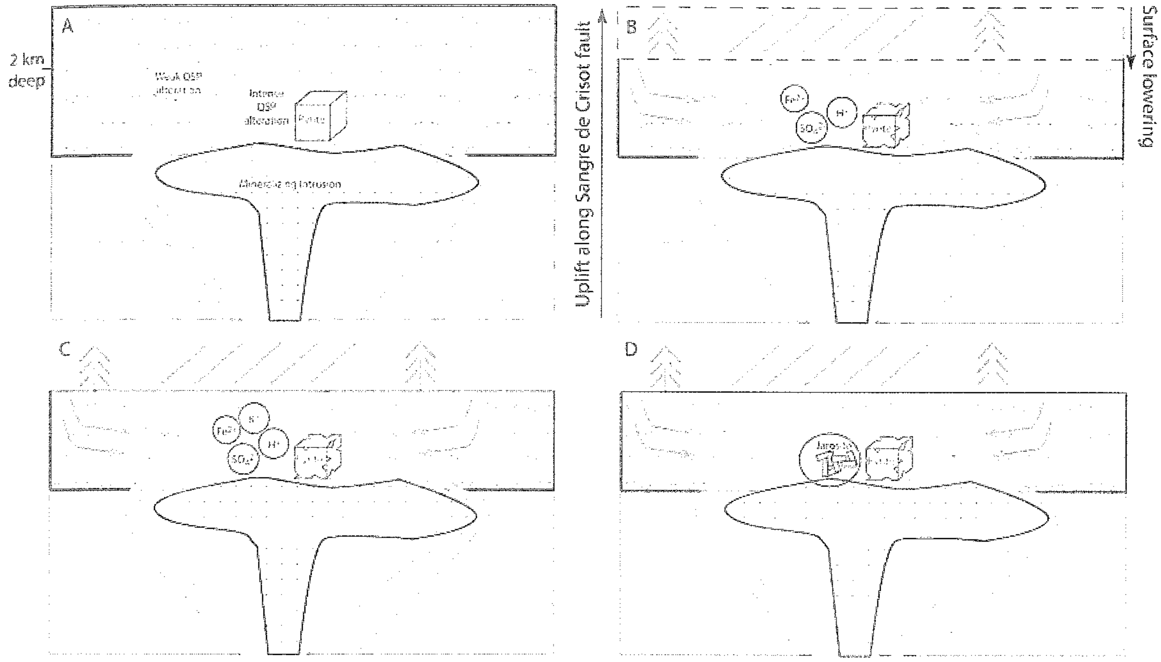

Figure 1-4. Schematic diagram of jarosite formation from pyrite oxidation. A) Pyrite forms under hydrothermal conditions several kilometers below the surface; B) Uplift and lowering of the surface exposes pyrite to vadose zone and surficial conditions. Pyrite oxidizes, putting sulfate, iron, and acid into solution; C) Acidic conditions lead to the dissolution of silicates, putting potassium into solution; D) Jarosite precipitates in acidic environments where the fluids become saturated with respect to its components.

Jarosite is preserved in weathered veins and ferricretes throughout the RRV. Modern ferricretes form in streambeds, and stranded ferricretes high above present channels are interpreted to preserve the elevation of pre-incised land surfaces in tributaries to the Red River (Figure 1-5). Previous efforts to date RRV jarosite yielded ages ranging from 0.31 ± 0.23 Ma to 8.45 ± 0.38 Ma (Lueth et al., 2006). δD values varied by ~80‰ with D/H ratios increasing with age.

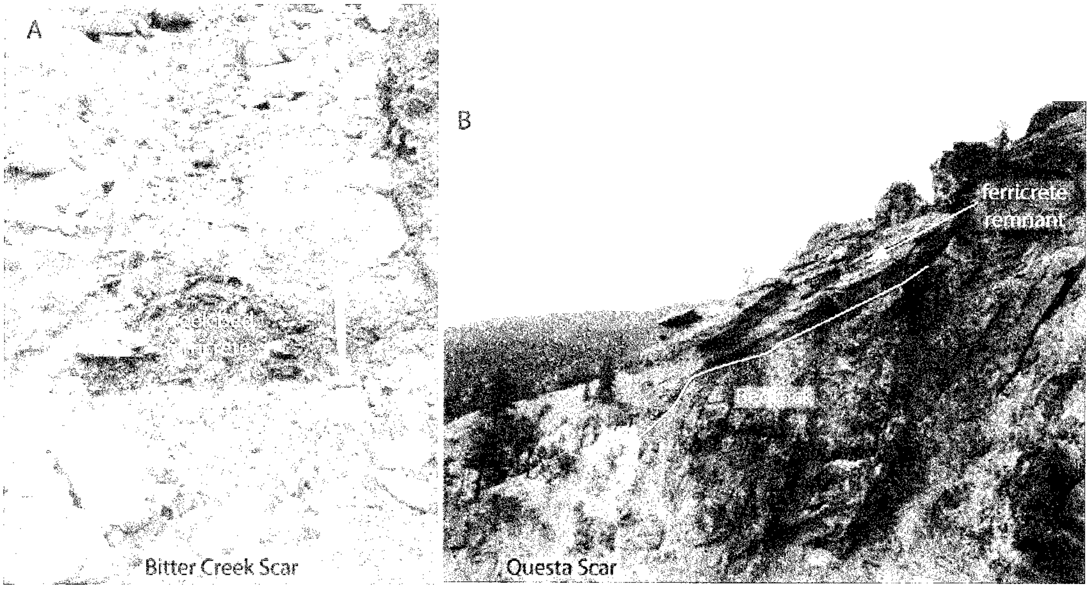

Figure 1-5. Ferricretes preserved in the landscape. A) Modern ferricretes in the RRV often form in streambeds at the base of scars. B) Ferricretes stranded high above the present scar base are resistant to erosion and form inverted topography where an old creek bed now forms a local high point.

A study in Creede, CO, which is on the western edge of the San Luis basin approximately 240 km northwest of Questa, NM, used alunite and jarosite ages and stable isotope compositions to reconstruct landscape evolution. As at Questa, older alunite-group minerals at Creede were heavier with respect to δD than younger samples (Rye et al., 2000). This study concluded that episodic regional uplift was responsible for both the age and isotopic progressions. Lueth et al. (2006) hypothesized that the RRV developed in a manner similar to Creede, CO, but they noted that sample ages reflected contamination with hypogene clay and were probably much younger than their results showed. It is impossible to evaluate the degree of contamination in Creede samples because those workers used conventional K/Ar, rather than $^{40}Ar/^{39}Ar$, geochronology.

This thesis refines Lueth et al.'s 2006 model for landscape evolution in the RRV based on new age and stable isotope data determined after minimizing silicate contamination.

The conceptual model for alteration scar development and the ways in which RRV erosion is linked to regional landscape evolution are presented in chapter four.

2. THE EFFECTS OF HF ON PURE JAROSITE

2.1. Introduction

Although hydrothermal jarosite has been dated by the $^{40}Ar/^{39}Ar$ method with a high degree of precision (Lueth et al., 2005), supergene jarosite does not consistently produce high-precision argon ages (Vasconcelos, 2003; Lueth et al., 2006). Removing older potassium-bearing phases that contaminate supergene samples and increase apparent age (Vasconcelos et al., 2003; Lueth et al., 2006) is essential to determining the timing of supergene jarosite formation. HF has been used to remove silicates from both jarosite and alunite prior to geochronology and stable isotope analysis, but studies that have done so have not critically evaluated the effects of HF on these minerals.

This chapter describes an experiment conducted on pure, hydrothermal jarosite of known age and on a mixture of that pure jarosite with pure sanidine of known age. This experiment was designed to answer the following questions:

1. What are the effects of HF on jarosite crystal chemistry and D/H ratios?
2. What are the effects of HF on jarosite's apparent age?
3. How do silicate contaminants affect the apparent age of jarosite samples?
4. How long does it take to dissolve sanidine from a jarosite sample?

2.2 Methods

2.2.1 Sample Preparation

Two series of experimental samples, A samples and B samples, were prepared for this study. "A" samples are pure, "gem-quality," hypogene jarosite (PB) from Peña Blanca, Mexico (Figure 2-1a). PB is predominantly jarosite with microscopic fluid inclusions (Figure 2-1b). PB is preferable to RRV jarosite for experimental work because it has been characterized chemically (Papike et al., 2006) and dated multiple times via both laser and furnace step-heating at the New Mexico Geochronology Research Lab (NMGRL), yielding a reproducible age of 9.5 ± 0.060 Ma (Lueth et al., 2005). Sample B is an 85:15 mixture of PB and Fish Canyon sanidine (FC-2), which has an assigned age of 28.02 Ma and is routinely used as a neutron flux monitor in $^{40}Ar/^{39}Ar$ analyses.

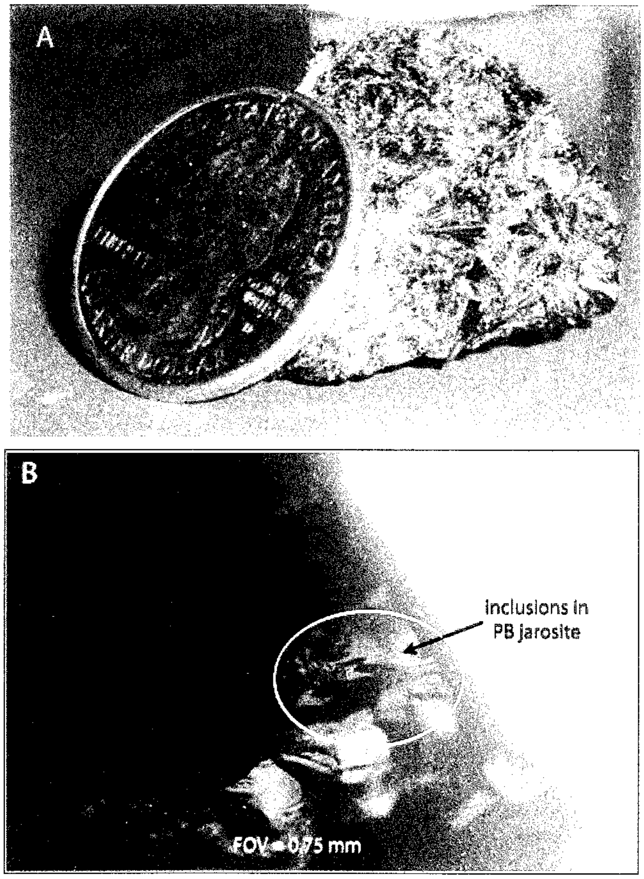

Figure 2-1. Peña Blanca jarosite (PB). A) Hand specimen of PB with large crystals; B) photomicrograph of PB showing aligned inclusions. FOV = field of view.

PB and FC-2 were crushed separately in a piston crusher and sieved to produce a maximum grain size of 270 mesh (58 μm). 400 mg of A samples and 470 mg of B samples (400 mg PB + 70 mg FC-2) were treated in 40mL of 25% HF for 0, 30, 240, and 480 min. HF was decanted after treatment, and samples were rinsed with DI water three times before being dried overnight in a 70°C oven. All samples experienced significant mass loss during HF treatment. Mass loss may be due to sample dissolution, to mechanical removal during decanting, or to some combination of both. Samples that underwent longer treatment times experienced greater mass loss, so jarosite dissolution is likely (Table 2-1).

Table 2-1. Experimental Samples

Sample	Description	Time in HF (min)	Initial Mass (mg)	Final Mass (mg)	Mass Loss (mg)	% mass loss
A-0*,#	PB jarosite	0	398.4	398.4	0	0
A-30#	PB jarosite	30	399.3	215.6	183.7	46
A-240	PB jarosite	240	400.0	174.7	225.3	56
A-480*	PB jarosite	480	399.6	165.6	224.9	56
B-0*	PB + FC-2	0	469.4	469.4	0	0
B-30*	PB + FC-2	30	469.9	272.1	197.8	42
B-240	PB + FC-2	240	470.0	203.9	266.1	57
B-480	PB + FC-2	480	472.0	184.3	287.7	61

*Dated samples

Stable isotope ratios determined

Sanidine dissolution rates were determined by placing 73 mg of crushed FC-2 in a Teflon beaker with 40mL of 25% HF. This beaker was monitored every 5 minutes to determine how long it took the sanidine to dissolve.

2.2.2. *Characterization*

Experimental samples were characterized by electron microprobe analysis (EMPA) at the New Mexico Bureau of Geology and Mineral Resources (NMBGMR) to assess morphological and chemical changes to jarosite after HF treatment. Quantitative chemical analysis was conducted on polished grain mounts, which were made by loading samples into 4-hole epoxy trays. Epoxy was cured overnight in a 50°C oven. Grain mounts were then hand-polished, using 30, 15, 6, and 1 μm diamond powders.

Morphological analysis using secondary electron imaging (SEI) was conducted on unpolished grains of each experimental sample mounted on carbon tape.

EMPA was conducted on a Cameca SX-100 microprobe. The microprobe is equipped with three wavelength dispersive spectrometers in addition to secondary electron (SE) and high speed back-scattered electron (BSE) detectors. The microprobe was operated with a 10 nA beam current and 10 μm spot size at 15 keV to minimize Na volatilization (Papike et al., 2006). Counting times were 20 s for major elements, 40 s for minor elements (F, Cl), and 60 s for trace elements (As, Mo). F was analyzed to determine whether or not F-bearing minerals formed after HF treatment; no evidence of new mineral precipitation was found.

2.2.3. $^{40}Ar/^{39}Ar$ Geochronology

Chemical composition can be evaluated by EMPA, but dating of samples is necessary to determine the effects of HF on apparent age. Twenty-four to thirty-five mg subsamples of each aliquot were wrapped in copper buckets and placed in 6-hole, machined Al disks with FC-2 as the flux monitor. Packets were irradiated at the USGS TRIGA reactor in Denver for 1 hour. Analyses were corrected for neutron-induced interfering reactions using the following correction factors: $(^{39}\text{Ar}/^{37}\text{Ar})_{\text{Ca}} = 0.0007 \pm 5 \times 10^{-5}$, $(^{36}\text{Ar}/^{37}\text{Ar})_{\text{Ca}} = 0.00028 \pm 1 \times 10^{-5}$, $(^{38}\text{Ar}/^{39}\text{Ar})_{\text{K}} = 0.013$, $(^{40}\text{Ar}/^{39}\text{Ar})_{\text{K}} = 0.01 \pm 0.002$. 7-10 mg of irradiated material was distributed evenly across the bottom of 4 x 4 mm square holes in a 9-hole copper laser tray. Samples A-0, A-480, B-0, and B-30 were step-heated with a CO_2 laser up to 16W at NMGRL. The heating schedule for each sample is listed in Appendix C.

Jarosite's sulfate and hydroxyl sites volatilize when the mineral is step-heated, so cleaning the gas during extraction is an important component of jarosite geochronology.

Insufficient removal of reactive gases leads to beam suppression, reflected by poor regressions (Figure 2-2). The mechanized cryotrap that is usually attached to the argon extraction line was not working when this experiment was conducted, so two different methods were tested to trap the volatilized water and SO_2. Initially, a Dewar flask filled with a mixture of acetone and dry ice was placed on a cold finger between the laser and 2nd stage. This trap was ineffective (Figure 2-2 A and B). The second trap consisted of a Dewar flask of liquid nitrogen placed on a stainless steel "finger" in the extraction line between the laser and 2nd stage. This cold trap effectively removed the reactive gases (Figure 2-2 C and D). Gas was further cleaned by 2 SAES GP-50 getters for 900 seconds. Once sample gas was isolated in the mass spectrometer, the extraction line was pumped out. Cold trap gases were qualitatively analyzed using a quadrupole mass spectrometer attached to the roughing line. The quadrupole showed that the cold trap had removed two gases in measurable concentrations: SO_2 (mass = 64) and water (mass = 18). Trapped argon was below quadrupole detection limits.

Argon isotope ratios were measured using an electron multiplier on an MAP-215-50 mass spectrometer operated in static mode. Blanks were monitored throughout the analysis and corrected by bracketing. Plateaus are defined as three or more contiguous degassing steps that overlap at 95% confidence level (2-sigma) and contain at least 50% of the sample gas.

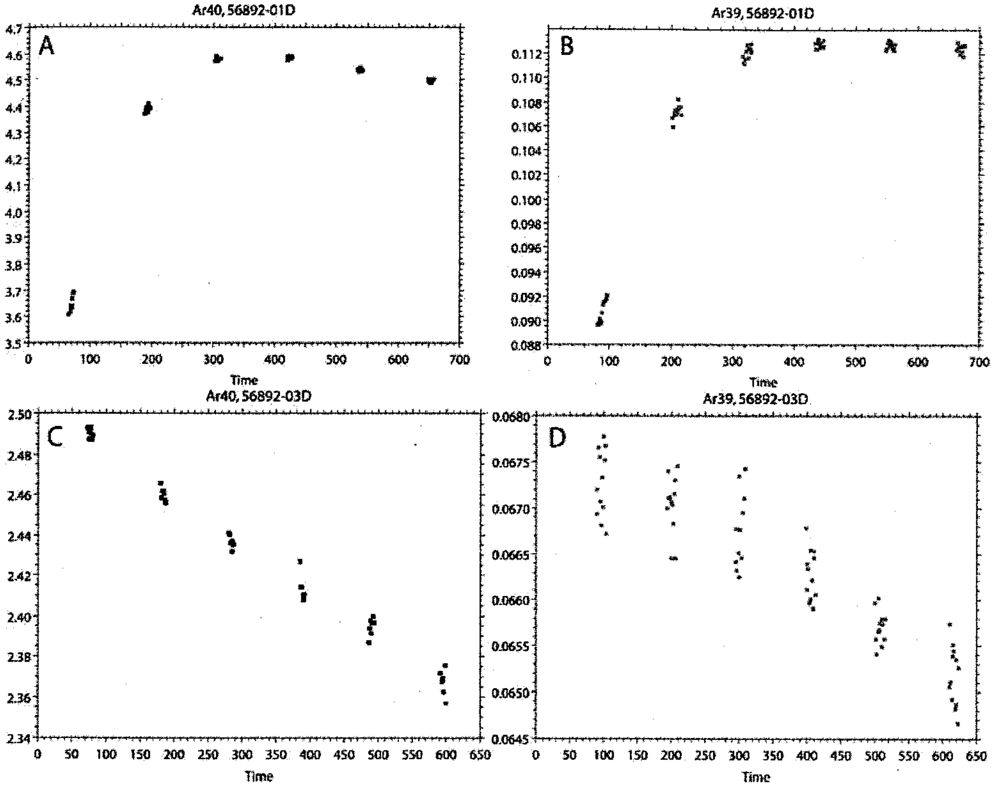

Figure 2-2. The effectiveness of cold traps in cleaning jarosite gas. Cold trap procedures were tested on sample A-0 (irradiation number 56892). Regressions for ^{40}Ar (A) and ^{39}Ar (B) with the acetone-dry ice cold trap trap show that this method of removing reactive gas was ineffective. A second aliquot of sample A-0 was analyzed with the liquid nitrogen cold trap added to the extraction line. Regressions for ^{40}Ar (C) and ^{39}Ar (D) improved after applying the liquid nitrogen cold trap (see text).

2.2.4. Hydrogen isotope analysis

In addition to age determinations, D/H ratios were measured on samples A-0 and A-30 to evaluate the degree to which jarosite hydrogen exchanged with HF during sample treatment. Samples were incinerated at 1450°C in a TC/EA high temperature reduction furnace, producing H_2 gas, which was analyzed in the mass spectrometer. All isotopic measurements were made by continuous flow mass spectrometry on a Finnigan MAT Delta Plus XP.

Raw δD values were corrected using solid standards with known values (δD_{HEKA} = -61‰, δD_{CH-7} = -100‰). D/H ratios of samples and standards were measured relative to an H_2 reference gas with a δD value of -52‰. The calculated δD of the sample was controlled, in part, by the relative size of the sample peak to reference peak, and the correction factor took this relationship into account. The reference gas becomes depleted over time, affecting δD, so the same solid standards were analyzed throughout the run to monitor reference gas depletion over time. Appendix E has a detailed explanation of stable isotope correction factors.

2.3. Results

2.3.1. EMPA Characterization results

Significant potassium loss during HF treatment would render jarosite undatable, so EMPA analysis was focused on the A-site cations (see chapter one). Sample A-0 has 7.93 to 9.74 wt% K_2O with an average of 8.89 wt% (Appendix D). Potassium concentrations of HF-treated samples overlap with potassium concentrations of untreated samples. EMPA on pure PB jarosite analyzed at the University of New Mexico had a K_2O range of 8.79 to 10.10 wt % with an average of 9.30 wt % (Paul Burger, pers. comm.). This discrepancy may be related to natural compositional variations or interlaboratory calibration problems. This sample has a negligible natrojarosite component with Na_2O below detection limits (<453 ppm). A-site cations (Na + K) do not add up to one, suggesting that some component of the jarosite was unanalyzed.

The A-site can house several different monovalent, divalent, and trivalent cations as described in chapter one (Papike et al., 2006 and Smith et al., 2006). Wave-length Dispersive Spectrometer scans of untreated PB (A-0) did not determine which A-site component was unanalyzed. Low A-site cation totals could indicate Na volatilization rather than substitution by a different cation (Papike et al., 2006). Low totals could alternatively indicate the presence of H_3O^+. Table 2-2 provides a summary of analyses with maximum and minimum K_2O, and appendix D provides chemistry for all points analyzed.

Table 2-2. Representative chemical analyses (wt % oxides).

	Minimum K_2O	**Maximum K_2O**	**Minimum K_2O**	**Maximum K_2O**
Point Name	**A-0-010**	**A-0-09**	**A-480-8**	**A-480-9**
time in HF (min)	0	0	480	480
K_2O	7.93	9.43	7.32	9.43
Na_2O	-0.04	0.01	-0.02	0.01
FeO (measured)	42.15	42.1	42.38	43.63
Fe_2O_3 (calculated)*	46.78	46.74	47.04	48.43
Al_2O_3	1.15	1.34	0.77	0.69
MoO_3	0.26	0.29	0.24	0.18
As_2O_3	0.31	0.1	0.38	0.29
SO_2 (measured)	24.7	24.81	24.57	24.78
SO_3 (calculated)$^+$	30.87	31	30.7	30.97
P_2O_5	0.06	0.07	0.09	0.05
F	0.25	0.12	0.02	0.09
Cl	0.03	0.01	-0.01	0.01
H_2O	12.4	10.88	13.47	9.84
Total	87.32	88.98	86.52	90.06
Cations				
K	0.79	0.93	0.74	0.93
Na	0	0	0	0
Fe	2.76	2.72	2.81	2.81
Al	0.11	0.12	0.07	0.06
Mo	0.01	0.01	0.01	0.01
S	1.81	1.8	1.83	1.79
P	0	0	0.01	0
As	0.02	0	0.02	0.01
F	0	0	0	0
Cl	0	0	0	0
Total	11.5	11.58	11.48	11.62
A (Na+K)	0.79	0.93	0.74	0.93
B (Fe+Al+Mo)	2.87	2.85	2.89	2.88
X (S + P + As)	1.83	1.8	1.85	1.81

$* Fe_2O_3 = FeO * 1.11$
$^+ SO_3 = SO_2 * 1.25$

Although crystal chemistry is consistent for treated and untreated samples, HF treatment does cause morphological changes in jarosite. Treated grains from all samples are pitted and rounded relative to untreated samples. The degree of pitting increases with treatment time. Pits are triangular and aligned along discrete planes, similar to the orientation of inclusions evident under the petrographic microscope (Figure 2-3).

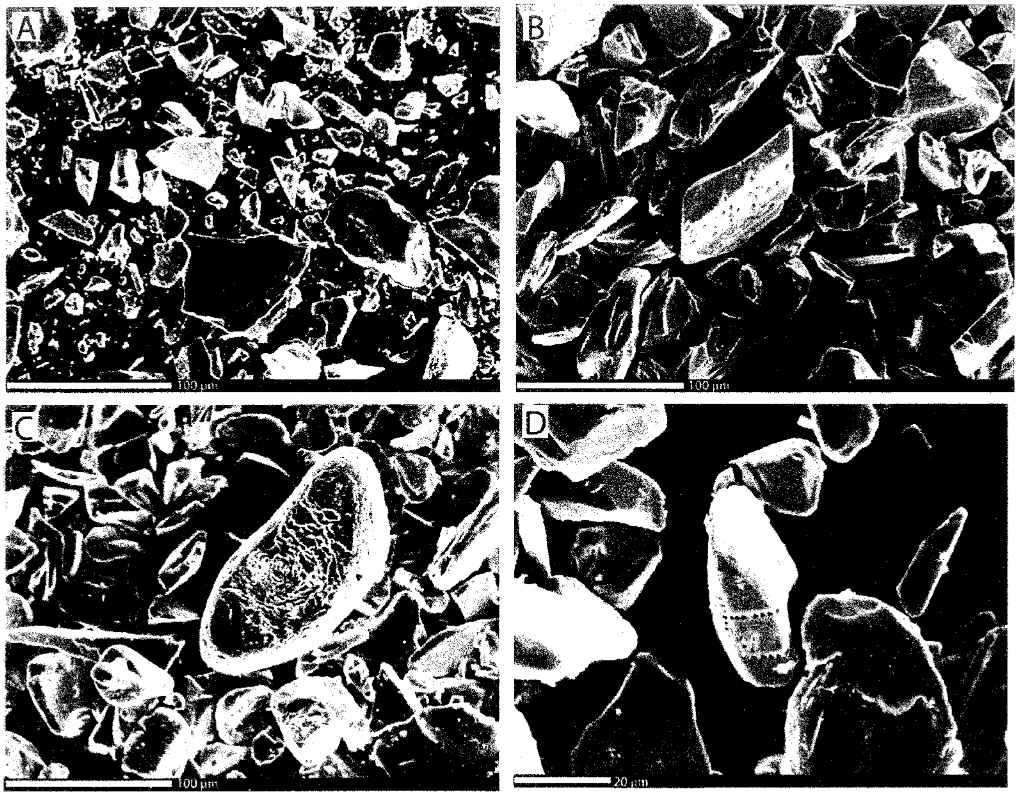

Figure 2-3. SE images of unpolished samples show the effects of HF on PB jarosite. A) Grains in A-0 are angular and unpitted. Grain size is variable, and the smallest grains are dust-sized. Large grains (>58 μm) show that sieving did not successfully control maximum grain size; B) A-30 grains are rounded and pitted relative to A-0; C) A-240 grains are more rounded and pitted than A-30; D) Grains in A-480 have pits along discrete planes, possibly due to preferential HF etching of fluid inclusions. The finest grains have been completely dissolved from this sample.

EMPA characterization allows the monitoring of sanidine dissolution in the artificial mixture of PB with FC-2 (B-samples). BSE images of unpolished B-0 show that

FC-2 can be distinguished from PB in the microprobe. X-ray scans showed that lower Z (darker) phases are sanidine (i.e. Si and K but no S or Fe) while brighter phases are jarosite (i.e. K, S and Fe but no Si) (Figure 2-4). Although FC-2 is clearly visible in sample B-0, only one grain of FC-2 was evident in BSE images of polished B-30. No FC-2 was found in BSE images of B samples treated for more than 30 minutes in HF. FC-2 placed in the beaker of HF disappeared within 25 minutes. Under the experimental conditions, HF dissolves crushed FC-2 in less than 30 minutes.

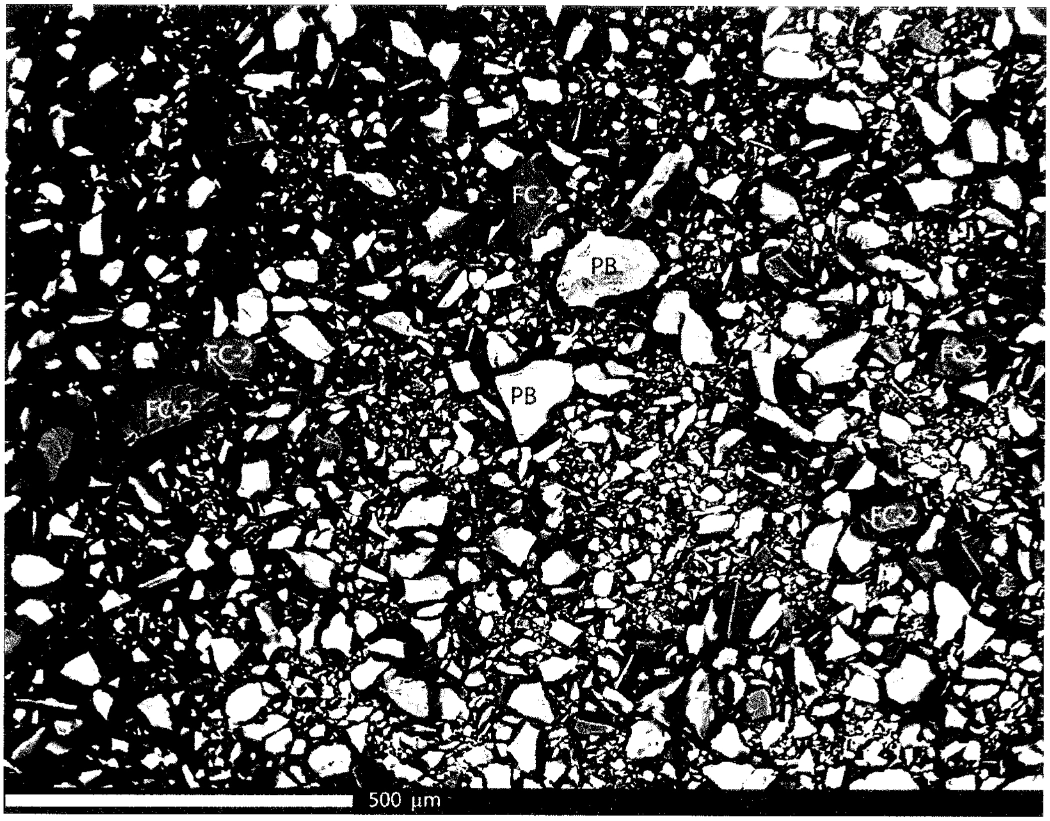

Figure 2-4. BSE images of unpolished B-0 show the relative amounts of PB (high-Z, bright phase) and FC-2 (lower-Z, darker phase).

2.3.2. $^{40}Ar/^{39}Ar$ Geochronology results

^{40}Ar/^{39}Ar ages, like major oxide concentrations, do not change with time in HF. The four analyzed samples produced plateau ages that overlap with each other and with previously-dated PB (Lueth et al., 2005) at 2-sigma. Sample A-0 produced a plateau age of 9.59 ± 0.05 Ma over 100% of the ^{39}Ar released. Sample A-480 produced a plateau age of 9.68 ± 0.08 Ma over 79.3% of the sample gas released. Treated PB (A-480) had high apparent ages in the first three heating steps (Figure 2-5). Sample B-0 produced high apparent ages in the 10-14 W steps, but apparent age decreases in the 16 W step. Sample B-30 did not have old apparent ages in the first three steps, and, unlike B-0, apparent age decreased in the 12-15 W steps (Figure 2-6). A summary of age results are presented in Table 2-3. Heating schedules are provided in Appendix C.

Table 2-3. Summary of age results

Sample	Time in HF (min)	% spectrum in plateau	Apparent age ± 2σ error (Ma)
A-0	0	100	9.59 ± 0.05
A-480	480	79.3	9.68 ± 0.08
B-0	0	81.6	9.60 ± 0.07
B-30	30	79.1	9.58 ± 0.05

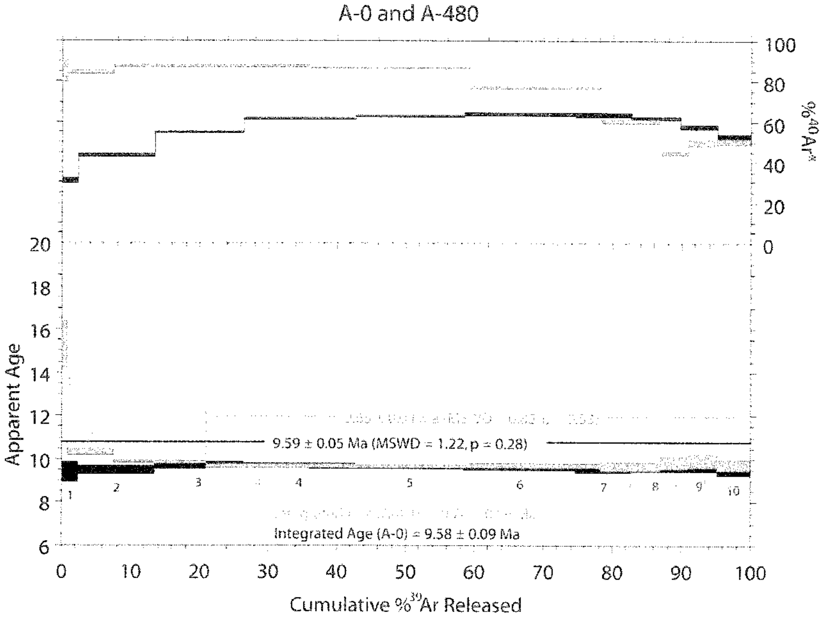

Figure 2-5. Plateau ages for untreated (A-0 - black) and treated (A-480 - green) PB overlap within error. A-480 has a higher radiogenic yield than A-0 over 75% of the spectrum. Old apparent ages at the beginning of the A-480 spectrum may be due to potassium loss along grain edges during HF treatment. Numbers associated with each step refer to laser wattage.

Although apparent ages of untreated and treated samples were identical within error, ^{40}Ar* varied. Radiogenic yield ranged from 29% to 87% in these experimental samples. HF-treated samples (A-480 and B-30) produced higher radiogenic yields than untreated samples (Figures 2-5 and 2-6). Radiogenic yield was low in initial steps, which may be due to atmospheric argon degassing from the edges of the samples (McDougall and Harrison, 1988). Radiogenic yield decreased in higher-wattage steps.

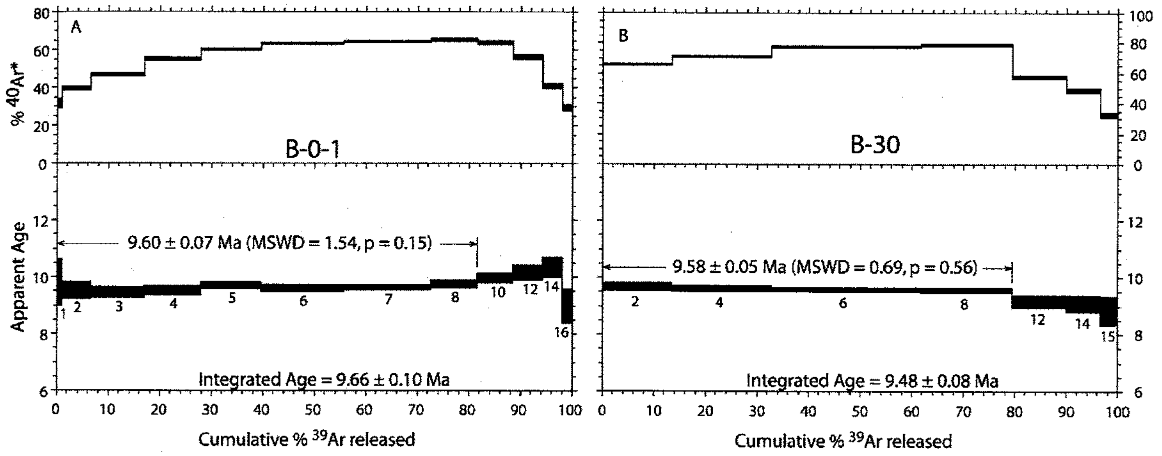

Figure 2-6. Age Spectra. Each step is labeled with the laser power in watts. A) B-0-1 yielded a PB plateau age before climbing in apparent age at high power steps. Older apparent ages in the 10-14W steps may be the result of FC-2 degassing. The decrease in radiogenic yield in these steps and apparent age in the 16W step may be the result of laser coupling with the cover slip instead of the sample; B) B-30's plateau age overlaps within error with pure PB samples. The decrease in apparent age at 12-15W may indicate that FC-2 is not influencing the apparent age of higher wattage steps in this analysis.

2.3.3. Stable Isotope results

Like apparent age, D/H ratios for untreated and treated PB were identical within 2-sigma. Results are summarized in Table 3-4. Standard deviation (1σ) established by standards run in August 2007 was ± 3‰. Standard deviation established by standards run in November 2007 was ± 2‰.

Table 2-4. Summary of stable isotope results

Sample	Time in HF (min)	Date analyzed	δD ± 2σ error (‰)
A-0	0	8/22/2007	-109 ± 6
A-0 (dup)	0	8/22/2007	-116 ± 6
A-0 (dup)	0	8/22/2007	-106 ± 6

A-0 (dup)	0	11/30/2007	-110 ± 4
A-0 (dup)	0	11/30/2007	-111 ± 4
A-0 (dup)	0	11/30/2007	-110 ± 4
A-30	30	11/30/2007	-109 ± 4
A-30 (dup)	30	11/30/2007	-108 ± 4

2.4. Discussion

2.4.1. Effects of HF on crystal chemistry and stable isotope geochemistry

EMPA shows that there is no systematic decrease in the concentration of any major oxides, particularly K_2O, with treatment time (Figure 2-7). However, these analyses were conducted with a relatively large (10μm) beam diameter. Papike et al. (2006) found that a 10 μm beam minimized Na volatilization but averaged fine-scale zones within the crystals. PB jarosite is uniform in composition with little to no zoning (P. Burger, pers. comm.), but the 10 μm beam used to analyze jarosite in this study made it impossible to determine whether HF-treatment created fine-scale gradients in K concentration from core to rim. Incongruent dissolution, preferentially dissolving potassium, would lead to old apparent ages.

HF-treated and untreated PB samples yielded δD values identical to each other within error. These analyses indicate that jarosite hydrogen does not undergo exchange with HF during chemical treatment.

2.4.2. Effects of HF on apparent age

Geochronology results were similar to crystal chemistry and stable isotope results in that HF treatment had no impact on PB's plateau age. Sample A-480 yielded a plateau age identical within 2-sigma to A-0 and to previously dated PB, showing that HF-treated jarosite samples can yield reproducible dates despite dissolution evident in SE images. HF treatment did, however, change PB's age spectrum in two ways: radiogenic yield increased and structure in the age spectrum increased. A-480 produced old apparent ages early in the analysis. B-30, the other treated sample analyzed, does not show the same increase in apparent age in the low wattage steps.

There are three possible explanations for old apparent ages at low power steps (Figure 2-6): excess argon, ^{39}Ar recoil, or potassium loss. It is unlikely that excess argon or ^{39}Ar recoil is responsible for old apparent ages during the initial heating steps. HF preferentially etches samples along discrete planes (Figure 2-3d). These planes may house fluid inclusions, which are common in PB jarosite (Lueth et al., 2005). Fluid inclusions can contain excess argon because they retain the argon signature of precipitating or crystallizing fluids (Kelley, 2002). Preferential removal of these excess argon reservoirs from jarosite during HF etching makes it unlikely is responsible for old apparent ages in the early heating steps.

Although grains in this experiment were fine-grained (< 58 μm), previous studies have determined that ^{39}Ar recoil has little to no effect the plateau ages of alunite-group minerals (see chapter one; Lueth et al., 1998; Polyak et al., 1998; Polyak et al., 2006). Additionally, ^{39}Ar recoil is most likely to affect the apparent age of the smallest particles, which disappear after 8 hours of acid treatment, so it is unlikely that ^{39}Ar recoil is responsible for high apparent ages in the low power steps.

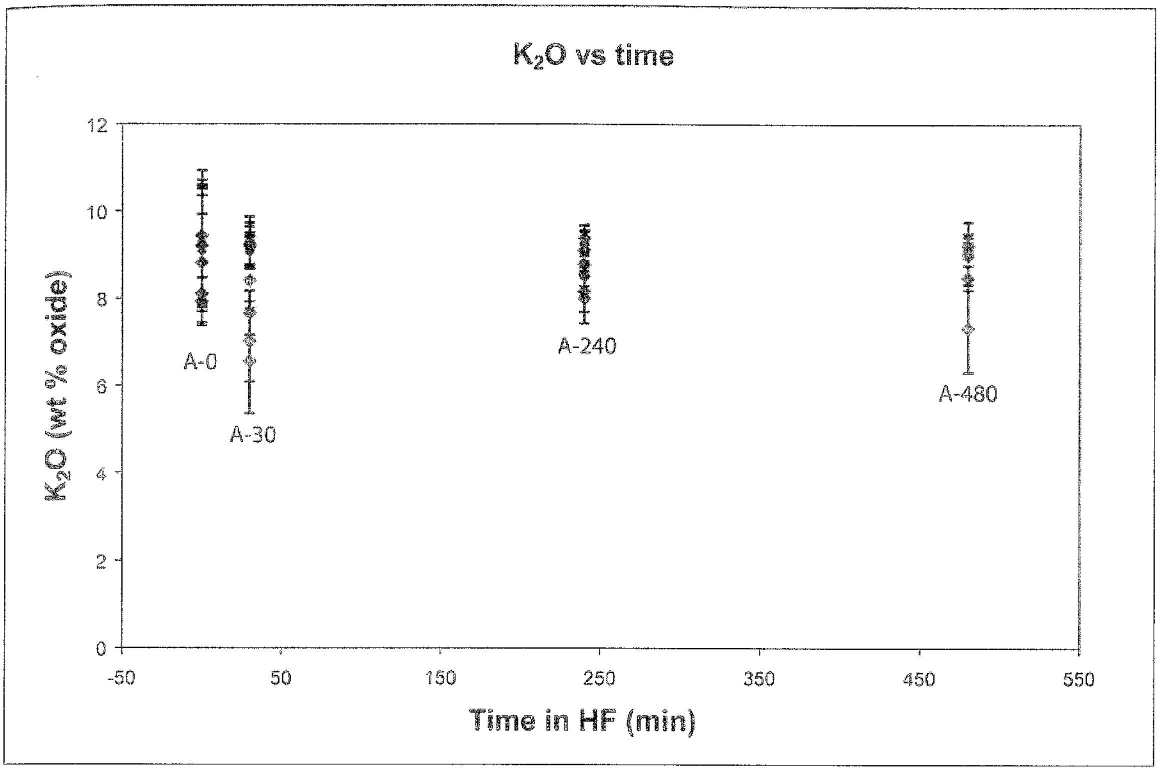

Figure 2-7. K_2O vs. time in HF. K_2O concentration falls within the same range in untreated (A-0) and HF-treated PB jarosite, indicating that there is no systematic decrease in K_2O concentration with time in acid. The blue band outlines the range of K_2O concentration in sample A-0. None of the other major oxides show a systematic decrease with time in acid.

2.4.3. The effects of sanidine on jarosite's apparent age

The above results indicate that jarosite can yield reproducible ages after up to 8 hours of HF treatment, so removing silicate contaminants with HF is feasible. The question of how the silicate contaminants affect jarosite's apparent age remains. Unfortunately, this experiment did not successfully answer this question because the sanidine did not degas.

If sanidine and jarosite degassed completely under the experimental conditions, the sample's apparent age would be controlled by a mixing equation that takes into account K_2O concentration for each phase, relative amount of each mineral in the mixture, and known age for each sample: $\%\,FC\text{-}2 * 28.02\ Ma * [K_2O]_{FC\text{-}2}/(\text{weighted mean } [K_2O])_{mixture} + \%PB * PB\ age * [K_2O]_{PB}/(\text{weighted mean } [K_2O])_{mixture} = $ *expected integrated age of the mixture.* FC-2 has an average K_2O concentration of 12.2 wt % (Bachmann et al., 2002), while PB has an average K_2O concentration of 8.89 wt %. The weighted mean K_2O concentration of an 85:15 mixture of PB and FC-2 is 9.28 wt %. Assuming the plateau age reflects the actual age of the PB jarosite, the expected integrated ages of samples B-0 and B-30 are 12.36 Ma and 12.35 Ma respectively (Table 2-5). Instead, the integrated ages and plateau ages are concordant within error. This discrepancy between expected integrated age and actual integrated age indicates that the mixture did not degas completely during laser step-heating.

Table 2-5. Hypothetical age calculations for B samples

Sample	% FC-2	Age FC-2 (Ma)	% PB	Weighted mean $[K_2O]$	Age PB (Ma)	Expected integrated age (Ma)	Actual integrated age (Ma)
B-0	15	28.02	85	9.28	9.60	13.25	9.66 ± 0.10
B-30	15	28.02	85	9.28	9.58	13.24	9.48 ± 0.08

The degassing behavior of each phase in the mixture controls the apparent age of each heating step. Sanidine degasses at higher temperatures than jarosite when heated in a furnace (McIntosh et al., 1991). This experiment shows that sanidine also degasses at higher wattage when the beam is defocused. Unfortunately, it is difficult to increase the laser power sufficiently to degas the sanidine in this mixture due to jarosite's composition. When jarosite is step-heated with a laser, some of the reactive material in the jarosite accumulates on the cover slip. As this material accumulates, the cover slip becomes opaque to the laser, and the laser degasses the cover slip rather than the sample.

The fact that sanidine-contaminated B samples yielded plateau ages indistinguishable from the uncontaminated A samples, at the 2-sigma confidence interval has two implications. First, this aspect of the experiment failed in that it was impossible to monitor the effects of feldspar on jarosite's age spectrum. However, this experiment also shows that sanidine does not degas during the same heating increments as jarosite, so sanidine contamination in supergene jarosite should not affect apparent age at all.

2.5. Conclusions

This experiment shows that HF can be used to remove silicate contaminants from pure, euhedral jarosite without compromising its datability. Although HF-treated samples showed no major potassium loss and yielded reproducible ages, long treatment times may leach potassium along grain edges, leading to older apparent ages in early heating steps. While this potassium loss had an impact on the size of the plateau, it had no effect on the plateau age. Similarly, HF treatment had no impact on δD, so reconstructing fluid compositions is still possible after HF treatment.

3. EFFECTS OF HF ON SUPERGENE JAROSITE

3.1. Introduction

Coarse-grained hydrothermal jarosite can be treated with HF without any impact on crystal chemistry or apparent age. This chapter focuses on the application of sample preparation techniques developed in chapter two to supergene jarosite from the RRV in an effort to answer the following questions:

1. Does thirty minutes of HF treatment completely remove silicate contaminants from supergene samples?
2. What are the effects of HF on supergene jarosite crystal chemistry?
3. What are the effects of HF on supergene jarosite apparent age?

RRV jarosite forms as a weathering product in hydrothermally-altered volcanic rocks, and mechanically separating jarosite from older, fine-grained, K-bearing silicate contaminants, including sanidine and illite, is difficult. These silicates are of known age, making it possible to evaluate the effects of contamination on apparent age.

The timing of volcanism, plutonism, and hydrothermal alteration in the RRV was first established by K/Ar dating of sanidine, hornblende, and biotite as well as fission track dating of zircon and apatite (Lipman et al., 1986). $^{40}Ar/^{39}Ar$ dating of minerals from volcanic and intrusive rocks has refined the geochronological model of Latir volcanic field development (Tappa et al., 2008; Zimmerer, 2008; Czamanske et al., 1990). Table

4-1 summarizes the most recent age determinations for precaldera volcanic rocks, Amalia tuff, and post-caldera intrusions from Tappa et al. (2008) and Zimmerer (2008). Hypogene alunite dating confirms that hydrothermal alteration occurred at 24.86 ± 0.15 Ma (Lueth et al., 2006), soon after the eruption of the Amalia tuff.

Table 3-1. Summary of Latir volcanic field $^{40}Ar/^{39}Ar$ age data from Tappa et al. (2008) and Zimmerer (2008).

Sample type	Rock type	Phase dated	Apparent Age (Ma)
Pre-caldera	andesite	Hornblende	28.31 ± 0.19
Pre-caldera	Tetilla Peak rhyolite	Sanidine	27.89 ± 0.06
Pre-caldera	Quartz latite	Biotite	27.76 ± 0.10
Pre-caldera	Cordova Creek rhyolite	Sanidine	25.27 ± 0.06
Caldera	Amalia tuff	Sanidine	25.23 ± 0.05
Pluton	Cabresto Lake	K-spar	24.70 ± 0.2
Pluton	Cabresto Lake	Biotite	24.68 ± 0.11
Pluton	Rio Hondo	K-spar	21.96 ± 0.13
Pluton	Rio Hondo	K-spar	21.73 ± 0.12
Pluton	Rio Hondo	K-spar	21.58 ± 0.09
Pluton	Rio Hondo	Biotite	21.08 ± 0.10

Although Meyer and Leonardson (1990) hypothesized that clays formed during silicate weathering, Graf (2008) found that alteration scar clays are hypogene in origin. Illite from the RRV has been submitted for dating, but the results are not available yet. Therefore, I have assumed that hydrothermal clay is contemporaneous with hydrothermal alunite and that all silicates are of known, Oligocene to Miocene age.

Untreated RRV jarosite was dated in 2006, and age spectra show that apparent age increased from Pleistocene or Pliocene in early heating steps to late Oligocene-Miocene in later steps, suggesting the degassing of primary volcanic feldspars and hypogene clays (Lueth et al., 2006).

3.2. Methods

3.2.1. Sample Preparation

RRV jarosite was treated with HF in an effort to remove silicate contaminants. Jarosite was scraped from the surfaces of drill core and hand samples. Large contaminants were removed manually. This process left 72.3 to 101.5 mg of RRV material, which was treated with 10 mL of 25% HF for 30 minutes. Treatment time was based on the amount of time necessary to completely dissolve FC-2 sanidine in HF (see chapter two). Samples were rinsed three times in deionized water after decanting the HF, and dried in a 70°C oven for 1.5 hours. RRV jarosite samples, like the experimental samples, lost between 59% and 74% of their initial mass during the process of HF treatment, rinsing, and decanting (Table 3-2).

Table 3-2. RRV Samples

Sample Name	Composition*	Time in HF (min)	Initial Mass (mg)	Final Mass (mg)
PIT VWL 0007	RRV jar + sil	30	72.3	29.8
PIT VWL 0005	RRV jar + sil	30	99.2	27.6
ESS VWL 0001	RRV jar + sil	30	101.5	41.0
CAS VWL 0002	RRV jar + sil	30	82.0	21.0

*jar = jarosite; sil = silicates (clay, kspar, quartz)

3.2.2. Characterization

Both treated and untreated RRV samples were characterized by EMPA on the NMBGMR Cameca SX-100 microprobe described in chapter three to evaluate the effects of HF on crystal chemistry and to determine the degree of contamination. Grain mounts were made for EMPA characterization by loading samples into 9-hole epoxy trays. As with experimental samples described in chapter two, epoxy was cured overnight in a 50°C oven, and grain mounts were hand-polished, using 30, 15, 6, and 1 μm diamond powders.

Grain size impeded quantitative chemical characterization of RRV samples. RRV grains are, on average, less than 10 μm in diameter, making it difficult to conduct quantitative analyses with the broad beam recommended to reduce Na volatilization

(Papike et al., 2006). Instead, analyses were conducted with a 5 μm beam. Even the 5 μm beam exceeded the diameter of most individual jarosite crystals, so areas with clusters of adjacent jarosite grains were chosen (Figure 3-1), and chemical analyses reflect the average composition for all jarosite grains in the vicinity of the beam.

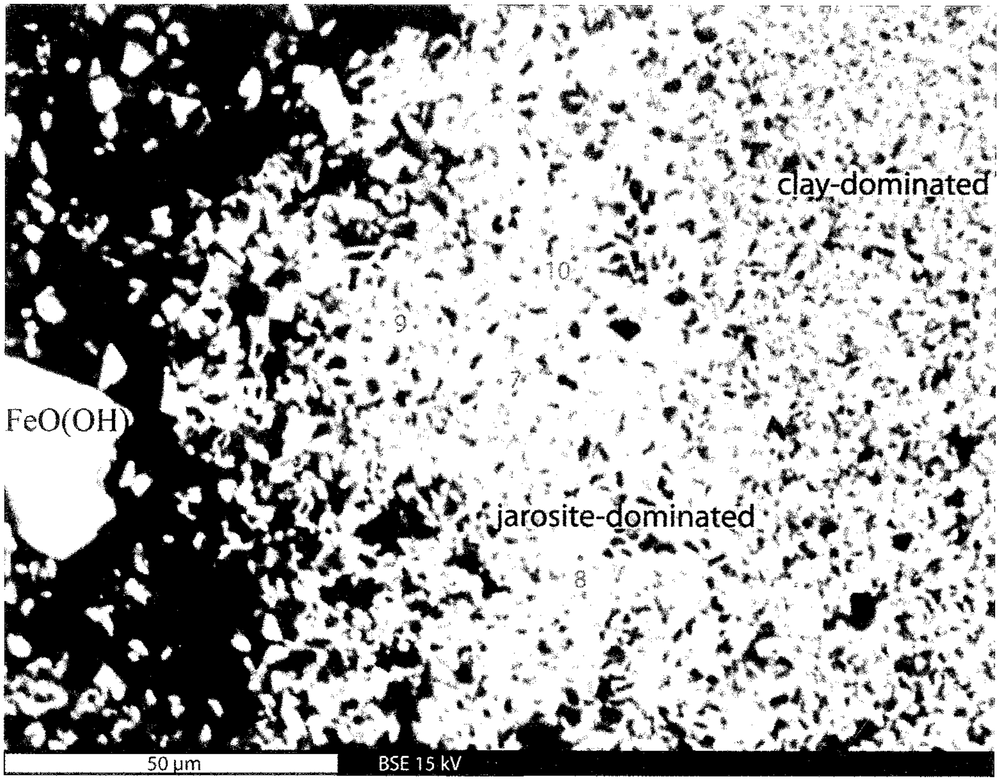

Figure 3-1. BSE image of intergrown clay and jarosite (sample CAS VWL 0002). RRV jarosite is fine-grained and individual crystals are typically smaller than the 5 μm beam. See appendix D for quantitative chemical data.

3.2.3. ^{40}Ar/^{39}Ar Geochronology

HF-treated samples were dated to evaluate the effects of HF on apparent age. 16-32 mg of each sample was placed in 6-hole, machined Al disks with FC-2 as the flux monitor. RRV samples were expected to be younger than PB (see chapter two), so disks were irradiated at the USGS TRIGA reactor in Denver for 30 minutes instead of one hour. Analyses were corrected for neutron-induced interfering reactions using the following correction factors: $(^{39}Ar/^{37}Ar)_{Ca} = 0.00068 \pm 5 \times 10^{-5}$, $(^{36}Ar/^{37}Ar)_{Ca} = 0.00028 \pm 2 \times 10^{-5}$, $(^{38}Ar/^{39}Ar)_K = 0.01077$, $(^{40}Ar/^{39}Ar)_K = 0 \pm 0.0004$.

After irradiation, samples were laser step-heated to extract gas. In order to maximize the amount of sample exposed to the laser, 6-8 mg of irradiated material was distributed evenly across the bottom of 4 x 4 mm squares in a 9-hole laser tray. Each sample was step-heated with a CO_2 laser up to 9W rather than 16W because experimental samples showed that higher-power steps degas the cover slip rather than the sample (see section 2.4.3). The heating schedule for each sample is listed in Appendix B.

Sample gas was cleaned using a mechanized cryotrap operated at $-140^{\circ}C$ and SAES getters for 15 minutes. The gas was then expanded into NMGRL's MAP-215-50 mass spectrometer where it was analyzed in static mode. Blank values were monitored throughout the analysis and corrected by bracketing. Plateaus are defined as three or more contiguous degassing steps that overlap at 95% confidence level (2-sigma) and contain at least 50% of the sample gas.

3.3. Results

3.3.1. EMPA Characterization results

Determining the types of contaminants present in RRV samples and the degree of contamination is essential to interpreting age data. Both treated and untreated RRV samples consist of a mixture of jarosite, quartz, potassium feldspar, clay, and goethite (Figure 3-2). HF-treated samples appear to have fewer contaminants than untreated samples, suggesting that HF treatment is responsible for dissolving some silicates. Although HF treatment removed some contaminants, K-bearing silicate phases make up ~20-30% of HF-treated samples based on estimates using BSE images.

Monitoring potassium concentrations in HF-treated samples is also essential to interpreting age data. All quantitative chemical analyses produced low cation totals because grains were generally smaller than the beam (Table 3-3). Although cation totals were low, K_2O concentration does not systematically decrease between untreated and HF-treated aliquots of PIT VWL 0007, ESS VWL 0001, and CAS VWL 0002 (Figure 3-3). Unfortunately, there was not enough untreated material of PIT VWL 0005 to compare potassium concentrations in this sample. Table 3-3 presents chemical data for analyses closest to the mean K_2O concentration for each sample. Detailed chemical data is provided in appendix D.

Table 3-3. Representative analyses for RRV jarosite given as weight % oxides and cations.

Sample	**PIT VWL 0007**	**PIT VWL 0007**	**ESS VWL 0001**	**ESS VWL 0001**	**CAS VWL 0002**	**CAS VWL 0002**
time in HF (min)	**0**	**30**	**0**	**30**	**0**	**30**
K_2O	7.15	6.82	6.79	7.17	7.03	5.57
Na_2O	0.11	0.13	0.07	0.21	0.12	0.43
FeO	39.76	33.40	37.69	39.57	33.51	34.99
Fe_2O_3 (calc)*	44.13	37.07	41.83	43.92	37.20	38.84
Al_2O_3	0.27	0.75	0.33	0.25	0.34	0.37
As_2O_3	0.04	0.04	0.01	0.00	0.03	0.05
MoO_3	0.00	0.00	0.00	0.00	0.00	0.00
SO_2	23.34	19.60	22.23	22.93	20.69	20.98
SO_3 (calc)$^+$	29.16	24.49	27.78	28.65	25.86	26.22
P_2O_5	0.43	0.16	1.00	1.22	0.18	0.11
SiO_2	0.78	1.22	0.82	0.48	0.14	0.65
H_2O	10.88	9.42	10.53	10.91	9.35	9.62
F	0.01	0.00	0.07	0.09	0.00	1.31
Cl	0.09	0.41	0.11	0.06	0.29	0.49
Total	82.83	71.94	79.65	82.88	71.68	74.55
Cations						
K	0.754	0.831	0.740	0.754	0.863	0.664
Na	0.017	0.024	0.012	0.034	0.023	0.078
A-site total	0.771	0.854	0.752	0.788	0.885	0.742
Fe	2.749	2.668	2.692	2.730	2.697	2.738
Al	0.026	0.084	0.034	0.025	0.039	0.041

As	0.002	0.003	0.000	0.000	0.002	0.003
B-site total	2.777	2.754	2.726	2.754	2.738	2.781
S	1.810	1.755	1.781	1.774	1.868	1.841
P	0.030	0.013	0.073	0.085	0.015	0.009
X-site total	1.840	1.768	1.853	1.859	1.883	1.850
Fe/Fe+Al	0.991	0.969	0.988	0.991	0.986	0.985
Na/Na+K	0.022	0.028	0.015	0.043	0.025	0.105

* $Fe_2O_3 = FeO * 1.11$

$^+SO_3 = SO_2 * 1.25$

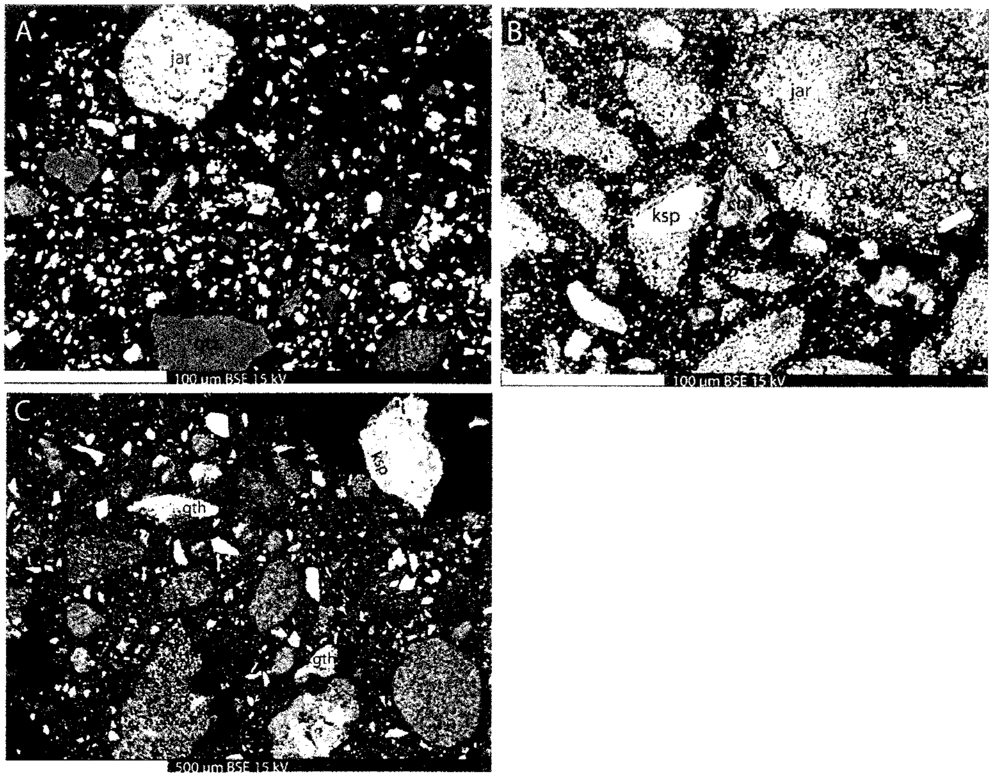

Figure 3-2. BSE images of untreated RRV samples show silicates and goethite mixed with jarosite. A) PIT VWL 0007; B) ESS VWL 0001; C) CAS VWL 0002. Sample PIT VWL 0005 had too little material to do EMPA work on untreated samples. jar = jarosite, qtz = quartz, ksp = potassium feldspar, chl = chlorite, gth = goethite.

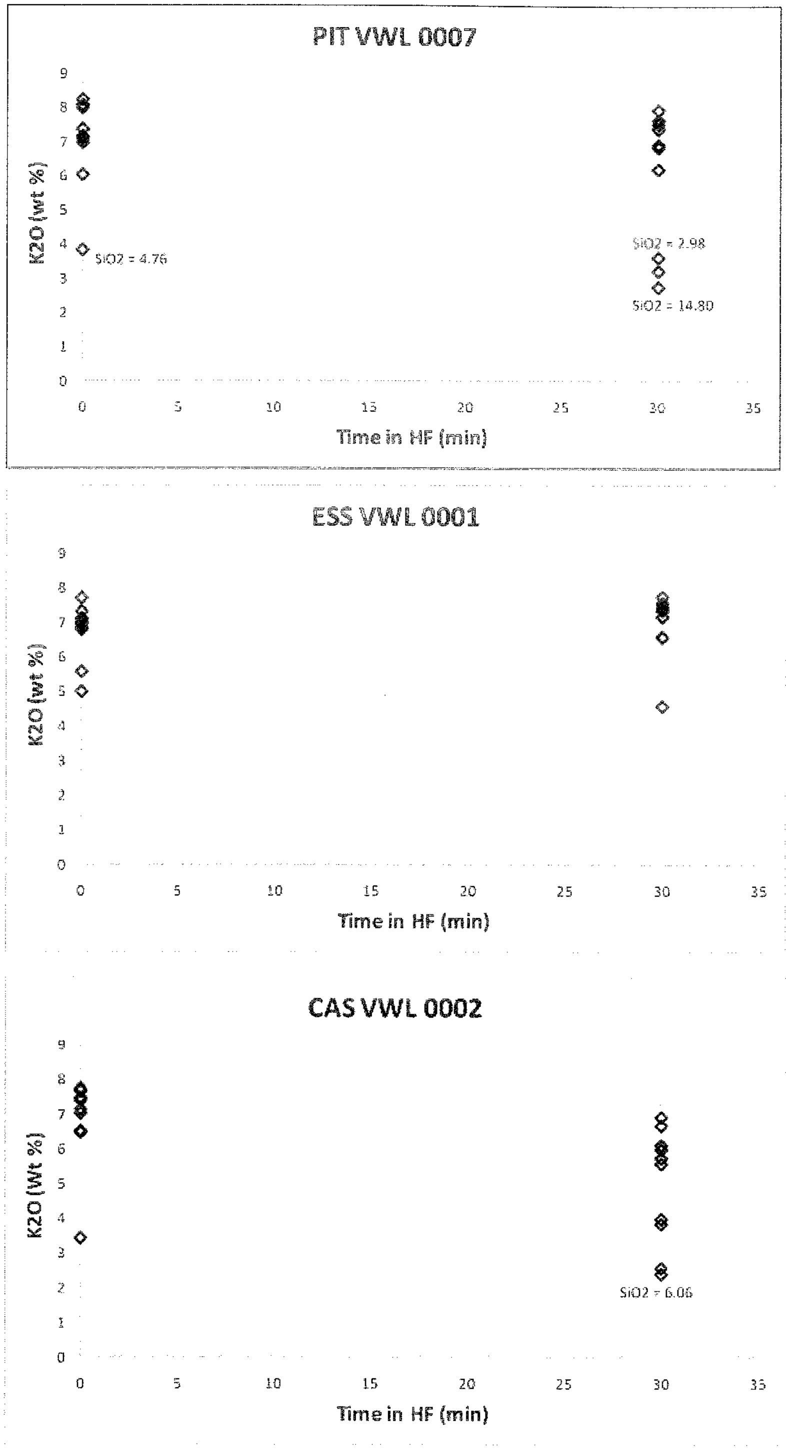

Figure 3-3. K_2O vs time in HF. Although cation totals are low, it is still possible to compare the relative K_2O concentrations in untreated (time in HF = 0 minutes) and treated samples (time in HF = 30 minutes). The blue field in each plot shows the range of K_2O concentrations in each untreated sample. For the most part, quantitative chemical analyses on HF-treated samples fall into the range defined by untreated samples unless the analysis had a relatively high SiO_2 concentration.

Three analyses in the treated aliquot of sample PIT VWL 0007 and two analyses in treated CAS VWL 0002 appear to have lower K_2O concentrations than measurements on the untreated sample. However, the analyses that have low K_2O concentrations have relatively high SiO_2 concentrations. Analysis 3 in the HF-treated aliquot of PIT VWL 0007 was collected from a grain that has a mottled appearance in BSE and is probably a mixture of jarosite and clay (Figure 3-4a). This analysis had 14.8 wt % SiO_2. Analysis 10 in the HF-treated aliquot of CAS VWL 0002 was collected from a grain less than 5 μm in diameter with 6.06 wt % SiO_2 (Figure 3-4b). These analyses on both PIT VWL 0007 and CAS VWL 0002 have cation totals of approximately 50% of the expected stoichiometric values for pure jarosite, suggesting that these phases are mixtures of jarosite and clay.

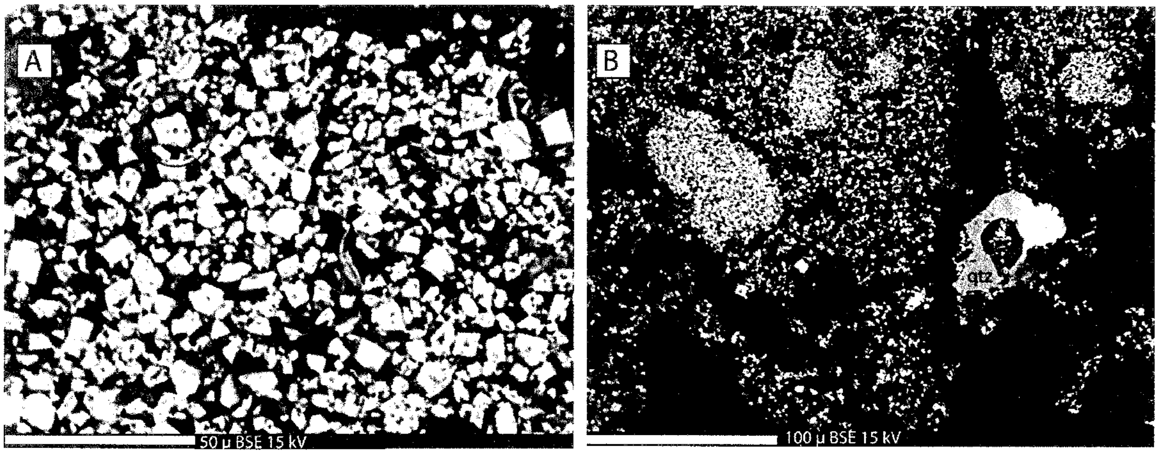

Figure 3-4. Low K_2O analyses. Analyses of HF-treated samples that had relatively low K_2O values tended to have relatively high SiO_2 concentrations. A) Analysis 3 in HF-treated PIT VWL 0007 conducted on a grain with a mottled appearance, suggesting a mixture of low-Z clay (darker phase) and higher-Z jarosite (bright phase). B) Analysis 10 in HF-treated CAS VWL 0002 was collected from a small grain with 6.06 wt % SiO_2. The circled red dots show locations of analyses.

3.3.2. $^{40}Ar/^{39}Ar$ Geochronology results

Age determinations for jarosite reflect changes in the degree of contamination seen in microprobe images. All analyses yielded apparent ages that are significantly younger than the previously-assigned maximum ages. These apparent ages are imprecise with large 2-sigma errors (Table 3-3). ESS VWL 0001, and CAS VWL 0002 produced weighted mean ages of 0.36 ± 0.17 Ma, and 0.15 ± 0.18 Ma over 65.9%, and 79.3% of the cumulative ^{39}Ar released respectively. Weighted mean ages of 0.24 ± 0.12 Ma and 0.09 ± 0.14 Ma approached, but did not meet plateau criteria, for samples PIT VWL 0007 and PIT VWL 0005 (Figure 3-5 and Appendix B). Apparent age increases in higher-power steps in samples PIT VWL 0007, PIT VWL 0005, and ESS VWL 0001 (Figure 3-5).

Table 3-3. Comparison of treated and untreated RRV sample ages.

Sample	2006 age ± $2\sigma^*$ (Ma)	2008 age ± 2σ (Ma)
PIT VWL 0007	8.45 ± 0.38	0.24 ± 0.12
PIT VWL 0005	0.80 ± 0.13	0.09 ± 0.14
ESS VWL 0001	1.24 ± 0.17	0.36 ± 0.17
CAS VWL 0002	no age assigned	0.15 ± 0.18

*From Lueth et al., 2006.

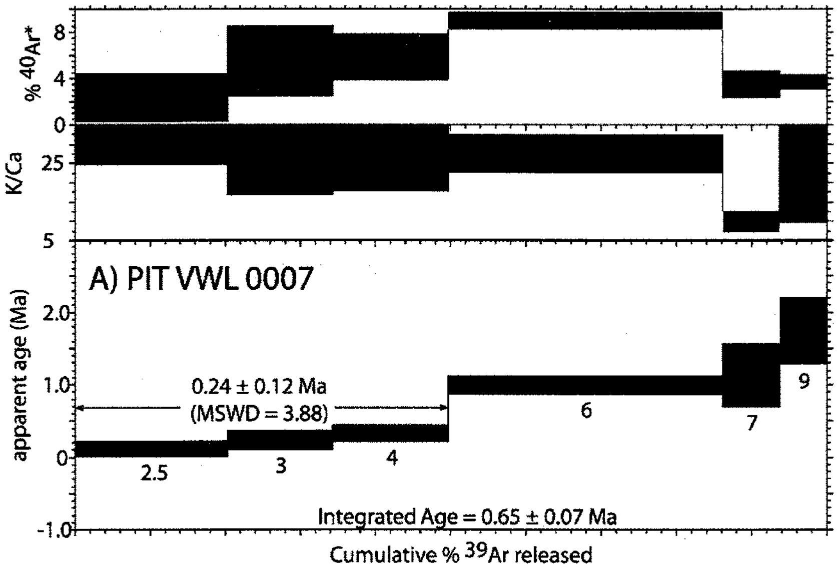

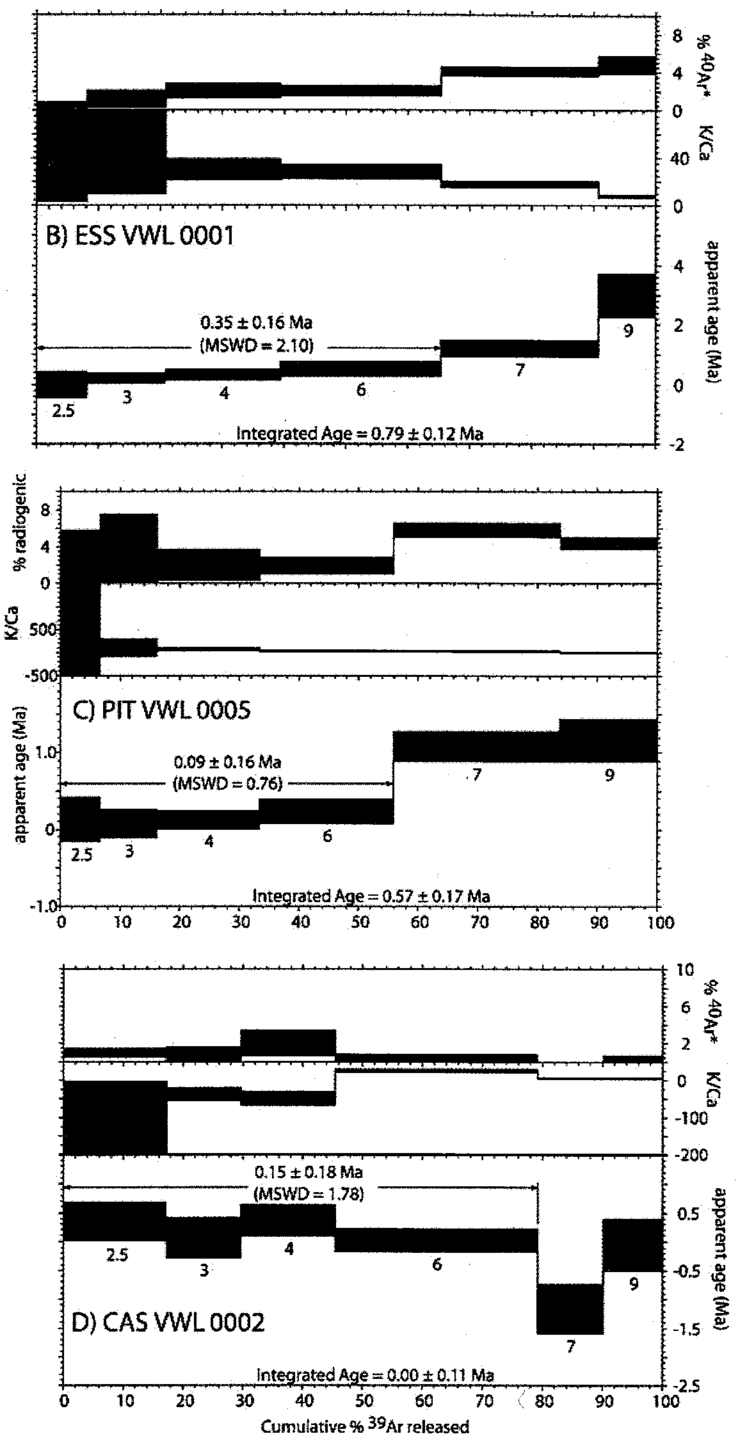

Figure 3-5. Age spectra for HF-treated RRV samples. Numbers beneath each temperature step refer to laser wattage for each heating step. HF-treated RRV jarosite produced plateau ages. Apparent age increased in higher wattage steps in samples PIT VWL 0007, PIT VWL 0005, and ESS VWL 0001 (A, B, C). This increase in apparent age is accompanied by an increase in radiogenic yield (% ^{40}Ar*) and, in sample ESS VWL 0001, a decrease in K/Ca, suggesting that a different, older phase is degassing in these steps.

Radiogenic yield and K/Ca provide compositional information about the sample as it degasses. Radiogenic yield was lower in treated RRV samples than in untreated RRV samples. ^{40}Ar* ranged from 5 to 60% in untreated samples (Lueth et al., 2006). Maximum radiogenic argon for PIT VWL 0007, PIT VWL 0005, ESS VWL 0001, and CAS VWL 0002 was 8.1%, 6.6%, 5.8%, and 2% respectively (Figure 3-5).

Increase in apparent age in untreated PIT VWL 0007, PIT VWL 0005, ESS VWL 0001, and CAS VWL 0002 is accompanied by both an increase in radiogenic yield and decrease in K/Ca. HF-treated aliquots of PIT VWL 0005 and ESS VWL 0001 retain this signature. HF-treated aliquots of PIT VWL 0007 and CAS VWL 0002 do not show this same relationship among K/Ca, radiogenic yield, and increased apparent ages in high wattage steps.

3.4. Discussion

The results presented above answer the three questions posed at the beginning of this chapter:

1. Does thirty minutes of HF treatment completely remove silicate contaminants?
2. What are the effects of HF on RRV jarosite crystal chemistry?
3. What are the effects of HF on RRV jarosite apparent age?

3.4.1. Continued Contamination

HF-treated samples contain fewer silicates than untreated samples, but, unfortunately, they do still contain up to 30% K-bearing silicates by volume. HF dissolved crushed sanidine in a beaker and removed most of the sanidine contamination from PB jarosite within 30 minutes (chapter two), but silicates, including illite and chlorite, remained in RRV samples after 30 minutes of contact with HF.

This difference in the effectiveness of HF in removing silicates may be due to one or more of the following factors: RRV samples are more contaminated than experimental samples; RRV jarosite grows on clay surfaces, and the jarosite somehow protects the illite from dissolution; the amount of HF used in this process was insufficient to dissolve silicates effectively even though sample sizes were smaller than those of experimental samples described in chapter two. Polyak et al. (1998 and 2006) found that gravitational settling separated fine-grained cave alunite from hydrated halloysite and yielded samples with 95% alunite. HF treatment removed the remaining silicates from those samples. However, illite is the potassium source for RRV jarosite, so the two phases are intimately intergrown, and it may be difficult to separate them through gravitational settling in water.

3.4.2. Effects of HF on crystal chemistry

HF partially dissolves silicates, but EMPA quantitative analysis suggests that RRV samples do not experience potassium loss when treated with HF. Although the supergene jarosite in these samples is fine-grained, it is crystalline and reacts to HF in a similar fashion to hypogene PB jarosite. Because there is no evidence of K-loss during HF treatment, using more HF and treating samples for longer periods of time should not compromise jarosite datability.

3.4.3. Effects of HF on apparent age

3.4.3.1. Silicate degassing during step-heating

The degassing of silicates observed in microprobe images can be monitored during age determination. K/Ca serves as a proxy for composition, and changes in this ratio can indicate the degassing of different phases throughout the analysis. EMPA shows that RRV jarosite has a negligible Ca concentration, so a decrease in K/Ca indicates the degassing of older, hypogene clays and feldspars that contaminate the samples. BSE images show that K-bearing silicates, including clay and potassium feldspar, are present in both untreated and HF-treated aliquots of all RRV jarosite, so the decreased K/Ca is probably due to the degassing of these silicate contaminants (Figure 3-1 and 3-4).

3.4.3.2. Imprecise ages

Supergene RRV jarosite produced imprecise ages, many of which overlap at the 2-sigma confidence level. Error for most $^{40}Ar/^{39}Ar$ analyses is approximately 50% of the sample age, but error ranges from 16% to 213% of the sample age. The lack of precision in these ages is probably the result of both low radiogenic yield and small sample size. The half-life for the decay of ^{40}K to ^{40}Ar is 1.25×10^9 years, so young samples (< 1Ma) have not accumulated a high concentration of $^{40}Ar^*$. Maximum ages for these four samples are less than 1 Ma, and radiogenic yield is less than 10%.

3.4.3.3. Maximum Ages

The question remains whether or not the imprecise plateau ages hold significance for jarosite formation or whether they reflect a mixture of supergene and hypogene ages. HF-treated samples still contain as much as 30% K-bearing silicates. The experiment described in chapter two showed that sanidine does not degas below 9W, so sanidine should not have any impact on RRV jarosite's apparent age. Hydrothermal clays in the RRV formed ca. 24.86 ± 0.15 Ma (Lueth et al., 2006). Mixing calculations allow a rough estimate of the expected integrated age of a 70:30 mixture of jarosite and K-bearing silicates, assuming complete degassing of all phases present in the sample:

*% silicates * 24.86 Ma + % jarosite * jarosite age = expected integrated age of the mixture.* Potassium concentration was not taken into consideration in this calculation because contaminant concentration and type differ in each sample.

If old silicates dominated the ^{40}Ar/^{39}Ar analysis, apparent age would be much older than the Pleistocene ages determined for RRV samples (Table 3-4). This result suggests that the mixture of jarosite and silicate contaminants does not degas completely, and that material younger than the hydrothermal clays dominates the apparent age.

Table 3-4. Hypothetical Age calculations

Sample	% silicates	Alteration Age (Ma)	% jarosite	Assumed jarosite age (Ma)	Calculated integrated age of mixture (Ma)	Actual Integrated Age (Ma)
PIT VWL 0007*	0.30	24.86	0.70	0.24	7.63	0.65 ± 0.07
PIT VWL 0005*	0.30	24.86	0.70	0.09	7.52	0.57 ± 0.17
ESS VWL 0001*	0.30	24.86	0.70	0.36	7.71	0.79 ± 0.12
CAS VWL 0002*	0.30	24.86	0.70	0.15	7.56	0.00 ± 0.11
Zero-Age^{+} jarosite	0.30	24.86	0.70	0.001	7.46	
Pliocene jarosite^{++}	0.30	24.86	0.70	5	10.96	

* Assuming that plateau age = jarosite age
$^{+}$ Assuming jarosite is very young (1 ka)
$^{++}$ Assuming jarosite is Pliocene in age

Feldspar and jarosite have been shown to degas at different temperatures when step-heated in a resistance furnace, but the lowest temperatures at which illite degasses overlap with temperatures of jarosite degassing. Jarosite releases most of its ^{39}Ar between 450°C and 700°C (Figure 3-6). Sanidine from the Mogollon-Datil volcanic field degassed when heated above 850°C (McIntosh et al., 1990). Illite degasses between 550°C and 1100°C, overlapping with jarosite in the low-temperature range (Jaboyedoff and Cosca, 1999).

It is difficult to correlate degassing temperatures with laser power because the laser couples differently with different minerals, and material in a laser tray is not heated uniformly from top to bottom. Additional variables that undermine attempts to correlate beam power with furnace temperature include sample size differences, beam power density, and laser focus (McDougall and Harrison, 1988). With these limitations in mind, it is possible to make some first-order observations about the approximate relationship between furnace temperature and laser power based on furnace and laser PB age spectra (Figure 3-6).

In the furnace, jarosite degassed between 450°C and 700°C (Lueth et al., 2004). When step-heated with a laser, Peña Blanca jarosite released most of its argon between 2W and 6W, roughly corresponding to the temperature range at which jarosite degasses in the furnace. Within this range, feldspar should not affect the apparent age of the jarosite. This assumption that feldspar will not affect apparent age at low power is upheld by the degassing of the experimental artificial mixture of PB and FC-2 described in chapter three. In this experimental mixture, FC-2 has no influence over apparent age until apparent age begins to climb slightly at 10W.

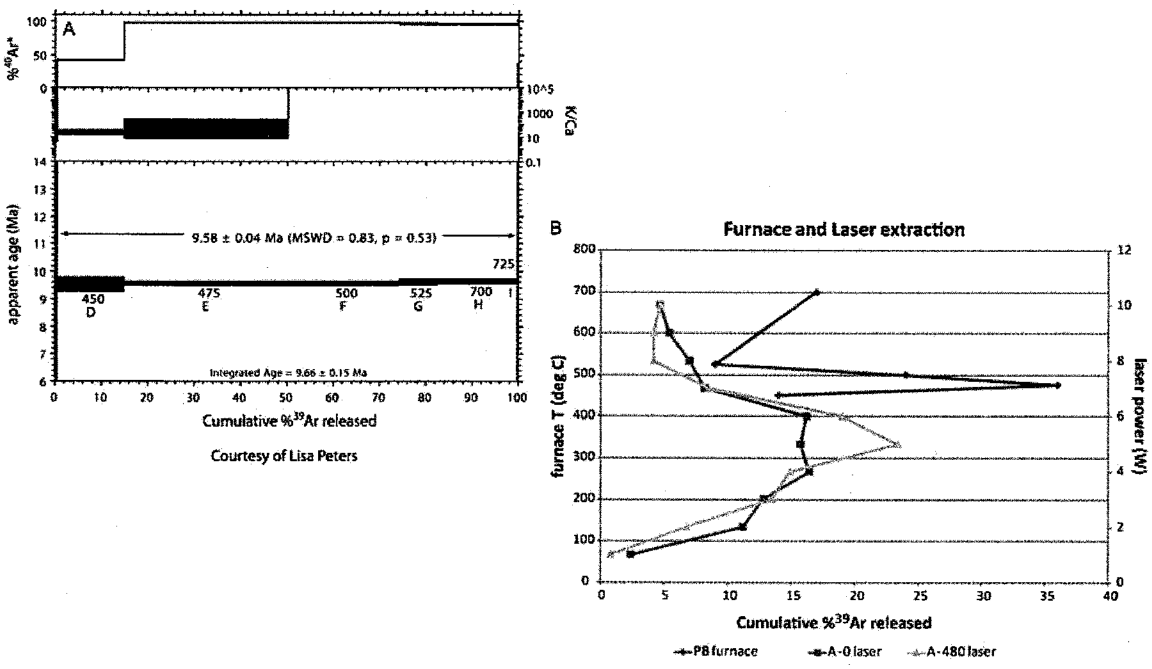

Courtesy of Lisa Peters

Figure 3-6. Furnace vs laser degassing of jarosite. A) Age spectrum for PB jarosite step-heating in a resistance furnace shows that pure, hypogene jarosite releases most of its argon between 450 and 700 degrees C. B) Laser-heated PB jarosite (samples A-0 and A-480 of chapter three) consistently releases most of its argon between 2 and 6 Watts.

Oligocene illite, however, may affect the apparent age within this step-heating schedule. With the exception of sample PIT VWL 0007, the young plateaus produced by RRV jarosite include the 6W step. Apparent age in samples PIT VWL 0007 and ESS VWL 0001 climbs as it approaches 6W, and higher-wattage steps do not overlap with plateau steps at the 2-sigma confidence level (Figure 3-5a and b).

Although illite begins to degas at lower temperatures than feldspar, young ages in early heating steps suggests that Oligocene phases are not degassing. The decrease in apparent age is accompanied by a lower radiogenic yield when compared to untreated aliquots of the same sample. The presence of silicates in these samples requires that all dates be interpreted as maximum ages, but it is likely that jarosite dominates the young plateau steps in samples where apparent age does not climb at low laser power, and that the plateau ages can be interpreted as the time of jarosite formation.

3.5. Conclusions

HF-treated RRV samples did not experience K loss when treated with HF, so it appears that fine-grained supergene jarosite behaves the same way in HF as hypogene jarosite. If this is the case, removing silicates from jarosite using HF does not compromise the datability of the sulfate.

The sanidine dissolution experiment described in chapter two showed that sanidine can dissolve within 30 minutes, implying that long treatment times are unnecessary. However, 30 minutes of HF treatment did not remove 100% of the clay and K-feldspar contaminants in RRV samples. These samples were treated with 10 mL of acid rather than 40 mL because the amount of RRV jarosite separated from drill core and hand samples was approximately four times smaller than the amount of PB jarosite used in the experiment. RRV samples do not show evidence of K-loss as a function of HF treatment, so longer treatment times in more HF when preparing fine-grained supergene jarosite for $^{40}Ar/^{39}Ar$ are feasible and recommended. Separating jarosite from older clay minerals may be possible using gravitational settling (Polyak et al., 1998 and 2006), but RRV jarosite that replaces illite may control the density of the aggregate material, making it difficult to separate them mechanically.

4. TIMING OF ALTERATION SCAR FORMATION IN THE RED RIVER VALLEY, TAOS COUNTY, NEW MEXICO

4.1. Introduction

The previous chapters established the datability of HF-treated, supergene jarosite. Additionally, chapters two and three showed that silicate contaminants exert little influence over the young plateau steps of HF-treated RRV jarosite. Therefore, jarosite ages have geologic significance and can be used to interpret the timing of landscape evolution. This chapter focuses on surficial processes in the RRV with the goal of answering the following questions:

1. How old are RRV alteration scars?
2. How do alteration scars form?
3. How is alteration scar formation controlled by regional landscape evolution?

The RRV, located on the eastern edge of the San Luis basin in northern New Mexico, underwent intense hypogene alteration during the development of the Oligocene Latir volcanic field. Pyrite and other sulfides formed during hydrothermal alteration of volcanic rocks as plutons intruded several kilometers below the surface. Once exposed to surface conditions, these altered rocks eroded to form bare amphitheaters called "alteration scars" (Figure 4-1).

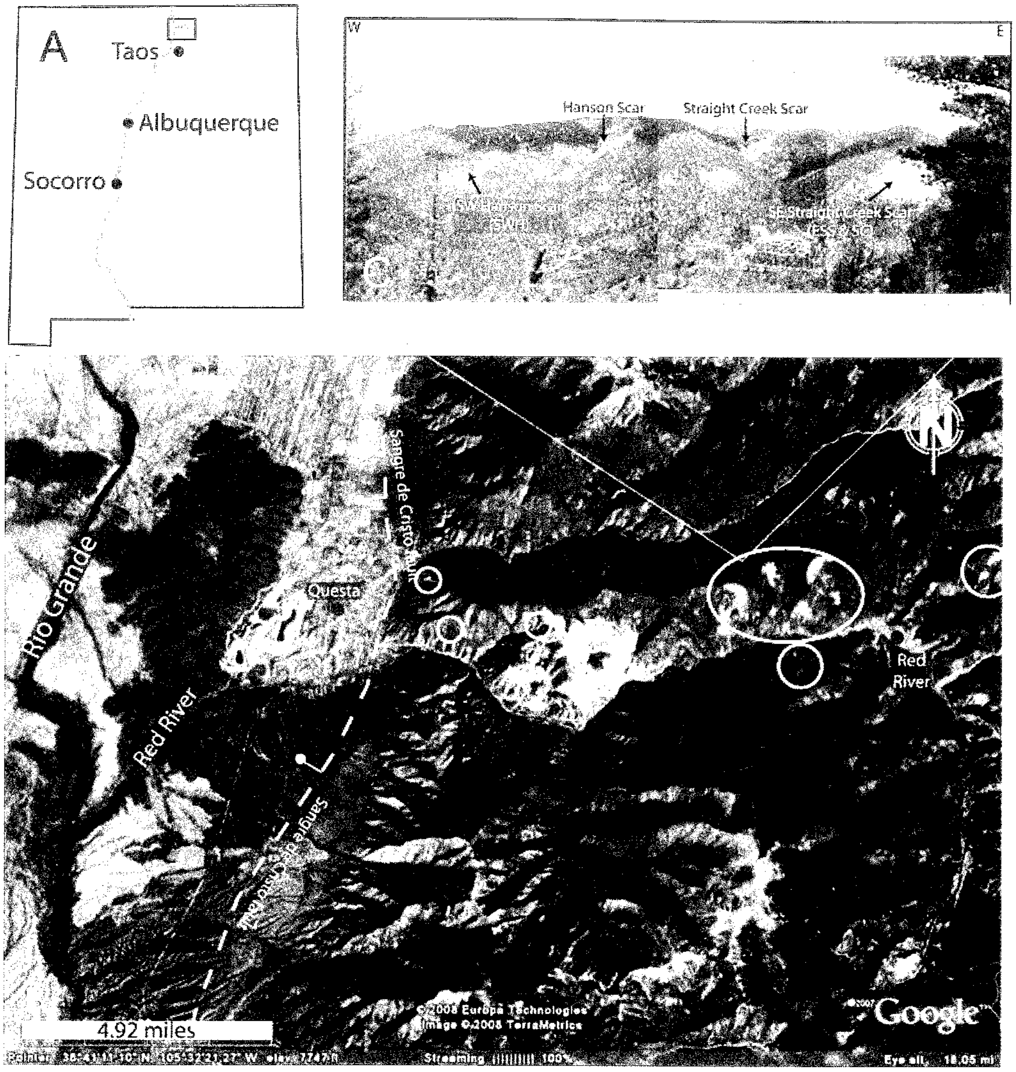

Figure 4-1. Location of the Red River Valley. A) The RRV (outlined in black) is located on the eastern edge of the San Luis basin of the Rio Grande rift in the Oligocene Latir volcanic field; B) Jarosite is preserved in unvegetated alteration scars (outlined in white). The uncircled bare feature is the open pit of the MolyCorp Mo mine; C) Alteration scars are found throughout the RRV, but they generally form on south-facing slopes in areas with pyrite-rich hydrothermally-altered rocks.

Jarosite precipitates during the weathering of these pyrite-rich, hydrothermally-altered rocks. Iron-cemented breccias (ferricretes) and weathered veins in alteration scars can preserve supergene jarosite, which forms in acidic, highly-oxidizing environments (Figure 4-2). Jarosite [ideally $KFe_3(SO_4)_2(OH)_6$] preserved in ferricretes records the timing of ferricrete formation and associated landscape evolution of the valley. Jarosite does not exchange constituents with meteoric water (Rye and Alpers, 1997) or dissolve easily (see chapter one); it is datable (Vasconcelos, 1999), and its stable isotope ratios ($^{34}S/^{32}S$, $^{18}O/^{16}O$, and D/H) record original fluid compositions (Rye and Stoffregen, 1995).

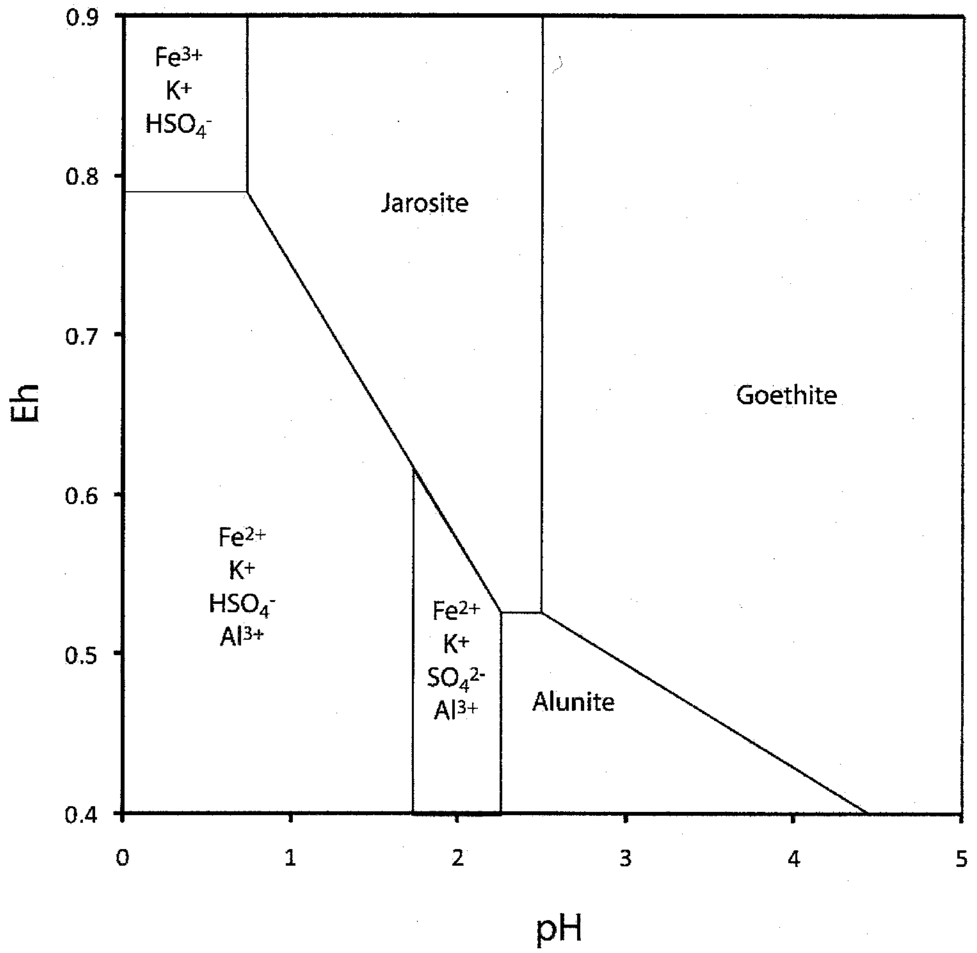

Figure 4-2. Jarosite stability field. This Eh-pH diagram modified from Lueth et al. (1998) shows that jarosite forms under highly-oxidizing and acidic conditions.

$^{40}Ar/^{39}Ar$ geochronology of jarosite preserved in veins and ferricretes can be a powerful tool for understanding the timing of RRV landscape evolution and the propagation of weathering fronts through the hydrothermally-altered volcanic rocks in the area. Modern ferricretes form in streambeds at the base of scars (Figure 4-3). Throughout the RRV, ferricretes are stranded high above the present base of scars, serving as stratigraphic markers for ancient land surfaces. Veins preserve continuous weathering profiles but lack stratigraphic context.

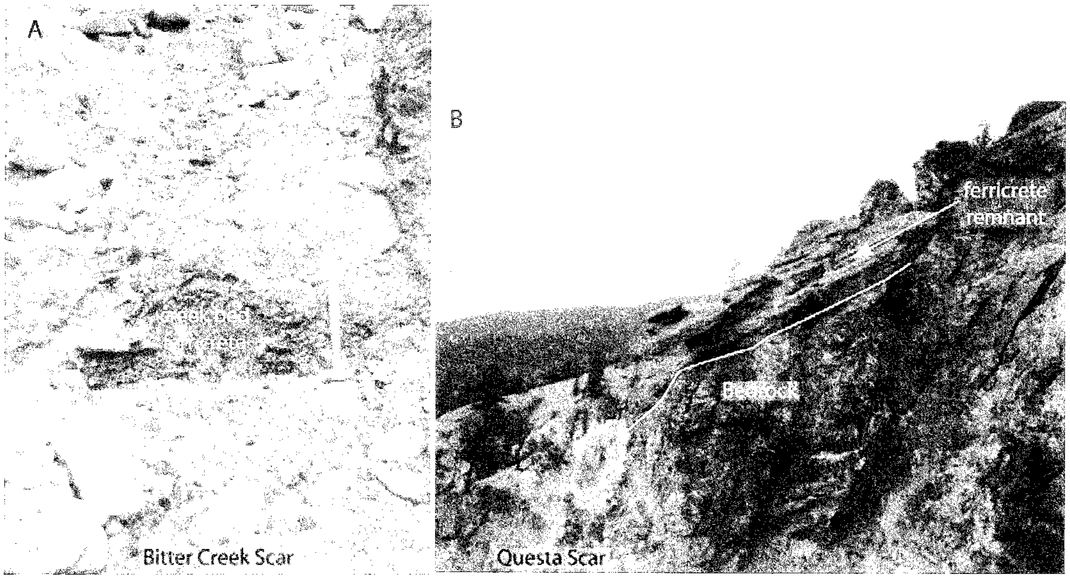

Figure 4-3. Ferricretes preserved in the RRV. A) Modern ferricretes in the RRV often form in streambeds at the base of scars. B) Ferricretes stranded high above the present scar base are resistant to erosion and form inverted topography where an ancient low point now stands high in the scar.

In addition to jarosite, organic material, including wood and charcoal, is preserved in ferricretes and debris flows. This material can be dated using radiocarbon methods. ^{14}C has a relatively short half-life of 5730 years, so it provides a record of recent ferricrete accumulation and debris flow activity, while jarosite ages and compositions provide insights into the longer weathering history of the valley.

4.2. Geologic Background

4.2.1. Tertiary Volcanic Rocks and Hydrothermal Alteration

The location of alteration scars is partially controlled by older geologic processes in the RRV. The RRV lies on the southern edge of the Questa caldera in the Latir volcanic field. The Latir volcanic field became active ca. 28 Ma as rifting began in northern New Mexico (Lipman et al., 1986). Normal faults dissect the volcanic field, and the rift-bounding Sangre de Cristo fault truncates the Questa caldera on its western edge.

The composition of volcanic rocks has varied over time. Pre-caldera stratovolcanoes and lava domes were buried by Amalia tuff (Lipman et al., 1986), which has an eruption age of 25.23 ± 0.05 Ma (Zimmerer, 2008). Pre-caldera volcanic rocks range in composition from basaltic andesite to rhyolite tuff with a majority of andesite and quartz latite porphyry flows (Lipman and Reed, 1989; Meyer and Foland, 1991).

After caldera collapse with the eruption of the Amalia tuff, mineralizing intrusions intensely altered the Latir volcanic field (Meyer and Foland, 1991). Hypogene fluids preferentially flowed along fractures and low-angle faults in the study area (Meyer and Foland, 1991). The most intense hypogene alteration occurred at the contact between Amalia tuff and the pre-caldera Latir andesite (Lueth and Campbell, 2006).

Alteration in the RRV is zoned. Phyllic, quartz-sericite-pyrite (QSP), and propylitic alteration succeed mineralizing intrusions upward and outward (Figure 4-4; Ludington et al., 2004). Propylitic alteration may have been a regional phenomenon that pre-dated the eruption of the Amalia tuff. The QSP zone, which overprints propylitic alteration, can contain more than 10 wt % sulfide with pyrite as the dominant sulfide phase (Ludington et al., 2004). Ore body sulfides have a magmatic $\delta^{34}S$ value of ~0‰ while scar pyrite ranges from $\delta^{34}S = 0‰$ to $\delta^{34}S = -13.1‰$ (Campbell and Lueth, 2008; Graf, 2008; this study). This variation has been attributed to evolving fluid compositions during intrusion and alteration (Campbell and Lueth, 2008).

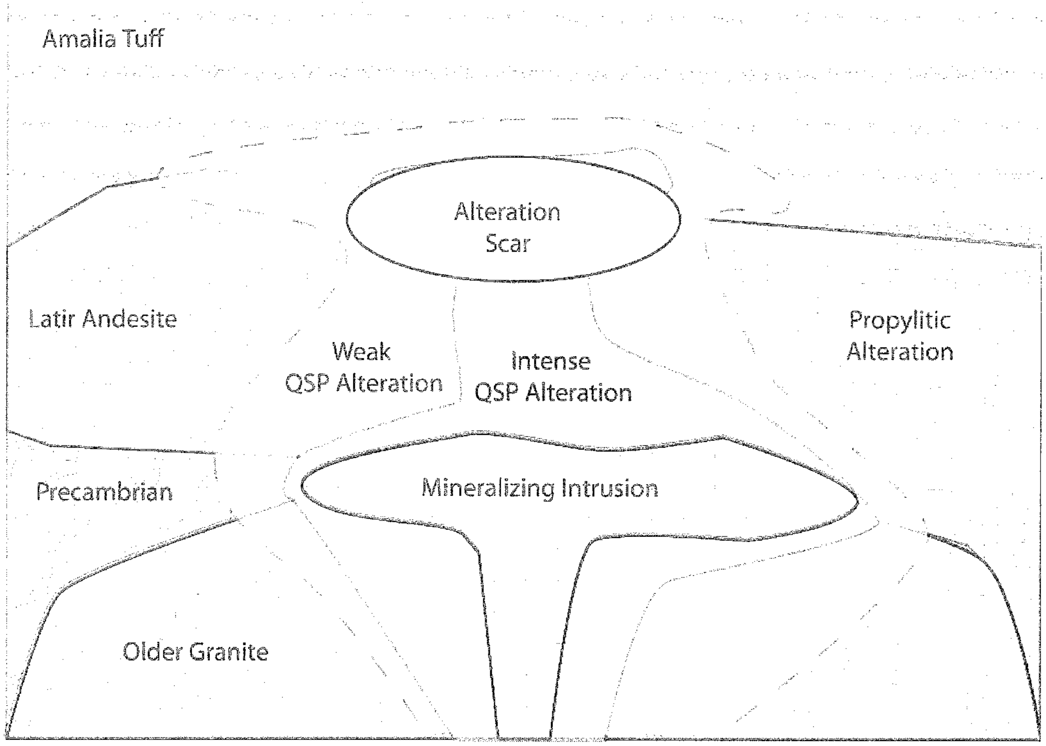

Figure 4-4. Schematic cross-section of zoning in RRV hydrothermal alteration. Propylitic alteration is overprinted by QSP alteration. Alteration scars often form at the interface of propylitically-altered andesite and Amalia tuff. Modified from Ludington et al., 2004 and Lueth and Campbell, 2006.

In addition to sulfides, alunite formed during alteration. ^{40}Ar/^{39}Ar dating of hypogene alunite yielded an age of 24.86 ± 0.15 Ma (Lueth et al., 2006), indicating that hydrothermal alteration closely followed Questa caldera collapse, which occurred at 25.23 ± 0.05 Ma (Zimmerer, 2008).

4.2.2. Alteration Scars

Alteration scars are the youngest major features in the RRV. Steep slopes, lack of vegetation, lack of soil, and erosion by mass wasting characterize RRV scars. Meyer and Leonardson (1990) categorized the scars into two groups: large, high-elevation "divide" scars and smaller, lower elevation "inner valley" scars (Figure 4-5).

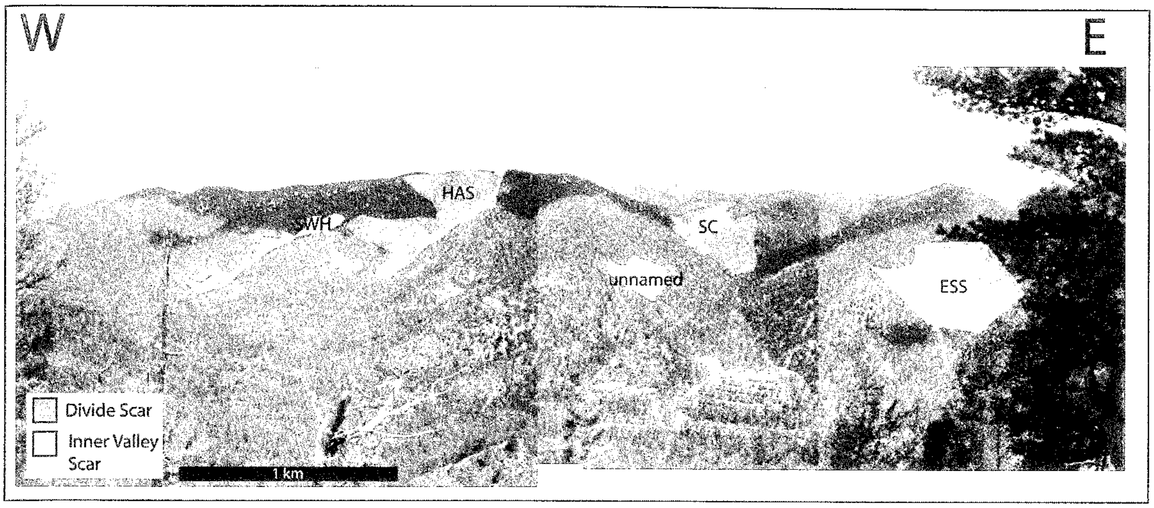

Figure 4-5. Divide and inner valley scars (Meyer and Leonardson, 1990). This panorama shows the two divide scars and three inner valley scars on the south-facing slopes. Abbreviations are as follows: SWH = Southwest Hansen, HAS = Hansen, SC = Straight Creek, ESS = Southeast Straight Creek. The inner valley scar on the southwest edge of SC is unnamed. It drains into the SC drainage.

Most scars occur on south-facing slopes in andesite or at the andesite-Amalia tuff contact (Lipman and Reed, 1989; Shaw et al., 2003). The Questa scar, which is located on the Sangre de Cristo fault, is a notable exception in that it formed on a west-facing slope entirely in Amalia tuff. The Sangre de Cristo fault forms the eastern rift margin in the San Luis basin, so tectonics may control scar formation here, but this hypothesis has not been tested. Hottentot and June Bug scars occur in pre-caldera quartz latite (Lipman and Reed, 1989; Caine, 2006). The June Bug scars are the only ones located on a north-facing slope.

Alteration scars are actively-eroding features, and debris flows originate in the scars during summer monsoon months (Nordstrom et al., 2005). Ephemeral and perennial streams in the scars continue to deposit ferricretes in creek beds, providing insights into where and how some ancient ferricretes, now stranded at high elevations in the scars, formed. Three radiocarbon dates presented in this thesis provide age constraints on younger processes while jarosite records the timing of ancient weathering.

Different models have been proposed to explain alteration scar formation. Early studies attributed scar formation to low-temperature fumarolic activity during Oligocene to Miocene volcanism (Schilling et al., 1956; Clark and Read, 1972). If this were the case, alteration scars would be 25 to 28 million years old. Meyer and Leonardson (1990) recognized that these are erosional, rather than volcanic, features. Meyer and Leonardson proposed that alteration scars form in areas where faulting and supergene weathering of pyrite enhances erosion. According to Meyer and Leonardson (1990), sulfuric acid produced during pyrite weathering reacts with feldspar, altering it to clay, and providing a zone of mechanical weakness along which the slope could fail. These researchers proposed that alteration scar formation began in the Pliocene.

More recent work in the area has refined the Meyer and Leonardson model of alteration scar formation and called into question the role of clay formation in alteration scar formation. Although pyrite weathering does produce sulfuric acid, there is no evidence that alteration scar clays formed from the acidic weathering of feldspar. Graf (2008) determined that alteration scar clays are hypogene rather than supergene in origin. Erosion is focused in areas where hydrothermal, rather than supergene, alteration compromised the strength of the original rock (Graf, 2008).

Physical weathering, rather than supergene clay formation, may be the dominant supergene factor in alteration scar formation. Graf (2008) found that physical weathering mechanisms include grain-size reduction, freeze-thaw action, and gypsum precipitation. Jarosite, but not clay, is a supergene byproduct of pyrite weathering. This thesis focuses on jarosite preserved in inner valley scars and in debris flows that emanated from high-elevation divide scars.

4.3. Methods

4.3.1. Mineral Separates

Jarosite was scraped from ferricrete and weathered vein samples and then hand-picked to remove coarse contaminants (i.e. goethite, gypsum, quartz, feldspar, and clay). Chemical treatments removed fine-grained gypsum and silicates from jarosite. Jarosite samples were first rinsed in DI water at room temperature for one hour to remove gypsum. Water was decanted, and samples dried at room temperature overnight. Visual inspection of samples using a binocular microscope and the electron microprobe verified the absence of gypsum. Jarosite samples were then treated with 10 mL of 25% HF for 30 minutes to remove silicate contaminants as described in chapter three of this thesis. Sample descriptions are provided in Table 4-1.

Table 4-1. RRV jarosite samples.

Sample	Environment	Elevation ASL (m)
KS-JB-3[*,#]	Supergene scar vein	2995
KS-JB-4[*,#]	Supergene ferricrete	2927
SWH GJG 0025[*,#]	Debris flow ferricrete	2647
KS-SC-2[*,#]	Debris flow ferricrete	2860
SWH-GJG-0001[*,#]	Supergene scar vein	2759
CAS VWL 0002[*,#]	Debris flow ferricrete	2500
SWH VWL 0001[%,#]	Debris flow ferricrete	2625
ESS VWL 0001[*,#]	Supergene scar vein	2680
PIT VWL 0005[*,#]	Drill core profile	2965
PIT VWL 0007[*,#]	Supergene scar vein	2991
SWH GJG 0024[*,#]	Debris flow ferricrete	2623
BCS VWL 0002[+]	Supergene scar vein	3180
GHS VWL 0007[#]	Supergene ferricrete	2734
HAS GJG 0001[#]	Supergene ferricrete	2774
SWH GJG 0004[#]	Supergene ferricrete	2738

[*] Sample was dated
[#] Stable isotope analysis conducted
[+] Isotopic data from Campbell and Lueth, 2008
[%] age data from Lueth et al., 2006.

4.3.2. Characterization

Samples were characterized to determine the degree of contamination with fine-grained silicates and to monitor chemistry before and after HF treatment (see chapter three). Jarosite samples were characterized using EMPA as described in chapters two and three of this thesis.

4.3.3. Stable Isotope Geochemistry

Stable isotopes record fluid compositions, and jarosite separates were analyzed for four stable isotope ratios: D/H, $(^{18}O/^{16}O)_{SO4}$, $(^{18}O/^{16}O)_{OH}$, and $^{34}S/^{32}S$. All isotopic measurements were made by continuous flow mass spectrometry on a Finnigan MAT Delta Plus XP. Duplicate measurements were made for each isotope to monitor reproducibility. See Appendix E for details. Samples were incinerated in a TC/EA high temperature reduction furnace operated at 1450°C for δD and $\delta^{18}O$ determinations. These gases were analyzed as H_2 and CO respectively. Sulfur was analyzed as SO_2, which was extracted in an EA. Appendix E has detailed information on stable isotope analyses, including correction factor calculations.

In order to distinguish $\delta^{18}O_{(OH)}$ from $\delta^{18}O_{(SO4)}$, minerals were analyzed in two steps. First, a 0.45-0.65 mg bulk sample was analyzed. Second, $\delta^{18}O_{(SO4)}$ analyses were conducted on $BaSO_4$ precipitated from jarosite according to the methods initially developed for alunite analysis by Wasserman et al. (1992). Jarosite was dissolved in a 0.5 N NaOH solution heated to 90°C. The solution was filtered to remove iron oxides that precipitate during jarosite dissolution and re-heated to 90°C. The heated filtrate was titrated with 10 N HCl to decrease the pH from 12 to 3. Care was taken to prevent precipitation of $Fe(OH)_3$ at intermediate pH. BaCl was added to the acidified filtrate and heated for 3 more hours at 90°C. The solution was then allowed to sit overnight before filtering to retrieve the precipitated $BaSO_4$. $BaSO_4$ dried at room temperature prior to analysis. $\delta^{18}O_{(OH)}$ was calculated based on the relative proportions of oxygen in each site along with the bulk and $\delta^{18}O_{(SO4)}$ analyses: $\delta^{18}O_{(OH)} = (\delta^{18}O_{bulk} - \delta^{18}O_{(SO4)} * 0.5714286) / 0.4285714$.

4.3.4. $^{40}Ar/^{39}Ar$ age determination

Jarosite ages were determined by $^{40}Ar/^{39}Ar$ geochronology. 24-35 mg of each sample was placed in a 6-hole machined Al disk with FC-2 sanidine (assigned age = 28.02 Ma) as the flux monitor. Additionally, 25 mg of crushed, HF-treated hypogene Peña Blanca jarosite was irradiated to monitor the effects of chemical treatment on samples. Disks were irradiated for 30 minutes in the USGS TRIGA reactor in Denver. Analyses were corrected for neutron-induced interfering reactions using the following correction factors: $(^{39}Ar/^{37}Ar)_{Ca} = 0.00068 \pm 5 \, x \, 10^{-5}$, $(^{36}Ar/^{37}Ar)_{Ca} = 0.00028 \pm 2 \, x \, 10^{-5}$, $(^{38}Ar/^{39}Ar)_K = 0.01077$, $(^{40}Ar/^{39}Ar)_K = 0 \pm 0.0004$.

After irradiation, 5-8 mg of irradiated jarosite were loaded into 9-hole copper laser trays and distributed evenly across the bottom of each 4 x 4 mm hole. Samples were step-heated with a CO_2 laser to a maximum of 9 W. The heating schedule for each sample is listed in Appendix B.

SO_4^{2-} and OH^- in jarosite volatilize and can cause beam suppression in the mass spectrometer due to high gas pressure. In order to minimize the deleterious effects of adding high levels of gas to the mass spectrometer, sample gas was cleaned using a cold trap and 2 getters. Gas initially expanded from the laser chamber to the cold trap, which was operated at a temperature of -140°C, trapping water and SO_2 before expanding into the 2nd stage. 2 SAES GP-50 getters are attached to 2nd stage. Gas remained in the 2nd stage for 15 minutes before moving to the mass spectrometer.

Sample gas was analyzed in an MAP-215-50 mass spectrometer operated in static mode. Argon isotopes were detected by an electron multiplier. Plateaus were defined as three or more contiguous steps that overlap at the 2-sigma confidence level and contain 50% or more of the sample gas.

4.3.5. Organic Material

Organic material was dated to determine the timing of recent (i.e. less than 50 ka) ferricrete accumulation and debris flows. Three samples were submitted to Geochron Laboratories in Billerica, Massachusetts for radiocarbon dating. Samples SWH GJG 0018 and KS-BC-3 are logs collected from ferricretes in the Southwest Hansen and Bitter Creek alteration scars. Sample MIN DCS 0010 is a charcoal sample from a pond deposit within a debris flow (Figure 4-6). SWH GJG 0018 and KS-BC-3 were large enough to analyze by conventional counting techniques while MIN DCS 0010 was submitted for Accelerator Mass Spectrometer (AMS) analysis. Sample descriptions are provided in Table 4-2.

Table 4-2. Radiocarbon samples

Sample Name	Material	Description
SWH GJG 0018	Wood	Log trapped in ferricrete; difficult to determine the orientation of the log or the depth of burial
KS-BC-3	Wood	Log trapped 5 feet deep in ferricrete
MIN DCS 0010	Charcoal	Fine-grained charcoal mixed with clay-sized particles.

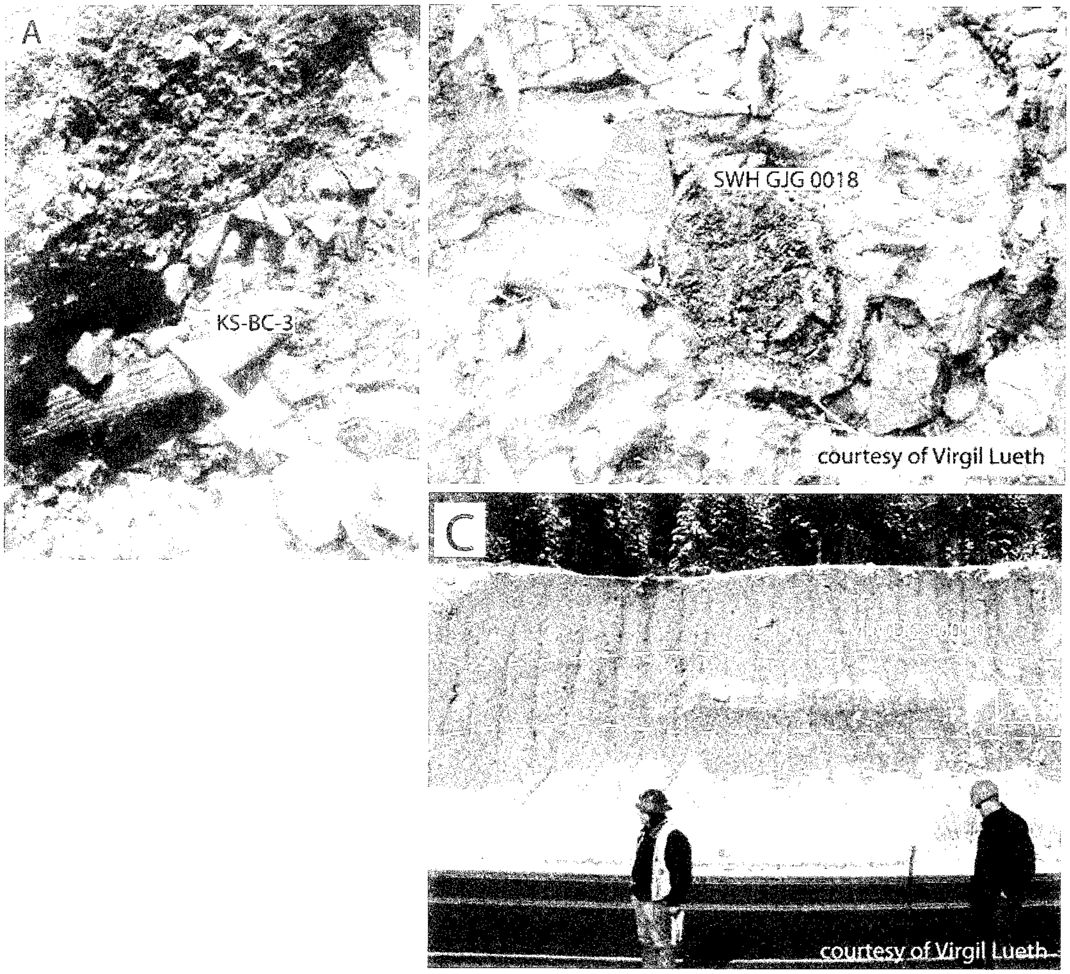

Figure 4-6. Radiocarbon samples. Organic samples submitted for radiocarbon dating included wood samples from ferricretes in the Bitter Creek scar (A), SW Hansen scar (B), and charcoal from a pond in a debris flow cut by the road through the RRV (C). The log in A is covered by 5 feet of ferricrete material in a stream that appears to be actively depositing iron oxides. It is difficult to determine how deeply the log in B (circled) is buried.

The staff of Geochron Laboratories prepared wood and charcoal samples by the following methods. Samples were cleaned of debris and split into small pieces. Carbonates were removed with hot, dilute HCl. Humic acids and other organic materials were removed with 0.1 N NaOH. After treatment with NaOH, the samples were again soaked in dilute HCl. The samples were then washed, dried, and combusted for CO_2

analysis. Additionally, Geochron Laboratories analyzed the samples for stable isotope ratios ($^{13}C/^{12}C$) in order to correct for "dead" (i.e. stable) carbon.

OxCal 4.0 (Bronk Ramsey, 1995 and 2001) was used to convert ^{14}C years BP to calendar years based on the IntCal04 calibration curve of Reimer et al. (2004). IntCal04 is calibrated for northern hemisphere ^{14}C fluctuations over the past 26,000 years based on tree ring data, corals, and foraminifera. See appendix F for details about calibration curves and converting ^{14}C ages to calendar ages.

4.4. Results

4.4.1. EMPA Characterization

Interpreting $^{40}Ar/^{39}Ar$ age spectra depends on identifying the composition of the dated phase and contaminants that may affect apparent age. RRV samples are predominantly potassium endmember jarosite although sample SWH GJG 0001 has a high natrojarosite component (Figure 4-7). Although HF treatment removed some silicates, all analyzed samples were contaminated with older clays, feldspar, and quartz. Quartz is the major silicate contaminant, but illite and potassium feldspar persist in all treated samples (see chapter three). Table 4-3 presents representative chemical analyses based on mean K_2O concentration. Appendix D provides detailed results of quantitative analysis.

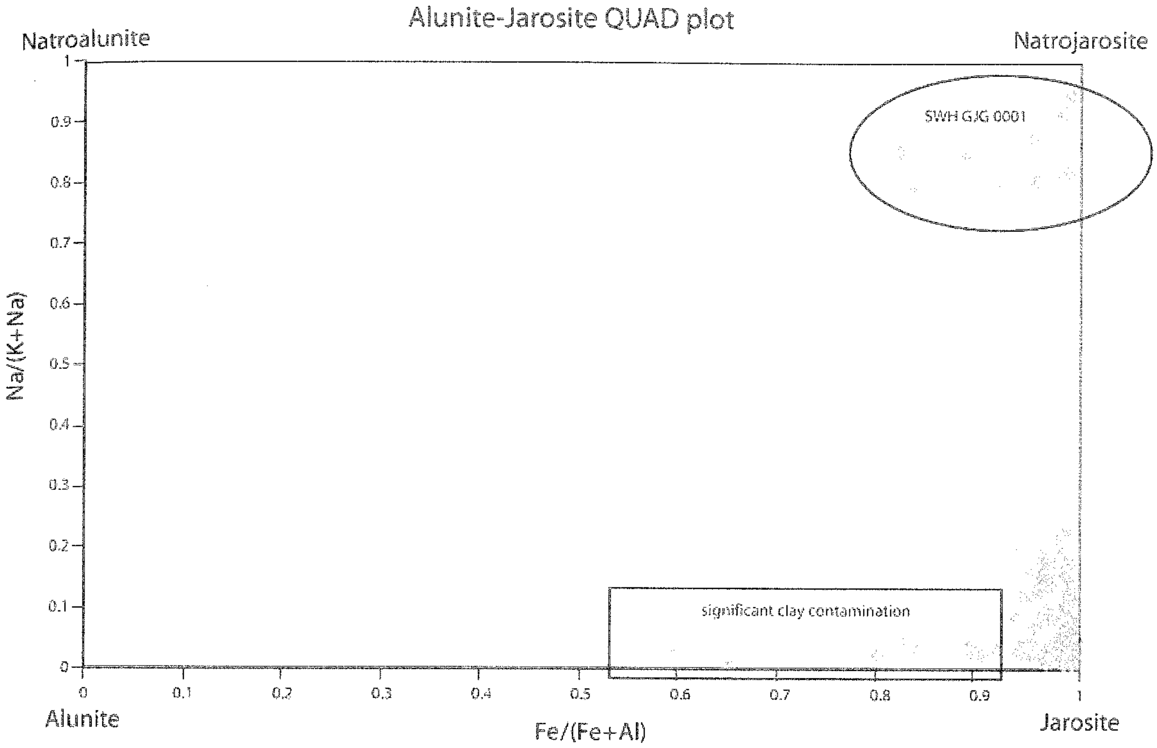

Figure 4-7. Alunite-Jarosite QUAD plot. SWH GJG 0001 (Southwest Hansen scar) had a high natrojarosite component. Analyses that show apparent alunite-jarosite solid solution have a relatively high Si concentration, suggesting that they are contaminated with clay.

Table 4-3. EMPA data for selected RRV samples (wt % oxides and cations).

Sample	SWH GJG 0025	SWH GJG 0004	KS-JB-3	SWH GJG 0001
Scar	SW Hansen	SW Hansen	June Bug	SW Hansen
time in HF (min)	30	30	30	30
K_2O	6.39	6.74	6.17	1.25
Na_2O	0.89	0.52	1.09	3.57
FeO	39.78	38.80	37.32	32.35
Fe_2O_3 (calc)*	44.16	43.07	41.42	35.91
Al_2O_3	0.22	0.35	0.59	0.43
As_2O_3	0.02	0.02	0.03	0.00
MoO_3	0.00	0.00	0.00	0.00
SO_2	23.80	23.07	23.19	20.12
SO_3 (calc)$^+$	29.74	28.84	28.99	25.14
P_2O_5	0.91	0.76	0.12	0.66
SiO_2	0.14	0.00	0.12	1.91
H_2O	10.98	10.64	10.44	9.64
F	0.22	0.20	0.09	0.59
Cl	0.01	0.08	0.12	0.52
Total	83.35	81.17	79.27	71.04

Cations				
K	0.668	0.727	0.678	0.149
Na	0.141	0.086	0.183	0.646
A-site total	0.809	0.813	0.860	0.795
Fe	2.726	2.744	2.689	2.525
Al	0.021	0.035	0.060	0.048
As	0.001	0.001	0.002	0.000
B-site total	2.747	2.780	2.750	2.573
S	1.829	1.831	1.874	1.761
P	0.064	0.054	0.009	0.052
X-site total	1.892	1.885	1.883	1.813
Fe/Fe+Al	0.993	0.988	0.978	0.982
Na/Na+K	0.174	0.106	0.212	0.812

$^*Fe_2O_3 = FeO * 1.11$
$^+SO_3 = SO_2 * 1.25$

4.4.2. Stable Isotope results

Stable isotope geochemistry is also essential for interpreting ages because isotopic ratios, particularly $^{34}S/^{32}S$, indicate whether jarosite formed under supergene or hypogene conditions. Pyrite and jarosite $\delta^{34}S$ values overlap throughout the RRV (Figure 4-8). $\delta^{34}S_{(jarosite)}$ ranges from +2.7‰ to -12.1‰. $\delta^{34}S_{(pyrite)}$ values range from +1.4‰ to -13.6‰ (Campbell and Lueth, 2008; Graf, 2008; and this study. See Table 4-4).

Stable isotope analysis confirms the supergene origin of RRV jarosite. Sulfur fractionates between sulfides and sulfates as a function of temperature: $10^3\ln\alpha_{SO4-H2S} = 5.26(10^6/T^2) + 6.0$ (Ohmoto and Rye, 1979). Sulfates, therefore, are always heavier than sulfides when they form from the same fluid. Alunite that formed at the time of mineralization (Lueth et al., 2006) has positive $\delta^{34}S$ and $\delta^{18}O$ values, indicating that it is of hypogene origin (Campbell and Lueth, 2008). $\delta^{34}S_{(jarosite)}$ overlaps with alteration scar pyrite, indicating that it inherited its sulfur during sulfide weathering rather than forming in equilibrium with the sulfide (Figure 4-8).

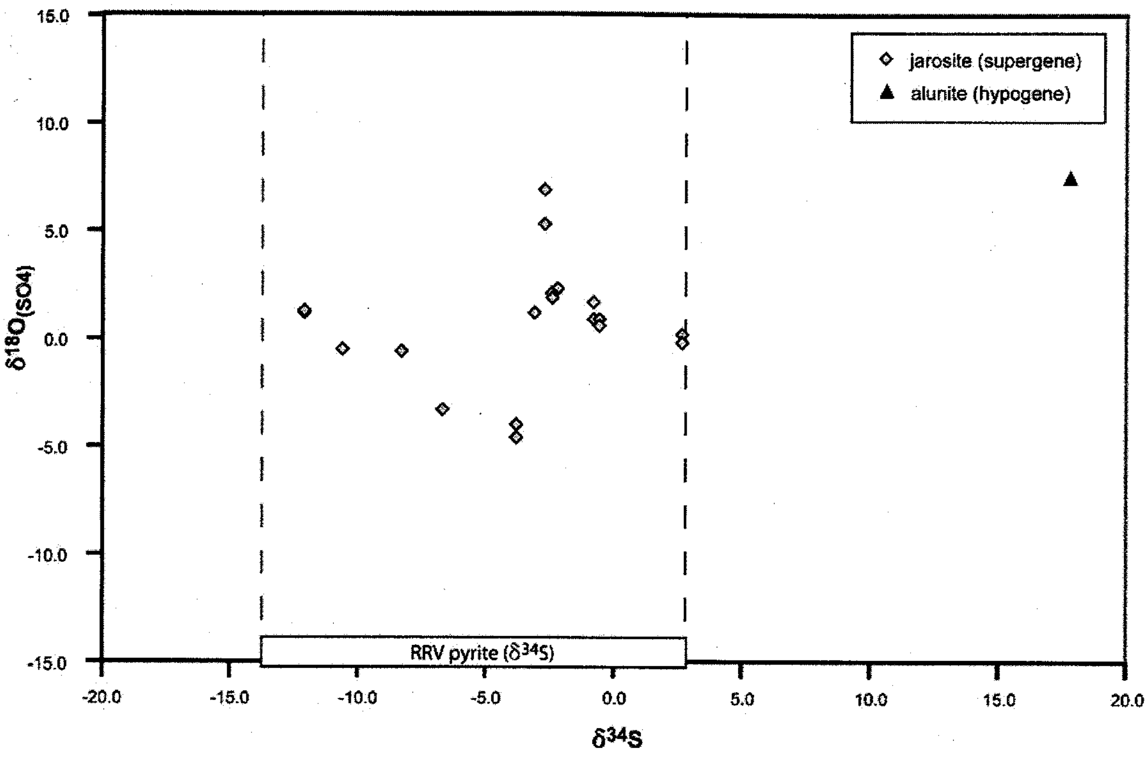

Figure 4-8. $\delta^{34}S$ values for RRV jarosite overlap with pyrite $\delta^{34}S$ values. Alunite $\delta^{34}S$ is more than 15‰ heavier than both pyrite and jarosite, indicating that alunite is a hypogene phase and jarosite formed by pyrite weathering.

Oxygen isotope compositions are controlled by pyrite weathering reactions. RRV jarosite precipitates from pyrite oxidation products in solution (chapter one). Pyrite oxidation to produce aqueous sulfate can occur through either of two basic reactions (Seal, 2003):

$$FeS_{2(py)} + 7/2O_2 + H_2O \rightarrow Fe^{2+} + 2SO_4^{2-} + 2H^+ (1)$$

$$FeS_{2(py)} + 14Fe^{3+} + 8H_2O \rightarrow 15Fe^{2+} + 2SO_4^{2-} + 16H^+ (2)$$

In reaction (1), atmospheric oxygen is the oxidant. In reaction (2), ferric iron oxidizes the pyrite. When atmospheric O_2 oxidizes pyrite, both water and atmospheric oxygen control the $\delta^{18}O$ signature of the resulting $(SO_4^{2-})_{aq}$. When Fe^{3+} oxidizes pyrite, water controls the $\delta^{18}O$ signature of the $(SO_4^{2-})_{aq}$ (Seal, 2003). $\delta^{18}O_{(SO4)}$ values range from +6.1‰ to -4.3‰, but most of the samples fall between -2‰ and +2‰ and are generally heavier than

$\delta^{18}O_{(OH)}$. $\delta^{18}O_{(SO4)}$ and $\delta^{18}O_{(OH)}$ do not appear to covary with δD (Figure 4-9). Jarosite compositions tend to form a line parallel to the Meteoric Water Line (MWL) when water controls $\delta^{18}O$ (Rye et al., 2000), so this lack of covariation may indicate that atmospheric oxygen played a role in pyrite oxidation in addition to meteoric water. Although it is difficult to determine which reaction put sulfate in solution, the narrow range of $\delta^{18}O_{(SO4)}$ values indicates that oxidizing conditions were consistent over time.

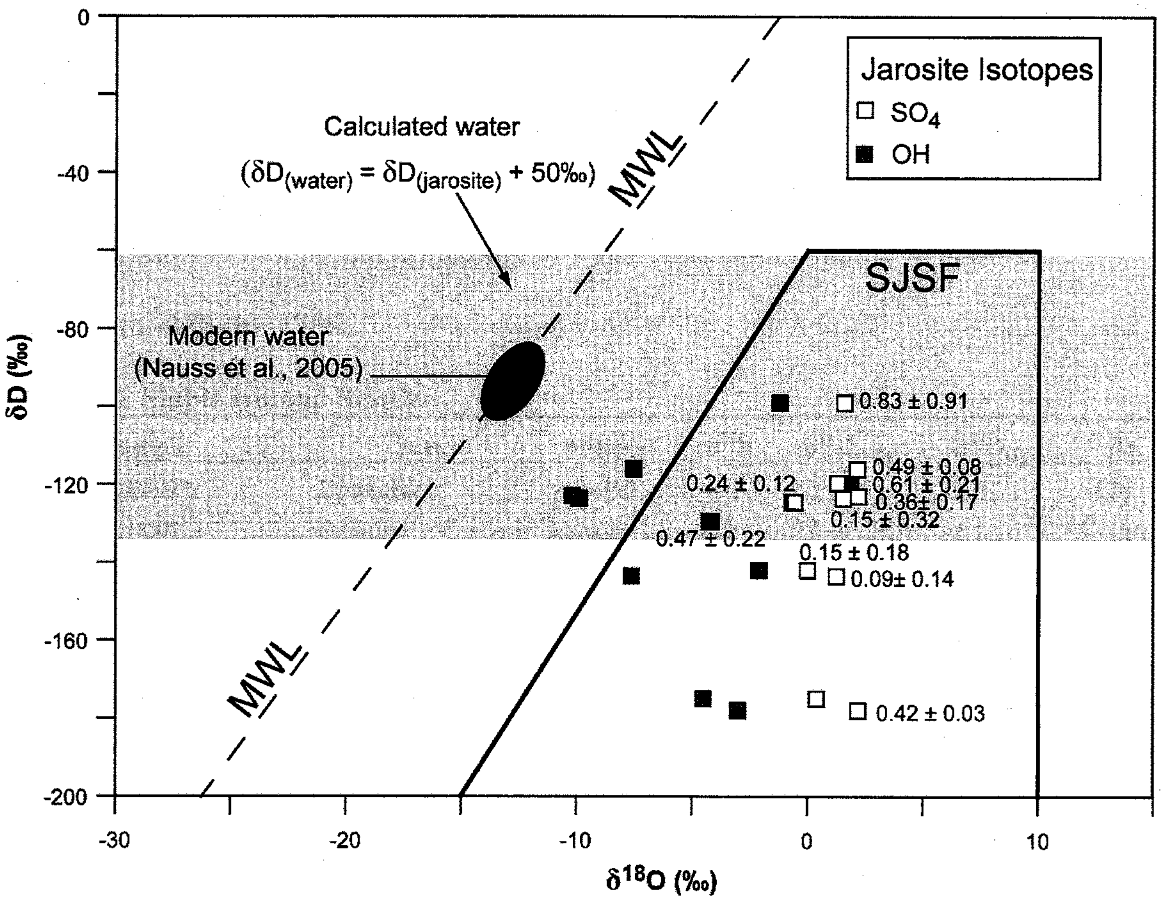

Figure 4-9. $\delta^{18}O$ vs δD diagram. Both $\delta^{18}O_{(OH)}$ and $\delta^{18}O_{(SO4)}$ were plotted. Jarosite sulfate oxygen places it in the supergene jarosite sulfate field (SJSF), confirming that it is supergene in origin. δD of the water that must have formed jarosite in this study was calculated based on the fractionation factor: $10_3\ln\alpha_{(H2O\text{-}Jarosite)} = 50 \pm 12$ ‰. RRV jarosite does not show a consistent decrease in δD with time. OH-site analyses are not consistently parallel to the Meteoric Water Line (MWL). Jarosite ages in Ma are listed next to each analysis.

RRV jarosite's $\delta^{18}O_{(SO4)}$ and δD values place it in the Supergene Jarosite Sulfate Field (SJSF) of Rye and Alpers, 1997, further indicating that jarosite formed under weathering, rather than hydrothermal, conditions in the RRV (Figure 4-9).

Although the origin of SO_4-site oxygen is ambiguous, hydrogen in the OH-site is derived solely from the water that forms the mineral. The fractionation factor between water and jarosite is not temperature-dependent: $10^3\ln\alpha_{H2O\text{-}Jarosite} = 50 \pm 12$ (Rye & Stoffregen, 1995). Although H_3O^+ in the A-site can undergo some isotopic exchange with meteoric water after jarosite precipitation (Alpers et al., 1992), the OH-site dominates the D/H signal, so isotopic exchange does not affect the δD value of RRV jarosite. These factors make δD a more reliable measure of water composition than $\delta^{18}O$. δD values range from -99‰ to -178‰.

Table 4-4. Stable Isotope Results

Sample	Scar	Mineral	$\delta^{34}S$	$\delta^{18}O_{(SO4)}$	$\delta^{18}O_{(OH)}$	δD
BCS VWL 0002*	Bittercreek	jarosite	-0.6	2.2	-3.0	-178
CAS VWL 0002	Capulin	jarosite	2.7	0.0	-2.1	-142
PIT VWL 0005	Goat Hill North	jarosite	-12.1	1.3	-7.6	-144
PIT VWL 0007	Goat Hill North	jarosite	-9.5	-0.6	-0.7	-125
KS-JB-4	June Bug	jarosite	-0.8	1.3	1.9	-120
KS-JB-3	June Bug	jarosite	-1.1	2.2	-7.5	-116
ESS VWL 0001	SE Straight Creek	jarosite	-2.3	2.2	-10.2	-123
KS-SC-2	SE Straight Creek	jarosite	-2.7	1.6	-1.2	-99
SWH GJG 0001	SW Hansen	jarosite	-2.8	1.6	-9.9	-124
SWH GJG 0025	SW Hansen	jarosite	-3.8	-4.3	-4.2	-130
SWH VWL 0001	SW Hansen	jarosite	-2.8	-1.8	-2.0	-163
GHS VWL 0007	Goat Hill South	jarosite	-2.7	6.1		
HAS GJG 0001	Hansen	jarosite	-6.7	-3.3		
SWH GJG 0004	SW Hansen	jarosite				-153
KS-BC-4	Bittercreek	pyrite	1.1			
KS-BC-2	Bittercreek	pyrite	1.2			
KS-JB-5	June Bug	pyrite	1.3			
KS-JB-2	June Bug	pyrite	1.4			
KS-SC-1	SE Straight Creek	pyrite	0.5			

*Campbell and Lueth, 2008

4.4.3. Age results

New RRV jarosite ages range from 0.09 ± 0.14 Ma to 1.31 ± 0.61 Ma (Figure 4-10), recording the timing of supergene pyrite oxidation. Table 4-5 summarizes age results, and Appendix B provides a detailed data table with the step-heating schedule. Four previously-dated samples were dated again: PIT VWL 0007, PIT VWL 0005, ESS VWL 0001, and CAS VWL 0002 (Lueth et al., 2006 and Lueth et al., 2008a; see chapter three). HF treatment decreased the apparent ages of all samples, but these samples continued to show increase in apparent age at higher power steps (see chapter three).

Precision in jarosite ages was low (Table 4-5). Of the new samples dated, sample KS-JB-3 produced the most well-behaved age spectrum with a plateau age of 0.49 ± 0.08 Ma over 100% of the ^{39}Ar released. Samples KS-JB-4, SWH GJG 024, SWH GJG 0025, and PIT VWL 0007 produced apparent ages with errors of 34%, 47%, 47%, and 50% of the age respectively. Error in jarosite dates for all other samples dated in this study exceeded the apparent age of the sample. When error is taken into account, sample KS-SC-2 produced apparent ages ranging from -0.83 to 1.74 Ma, making it impossible to interpret the age of this sample based on its argon date.

Data from Lueth et al. (2006) is included in the interpretation of jarosite ages. Samples BCS VWL 0002, SWH VWL 0001, and GHR VWL 0011 were not re-dated, but they yielded relatively flat age spectra when dated by Lueth et al. (2006), so their plateau ages of 0.42 ± 0.03 Ma, 0.31 ± 0.23 Ma, and 1.48 ± 0.52 Ma are included in the interpretation of the significance of jarosite dates for landscape evolution. Other samples dated by Lueth et al. (2006) could not be re-dated because not enough jarosite was available. These samples produced maximum ages as old as 4.63 ± 0.80 Ma. Structure in the age spectra for these samples suggests that silicate contamination exerted a strong control over apparent age, and the jarosite is probably younger (Lueth et al., 2008b).

Table 4-5. Summary of $^{40}Ar/^{39}Ar$ results as presented in Lueth et al., 2008a.

Sample	Phase	Environment	Age ± 2σ (Ma)	Comments
KS-JB-3	Jarosite	Supergene scar vein	0.49 ± 0.08	Plateau
KS-JB-4	Jarosite	Supergene ferricrete	0.61 ± 0.21	Plateau
SWH GJG 0025	Jarosite	Debris flow ferricrete	0.47 ± 0.22	Plateau
KS-SC-2	Jarosite	Debris flow ferricrete	0.83 ± 0.91	Plateau
SWH-GJG-0001	Jarosite	Supergene scar vein	0.15 ± 0.32	Plateau
CAS VWL 0002	Jarosite	Debris flow ferricrete	0.15 ± 0.18	Plateau
ESS VWL 0001*	Jarosite	Supergene scar vein	0.36 ± 0.17	Plateau
PIT VWL 0005*	Jarosite	Drill core profile	0.09 ± 0.14	Weighted mean^
PIT VWL 0007*	Jarosite	Supergene scar vein	0.24 ± 0.12	Weighted mean ^
SWH GJG 0024	Jarosite	Debris flow ferricrete	1.31 ± 0.61	Weighted mean ^
BCS VWL 0002^{+}	Jarosite	Supergene scar vein	0.42 ± 0.03	Plateau
SWH VWL 0001^{+}	Jarosite	Debris flow ferricrete	0.31 ± 0.23	Plateau
GHR VWL 0011^{+}	Jarosite	Supergene scar vein	1.48 ± 0.52	Plateau

* redated sample from Lueth et al., 2006 with new age assigned.

$^{+}$ Lueth et al., 2006

^ sample gas approached but did not reach plateau criteria

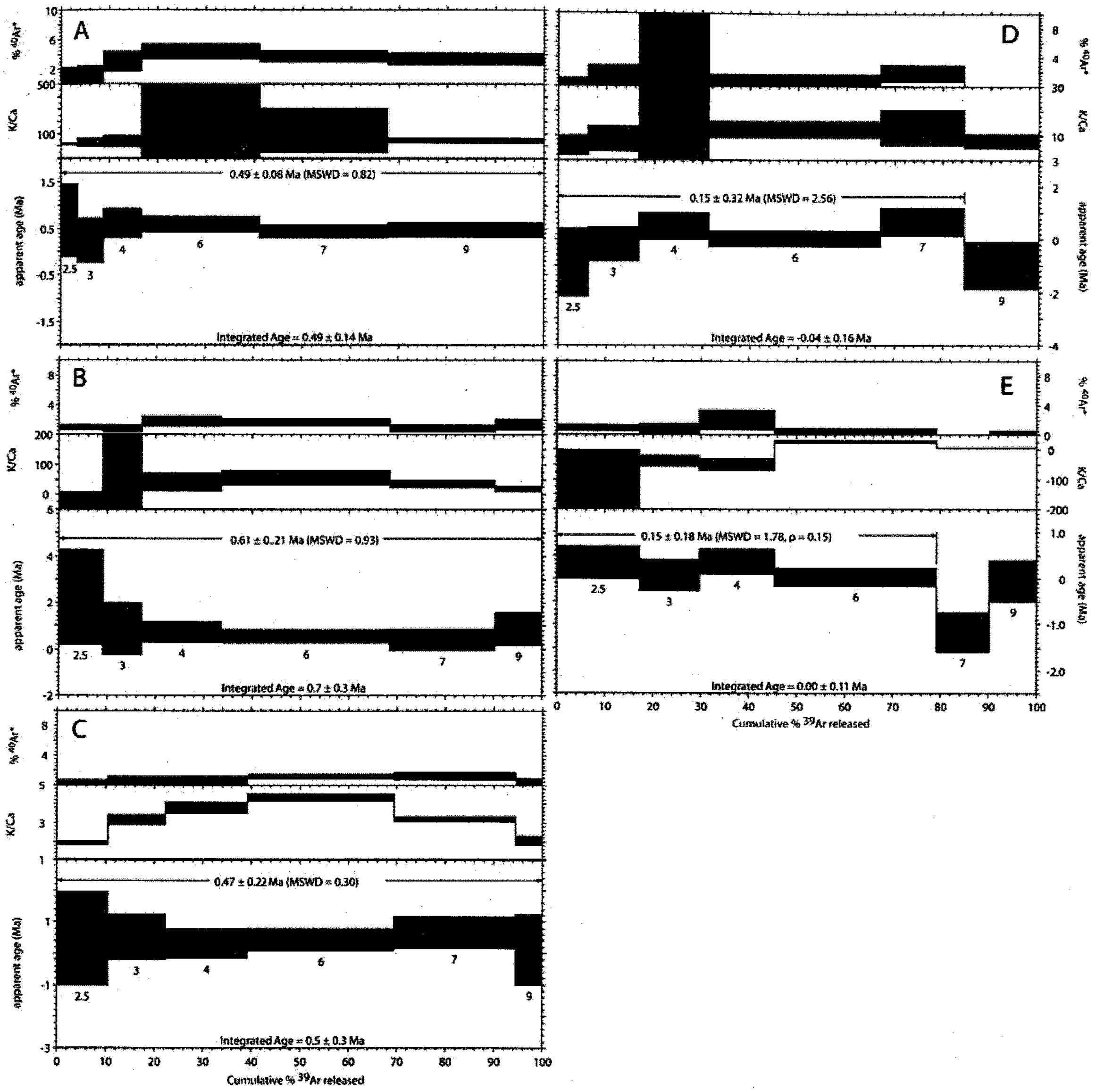

Figure 4-10. Age Spectra. A) KS-JB-3; B) KS-JB-4; C) SWH GJG 0025; D) SWH GJG 0001; E) CAS VWL 0002.

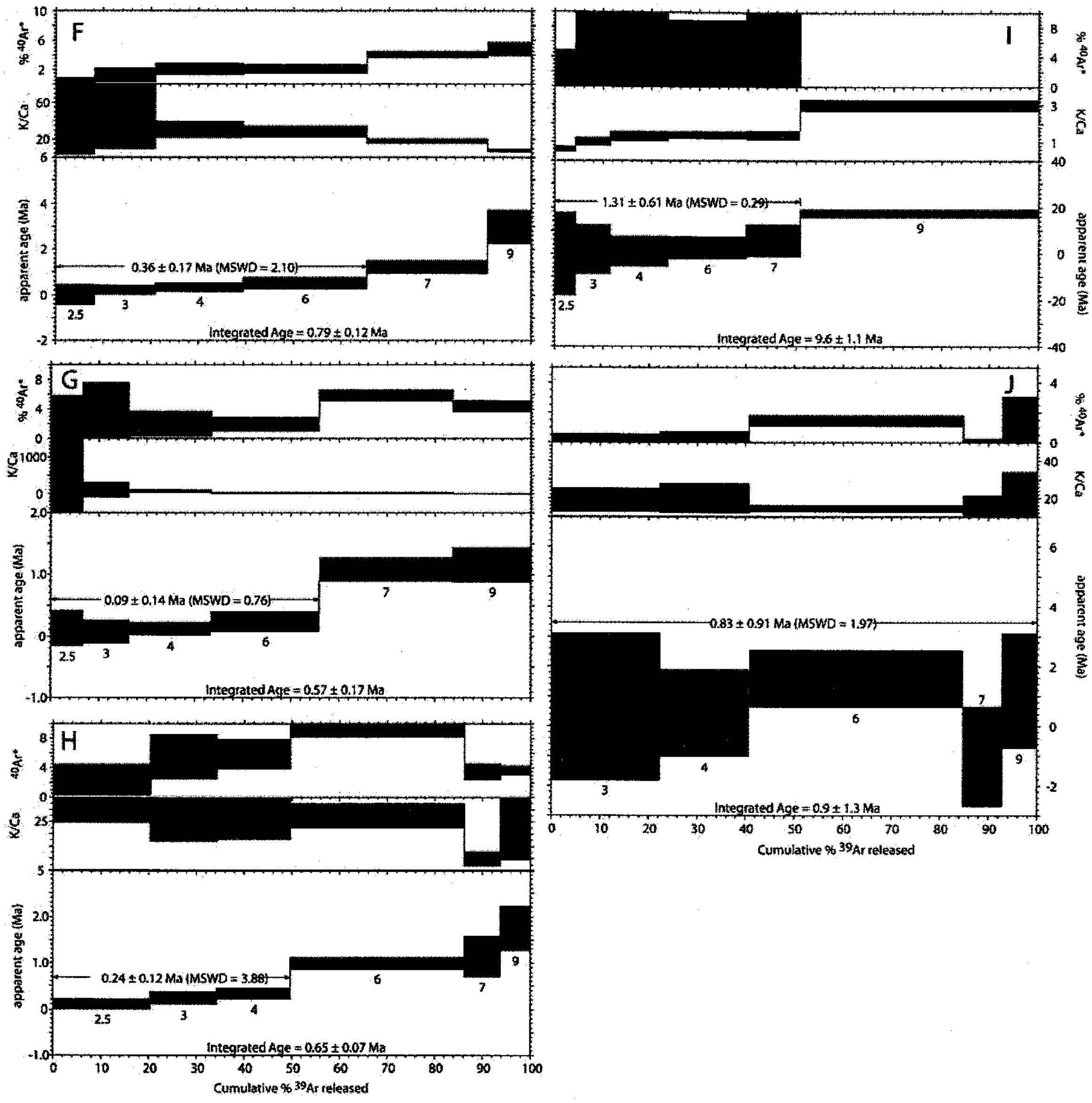

Figure 4-10 (cont'd). Age Spectra. F) ESS VWL 0001; G) PIT VWL 0005; H) PIT VWL 0007; I) SWH GJG 0024; J) KS-SC-2.

4.4.5. Radiocarbon Ages

^{14}C ages of organic material, like jarosite ages, lack precision. The three organic samples produced a broad range of calendar ages. The 419 year range of calendar ages for sample SWH GJG 0018 is related to error in radiocarbon measurements and the relatively constant radiocarbon in the atmosphere during this period (Figure 4-11a). The ^{14}C age for sample KS-BC-3 intersects the calibration curve in two places, producing a bimodal distribution of calendar ages (Figure 4-11b). Although the radiocarbon age for sample MIN DCS 0010 is relatively precise, the Gaussian distribution of ages intersects IntCal04 (Reimer et al., 2004) in an area where the slope of the curve decreases, and the calibrated calendar ages fall into four populations (Figure 4-11c). The assigned age of 4917 years old (2909 BC) is based on the date where the peak of the ^{14}C age curve intersects the calibration curve. Other possible ages in order of decreased confidence are: 4846 years old (2838 BC), 4823 years old (2815 BC), 4682 years old (2674 BC). Sample ages and $\delta^{13}C$ are listed in Table 4-6.

Table 4-6. Radiocarbon results

Sample	**Material**	**$\delta^{13}C$ (‰)**	**^{14}C age ± 1σ* (years BP)**	**Calibrated ages (calendar years BP)$^{+}$**	
				Intercept$^{\#}$	1σ range
SWH GJG 0018	Wood	-23.4	1540 ± 110	1478	1337-1756
KS-BC-3	Wood	-24.4	670 ± 80	718	584-793
MIN DCS 0010	charcoal	-24.3	4220 ± 40	4917	4682-4917

* Radiocarbon ages $\delta^{13}C$ corrected based on the Libby half-life ($t_{1/2}$ = 5570 years) as reported by Geochron Laboratories in ^{14}C years before AD 1950.

$^{+}$ ^{14}C ages converted to calendar years before present (BP), using IntCal04 curve (Reimer et al., 2004) and OxCal v. 4.0.5 (Bronk Ramsey, 1995 and 2001).

$^{\#}$ The intersection of the ^{14}C age curve and calibration curve

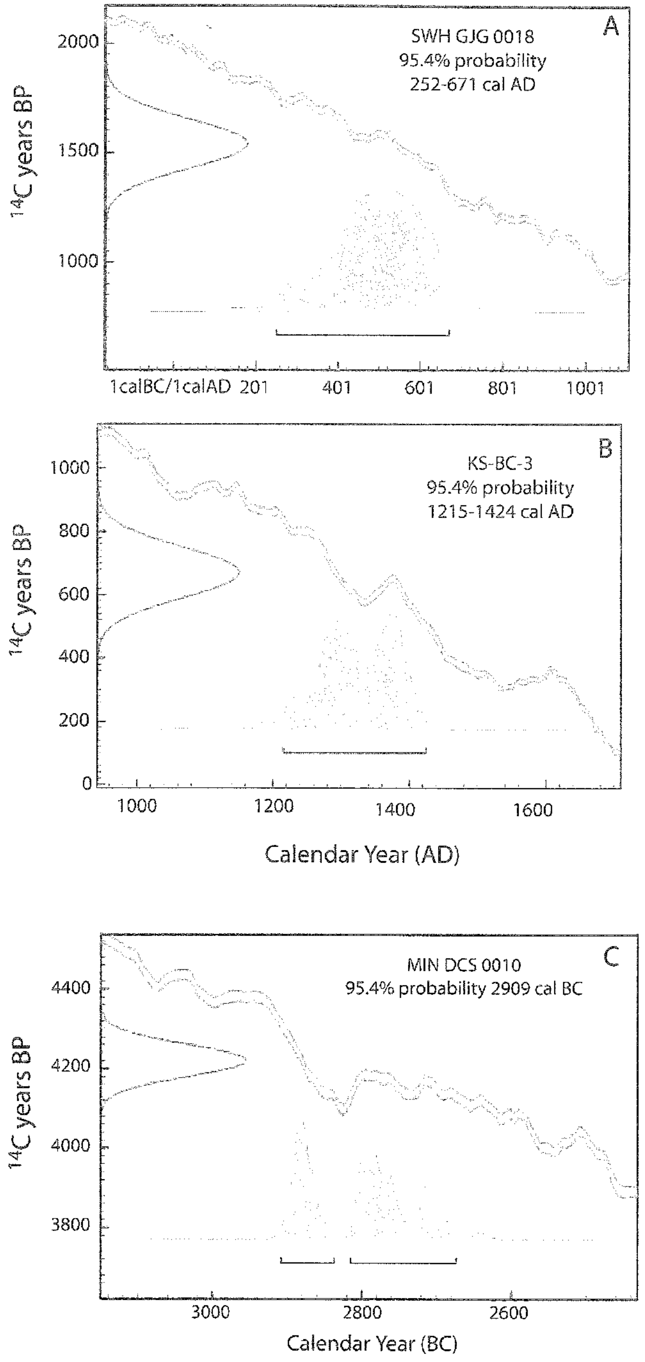

Figure 4-11. Calibrated radiocarbon dates. Radiocarbon years before present (BP) were converted to calendar ages. A) Sample SWH GJG 0018 formed 1478 years ago; B) Sample KS-BC-3 formed 718 years ago; C) Sample MIN DCS 0010 formed 4917 years ago. See text and Appendix F for a description of the calibration process.

4.5. Discussion

Jarosite ages can be used to constrain the timing of alteration scar formation. These ages, coupled with stable isotope compositions, can also be used to evaluate models of alteration scar formation. Correlating ages and isotopic compositions with previous work allows for an evaluation of the relationship between RRV alteration scar development, climate, and regional landscape evolution.

4.5.1. How old are the scars?

Jarosite samples dated in this study range in age from 0.09 ± 0.14 Ma to 1.48 ± 0.52 Ma. Based on these ages, alteration scar formation began at least 1 million years ago. Most of the dated jarosite formed less than 0.50 million years ago (Figure 4-12). The prevalence of young ages may be the result of sampling bias, incomplete preservation of older jarosite, or regional changes after 0.5 Ma that led to increased jarosite formation.

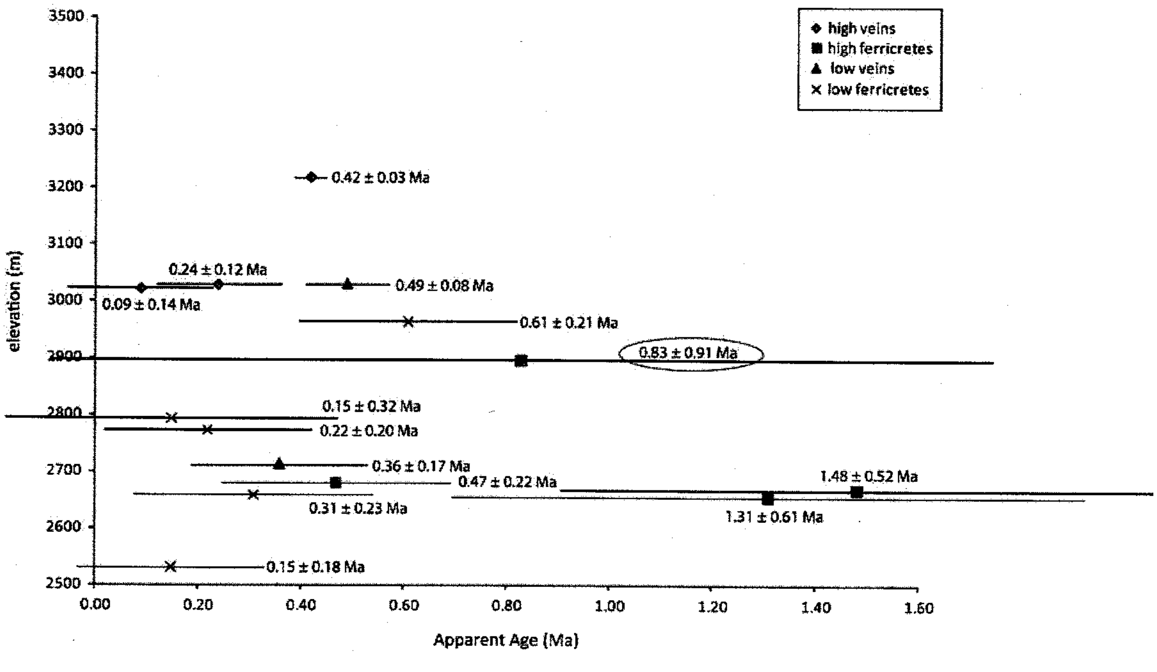

Figure 4-12. Distribution of ^{40}Ar/^{39}Ar dates. Jarosite ages range from 0.15 ± 0.18 Ma to 1.48 ± 0.52 Ma. Most samples dated are 0.50 Ma or younger. Jarosite precision is variable but typically low. Sample KS-SC-2 (circled) yielded an apparent age of 0.83 ± 0.91 Ma, making it difficult to interpret this sample's relationship to regional landscape evolution.

Ages show no systematic variation with distance from the Rio Grande rift (Figure 4-13). While uplift along the Sangre de Cristo fault and faults throughout the RRV was a key factor for exposing hydrothermally-altered rocks to surficial conditions, the ages presented here make it difficult to link alteration scar formation directly to faulting. Both young ages and apparently reliable older ages determined by Lueth et al. (2006) may correlate to the timing of Rio Grande stream capture events and regional weather patterns determined by other studies. These factors are discussed in a later section.

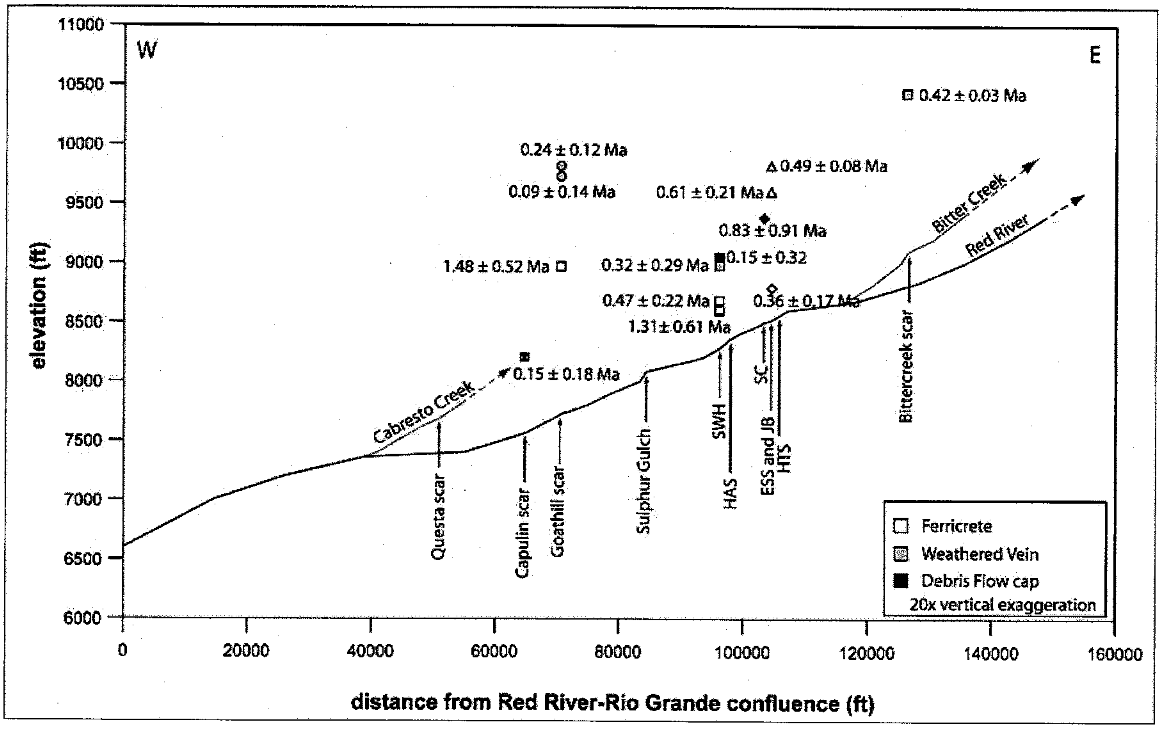

Figure 4-13. East to west distribution of RRV jarosite dates. This longitudinal profile shows samples and sample age relative to distance from the Rio Grande - Red River confluence (x = 0). There is no systematic variation in age from west to east.

4.5.2. How do alteration scars form?

Lueth et al. (2006) proposed a model for alteration scar development based on jarosite ages and stable isotope compositions. Their hypothesis states that abandoned ferricretes at three bands of elevation within scars record lowering of the water table, which intersected the land surface at different elevations at different times (Figure 4-14).

If this were the case, jarosite ages would decrease with decreasing elevation within an individual scar and, barring the influence of local faulting, be constant at a given elevation throughout the RRV (Lueth and Campbell, 2006). Lueth et al. (2006) attributed base level changes to uplift along the Sangre de Cristo fault because δD values decreased in apparently younger samples, suggesting that younger jarosite formed at higher elevations.

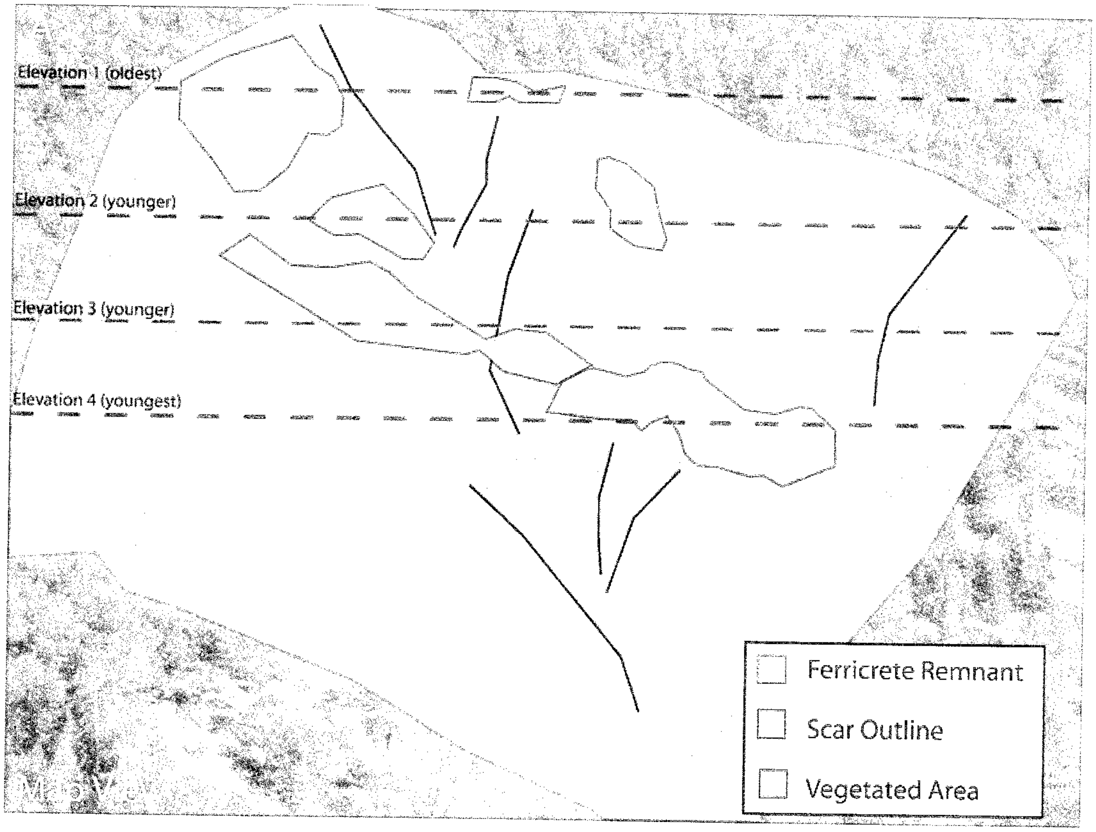

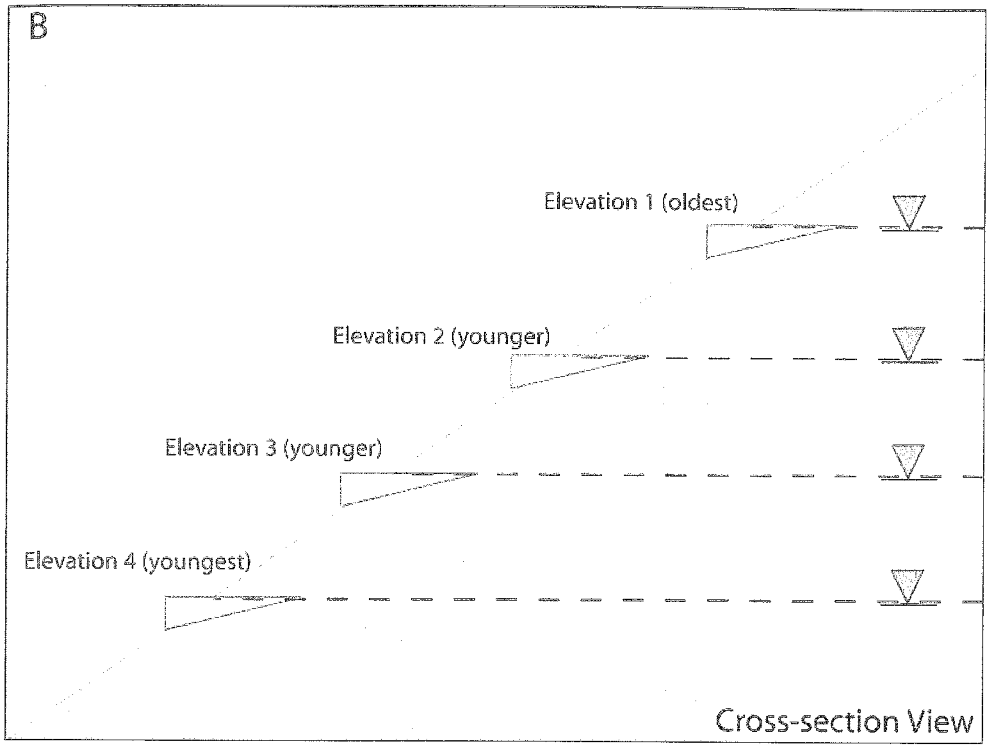

Figure 4-14. Cartoon of expected relationship between ferricrete elevation and age. Ferricrete remnants at different elevations within individual scars were initially thought to have formed at different times as the paleo-water table changed in the scar. If this were the case, remnants would become progressively younger at lower elevations. A) Map view of hypthesized relationship; B) Cross sectional view of hypothesized relationship.

Lueth et al. (2006) recognized that old silicate contaminants could make the apparent ages of jarosite older, so this thesis work was undertaken to refine sample preparation techniques and evaluate this hypothesis based on new dates.

4.5.2.1. Jarosite age and elevation

The hypothesized age progression does occur in weathered veins where samples from lower elevations are younger than those at higher elevations. Sample PIT VWL 0007, taken from a borehole through a weathered vein on the edge of Molycorp's open pit, yielded an age of 0.24 ± 0.12 Ma. Sample PIT VWL 0005, which is in the middle of the same core, produced an imprecise age of 0.09 ± 0.14 Ma. The lack of precision in these measurements makes them difficult to interpret because apparent age overlaps in this weathered vein. However, it appears that age decreases with depth in the borehole. This age is expected if the weathering front that propagated through this vein weathered material closer to the surface before percolating through and oxidizing deeper material.

Ferricrete ages crudely follow the hypothesized age progression, but they are not consistently younger at lower elevations within a single scar. In the Southwest Hansen scar, most ferricretes overlap in age within the 2-sigma confidence interval (Figure 4-15). These samples are from ferricretes that formed in the lower part of the Southwest Hansen scar. Two samples, SWH GJG 0025 and SWH GJG 0024, collected from the same ferricrete at elevations of 2680 meters and 2655 meters respectively produced apparent ages of 0.47 ± 0.22 Ma and 1.31 ± 0.61 Ma with the older sample lower than the younger sample (Figure 4-16). Although these samples almost overlap at 2-sigma, their formation was separated temporally by at least 10 ka. The age progression is consistent with a depositional environment. Field evidence suggests that this ferricrete formed in a debris flow that had its source at a much higher elevation in the scar.

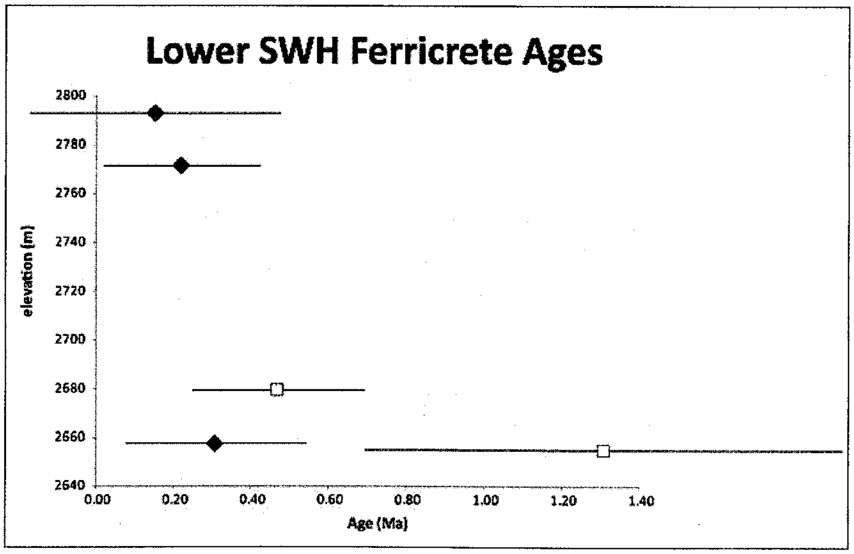

Figure 4-15. Age versus elevation for SWH ferricretes. Most SWH ferricrete samples overlap in age (blue diamonds). Samples SWH GJG 0024 and SWH GJG 0025 (white

squares) are from a debris flow that had its source area at a higher elevation in the SWH scar.

Rather than recording a drop in water table levels from top to bottom, the difference in age from the bottom to the top of the debris flow ferricrete may record the amount of time necessary to build a thick debris flow and cement it with iron oxides. Within error, the age difference between these samples ranges from 0.01 Ma to 1.67 Ma. Using the ferricrete accumulation rate calculated based on radiocarbon dating at the Bitter Creek scar, it would take 0.01 Ma (11905 years) to build a 24-meter thick ferricrete if water flowed through it continuously if ferricrete thickness, but not volume, is taken into consideration.

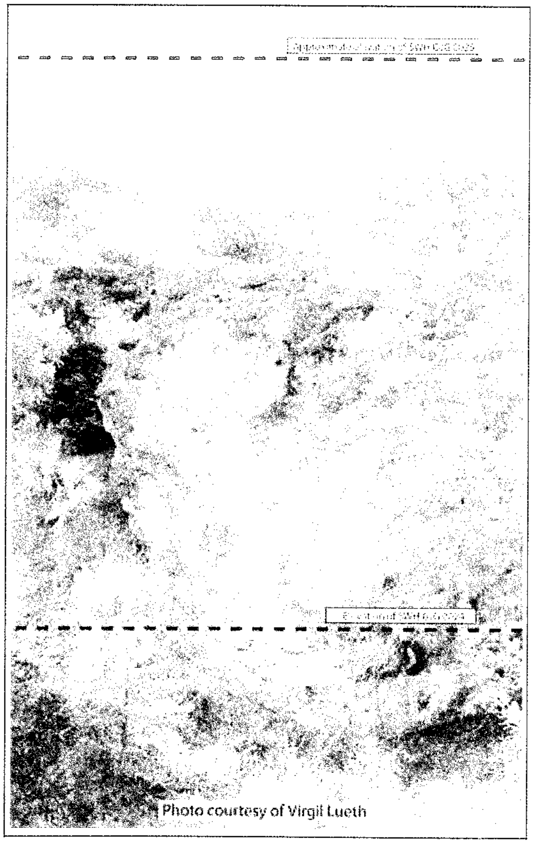

Figure 4-16. Photo of sample elevations for SWH GJG 0024 and SWH GJG 0025. Location of sample SWH GJG 0025 is not shown. Elevations of samples are marked with dashed lines. SWH GJG 0024 yielded an age of 1.31 ± 0.61 Ma. SWH GJG 0025 yielded an age of 0.47 ± 0.22 Ma.

If ferricrete locations recorded water table elevation at a given time, jarosite ferricretes at a given elevation in the RRV would be the same age. (Figure 4-17).

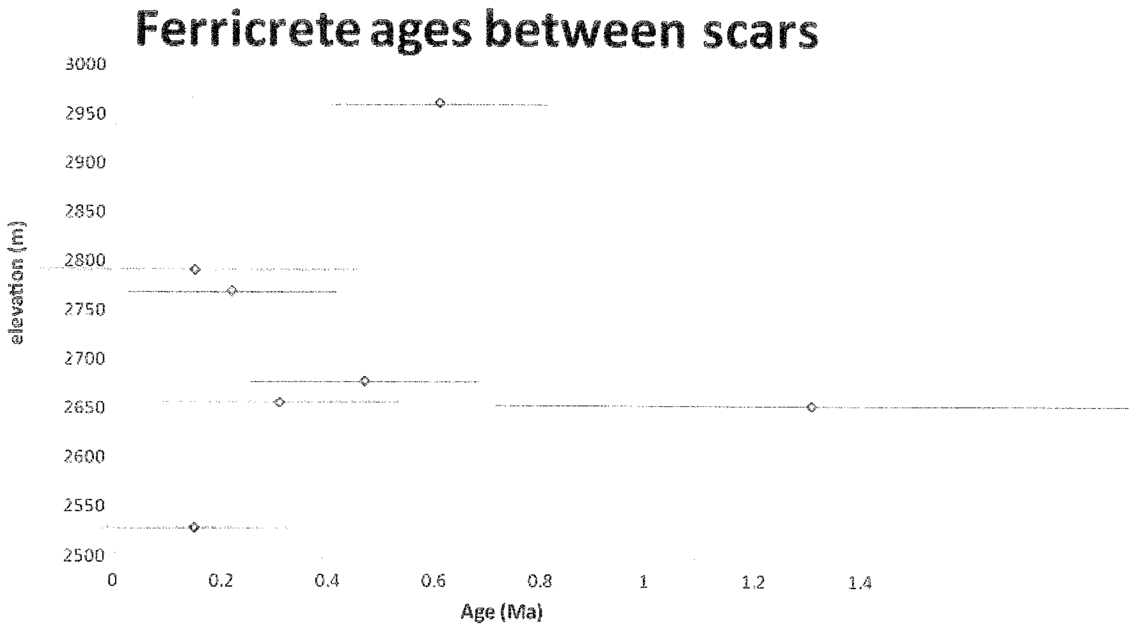

Figure 4-17. Sample elevation vs. sample age. Red lines show error in age determination. Ferricrete ages are not constant at a given elevation.

Ferricrete remnants that overlap in apparent age preserved at different elevations within a scar may be the result of factors other than a steadily-dropping water table. Ferricrete bedding planes in the Questa, Capulin, and Straight Creek scars are at constant orientations with respect to each other and the hillslope (Figure 4-18). Jarosite ages are not the same at a constant elevation (Figure 4-17). Ferricretes appear to mantle hillslopes during periods of relative stability. Although the underlying rock is mantled and initially protected from erosion, ultimately, the ferricrete is breached, and the underlying rock erodes rapidly during mass wasting events.

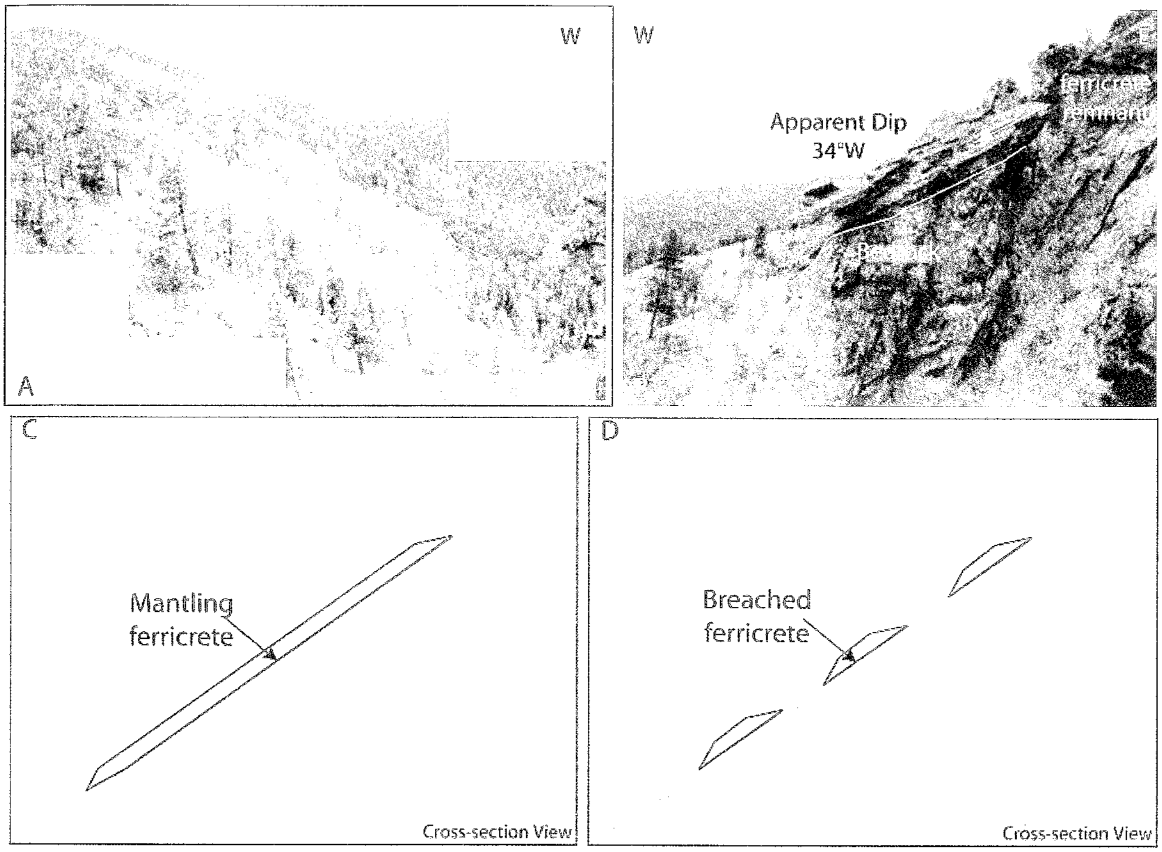

Figure 4-18. Mantling ferricretes. Bedding planes in ferricrete remnants are coincident with slope, suggesting they once mantled slopes prior to being breached. A) Ferricrete remnants in the Questa scar. Base of ferricretes is outlined in white; B) Close-up of ferricrete remnant in the Questa scar with an apparent dip of 34° to the west; C) Cartoon of ferricrete mantling a slope of hydrothermally-altered rock; D) Cartoon of breached mantling ferricrete with eroded scar material.

4.5.2.2. Jarosite ages between scars and drainage basin area

Meyer and Leonardson (1990) distinguished between low-elevation "inner valley" scars and high-elevation "divide" scars. Although ferricretes are not of a constant age at a given elevation, divide scars (Straight Creek (SC), Hansen (HAS), and Hottentot (HTS)), have larger drainage basin areas and older apparent ages than the inner valley scars (SWH, Southeast Straight Creek (ESS), and June Bug (JB)).

Both the SWH and SC scar samples exhibit this relationship between drainage basin area and relative age. A small scar is forming between the SWH drainage and the

HAS scar (Figure 4-19). The youngest SWH sample (0.15 ± 0.32 Ma) formed in a debris flow at the mouth of this subsidiary scar. This smaller scar has a drainage basin area of 0.39 km^2, while the main SWH drainage has a drainage basin area of 1.21 km^2. An age of 1.31 ± 0.61 Ma at the base of the large debris flow at the base of the SWH scar attests to the antiquity of the scar.

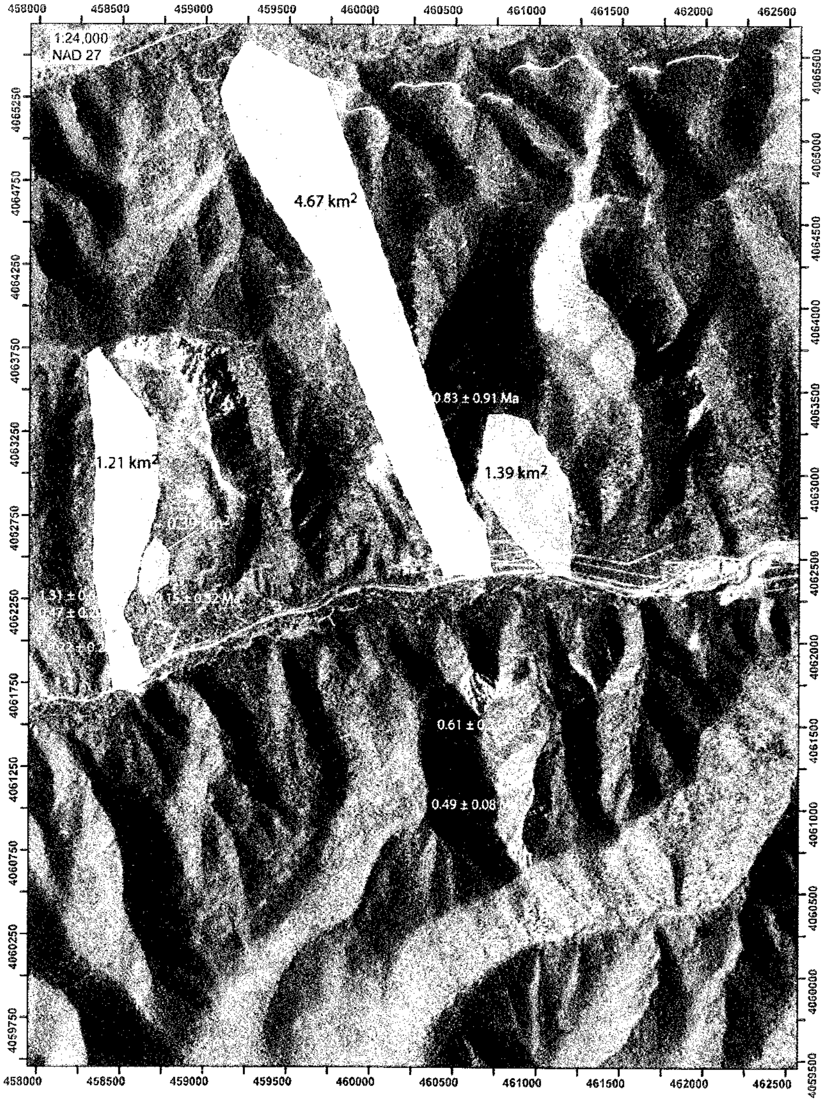

Figure 4-19. Relative ages and sizes of scar drainage basins. Scars with larger drainage basin areas yielded older jarosite ages than those with smaller drainage basin areas. Drainage basin area was calculated by approximating the shape of the area as an ellipse. This air photo shows SWH, HAS, SC, ESS, and HTS from east to west. JB is south of the river.

The Straight Creek scar (SC) is made up of the main drainage that extends 2385 m north of its confluence with the Red River and the Southeast Straight Creek scar (ESS), which has incised only 981 m into the mountain front. Sample KS-SC-2 was collected from a thin ferricrete that caps a debris flow more than 4 m thick on the edge of the main SC drainage (Figure 4-20). This debris flow sample gave an imprecise plateau age of 0.83 ± 0.91, making it impossible to interpret based on age data alone.

Some inferences about the relative age of sample KS-SC-2 can be made when stratigraphic position is taken into account. The debris flow that originally housed this sample has been incised. The present drainage for the Straight Creek scar is at an elevation of 2765 m. The debris flow is currently at an elevation of 2895 m, suggesting that it is an ancient surface. Debris flows are deposited at the mouths of alteration scars. The presence of this thick debris flow suggests that the mouth of the scar was 2 km north of the modern confluence of the Red River and Straight Creek scar when the debris flow was deposited. These stratigraphic indicators suggest that sample KS-SC-2 is relatively old.

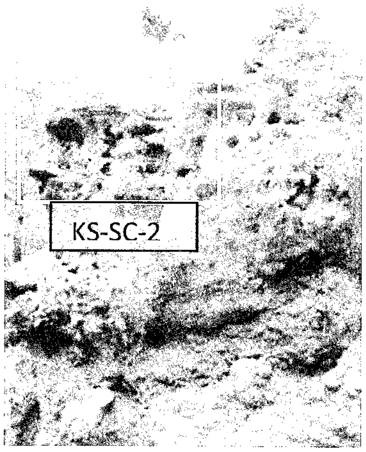

Figure 4-20. Photo of sample location for KS-SC-2 (0.83 ± 0.91 Ma). Ferricrete caps debris flow. Ryan Crow (2 meters tall) for scale.

Drainage basin area can also suggest geomorphic information about the relative ages of samples. The ESS sample is from a weathered vein at the edge of the ESS scar. Although the lack of precision on the SC sample makes sample ESS VWL 0001 (0.36 ± 0.17 Ma) the same age as KS-SC-2 within 2-sigma error, the ESS sample is probably younger than the SC sample based on drainage basin area for each scar. The main SC scar has a drainage basin area of 4.67 km^2 while the ESS scar has a drainage basin area of 1.39 km^2. Smaller scars may have had less time to erode than larger, older scars (Figure 4-19).

4.5.2.3. Origin and Evolution of Weathering in Alteration Scars

New jarosite ages can be used to refine hypotheses of alteration scar formation. Figure 4-21 provides a schematic view of scar initiation and evolution in the RRV. More than 7 km of uplift along the Sangre de Cristo fault (Figure 4-21a) exposed hydrothermally-altered rocks to surficial conditions (Caine, 2006), and formed the steep slopes associated with the scars (Meyer and Leonardson, 1990).

Altered rocks are mechanically-unstable due to grain size reduction during hydrothermal alteration and physical weathering, specifically freeze-thaw weathering patterns, and the formation of gypsum within fractures (Graf, 2008). Pyrite oxidation generates sulfuric acid. The material's low pH (Shaw et al., 2003; Nordstrom et al., 2005) makes it difficult for plants to grow, leaving the scar areas relatively unvegetated with little to no soil development (Meyer and Leonardson, 1990).

Ferricretes play a role in alteration scar formation by mantling streambeds and hillslopes at springs, shielding weak rock from erosion (Figure 4-21b). This would result in ferricrete remnants from different elevations overlapping in apparent age. Although ferricretes protect hydrothermally-altered rocks from physical erosion, water that passes through the underlying bedrock continues to dissolve silicate minerals as exhibited by high concentrations of dissolved SiO_2 and Al_2O_3 in ground and surface water that comes from the scars (Nordstrom et al., 2005; Graf, 2008), reducing grain-size further (Graf, 2008).

When the mantling ferricrete is incised, the further weakened hydrothermally-altered material rapidly erodes, and scars continue to grow by mass wasting processes (Figure 4-21c). Scars continue to grow until they erode into less altered, more competent rock, leaving older scars with steep head walls (Figure 4-21d). Dates presented in this study indicate that this process began between 1 and 2 Ma.

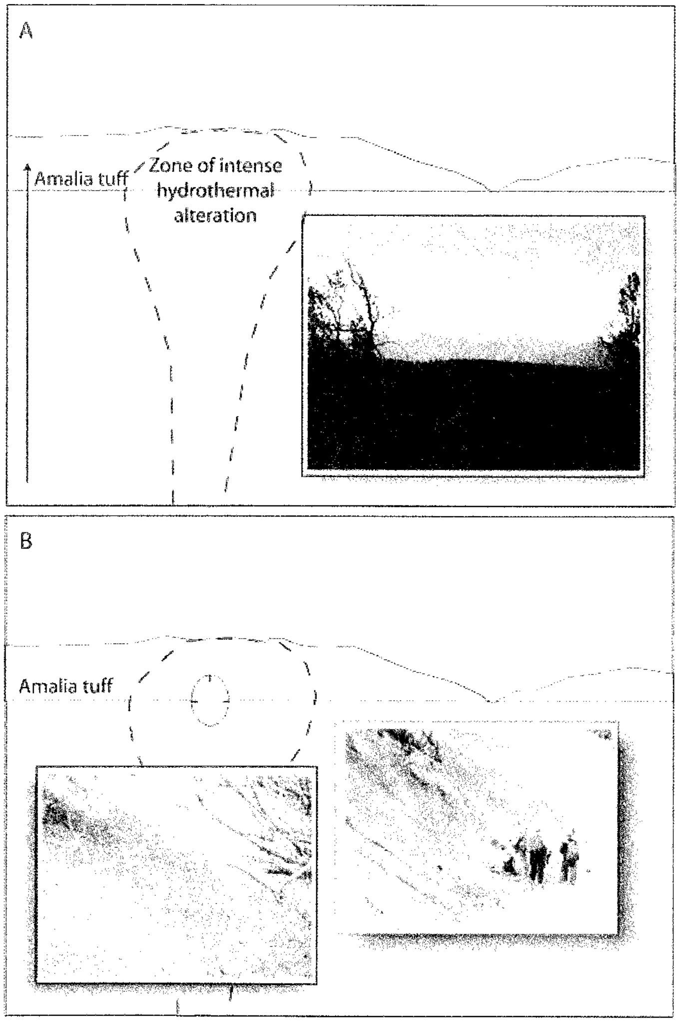

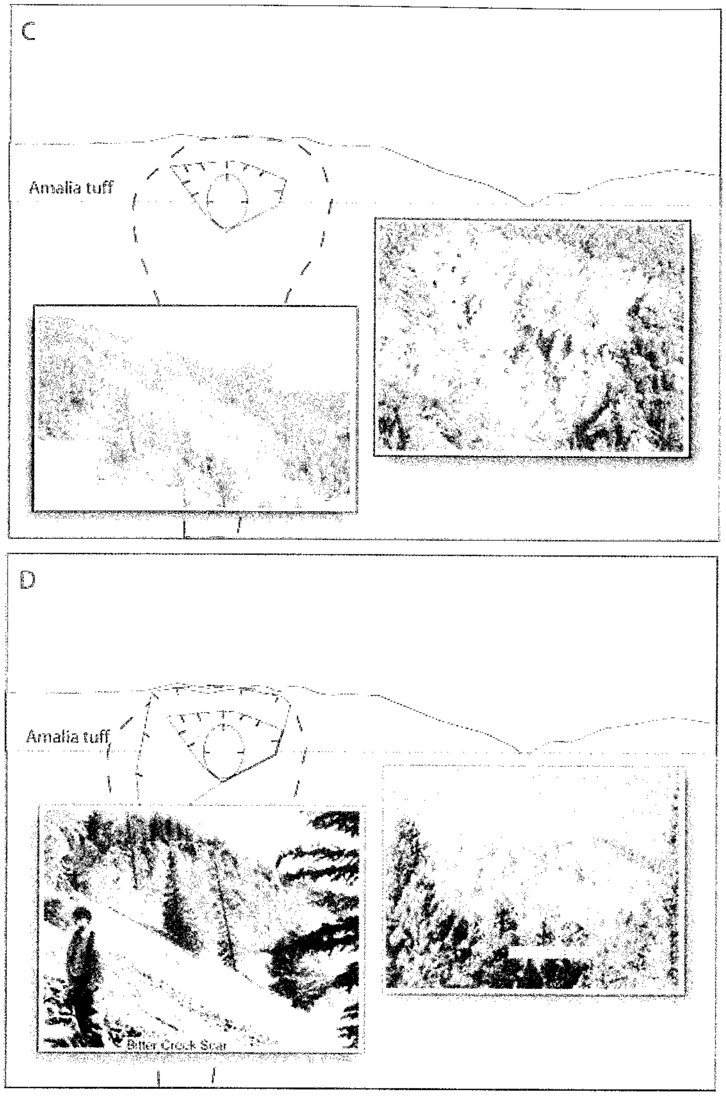

Figure 4-21. Alteration scar formation. Photos courtesy of Virgil Lueth. A) Uplift along the Sangre de Cristo fault after the eruption of Amalia tuff (ca. 25 Ma) exposed mechanically-weak, hydrothermally-altered volcanic rocks throughout the Red River valley; B) Pervasive fractures enhance weathering of hydrothermally-altered, pyrite-rich rocks (Caine, 2006). Mantling ferricretes initially inhibit erosion of weakened, hydrothermal material. Inset images show nascent ferricrete formation on early scar materials; C) Rapid erosion occurs when mantling ferricretes are incised. Scars continue to grow by mass wasting processes. Inset images show the Questa scar. Breached, mantling ferricretes (red-orange) cap more easily eroded gray clay layers; D) Scars grow until they reach less altered rock, leaving older/ scars with steep head walls. Inset images show steep head walls in the Bitter Creek (left) and Hansen (right) scars.

4.5.3. Alteration scar formation and climate

Some studies have hypothesized that alteration scar formation was initiated during glacial periods (Lueth and Campbell, 2006). Other regional studies have hypothesized a link between terraces and transitional periods from glacial (pluvial) to interglacial periods (Newell et al., 2004). Stable isotope compositions, particularly hydrogen isotope ratios, should provide direct measurements of environmental influences during jarosite precipitation (Arehart and O'Neil, 1993). δD values for RRV jarosite range from -99‰ to -178‰, which corresponds to a range in meteoric water δD of -49‰ to -128‰. A number of factors can influence δD variations in meteoric water, including changes in paleolatitude, paleoaltitude, and paleoclimate as well as seasonal temperature fluctuations (Arehart and O'Neil, 1993).

Changes in paleolatitude and seasonal temperature fluctuations can be eliminated as potential sources of δD variation in RRV jarosite. Jarosite in this study formed at a latitude of 36°, and the RRV's latitude has not changed significantly during the Quaternary. Individual jarosite grains are too small to be analyzed, so stable isotope determinations were made on bulk samples. This approach averages out fine-scale seasonal δD variations (Arehart and O'Neil, 1993).

Like paleolatitude and seasonal variations, changes in paleoelevation cannot explain the 80‰ fluctuations in δD. Meteoric water becomes isotopically-lighter as elevation increases at a rate of $\Delta^{18}O/\Delta h = -0.28‰/100$ m (Poage and Chamberlain, 2001). Since $\delta^{18}O$ and δD vary together in meteoric water, hydrogen isotope ratios should decrease at a rate of $\Delta D/\Delta h = 8 * \Delta^{18}O/\Delta h = -2.24‰/100$ m.

The RRV has undergone episodic isostatic uplift during the Cenozoic due to Rio Grande rift extension. Although exhumation rates have varied both spatially and temporally (Bauer and Kelson, 2004; Kelson and Olig, 1995), uplift rates of 150 to 250 m/Ma have occurred along the Sangre de Cristo fault over the past 1.8 Ma. At this rate, the elevation of the RRV should have increased by 222 to 485 m over the past 1.48 Ma, leading to a decrease of only 5‰ to 11‰ in δD composition.

Continuous uplift over this period would be reflected as a steady decrease in D/H ratio. Rye et al. (2000) attributed steady decreases in δD at Creede, CO to tectonic uplift rather than climate variations, but δD fluctuates over time in the RRV (Figure 4-22) rather than steadily decreasing as at Creede, CO.

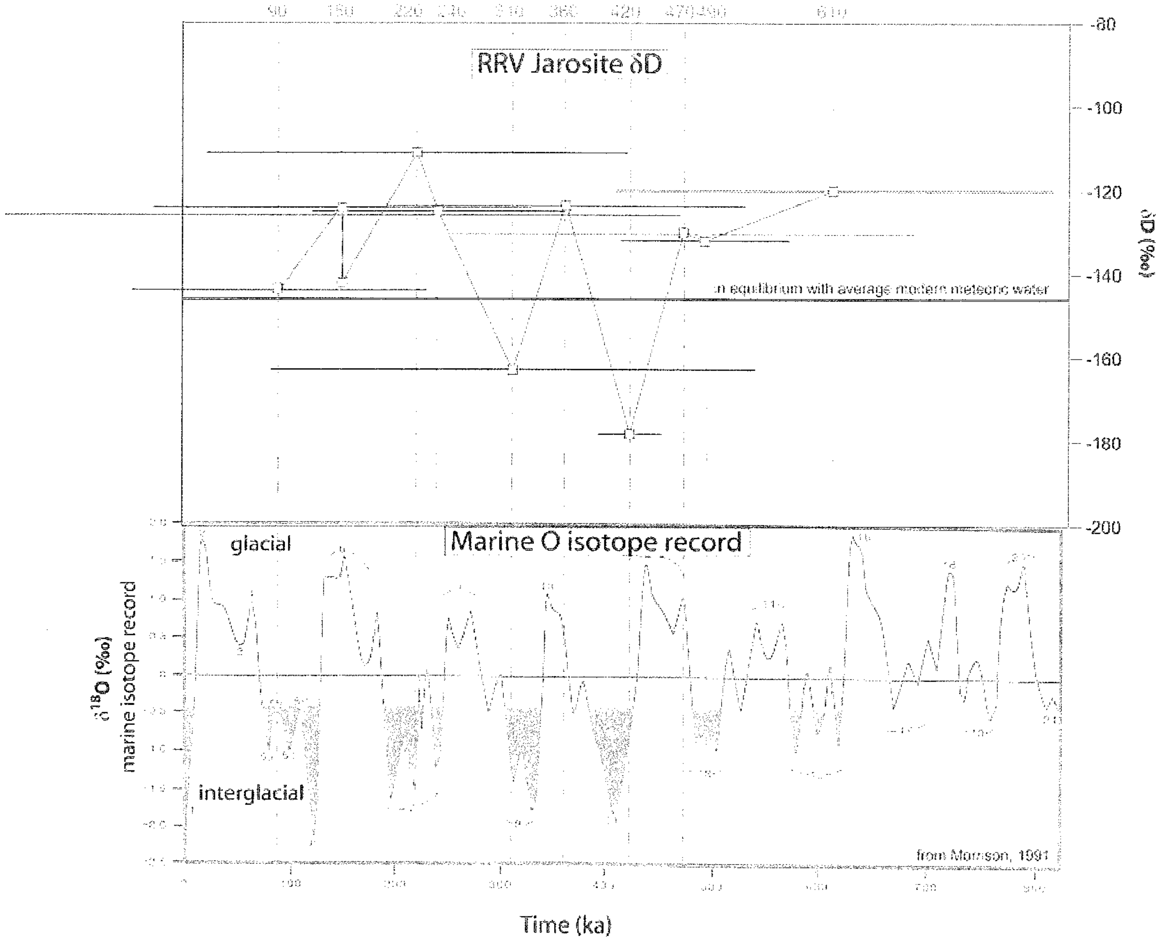

Figure 4-22. RRV jarosite δD and the marine isotope record. δD variations do not align with the climate information recorded in the marine isotope record. Lack of precision in jarosite ages may help to explain this lack of correlation. Horizontal bars at each data point represent 2-sigma error in apparent age. Sample KS-SC-2 (0.83 ± 0.91 Ma) has a

δD value of -99‰, but the apparent age is so imprecise, that it is unusable in a diagram that shows isotopic composition as a function of age, so it is excluded from this diagram.

Climate shifts are the most likely cause of δD fluctuations in RRV jarosite over the past 1.48 Ma. Jarosite records local climate variations with lighter values representing cooler, wetter periods, and heavier values designating warmer, drier periods (Arehart and O'Neil, 1993). Samples BCS VWL 0002 (0.42 ± 0.03 Ma; δD = -178‰) and SWH VWL 0001 (0.31 ± 0.23 Ma; δD = -163‰) formed under cooler, wetter conditions than those in the modern RRV. All other jarosite samples appear to have formed under warmer, drier conditions.

Correlating local climate variations with global climate records is difficult. Rayleigh distillation processes control the condensation of water vapor and, ultimately, precipitation from evaporated seawater. Water vapor is isotopically-lighter than its source liquid water, and precipitation becomes lighter with respect to $\delta^{18}O$ as it moves inland from the oceans (Figure 4-23). During Quaternary glacial periods, large volumes of water were stored on land as isotopically-light glacial ice, making the oceans isotopically heavier (Morrison, 1991). δD varies linearly with $\delta^{18}O$ in meteoric water, so continental δD values should be lighter during glacial periods and heavier during interglacial periods.

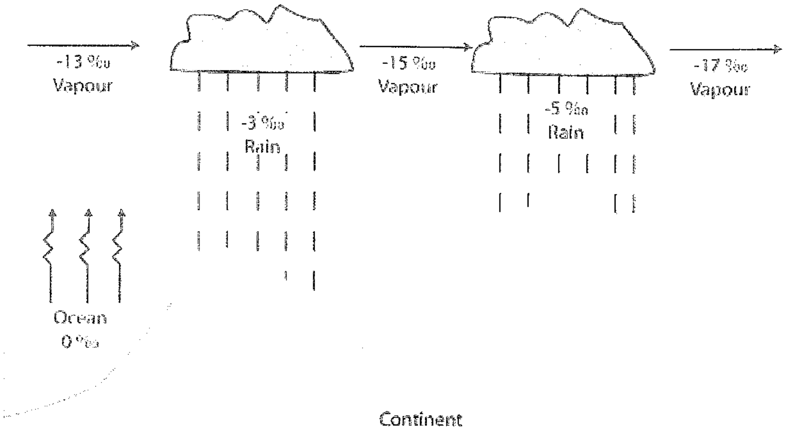

from Hoefs, 2004

Figure 4-23. Cartoon of meteoric water isotopic compositions. Meteoric water has its origin in the ocean. $\delta^{18}O$ decreases as the ocean evaporates and as clouds move inland. During glacial periods, oceanic $\delta^{18}O$ became heavier as isotopically-light water was stored on land as glacial ice. δD varies with $\delta^{18}O$ in meteoric water, so δD values should follow the same trend with light water on land corresponding to glacial periods.

Continental climate records do not correlate perfectly with the marine isotope record, so it is important to compare δD variations in RRV jarosite with local climate proxies studied by other workers. Rogers et al. (1992) studied flora, fauna, organic and inorganic $\delta^{13}C$, and sediments to determine climate recorded in the Alamosa formation in the San Luis basin of southern Colorado. Stratigraphic sections used in the Rogers et al. (1992) study were bracketed by Huckleberry Ridge and Bishop tuff, indicating that they formed between 2.02 and 0.74 Ma. They used paleomagnetic data to subdivide this age range.

Only sample KS-SC-2 yielded an apparent age within this age range, but the large error associated with that age makes it difficult to correlate it with Rogers et al.'s (1992) paleoclimate record. This sample's δD value is heavier than a jarosite that formed in equilibrium with modern meteoric water would be (Figure 4-24), so it is interpreted to have formed during a warmer period. Rogers et al. (1992) found evidence of a short warmer period from 0.82 to 0.81 Ma in a predominantly colder period.

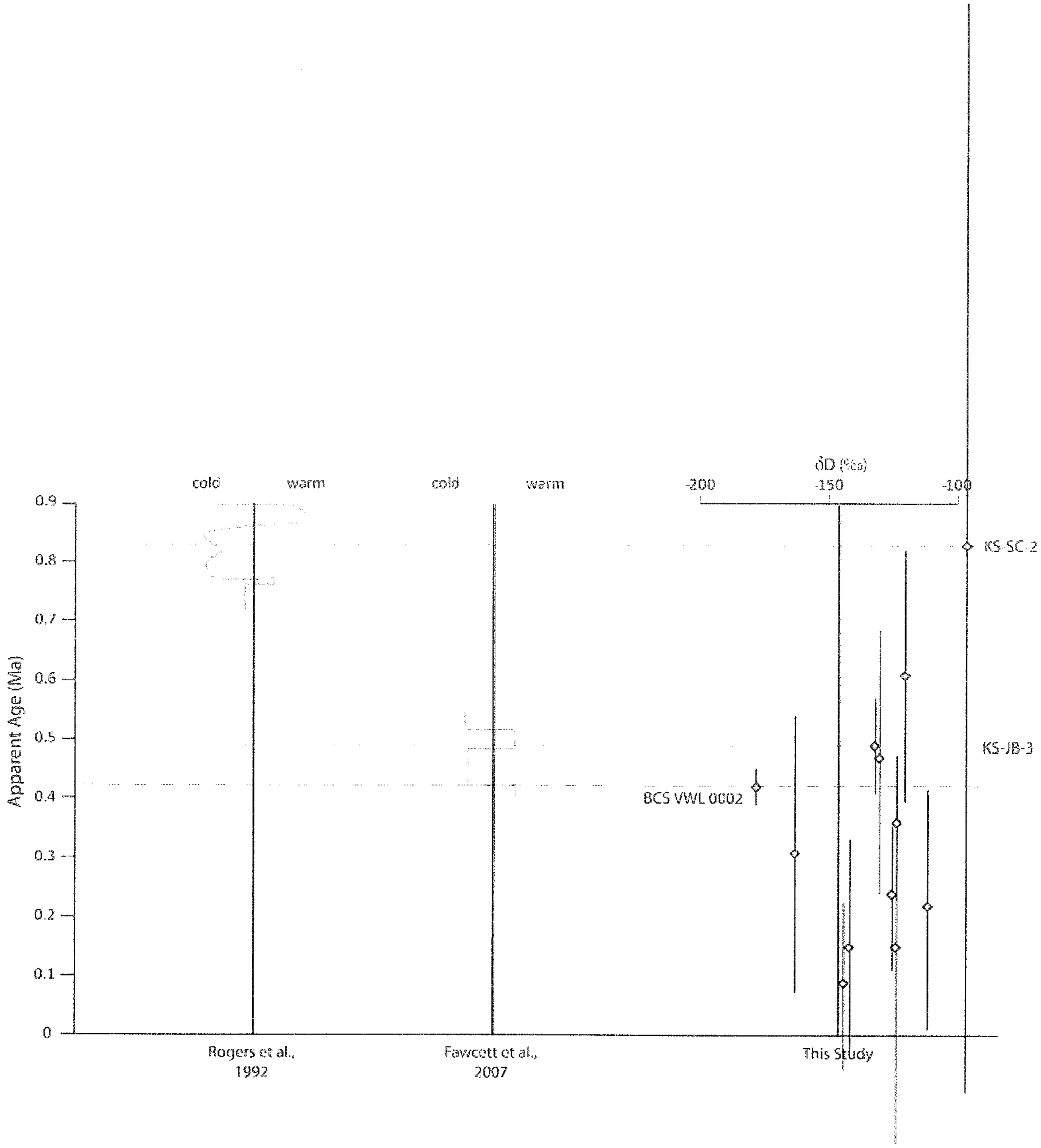

Figure 4-24. δD and local climate variations. δD variations in RRV jarosite do not correlate perfectly with local paleoclimate records from the San Luis basin in southern Colorado (Rogers et al., 1992) or Jemez Mountains (Fawcett et al., 2007). Sample KS-SC-2 corresponds roughly with a brief warm period during a longer glacial period from 0.82-0.81 Ma (Rogers et al., 1992), but error in apparent age makes this correlation suspect. Samples KS-JB-3 and BCS VWL 0002 roughly reflect other local climate shifts. Errors in age (vertical lines) make it difficult or impossible to interpret δD values.

Fawcett et al. (2007) identified climate fluctuations in Valle Grande lake sediments from ca. 0.55 to 0.40 Ma. The base of the core contained South Mountain rhyolite ash, which they dated at ca. 552 ka. Subsequent age control was provided by magnetostratigraphy (Donohoo-Hurley et al., 2007). Fawcett et al. (2007) identified warm periods based on mud cracks, total organic carbon, and the $\delta^{13}C$ composition of organic carbon. One warm period from 0.53 to 0.49 Ma roughly corresponds to periods of high δD values in RRV jarosite, but these samples also overlap with cooler periods within error in age determination.

Unfortunately, although RRV jarosite δD values roughly correspond to local climate fluctuations documented by other workers, lack of precision in $^{40}Ar/^{39}Ar$ ages makes it impossible to trust jarosite to fill in temporal gaps in the local paleoclimate record.

4.5.4. Rio Grande integration and Red River incision

Although jarosite stable isotopes cannot be used to evaluate the connection between alteration scar formation and climate, jarosite ages correlate to times of Rio Grande stream capture events. Water from alteration scars flows into the Red River, which joins the Rio Grande west of Questa in the Rio Grande gorge. Base level changes in the Red River may control headward erosion in the scars. Red River incision is, in turn, affected by base level changes in the Rio Grande.

The Rio Grande rift began as a series of internally-drained tectonic basins (Figure 4-25). Gravel deposits of Jemez mountains volcanic rocks in the Albuquerque-Belen basin indicate that an axial drainage connected the Albuquerque-Belen with the Española basins between 10 and 7 Ma (Connell, 2004). Bearhead rhyolite overlies gravels primarily composed of Tusas Mountains quartzite and metavolcanics, indicating that the

Española and southern San Luis basins were connected by 6.96 Ma (Smith, 2004). The headwaters of this ancestral Rio Grande were probably in the Rio Chama (Newell et al., 2004). Jemez volcanic field pumice rafted downstream at 3.1, 2.0, 1.6, and 1.3 Ma, forming gravel beds in the Camp Rice formation near Las Cruces. The presence of Jemez pumice near Las Cruces indicates that the rift was drained by an axial stream to its mouth during the Pliocene (Mack et al., 1996).

Although the Rio Grande was a through-going stream south of the Red River before RRV jarosite formed, the northernmost part of the rift was integrated into this drainage system during the Pleistocene. The two oldest RRV jarosite samples in this study produced ages of 0.83 ± 0.91 Ma and 1.48 ± 0.52 Ma. Two regional events, identified by previous workers, may have influenced jarosite formation and scar erosion during this period. River terraces near the confluence of the Rio Grande and the Red River indicate that the Rio Grande headwaters shifted north from the Chama River to the Red River sometime in the Pleistocene (Wells et al., 1987) probably between 2 Ma and 0.65 Ma (Bauer, 2008). Stream capture led to incision in the Red River, although the Red River's convex up profile near its confluence with the Rio Grande suggests that incision did not bring it into equilibrium with the Rio Grande (Figure 4-13). Base level drop in the rift, however, may have led to vadose zone jarosite growth and hillslope instability/ erosion. There is also evidence that monsoon weather patterns with high levels of rainfall started in the San Luis basin in southern Colorado after 1.6 Ma (Rogers et al., 1992). Modern debris flows in alteration scars occur during these heavy storms, so the onset of this weather pattern may have led to increased erosion if monsoons began in the RRV at the same time.

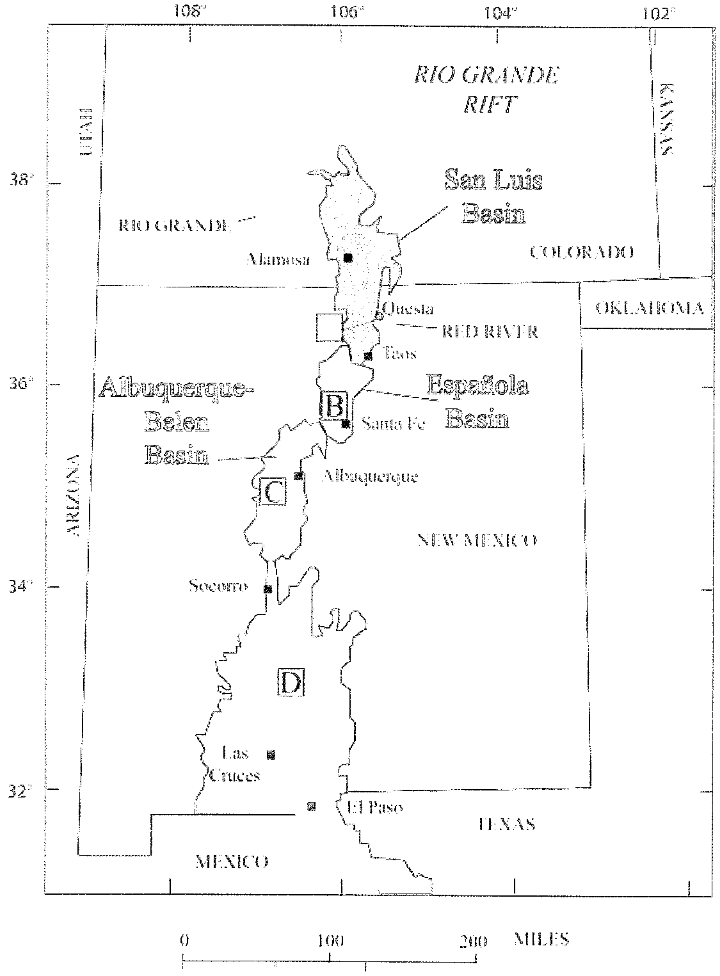

Modified from:
http://cires.colorado.edu/science/groups/sheehan/projects/riogrande/images/faq2.jpg

Figure 4-25. Timing of Rio Grande rift integration. The Rio Grande rift started as a series of internally-drained tectonic basins. The Rio Grande became the axial drainage for the rift in stages. A) The Red River became the headwaters of the Rio Grande sometime between 2 and 0.65 Ma (Bauer, 2008). The San Luis basin north of the San Luis hills was internally drained by Lake Alamosa until ca. 0.44 Ma (Machette et al., 2007); B) The southern San Luis and Española basins were connected by the ancestral Rio Grande by 6.96 Ma as indicated by Tusas Mountains and Latir volcanic field gravels overlain by Jemez Mountains volcanics (Smith, 2004); C) The Albuquerque-Belen and Española basins were integrated between 10 Ma and 7 Ma. This river ended in a playa lake in the Albuquerque-Belen basin (Connell, 2004); D) The ancestral Rio Grande flowed through southern New Mexico by 3 Ma as indicated by Jemez pumice beds deposited near Las Cruces (Mack et al., 1996).

A stream capture event may also explain the high occurrence of jarosite ages between 0.3 Ma and 0.6 Ma. A 180-meter high knickpoint north of the Red River Rio

Grande confluence indicates that the axial stream that integrates the rift is relatively young upstream of its confluence with the Red River (Wells et al., 1987). Before the Rio Grande became the axial drainage of the Rio Grande rift in southern Colorado, the San Luis basin north of the Sunshine Hills was drained internally, as documented by a large playa lake (Lake Alamosa) in the northern San Luis Basin (see especially, Wells et al., 1987; Machette et al., 2007). Recent ^{3}He dating of a reworked basalt boulder in a shoreline deposit has indicated that this integration could have occurred as recently as 440 ka (Machette et al., 2007). The integration of the northern and southern parts of the San Luis basin would have led to increased stream power and incision in the Rio Grande, lowering Red River base level, and increasing erosion in the RRV.

4.5. Conclusions

Dating supergene jarosite has some serious limitations. Separating fine-grained supergene jarosite from older, potassium-bearing minerals is difficult. HF does not preferentially remove potassium from jarosite, so it can be used to dissolve older silicates, but longer treatment times than those used in this study are necessary to remove a larger percentage of the clays. Clays start to degas in the same temperature range as jarosite and can increase the apparent age of the sulfate. Additionally, RRV jarosite is young, so radiogenic yield is low, which affects precision.

Despite these limitations, RRV jarosite ages do make sense stratigraphically and can be used to refine the models of landscape evolution in the RRV. RRV jarosite ages and isotopic compositions suggest that scar formation was initiated at least 1 million years age. Scars erode via mass wasting (debris flow) events rather than gradual processes, so the onset of monsoons after 1.6 Ma may have led to conditions conducive to alteration scar growth. Rio Grande stream capture events between 2 and 0.65 Ma and again at 0.44 Ma led to base level drop in the Red River. Alteration scar formation was probably initiated through a combination of base level drop and onset of monsoons.

Earlier studies indicated that alteration scars began forming anywhere from 25 Ma (Schilling, 1956) to the Pliocene (Meyer and Leonardson, 1990). Previous dating efforts (Lueth and Campbell, 2006) hypothesized that jarosite recorded the progressive lowering of the water table between ca. 4.5 Ma and 0.34 Ma due to regional uplift, similar to the conditions under which jarosite and alunite formed at Creede, CO. However, Lueth et al. (2006) recognized that their reported jarosite ages were influenced by older, hypogene clay and volcanic feldspar and that jarosite probably formed much more recently.

The current study shows that Lueth et al. (2006) were correct in assuming that their dates were too old, and alteration scar formation probably began ca. 1.5 Ma. Rye et al.'s (2000) supergene jarosite and alunite may also have been contaminated with older K-bearing phases, but there is no way to evaluate that based on conventional K/Ar dates. Re-dating Creede samples using the $^{40}Ar/^{39}Ar$ method may show that Creede and the Red River responded to regional conditions at the same time.

5. FUTURE WORK

As with all research projects, this research has inspired new questions. The following is a list of potential follow-up projects.

5.1. Precision, precision, precision

Although reducing the concentrations of silicate contaminants from RRV jarosite led to increased accuracy in ^{40}Ar/^{39}Ar jarosite dates, these dates are imprecise, making it difficult or impossible to correlate the alteration scar ages with any regional landscape evolution processes. Radiogenic yield is the main source of error in RRV jarosite age measurements. Dilution of ^{40}Ar* with atmospheric argon may be the culprit that reduces radiogenic yield.

The source of atmospheric argon in these analyses is unknown. Fluid inclusions in RRV jarosite may be the main source of atmospheric argon. Reducing the number of fluid inclusions may increase radiogenic yield, improving precision in supergene jarosite ages. The fluid inclusions need to be characterized. Fluid inclusions were not observed in BSE images of RRV jarosite. In PB jarosite, inclusions were only seen in SE images of unpolished samples. This type of imaging needs to be done on untreated and HF-treated jarosite to characterize the inclusions. Additional gettering time using more reactive metals (e.g. silver getters) may improve supergene jarosite argon dating by removing more reactive gases.

5.1. Classification of ferricretes

Ferricretes currently form in creekbeds and at seeps that represent local base level near the Red River. Little attention was paid in this thesis to the different types of ferricretes and the potentially different implications of ages from different types of ferricretes. Careful mapping of both ancient and active ferricretes could resolve this issue.

5.2. Faults in alteration scars

Several studies allude to the presence of faults in the scars (Meyer and Leonardson, 1990; Caine, 2006), and slickenlines can be observed in scars. Scar faults are not documented in published geologic maps (Lipman and Reed, 1989). Comprehensive mapping of scars with special attention paid to faults could aid in interpretation of ages from west to east.

5.3. Relationship between terraces (deposition) and scars (erosion)

Pazzaglia and Wells (1990) indicate that terraces established in the RRV are associated with climate change and regional base level changes. However, the relationship between terraces and scars has not been studied. Determining this relationship could help in refining the understanding of when the Red River became the headwaters of the Rio Grande and the timing of the capture of Lake Alamosa.

5.4. Debris flow timing and frequency

Debris fans are frequently preserved at the mouths of scars in the RRV. Trees that are not uprooted often continue to grow after being caught in a debris flow. Debris flows are then incised by new streams, so multiple generations of debris flows are preserved in debris fans. Mapping debris flows within an individual scar (ie. Questa or Bitter Creek) could help to refine the understanding of alteration scar development. Trees caught in debris flows could be cored for dendrochronology work.

5.5. Remove the silicates!

HF treatment in this study failed to remove all silicate contaminants. Although ages appeared to be meaningful geologically, improving sample preparation techniques to remove more silicates may lead to changes in apparent age and interpretation of landscape evolution in the RRV.

APPENDIX A: MANGANESE OXIDE GEOCHRONOLOGY RESULTS

A.1. Manganese Oxides

K-bearing manganese (Mn)-oxides are relatively common in weathering profiles. However, not all K-bearing Mn-oxides are datable by the K-Ar and $^{40}Ar/^{39}Ar$ methods (Table A-1). Hollandite-group minerals, particularly hollandite and cryptomelane, can give reliable dates (Vasconcelos, 1999 and references therein). These minerals have the general formula $(A)_{1-2}B_8O_{16} \cdot xH_2O$. Monovalent cations, such as K^+, Na^+, or Cu^+, reside in the A-site, which forms a tunnel through the crystal. This tunnel site can also accommodate divalent cations, including Ba^{2+}, Pb^{2+}, Rb^{2+}, Sr^{2+}, Cs^{2+} (Vasconcelos et al., 1994b). Hollandite group minerals have a 2 x 2 tunnel structure, which retains Ar and K more effectively than romanechite's 2 x 3 structure or todorokite's 3 x 3 structure (Figure A-1; Vasconcelos, 1999). The exact mechanism for argon and potassium retention in the hollandite group's tunnel structure is unknown, but tunnel diameter may control retentivity. Zeolites, which also have tunnel structures, have been shown to experience argon loss (V. Lueth, personal communication).

Table A-1. Suitability of K-bearing Mn-oxides for $^{40}Ar/^{39}Ar$ geochronology (Vasconcelos, 1999).

Mineral	Approximate Formula	Group	Suitability for $^{40}Ar/^{39}Ar$ geochronology
hollandite	$(Ba,K)_{1\text{-}2}Mn_8O_{16}\cdot xH_2O$	hollandite	Suitable
cryptomelane	$(K,Ba)_{1\text{-}2}Mn_8O_{16}\cdot xH_2O$	hollandite	Suitable
coronadite	$(Pb,Ba,K)_{1\text{-}2}Mn_8O_{16}\cdot xH_2O$	hollandite	Undetermined
romanechite	$(Ba,K,Mn^{2+},Co)_2Mn_5O_{10}\cdot xH_2O$	romanechite	leaks argon (unsuitable)
todorokite	$(Ca,Na,K)(Mg,Mn^{2+})Mn_5O_{12}\cdot xH_2O$	todorokite	cation exchange (unsuitable)
Birnessite	$(Na,Ca,K)(Mg,Mn)Mn_6O_{14}\cdot 5H_2O$	birnessite	structural instability (unsuitable)

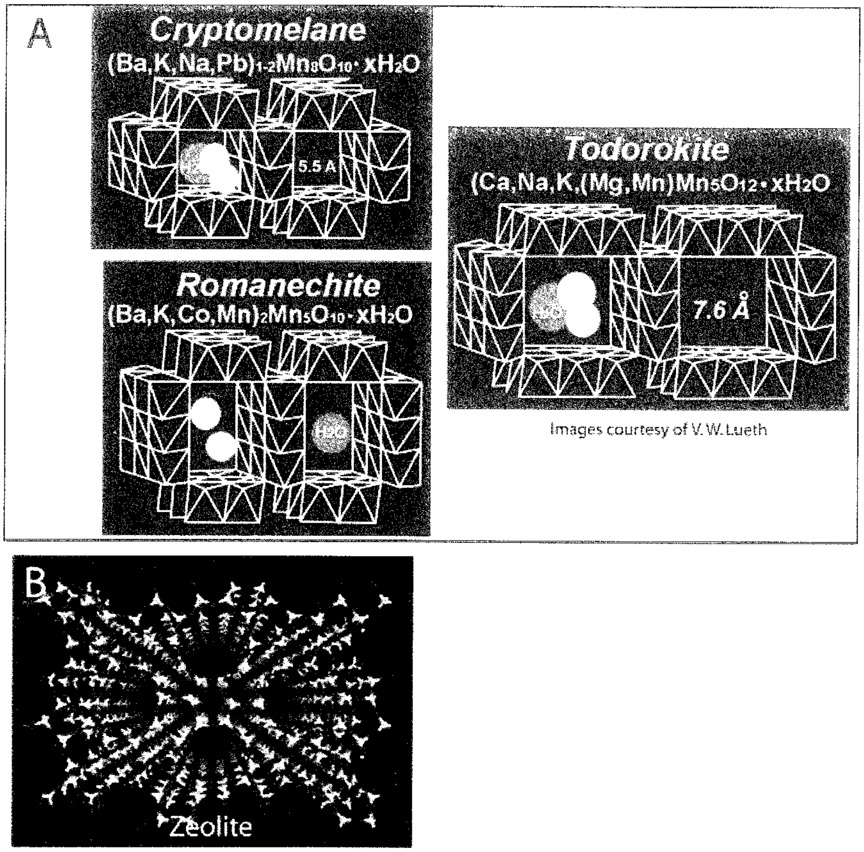

Images courtesy of V. W. Lueth

http://catalystdesign.envision.purdue.edu/index.php?page=zeolite

Figure A-1. Mn-oxide structure dictates whether or not it can be dated using the $^{40}Ar/^{39}Ar$ method. A) Cryptomelane's 2 x 2 tunnel structure retains both K and Ar more effectively than romanechite's 3 x 2 structure or todorokite's 3 x 3 structure. Images courtesy of Virgil W. Lueth. B) Although cryptomelane's tunnel sites retain K and Ar, the mechanism is poorly-understood. Zeolites, which also have tunnel structures, are undatable via the 40Ar/39Ar method because their tunnel structures do not retain K and Ar.

Although cryptomelane is the most suitable hollandite group mineral for $^{40}Ar/^{39}Ar$ dating, experiments on both natural and synthetic cryptomelane have shown a high degree of alkali exchange between cryptomelane and surrounding fluids. However, Vasconcelos (1999) indicates that these studies are inconclusive and that the degree to which cryptomelane exchanges K with weathering solutions may depend on the crystallinity of individual samples.

Cryptomelane's composition dictates its behavior when heated under vacuum. K-rich cryptomelane is more resistant to phase transformations at high temperatures than cryptomelane with a high concentration of Cu^+ in the A-site. Cu-rich samples start to break down at 330°C while K-rich cryptomelane breaks down at 648°C (Vasconcelos et al, 1994b).

Supergene cryptomelane can precipitate directly from solution or through oxidation and K-metasomatism of primary minerals. Direct precipitation occurs through the reaction: $K^+_{(aq)} + 8Mn^{2+}_{(aq)} + 8H_2O_{(l)} + 4O_{2(aq)} + OH^-_{(aq)} \leftrightarrow KMn_8O_{16}(OH)_{(crypt)} + 16H^+_{(aq)}$. Cryptomelane can form through oxidation/ dissolution and subsequent K-metasomatism of rhodochrosite: $8MnCO_{3(rds)} + K^+_{(aq)} + 4O_{2(aq)} + 8H_2O_{(l)} + OH^- \leftrightarrow KMn_8O_{16}(OH)_{(crypt)} + 8H_2CO_{3(aq)}$ or Mn-silicates: $8MnSiO_{3(rdn)} + K^+_{(aq)} + 4O_{2(aq)} + 16H_2O_{(l)} + OH^-_{(aq)} \leftrightarrow KMn_8O_{16}(OH)_{(crypt)} + 8H_4SiO_{4(aq)}$.

Supergene Mn-oxides form in many geologic settings. Cryptomelane generally forms botryoidal intergrowths with other Mn-oxides in reducing conditions (Vasconcelos, 1999). Supergene cryptomelane has been used to date weathered Mn-ore deposits (Vasconcelos, 1999) and Mn-rich shale (Vasconcelos and Conroy, 2003). Manganocretes form locally in Red River valley, NM debris flows and alteration scars (Fig. 10). Although these MnOx samples contain cryptomelane, dating efforts were unsuccessful.

A.2. MnOx Characterization

Two MnOx samples were dated in this study. XRD analysis of Mn-oxides was performed by Jim Connolly, who provided the raw scans, at the University of New Mexico Department of Earth and Planetary Sciences. Connolly provided the following summary of analytical conditions. XRD analyses were performed on a Scintag Pad V diffractometer with DataScan 4 software from Materials Data, Inc. (MDI) for system automation and data collection. Cu-K-ά radiation (40 kV, 35 mA) was used with a Bicron Scintillation detector (with a pyrolitic graphite curved crystal monochromator). Samples were run between 10 and 70 deg 2-Θ with a 0.02 deg 2- Θ step size in step-scan mode with a dwell time of 1.2 sec/step. This is an effective scan rate of 1 deg 2- Θ /min. The range was chosen to cover all of the significant peaks likely in most Mn and Mn/Fe Oxides (J. Connolly, pers. comm.). XRD analysis identified these samples as predominantly a mixture of todorokite and cryptomelane with silicate contaminants. The two samples were also characterized by EMPA at the New Mexico Bureau of Geology and Mineral Resources. Samples were prepared according to methods described in chapter 2. Quantitative analysis was not conducted on these samples. Back-scattered electron imaging shows that in KSQ-1, clasts of FeOx-coated quartz + kspar contaminated the sample (Figure A-2).

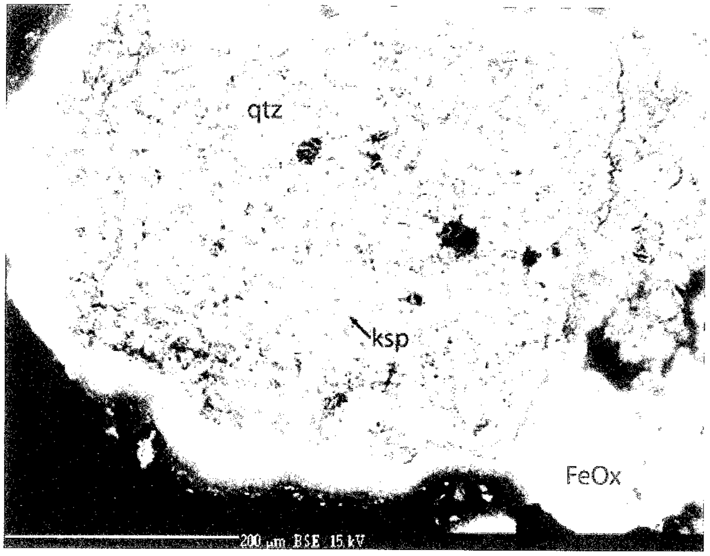

Figure A-2. Contaminated MnOx. Sample KSQ-1 consisted of a mixture of Mn-oxides and silicate contaminants, including this large clast of quartz (qtz) and potassium feldspar (ksp) surrounded by Fe-oxides. Because the Fe-oxides are black and difficult to distinguish from the Mn-oxides under a binocular microscope, this type of contaminant was not removed from the sample during the mineral separation process.

A.3. Geochronology Results

GHD VWL 0002 produced a slightly-disturbed age spectrum with a plateau age of 64.2 ± 2.4 Ma over 50.9% of the ^{39}Ar released (Figure A-3a). K/Ca ranges from 0.11 to 3.2 over the course of the analysis. Although K/Ca is relatively constant and low, radiogenic yield increases progressively over the course of the analysis. At higher wattage, apparent age fluctuates, producing a hump-shaped spectrum.

Although this sample produced a plateau age, the age is geologically-unreasonable. GHD VWL 0002 MnOx cements a debris flow within boundaries of the Questa caldera. Any debris flow that predates the eruption of the Amalia tuff ~25 Ma would have been obliterated during caldera collapse. There are several possible explanations for the old apparent ages: 1) the manganese oxides could be contaminated with older K-bearing phases (Chapter three; Appendix B); 2) the sample could have experienced recoil loss of ^{39}Ar in the reactor. This sample has not been assigned an age.

In KSQ-1, apparent age increased over the course of the analysis (Figure A-3b). Like GHD VWL 0002, radiogenic yield increased over the course of this analysis. K/Ca is higher than in GHD VWL 0002 and more variable. The hump-shaped structure at high-wattage steps in GHD VWL 0002 appear in KSQ-1's age spectrum as well. No age was assigned to KSQ-1.

Encapsulation experiments on pure, hypogene, highly-crystalline cryptomelane showed that there is no recoil loss of ^{39}Ar under these ideal conditions (Lueth et al., 2004; Figure A-4). However, this experiment has not been replicated on supergene cryptomelane.

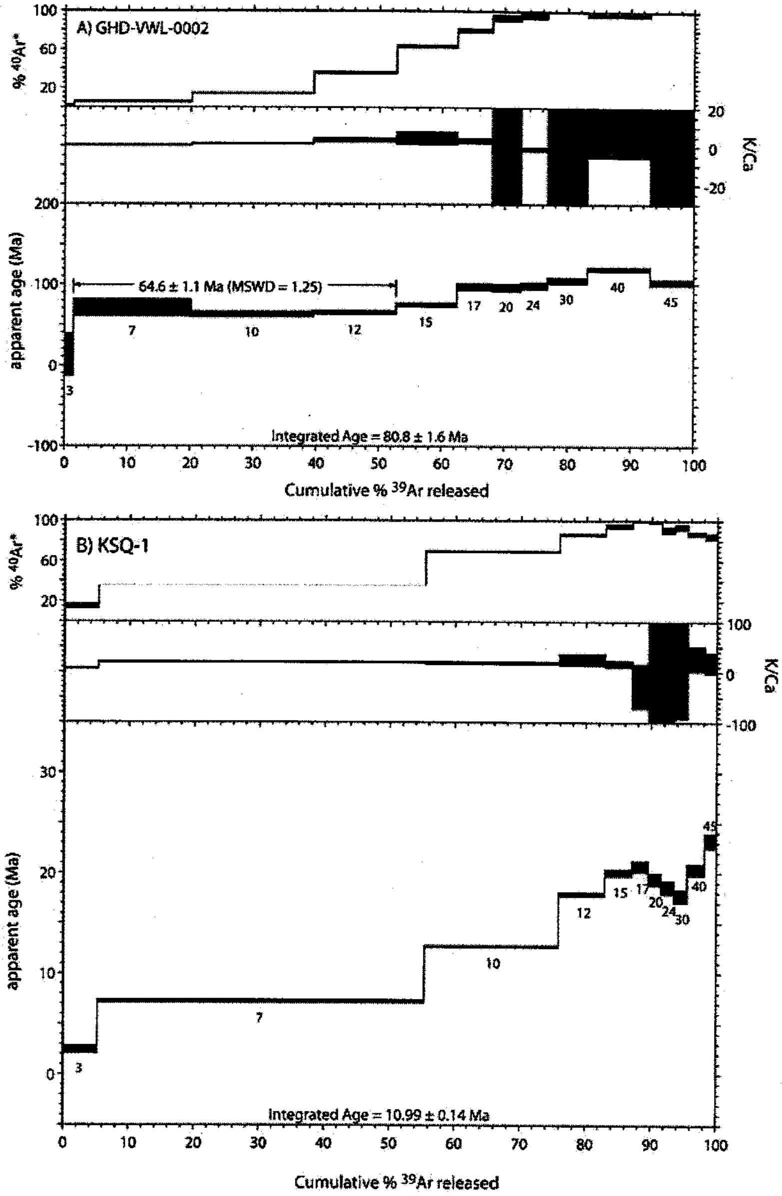

Figure A-3. Age spectra for MnOx samples. A) Sample GHD VWL 0002 gives an apparent plateau age of 64.6 ± 1.1 Ma. However, there are no rocks of Cretaceous or early Tertiary age in the area, so it is unlikely that this is the age of a contaminant. This sample is a mixture of cryptomelane, todorokite, and older silicate contaminants, so it is possible that the old apparent age is controlled by 39Ar recoil. B) KSQ-1 produced a hump-shaped spectrum typical of recoil. The apparent age of this sample approaches that of the Amalia tuff in the highest wattage steps.

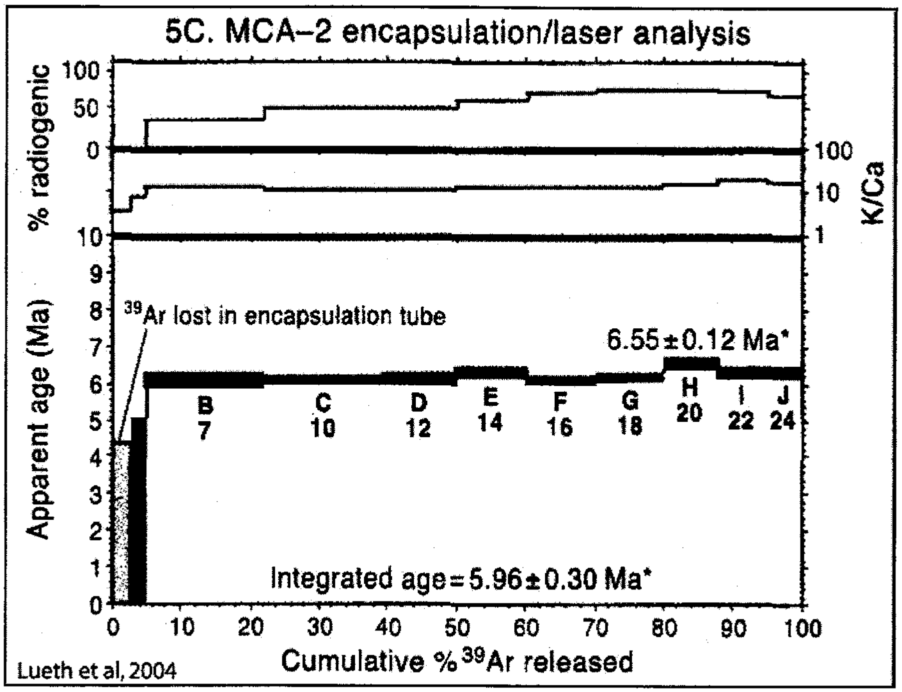

Figure A-4. Lueth et al. (2004) conducted encapsulation experiments on hypogene cryptomelane from the Luis Lopez mining district, NM. ~2% of the cumulative 39Ar released recoiled out of the sample during irradiation. The recoiled 39Ar did not affect the apparent age of the sample. This experiment has not been replicated on supergene mixtures of cryptomelane and todorokite.

APPENDIX B: RRV JAROSITE GEOCHRONOLOGY DATA

Table B-1. RRV jarosite 40Ar/39Ar Data Table.

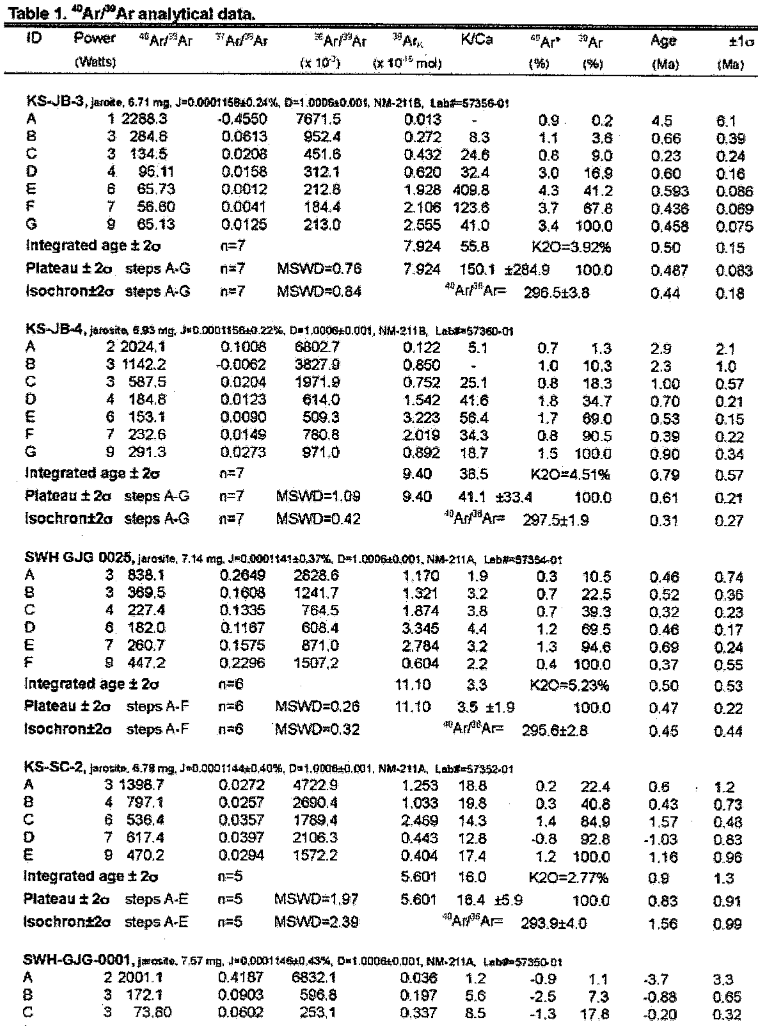

Table 1. ^{40}Ar/^{39}Ar analytical data.

ID	Power (Watts)	^{40}Ar/^{39}Ar	^{37}Ar/^{39}Ar	^{36}Ar/^{39}Ar (x 10^{-3})	^{39}Ar$_K$ (x 10^{-15} mol)	K/Ca	^{40}Ar* (%)	^{39}Ar (%)	Age (Ma)	±1σ (Ma)
KS-JB-3, jarosite, 6.71 mg, J=0.0001158±0.24%, D=1.0006±0.001, NM-211B, Lab#=57356-01										
A	1	2288.3	-0.4550	7671.5	0.013	-	0.9	0.2	4.5	6.1
B	3	284.6	0.0613	952.4	0.272	8.3	1.1	3.6	0.66	0.39
C	3	134.5	0.0208	451.6	0.432	24.6	0.8	9.0	0.23	0.24
D	4	95.11	0.0158	312.1	0.620	32.4	3.0	16.9	0.60	0.16
E	6	65.73	0.0012	212.8	1.928	409.8	4.3	41.2	0.593	0.086
F	7	56.60	0.0041	184.4	2.106	123.6	3.7	67.8	0.436	0.069
G	9	65.13	0.0125	213.0	2.555	41.0	3.4	100.0	0.458	0.075
Integrated age ± 2σ			n=7		7.924	55.8	K2O=3.92%		0.50	0.15
Plateau ± 2σ	steps A-G		n=7	MSWD=0.76	7.924	150.1 ±284.9		100.0	0.487	0.083
Isochron±2σ	steps A-G		n=7	MSWD=0.84		^{40}Ar/^{36}Ar=	296.5±3.8		0.44	0.18
KS-JB-4, jarosite, 6.93 mg, J=0.0001156±0.22%, D=1.0006±0.001, NM-211B, Lab#=57360-01										
A	2	2024.1	0.1008	6802.7	0.122	5.1	0.7	1.3	2.9	2.1
B	3	1142.2	-0.0062	3827.9	0.850	-	1.0	10.3	2.3	1.0
C	3	587.5	0.0204	1971.9	0.752	25.1	0.8	18.3	1.00	0.57
D	4	184.8	0.0123	614.0	1.542	41.6	1.8	34.7	0.70	0.21
E	6	153.1	0.0090	509.3	3.223	56.4	1.7	69.0	0.53	0.15
F	7	232.6	0.0149	780.8	2.019	34.3	0.8	90.5	0.39	0.22
G	9	291.3	0.0273	971.0	0.892	18.7	1.5	100.0	0.90	0.34
Integrated age ± 2σ			n=7		9.40	38.5	K2O=4.51%		0.79	0.57
Plateau ± 2σ	steps A-G		n=7	MSWD=1.09	9.40	41.1 ±33.4		100.0	0.61	0.21
Isochron±2σ	steps A-G		n=7	MSWD=0.42		^{40}Ar/^{36}Ar=	297.5±1.9		0.31	0.27
SWH GJG 0025, jarosite, 7.14 mg, J=0.0001141±0.37%, D=1.0006±0.001, NM-211A, Lab#=57354-01										
A	3	838.1	0.2649	2828.6	1.170	1.9	0.3	10.5	0.46	0.74
B	3	369.5	0.1608	1241.7	1.321	3.2	0.7	22.5	0.52	0.36
C	4	227.4	0.1335	764.5	1.874	3.8	0.7	39.3	0.32	0.23
D	6	182.0	0.1167	608.4	3.345	4.4	1.2	69.5	0.46	0.17
E	7	260.7	0.1575	871.0	2.784	3.2	1.3	94.6	0.69	0.24
F	9	447.2	0.2296	1507.2	0.604	2.2	0.4	100.0	0.37	0.55
Integrated age ± 2σ			n=6		11.10	3.3	K2O=5.23%		0.50	0.53
Plateau ± 2σ	steps A-F		n=6	MSWD=0.26	11.10	3.5 ±1.9		100.0	0.47	0.22
Isochron±2σ	steps A-F		n=6	MSWD=0.32		^{40}Ar/^{36}Ar=	295.6±2.8		0.45	0.44
KS-SC-2, jarosite, 6.78 mg, J=0.0001144±0.40%, D=1.0006±0.001, NM-211A, Lab#=57352-01										
A	3	1398.7	0.0272	4722.9	1.253	18.8	0.2	22.4	0.6	1.2
B	4	797.1	0.0257	2690.4	1.033	19.8	0.3	40.8	0.43	0.73
C	6	536.4	0.0357	1789.4	2.469	14.3	1.4	84.9	1.57	0.48
D	7	617.4	0.0397	2106.3	0.443	12.8	-0.8	92.8	-1.03	0.83
E	9	470.2	0.0294	1572.2	0.404	17.4	1.2	100.0	1.16	0.96
Integrated age ± 2σ			n=5		5.601	16.0	K2O=2.77%		0.9	1.3
Plateau ± 2σ	steps A-E		n=5	MSWD=1.97	5.601	16.4 ±5.9		100.0	0.83	0.91
Isochron±2σ	steps A-E		n=5	MSWD=2.39		^{40}Ar/^{36}Ar=	293.9±4.0		1.56	0.99
SWH-GJG-0001, jarosite, 7.57 mg, J=0.0001146±0.43%, D=1.0006±0.001, NM-211A, Lab#=57350-01										
A	2	2001.1	0.4187	6832.1	0.036	1.2	-0.9	1.1	-3.7	3.3
B	3	172.1	0.0903	596.8	0.197	5.6	-2.5	7.3	-0.88	0.65
C	3	73.60	0.0602	253.1	0.337	8.5	-1.3	17.8	-0.20	0.32

	D	4	47.45	0.0183	152.5	0.464	27.9	5.0	32.2	0.49	0.25
	E	6	81.24	0.0413	274.7	1.135	12.3	0.1	67.5	0.01	0.15
	F	7	182.0	0.0394	604.8	0.555	13.0	1.8	84.8	0.67	0.27
Xi	G	9	293.4	0.0680	1009.2	0.490	7.5	-1.6	100.0	-1.00	0.45
	Integrated age ± 2σ			n=7		3.214	10.0	K2O=1.42%		-0.08	0.33
	Plateau ± 2σ		steps A-F	n=6	MSWD=2.32	2.724	14.0 ±18.4		84.8	0.15	0.32
	Isochron±2σ		steps A-F	n=6	MSWD=2.85	^{40}Ar/^{36}Ar=		294.6±4.0		0.21	0.12

CAS VWL 0007, jarosite, 9.03 mg, J=0.0001141±0.36%, D=1.0006±0.001, NM-211A, Lab#=57353-01

	A	3	186.1	-0.0031	624.0	3.480	-	0.9	17.4	0.34	0.18
	B	3	107.9	-0.0130	364.0	2.491	-	0.3	29.8	0.06	0.17
	C	4	84.60	-0.0102	280.5	3.132	-	2.0	45.5	0.35	0.14
	D	6	87.94	0.0198	297.2	6.776	25.7	0.1	79.3	0.021	0.097
Xi	E	7	142.4	0.0807	501.2	2.183	6.3	-4.0	90.2	-1.18	0.21
Xi	F	9	183.7	0.0794	622.8	1.958	6.4	-0.2	100.0	-0.06	0.22
	Integrated age ± 2σ			n=6		20.02	26.1	K2O=8.39%		0.00	0.22
	Plateau ± 2σ		steps A-D	n=4	MSWD=1.78	15.88	25.7 ±0.0		79.3	0.15	0.18
	Isochron±2σ		steps A-D	n=4	MSWD=2.21	^{40}Ar/^{36}Ar=		298.2±5.7		-0.044	0.041

ESS VWL 0001, jarosite, 6.25 mg, J=0.000115±0.25%, D=1.0006±0.001, NM-211B, Lab#=57358-01

	A	2	1290.8	0.5157	4322.5	0.145	0.98	1.1	1.1	2.8	1.4
	B	3	191.4	0.0068	647.0	1.104	75.3	0.1	9.2	0.05	0.22
	C	3	76.39	0.0042	254.4	1.722	121.3	1.6	21.9	0.251	0.094
	D	4	68.74	0.0116	226.7	2.471	44.0	2.6	40.0	0.364	0.080
	E	6	116.2	0.0111	383.6	3.515	45.9	2.4	65.9	0.58	0.12
Xi	F	7	139.5	0.0187	450.3	3.409	27.3	4.6	91.0	1.33	0.13
Xi	G	9	282.9	0.0314	901.4	1.226	16.2	5.8	100.0	3.43	0.36
	Integrated age ± 2σ			n=7		13.59	26.7	K2O=7.26%		0.92	0.24
	Plateau ± 2σ		steps A-E	n=5	MSWD=2.49	8.96	62.8 ±88.9		65.9	0.36	0.17
	Isochron±2σ		steps A-E	n=5	MSWD=2.73	^{40}Ar/^{36}Ar=		297.3±2.7		0.25	0.13

PIT VWL 0005, jarosite, 7.92 mg, J=0.0001146±0.34%, D=1.0006±0.001, NM-211A, Lab#=57351-01

X	A	2	284.5	0.1694	951.4	0.189	3.0	1.2	1.4	0.69	0.54
X	B	3	43.30	0.0077	146.6	0.885	66.6	-0.1	8.1	0.00	0.14
X	C	3	26.77	0.0138	91.87	1.248	36.9	-1.4	17.4	-0.079	0.087
X	D	4	27.42	0.0064	89.92	2.271	79.6	3.1	34.5	0.174	0.058
X	E	6	58.39	0.0200	192.5	2.952	25.5	2.6	56.7	0.312	0.077
X	F	7	86.67	0.0145	274.0	3.667	35.1	6.6	84.2	1.180	0.098
X	G	9	122.6	0.0218	392.3	2.105	23.4	5.5	100.0	1.38	0.14
	Integrated age ± 2σ			n=7		13.32	29.7	K2O=5.64%		0.64	0.13
	Plateau ± 2σ		no plateau	n=0	MSWD=0.00	0.000	0.000±0.000		0.0	0.00	0.000
	Isochron±2σ		steps A-G	n=7	MSWD=10.34	^{40}Ar/^{36}Ar=		313.4±3.5		-0.239	0.061

PIT VWL 0007, Jarosite, 6.27 mg, J=0.0001143±0.48%, D=1.0006±0.001, NM-211A, Lab#=57355-01

X	A	3	21.71	0.0146	71.16	2.353	35.0	3.1	20.4	0.138	0.049
X	B	3	18.83	0.0144	58.52	1.610	35.4	8.1	34.4	0.314	0.058
X	C	4	27.31	0.0204	87.20	1.769	25.1	5.6	49.7	0.317	0.057
X	D	6	54.11	0.0194	166.9	4.209	26.3	8.8	86.3	0.986	0.062
X	E	7	161.0	0.0575	526.6	0.858	8.9	3.4	93.7	1.12	0.22
X	F	9	238.5	0.0313	778.4	0.725	16.3	3.5	100.0	1.74	0.24
	Integrated age ± 2σ			n=6		11.53	23.8	K2O=6.18%		0.67	0.11
	Plateau ± 2σ		no plateau	n=0	MSWD=0.00	0.000	0.000±0.000		0.0	0.00	0.000
	Isochron±2σ		steps A-F	n=6	MSWD=15.44	^{40}Ar/^{36}Ar=		308.8±2.7		0.133	0.031

SWH GJG 0024, jarosite, 7.38 mg, J=0.0001153±0.25%, D=1.0006±0.001, NM-211B, Lab#=57357-01

X	A	2	1726.3	0.8254	5927.2	0.216	0.62	-1.5	5.0	-5.2	1.7
X	B	3	1851.3	0.8088	6267.7	0.174	0.63	0.0	9.0	-0.1	2.0
X	C	3	548.0	0.4432	1821.8	0.296	1.2	1.8	15.8	2.01	0.68
X	D	4	242.1	0.3284	800.4	0.479	1.6	2.3	26.8	1.16	0.35
X	E	6	369.3	0.3286	1206.7	0.670	1.6	3.4	42.3	2.64	0.40
X	F	7	401.3	0.2977	1256.0	0.447	1.7	7.5	52.6	6.26	0.45
X	G	9	362.0	0.1504	939.9	2.060	3.4	23.3	100.0	17.45	0.28
	Integrated age ± 2σ			n=7		4.342	1.7	K2O=1.96%		9.35	0.80
	Plateau ± 2σ	no plateau		n=0	MSWD=0.00	0.000	0.000±0.000		0.0	0.00	0.000
	Isochron±2σ	steps A-G		n=7	MSWD=351.46		^{40}Ar/^{36}Ar=	283.5±2.3		11.83	0.42

Notes:

Isotopic ratios corrected for blank, radioactive decay, and mass discrimination, not corrected for interfering reactions.
Errors quoted for individual analyses include analytical error only, without interfering reaction or J uncertainties.
Integrated age calculated by summing isotopic measurements of all steps.
Integrated age error calculated by quadratically combining errors of isotopic measurements of all steps.
Plateau age is inverse-variance-weighted mean of selected steps.
Plateau age error is inverse-variance-weighted mean error (Taylor, 1982) times root MSWD where MSWD>1.
Plateau error is weighted error of Taylor (1982).
Decay constants and isotopic abundances after Steiger and Jäger (1977).
symbol preceding sample ID denotes analyses excluded from plateau age calculations.
Weight percent K_2O calculated from ^{39}Ar signal, sample weight, and instrument sensitivity.
Ages calculated relative to FC-2 Fish Canyon Tuff sanidine interlaboratory standard at 27.84 Ma
Decay Constant (LambdaK (total)) = 5.543e-10/a
Correction factors:
$(^{39}Ar/^{37}Ar)_{Ca}$ = 0.0007 ± 5e-05
$(^{36}Ar/^{37}Ar)_{Ca}$ = 0.00028 ± 2e-05
$(^{38}Ar/^{39}Ar)_{K}$ = 0.013
$(^{40}Ar/^{39}Ar)_{K}$ = 0.01 ± 0.002

APPENDIX C: AGE DATA FOR EXPERIMENTAL SAMPLES

Table C-1. PB jarosite ^{40}Ar/^{39}Ar Data Table.

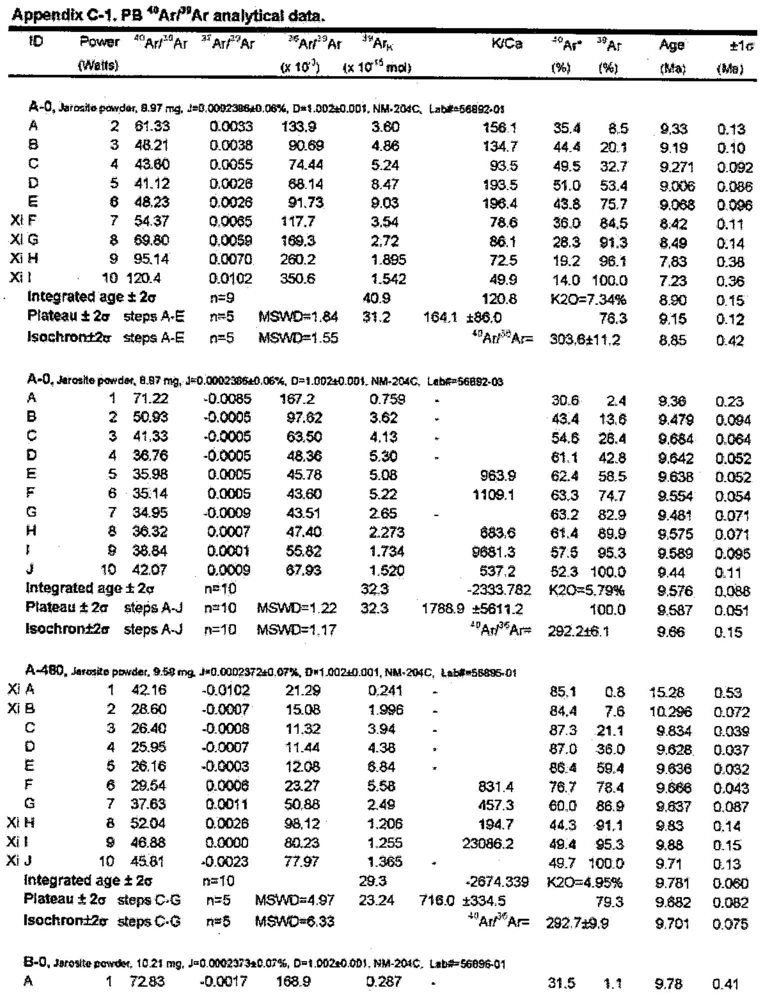

Appendix C-1. PB ^{40}Ar/^{39}Ar analytical data.

ID	Power (Watts)	^{40}Ar/^{39}Ar	^{37}Ar/^{39}Ar	^{36}Ar/^{39}Ar (x 10^{-3})	^{39}Ar$_K$ (x 10^{-15} mol)	K/Ca	^{40}Ar* (%)	^{39}Ar (%)	Age (Ma)	±1σ (Ma)
A-0, Jarosite powder, 8.97 mg, J=0.0002386±0.06%, D=1.002±0.001, NM-204C, Lab#=56892-01										
A	2	61.33	0.0033	133.9	3.60	156.1	35.4	8.5	9.33	0.13
B	3	48.21	0.0038	90.69	4.86	134.7	44.4	20.1	9.19	0.10
C	4	43.60	0.0055	74.44	5.24	93.5	49.5	32.7	9.271	0.092
D	5	41.12	0.0026	68.14	8.47	193.5	51.0	53.4	9.006	0.086
E	6	48.23	0.0026	91.73	9.03	196.4	43.8	75.7	9.068	0.096
Xi F	7	54.37	0.0065	117.7	3.54	78.6	36.0	84.5	8.42	0.11
Xi G	8	69.80	0.0059	169.3	2.72	86.1	28.3	91.3	8.49	0.14
Xi H	9	95.14	0.0070	260.2	1.895	72.5	19.2	96.1	7.83	0.38
Xi I	10	120.4	0.0102	350.6	1.542	49.9	14.0	100.0	7.23	0.36
Integrated age ± 2σ			n=9		40.9	120.8	K2O=7.34%		8.90	0.15
Plateau ± 2σ	steps A-E		n=5	MSWD=1.84	31.2	164.1 ±86.0		76.3	9.15	0.12
Isochron±2σ	steps A-E		n=5	MSWD=1.55		^{40}Ar/^{36}Ar=	303.6±11.2		8.85	0.42
A-0, Jarosite powder, 8.97 mg, J=0.0002386±0.06%, D=1.002±0.001, NM-204C, Lab#=56892-03										
A	1	71.22	-0.0085	167.2	0.759	-	30.6	2.4	9.36	0.23
B	2	50.93	-0.0005	97.62	3.62	-	43.4	13.6	9.479	0.094
C	3	41.33	-0.0005	63.50	4.13	-	54.6	26.4	9.684	0.064
D	4	36.76	-0.0005	48.36	5.30	-	61.1	42.8	9.642	0.052
E	5	35.98	0.0005	45.78	5.08	963.9	62.4	58.5	9.638	0.052
F	6	35.14	0.0005	43.60	5.22	1109.1	63.3	74.7	9.554	0.054
G	7	34.95	-0.0009	43.51	2.65	-	63.2	82.9	9.481	0.071
H	8	36.32	0.0007	47.40	2.273	683.6	61.4	89.9	9.575	0.071
I	9	38.84	0.0001	55.82	1.734	9681.3	57.5	95.3	9.589	0.095
J	10	42.07	0.0009	67.93	1.520	537.2	52.3	100.0	9.44	0.11
Integrated age ± 2σ			n=10		32.3	-2333.782	K2O=5.79%		9.576	0.088
Plateau ± 2σ	steps A-J		n=10	MSWD=1.22	32.3	1788.9 ±5611.2		100.0	9.587	0.051
Isochron±2σ	steps A-J		n=10	MSWD=1.17		^{40}Ar/^{36}Ar=	292.2±6.1		9.66	0.15
A-480, Jarosite powder, 9.58 mg, J=0.0002372±0.07%, D=1.002±0.001, NM-204C, Lab#=56895-01										
Xi A	1	42.16	-0.0102	21.29	0.241	-	85.1	0.8	15.28	0.53
Xi B	2	28.60	-0.0007	15.08	1.996	-	84.4	7.6	10.296	0.072
C	3	26.40	-0.0008	11.32	3.94	-	87.3	21.1	9.834	0.039
D	4	25.95	-0.0007	11.44	4.38	-	87.0	36.0	9.628	0.037
E	5	26.16	-0.0003	12.08	6.84	-	86.4	59.4	9.636	0.032
F	6	29.54	0.0006	23.27	5.58	831.4	76.7	78.4	9.666	0.043
G	7	37.63	0.0011	50.88	2.49	457.3	60.0	86.9	9.837	0.087
Xi H	8	52.04	0.0026	98.12	1.206	194.7	44.3	91.1	9.83	0.14
Xi I	9	46.88	0.0000	80.23	1.255	23086.2	49.4	95.3	9.88	0.15
Xi J	10	45.81	-0.0023	77.97	1.365	-	49.7	100.0	9.71	0.13
Integrated age ± 2σ			n=10		29.3	-2674.339	K2O=4.95%		9.781	0.060
Plateau ± 2σ	steps C-G		n=5	MSWD=4.97	23.24	716.0 ±334.5		79.3	9.682	0.082
Isochron±2σ	steps C-G		n=5	MSWD=6.33		^{40}Ar/^{36}Ar=	292.7±9.9		9.701	0.075
B-0, Jarosite powder, 10.21 mg, J=0.0002373±0.07%, D=1.002±0.001, NM-204C, Lab#=56896-01										
A	1	72.83	-0.0017	168.9	0.287	-	31.5	1.1	9.78	0.41

B	2	56.66	0.0026	116.3	1.426		192.9	39.3	6.5	9.52	0.15
C	3	47.73	0.0004	86.76	2.72		1186.5	46.3	16.9	9.431	0.093
D	4	40.77	-0.0012	62.62	2.91	-		54.6	28.1	9.505	0.073
E	5	38.01	-0.0004	51.81	3.03	-		59.7	39.6	9.688	0.068
F	6	35.69	0.0001	44.84	4.21		3525.9	62.9	55.7	9.576	0.060
G	7	35.11	0.0008	42.57	4.43		671.9	64.2	72.6	9.617	0.048
H	8	35.11	0.0005	41.66	2.359		1098.9	64.9	81.6	9.732	0.072
Xi J	10	36.75	0.0020	45.53	1.837		257.9	63.4	88.6	9.943	0.087
Xi K	12	42.42	-0.0018	63.15	1.494	-		56.0	94.4	10.14	0.12
Xi L	14	59.98	-0.0019	121.0	0.982	-		40.4	98.1	10.34	0.17
Xi M	16	71.95	0.0022	172.4	0.496		233.0	29.2	100.0	8.97	0.29
Integrated age ± 2σ			n=12		26.2		2649.3	K2O=4.15%		9.661	0.095
Plateau ± 2σ	steps A-H		n=8	MSWD=1.54	21.37	1513.9	±2034.4		81.6	9.603	0.066
Isochron±2σ	steps A-H		n=8	MSWD=1.24			^{40}Ar/^{36}Ar=	289.8±6.7		9.73	0.16

B-30, Jarosite powder, 8.8 mg, J=0.000238±0.07%, D=1.002±0.001, NM-204C, Lab#=56897-01

A	2	34.47	0.0010	40.27	2.65		512.6	65.5	13.6	9.658	0.070
B	4	31.68	-0.0011	31.30	3.71	-		70.8	32.7	9.600	0.053
C	6	28.86	-0.0004	22.06	5.62	-		77.4	61.5	9.561	0.037
D	8	28.41	-0.0007	20.65	3.43	-		78.5	79.1	9.548	0.050
Xi E	10	########	0.0713	55241.5	0.082		7.2	-10.1	79.6	-793.3	96.9
Xi F	12	37.29	0.0006	53.94	2.078		876.2	57.2	90.2	9.141	0.098
Xi G	14	43.88	-0.0023	76.80	1.233	-		48.3	96.6	9.07	0.14
Xi H	15	64.12	0.0011	147.2	0.669		453.8	32.1	100.0	8.83	0.25
Integrated age ± 2σ			n=8		19.47		-9644.193	K2O=3.57%		6.75	0.43
Plateau ± 2σ	steps A-D		n=4	MSWD=0.69	15.41	88.1	±0.0		79.1	9.578	0.050
Isochron±2σ	steps A-D		n=4	MSWD=0.01			^{40}Ar/^{36}Ar=	307.8±18.0		9.44	0.21

B-0, Jarosite powder, 7.03 mg, J=0.0002373±0.07%, D=1.002±0.001, NM-204C, Lab#=56896-02

A	2	48.59	0.0017	88.52	2.97		293.6	46.2	12.0	9.573	0.087
B	4	35.98	0.0004	44.64	9.44		1398.6	63.3	50.4	9.724	0.044
C	6	36.19	0.0008	41.79	5.28		607.0	65.9	71.8	10.173	0.054
Xi D	8	41.85	0.0005	55.81	2.45		1094.2	60.6	81.8	10.818	0.084
Xi E	10	104.1	0.0002	273.2	2.237		2738.6	22.5	90.8	9.98	0.23
Xi G	14	120.9	0.0006	328.6	2.254		786.1	19.7	100.0	10.17	0.26
Integrated age ± 2σ			n=6		24.6		781.9	K2O=5.67%		9.98	0.13
Plateau ± 2σ	steps A-C		n=3	MSWD=26.91	17.68	976.8	±1139.0		71.8	9.86	0.33
Isochron±2σ	steps A-C		n=3	MSWD=38.28			^{40}Ar/^{36}Ar=	277.3±9.5		10.25	0.21

Notes:

Isotopic ratios corrected for blank, radioactive decay, and mass discrimination, not corrected for interfering reactions.

Errors quoted for individual analyses include analytical error only, without interfering reaction or J uncertainties.

Integrated age calculated by summing isotopic measurements of all steps.

Integrated age error calculated by quadratically combining errors of isotopic measurements of all steps.

Plateau age is inverse-variance-weighted mean of selected steps.

Plateau age error is inverse-variance-weighted mean error (Taylor, 1982) times root MSWD where MSWD>1.

Plateau error is weighted error of Taylor (1982).

Decay constants and isotopic abundances after Steiger and Jäger (1977).

symbol preceding sample ID denotes analyses excluded from plateau age calculations.

Weight percent K_2O calculated from ^{39}Ar signal, sample weight, and instrument sensitivity.

Ages calculated relative to FC-2 Fish Canyon Tuff sanidine interlaboratory standard at 28.02 Ma

Decay Constant (LambdaK (total)) = 5.543e-10/a

Correction factors:

$(^{39}Ar/^{37}Ar)_{Ca} = 0.0007 \pm 5e\text{-}05$

$(^{36}Ar/^{37}Ar)_{Ca} = 0.00028 \pm 1e\text{-}05$

$(^{38}Ar/^{39}Ar)_{K} = 0.013$

$(^{40}Ar/^{39}Ar)_{K} = 0.01 \pm 0.002$

APPENDIX D: MICROPROBE DATA

This appendix provides quantitative chemical data for jarosite. Table D-1 gives chemical data for untreated and HF-treated jarosite from the RRV. Table D-2 has chemical data for analyses on untreated (A-0) and HF-treated (A-480) PB jarosite, which are discussed in chapter two only.

The microprobe reports all iron as FeO (Fe^{2+}) and all sulfur as SO_2 (S^{4+}). However, jarosite forms under oxidizing conditions, and the iron is present as Fe^{3+} and sulfur is present as S^{6+}. In order to convert FeO to Fe_2O_3, all reported FeO was multiplied by 1.11. In order to convert SO_2 to SO_3, all reported SO_2 was multiplied by 1.25.

Table D-1. RRV Jarosite EMPA Quantitative Analysis.

Sample Scar	PIT VWL 0007 Goat Hill	PIT VWL 0007 Goat Hill	PIT VWL 0007 Goat Hill	PIT VWL 0007 Goat Hill	PIT VWL 0007 Goat Hill	PIT VWL 0007 Goat Hill	PIT VWL 0007 Goat Hill	PIT VWL 0007 Goat Hill	PIT VWL 0007 Goat Hill	PIT VWL 0007 Goat Hill
time in HF (min)	0	0	0	0	0	0	0	0	0	0
K_2O	7.07	8.21	6.96	8.05	7.15	7.35	6.02	7.95	6.02	3.81
Na_2O	0.09	0.16	0.15	0.11	0.11	0.15	0.03	0.11	0.06	0.11
FeO	36.50	38.20	38.97	39.70	39.76	35.70	40.56	38.07	39.76	18.30
Fe_2O_3 (calc)	40.52	42.40	43.26	44.07	44.13	39.63	45.02	42.25	44.14	20.31
Al_2O_3	1.34	0.29	0.17	0.11	0.27	0.94	0.22	2.87	0.06	2.76
As_2O_3	0.00	0.03	0.01	0.00	0.04	0.02	0.05	0.00	0.04	0.00
MoO_3	0.00	0.00	0.00	0.00	0.00	0.00	0.00	0.00	0.00	0.00
SO_2	22.96	23.20	23.20	22.74	23.34	20.03	25.18	19.64	23.09	10.97
SO_3 (calc)	28.70	28.99	28.99	28.41	29.16	25.03	31.46	24.55	28.85	13.71
P_2O_5	0.32	0.20	0.25	0.31	0.43	0.26	0.32	0.21	0.26	0.04

SiO_2	1.83	0.58	0.25	0.22	0.78	1.68	0.18	3.82	0.15	4.76
H_2O	10.91	10.66	10.54	10.59	10.88	10.00	11.11	11.18	10.47	6.80
F	0.08	0.09	0.12	0.09	0.01	0.04	0.04	0.08	0.01	0.10
Cl	0.18	0.10	0.08	0.08	0.09	0.24	0.01	0.17	0.03	0.83
Total	81.28	81.71	80.71	81.99	82.83	76.40	83.71	84.11	79.94	48.49
K	0.744	0.883	0.757	0.873	0.754	0.843	0.621	0.816	0.660	0.643
Na	0.014	0.026	0.025	0.018	0.017	0.026	0.005	0.018	0.011	0.027
A-site total	0.758	0.909	0.782	0.890	0.771	0.869	0.626	0.834	0.670	0.670
Fe	2.518	2.695	2.781	2.822	2.749	2.685	2.746	2.561	2.859	2.025
Al	0.130	0.029	0.017	0.011	0.026	0.100	0.021	0.273	0.006	0.431
As	0.000	0.002	0.001	0.000	0.002	0.001	0.003	0.000	0.002	0.000
B-site total	2.648	2.725	2.798	2.832	2.777	2.786	2.769	2.834	2.867	2.455
S	1.776	1.836	1.857	1.812	1.810	1.690	1.912	1.482	1.861	1.362
P	0.022	0.015	0.018	0.023	0.030	0.020	0.022	0.014	0.019	0.005
X-site total	1.798	1.850	1.875	1.835	1.840	1.709	1.934	1.496	1.880	1.367
Fe/Fe+Al	0.951	0.990	0.994	0.996	0.991	0.964	0.992	0.904	0.998	0.825
Na/Na+K	0.018	0.029	0.032	0.020	0.022	0.029	0.008	0.021	0.016	0.040

Sample	PIT VWL 0007 Goat Hill	PIT VWL 0007 Goat Hill	PIT VWL 0007 Goat Hill	PIT VWL 0007 Goat Hill	PIT VWL 0007 Goat Hill	PIT VWL 0007 Goat Hill	PIT VWL 0007 Goat Hill	PIT VWL 0007 Goat Hill	PIT VWL 0007 Goat Hill	PIT VWL 0007 Goat Hill
Scar time in HF (min)	30	30	30	30	30	30	30	30	30	30
K_2O	6.82	2.72	3.58	3.19	7.61	7.91	6.17	6.90	7.49	7.36
Na_2O	0.13	0.04	0.04	0.15	0.12	0.14	0.13	0.07	0.05	0.05
FeO	33.40	12.88	15.28	15.72	38.43	34.52	28.71	33.89	37.43	36.33
Fe_2O_3 (calc)	37.07	14.30	16.97	17.45	42.65	38.31	31.87	37.62	41.55	40.32
Al_2O_3	0.75	2.32	0.60	0.54	0.18	2.98	0.29	0.17	0.20	0.89
As_2O_3	0.04	0.03	0.00	0.04	0.03	0.02	0.03	0.02	0.03	0.03
MoO_3	0.00	0.00	0.00	0.00	0.00	0.00	0.00	0.00	0.00	0.00
SO_2	19.60	7.27	10.72	9.16	23.36	21.04	16.94	19.25	21.82	20.96
SO_3 (calc)	24.49	9.09	13.40	11.44	29.20	26.30	21.17	24.06	27.27	26.19
P_2O_5	0.16	0.10	0.11	0.11	0.21	0.16	0.16	0.21	0.31	0.29
SiO_2	1.22	2.98	14.80	0.90	0.26	3.84	0.55	0.57	0.33	1.13
H_2O	9.42	4.69	8.50	4.56	10.57	11.16	7.94	9.10	10.12	10.14

F	0.00	0.00	0.00	0.00	0.14	0.00	0.00	0.02	0.04	0.12
Cl	0.41	1.14	0.52	0.74	0.21	0.25	0.63	0.24	0.18	0.17
Total	71.94	34.16	54.14	35.10	81.11	82.01	61.54	70.46	77.98	77.47
K	0.831	0.665	0.484	0.802	0.826	0.813	0.892	0.870	0.850	0.833
Na	0.024	0.016	0.008	0.058	0.019	0.023	0.028	0.014	0.009	0.008
A-site total	0.854	0.681	0.492	0.860	0.845	0.836	0.920	0.884	0.859	0.841
Fe	2.668	2.067	1.354	2.592	2.736	2.327	2.720	2.801	2.783	2.694
Al	0.084	0.524	0.075	0.125	0.018	0.284	0.038	0.020	0.021	0.094
As	0.003	0.003	0.000	0.004	0.002	0.001	0.002	0.002	0.002	0.002
B-site total	2.754	2.594	1.429	2.720	2.755	2.612	2.760	2.823	2.806	2.789
S	1.755	1.309	1.065	1.693	1.865	1.591	1.800	1.785	1.820	1.744
P	0.013	0.016	0.010	0.019	0.016	0.011	0.016	0.018	0.023	0.022
X-site total	1.768	1.325	1.075	1.712	1.881	1.602	1.815	1.802	1.843	1.766
Fe/Fe+Al	0.969	0.798	0.947	0.954	0.993	0.891	0.986	0.993	0.993	0.966
Na/Na+K	0.028	0.023	0.016	0.067	0.022	0.027	0.030	0.016	0.010	0.010

Sample	ESS VWL 0001 SE Straight Creek	ESS VWL 0001 SE Straight Creek	ESS VWL 0001 SE Straight Creek	ESS VWL 0001 SE Straight Creek	ESS VWL 0001 SE Straight Creek	ESS VWL 0001 SE Straight Creek	ESS VWL 0001 SE Straight Creek	ESS VWL 0001 SE Straight Creek	ESS VWL 0001 SE Straight Creek	ESS VWL 0001 SE Straight Creek	ESS VWL 0001 SE Straight Creek
scar time in HF (min)	0	0	0	0	0	0	0	0	0	0	0
K_2O	7.70	6.86	6.79	6.95	7.12	6.86	7.32	7.01	7.10	5.57	4.99
Na_2O	0.18	0.09	0.07	0.09	0.15	0.18	0.22	0.20	0.17	0.11	0.08
FeO	37.12	33.69	37.69	34.04	35.10	33.41	37.72	35.53	39.95	26.35	20.78
Fe_2O_3 (calc)	41.21	37.39	41.83	37.79	38.96	37.08	41.86	39.44	44.34	29.25	23.07
Al_2O_3	0.22	1.01	0.33	0.74	2.22	2.92	1.64	1.22	0.32	1.21	1.61
As_2O_3	0.02	0.03	0.01	0.01	0.00	0.01	0.00	0.04	0.01	0.00	0.01
MoO_3	0.00	0.00	0.00	0.00	0.00	0.00	0.00	0.00	0.00	0.00	0.00
SO_2	22.71	19.59	22.23	20.54	19.99	19.87	22.04	21.18	23.66	15.81	13.41
SO_3 (calc)	28.39	24.48	27.78	25.67	24.98	24.83	27.55	26.47	29.57	19.76	16.76
P_2O_5	0.77	1.04	1.00	1.03	0.98	0.98	0.92	0.71	0.84	0.75	0.63

SiO_2	0.54	2.72	0.82	2.49	6.29	7.46	3.20	3.50	0.59	2.79	3.75
H_2O	10.52	10.13	10.53	10.28	11.58	11.81	11.44	10.90	11.05	8.31	7.39
F	0.07	0.00	0.07	0.00	0.00	0.00	0.04	0.10	0.00	0.15	0.04
Cl	0.16	0.22	0.11	0.22	0.12	0.30	0.09	0.17	0.05	0.64	0.77
Total	80.00	75.38	79.65	76.39	83.54	83.79	84.60	80.55	83.73	61.68	53.47
K	0.840	0.778	0.740	0.777	0.706	0.667	0.734	0.738	0.738	0.769	0.775
Na	0.029	0.016	0.012	0.015	0.023	0.026	0.033	0.032	0.027	0.024	0.020
A-site total	0.869	0.793	0.752	0.791	0.729	0.693	0.767	0.770	0.765	0.793	0.795
Fe	2.656	2.502	2.692	2.492	2.280	2.128	2.481	2.453	2.719	2.386	2.116
Al	0.023	0.106	0.034	0.076	0.204	0.262	0.152	0.119	0.031	0.155	0.231
As	0.001	0.002	0.000	0.001	0.000	0.001	0.000	0.002	0.001	0.000	0.001
B-site total	2.679	2.609	2.726	2.568	2.484	2.390	2.633	2.574	2.750	2.541	2.348
S	1.822	1.632	1.781	1.686	1.457	1.420	1.627	1.640	1.806	1.606	1.532
P	0.056	0.079	0.073	0.077	0.065	0.063	0.061	0.050	0.058	0.069	0.065
X-site total	1.878	1.710	1.853	1.763	1.521	1.483	1.688	1.690	1.864	1.674	1.597
Fe/Fe+Al	0.992	0.960	0.988	0.970	0.918	0.890	0.942	0.954	0.989	0.939	0.902
Na/Na+K	0.033	0.020	0.015	0.018	0.032	0.038	0.043	0.042	0.035	0.030	0.025

Sample	ESS VWL 0001 SE Straight Creek	ESS VWL 0001 SE Straight Creek	ESS VWL 0001 SE Straight Creek	ESS VWL 0001 SE Straight Creek	ESS VWL 0001 SE Straight Creek	ESS VWL 0001 SE Straight Creek	ESS VWL 0001 SE Straight Creek	ESS VWL 0001 SE Straight Creek	ESS VWL 0001 SE Straight Creek	ESS VWL 0001 SE Straight Creek	ESS VWL 0001 SE Straight Creek
scar time in HF (min)	30	30	30	30	30	30	30	30	30	30	30
K_2O	6.59	7.35	7.43	7.43	7.37	6.57	7.17	4.56	7.18	7.74	7.55
Na_2O	0.33	0.24	0.20	0.16	0.38	0.28	0.21	0.04	0.23	0.12	0.16
FeO	40.83	38.22	38.88	39.67	39.81	35.47	39.57	39.90	39.50	38.12	39.48
Fe_2O_3 (calc)	45.32	42.42	43.15	44.03	44.19	39.37	43.92	44.28	43.84	42.31	43.82
Al_2O_3	0.14	0.15	0.20	0.21	0.28	0.18	0.25	0.07	0.02	0.34	0.15
As_2O_3	0.01	0.01	0.04	0.01	0.01	0.03	0.00	0.04	0.01	0.01	0.00
MoO_3	0.00	0.00	0.00	0.00	0.00	0.00	0.00	0.00	0.00	0.00	0.00
SO_2	22.59	22.58	22.96	22.66	23.08	20.55	22.93	24.27	23.66	22.45	23.29
SO_3	28.23	28.22	28.70	28.32	28.85	25.68	28.65	30.33	29.57	28.06	29.11

(calc)											
P_2O_5	1.63	0.68	0.71	0.74	0.99	0.83	1.22	1.21	1.04	1.20	1.17
SiO_2	0.23	0.16	0.13	0.15	0.11	0.20	0.48	0.05	0.03	0.45	0.22
H_2O	10.95	10.45	10.63	10.64	10.86	9.66	10.91	10.88	10.86	10.68	10.91
F	0.34	0.01	0.16	0.16	0.17	0.12	0.09	0.10	0.27	0.00	0.17
Cl	0.01	0.12	0.12	0.13	0.06	0.20	0.06	0.01	0.00	0.12	0.06
Total	83.65	79.97	81.46	81.97	83.11	74.09	82.88	81.13	82.78	81.22	83.16
K	0.691	0.808	0.803	0.802	0.779	0.780	0.754	0.482	0.759	0.832	0.795
Na	0.052	0.041	0.033	0.026	0.061	0.050	0.034	0.006	0.036	0.020	0.025
A-site total	0.743	0.848	0.836	0.828	0.840	0.830	0.788	0.487	0.795	0.852	0.820
Fe	2.805	2.753	2.753	2.804	2.759	2.762	2.730	2.759	2.737	2.686	2.723
Al	0.014	0.015	0.021	0.022	0.028	0.020	0.025	0.007	0.002	0.034	0.015
As	0.001	0.001	0.002	0.001	0.001	0.002	0.000	0.002	0.001	0.001	0.000
B-site total	2.820	2.768	2.775	2.826	2.787	2.783	2.754	2.768	2.739	2.720	2.738
S	1.741	1.824	1.824	1.796	1.794	1.795	1.774	1.882	1.838	1.774	1.802
P	0.113	0.050	0.051	0.053	0.070	0.066	0.085	0.085	0.073	0.086	0.082
X-site total	1.854	1.874	1.875	1.849	1.864	1.860	1.859	1.967	1.911	1.860	1.884
Fe/Fe+Al	0.995	0.995	0.993	0.992	0.990	0.993	0.991	0.997	0.999	0.988	0.995
Na/Na+K	0.070	0.048	0.039	0.031	0.072	0.060	0.043	0.011	0.045	0.023	0.031

Sample	CAS VWL 0002 Capulin	CAS VWL 0002 Capulin	CAS VWL 0002 Capulin	CAS VWL 0002 Capulin	CAS VWL 0002 Capulin	CAS VWL 0002 Capulin	CAS VWL 0002 Capulin	CAS VWL 0002 Capulin	CAS VWL 0002 Capulin	CAS VWL 0002 Capulin
scar time in HF (min)	0	0	0	0	0	0	0	0	0	0
K_2O	7.03	7.66	3.42	7.39	6.46	6.52	7.47	7.73	7.40	7.14
Na_2O	0.12	0.03	0.03	0.09	0.19	0.20	0.09	0.12	0.06	0.15
FeO	33.51	36.78	19.56	34.72	30.21	31.82	37.36	38.04	36.53	34.88
Fe_2O_3 (calc)	37.20	40.82	21.71	38.54	33.53	35.32	41.47	42.23	40.55	38.71
Al_2O_3	0.34	0.40	0.15	0.48	1.16	0.42	0.39	0.44	0.40	0.40
As_2O_3	0.03	0.03	0.00	0.01	0.00	0.01	0.02	0.02	0.00	0.02
MoO_3	0.00	0.00	0.00	0.00	0.00	0.00	0.00	0.00	0.00	0.00
SO_2	20.69	22.18	11.21	22.19	14.35	18.59	23.94	23.74	21.70	21.61
SO_3	25.86	27.72	14.01	27.74	17.94	23.23	29.92	29.66	27.12	27.00

(calc)										
P_2O_5	0.18	0.04	0.00	0.00	0.06	0.05	0.03	0.01	0.01	0.02
SiO_2	0.14	0.10	0.07	0.05	1.65	0.16	0.09	0.03	0.17	0.08
H_2O	9.35	10.06	5.14	9.82	7.96	8.61	10.53	10.57	9.91	9.68
F	0.00	0.00	0.01	0.07	0.09	0.11	0.01	0.09	0.00	0.13
Cl	0.29	0.16	0.92	0.33	0.43	0.60	0.12	0.12	0.16	0.21
Total	71.68	77.44	40.52	75.13	62.55	67.09	80.05	80.90	76.34	74.30
K	0.863	0.874	0.764	0.864	0.932	0.868	0.815	0.840	0.857	0.847
Na	0.023	0.006	0.012	0.016	0.041	0.042	0.016	0.019	0.011	0.027
A-site total	0.885	0.880	0.775	0.879	0.972	0.910	0.830	0.859	0.868	0.874
Fe	2.697	2.750	2.861	2.660	2.854	2.780	2.669	2.708	2.774	2.711
Al	0.039	0.043	0.032	0.052	0.155	0.051	0.040	0.044	0.043	0.044
As	0.002	0.002	0.000	0.001	0.000	0.001	0.001	0.001	0.000	0.001
B-site total	2.738	2.794	2.893	2.712	3.008	2.832	2.709	2.753	2.817	2.755
S	1.868	1.860	1.839	1.907	1.521	1.821	1.918	1.895	1.848	1.884
P	0.015	0.003	0.000	0.000	0.006	0.005	0.002	0.001	0.001	0.002
X-site total	1.883	1.863	1.839	1.907	1.527	1.826	1.920	1.896	1.849	1.886
Fe/Fe+Al	0.986	0.985	0.989	0.981	0.949	0.982	0.985	0.984	0.985	0.984
Na/Na+K	0.025	0.007	0.015	0.018	0.042	0.046	0.019	0.022	0.013	0.030

Sample	CAS VWL 0002 Capulin	CAS VWL 0002 Capulin	CAS VWL 0002 Capulin	CAS VWL 0002 Capulin	CAS VWL 0002 Capulin	CAS VWL 0002 Capulin	CAS VWL 0002 Capulin	CAS VWL 0002 Capulin	CAS VWL 0002 Capulin	CAS VWL 0002 Capulin
scar time in HF (min)	30	30	30	30	30	30	30	30	30	30
K_2O	2.56	5.57	5.72	6.92	3.83	6.10	5.98	6.67	3.97	2.39
Na_2O	0.15	0.43	0.23	0.22	0.07	0.13	0.17	0.19	0.09	0.04
FeO	11.40	34.99	27.40	34.00	16.84	29.79	28.62	32.27	18.61	7.06
Fe_2O_3 (calc)	12.66	38.84	30.41	37.74	18.69	33.07	31.76	35.82	20.66	7.83
Al_2O_3	0.26	0.37	0.42	0.29	0.12	0.37	0.27	0.27	0.14	3.42
As_2O_3	0.00	0.05	0.01	0.01	0.00	0.00	0.03	0.00	0.00	0.02
MoO_3	0.00	0.00	0.00	0.00	0.00	0.00	0.00	0.00	0.00	0.00
SO_2	8.75	20.98	17.08	21.07	10.99	18.59	17.69	19.92	11.72	6.12
SO_3	10.94	26.22	21.34	26.33	13.73	23.23	22.11	24.89	14.65	7.64

(calc)										
P_2O_5	0.04	0.11	0.03	0.04	0.00	0.05	0.00	0.06	0.05	0.05
SiO_2	0.42	0.65	0.54	0.37	0.19	0.55	0.47	0.53	0.30	6.06
H_2O	3.74	9.62	7.80	9.50	4.86	8.44	8.04	9.05	5.29	4.78
F	0.54	1.31	0.68	0.13	0.13	0.08	0.08	0.20	0.00	0.03
Cl	1.06	0.49	0.43	0.34	1.61	0.65	0.59	0.40	1.65	1.12
Total	28.92	74.55	60.34	72.89	38.64	64.74	61.93	69.54	41.82	31.09
K	0.786	0.664	0.842	0.836	0.905	0.830	0.853	0.846	0.862	0.574
Na	0.072	0.078	0.052	0.041	0.025	0.028	0.037	0.036	0.031	0.014
A-site total	0.858	0.742	0.894	0.876	0.929	0.857	0.890	0.882	0.893	0.587
Fe	2.293	2.738	2.642	2.692	2.608	2.657	2.678	2.682	2.650	1.110
Al	0.073	0.041	0.057	0.033	0.027	0.046	0.036	0.032	0.027	0.759
As	0.000	0.003	0.001	0.001	0.000	0.000	0.002	0.000	0.000	0.002
B-site total	2.366	2.781	2.699	2.725	2.634	2.703	2.716	2.714	2.677	1.870
S	1.974	1.841	1.847	1.871	1.909	1.859	1.857	1.857	1.871	1.079
P	0.009	0.009	0.003	0.003	0.001	0.004	0.000	0.005	0.008	0.007
X-site total	1.983	1.850	1.850	1.874	1.909	1.863	1.857	1.862	1.879	1.086
Fe/Fe+Al	0.969	0.985	0.979	0.988	0.990	0.983	0.987	0.988	0.990	0.594
Na/Na+K	0.084	0.105	0.058	0.046	0.026	0.032	0.041	0.041	0.035	0.023

Sample	SWH GJG 0004 SW Hansen	SWH GJG 0004 SW Hansen	SWH GJG 0004 SW Hansen	SWH GJG 0004 SW Hansen	SWH GJG 0004 SW Hansen	SWH GJG 0004 SW Hansen	SWH GJG 0004 SW Hansen	SWH GJG 0004 SW Hansen	SWH GJG 0004 SW Hansen	SWH GJG 0004 SW Hansen
scar time in HF (min)	0	0	0	0	0	0	0	0	0	0
K_2O	6.53	6.61	6.07	4.90	6.63	6.25	6.74	6.72	6.07	4.47
Na_2O	0.81	0.70	0.72	0.75	0.60	0.97	0.35	0.71	0.44	0.52
FeO	38.47	39.88	35.10	29.12	39.73	35.95	39.46	39.06	33.68	27.16
Fe_2O_3 (calc)	42.70	44.27	38.96	32.32	44.10	39.90	43.80	43.36	37.39	30.15
Al_2O_3	1.33	0.75	0.38	1.38	0.39	0.46	0.58	0.78	0.77	0.76
As_2O_3	0.01	0.01	0.03	0.01	0.02	0.02	0.03	0.02	0.02	0.01
MoO_3	0.00	0.00	0.00	0.00	0.00	0.00	0.00	0.00	0.00	0.00
SO_2	22.44	22.81	20.71	16.75	23.44	21.96	23.43	23.12	19.97	15.68

SO_3 (calc)	28.04	28.51	25.88	20.93	29.30	27.45	29.28	28.90	24.95	19.59
P_2O_5	1.12	1.09	0.89	0.82	0.96	1.04	0.98	1.20	0.71	0.65
SiO_2	1.86	0.96	0.35	1.91	0.10	0.11	0.42	1.01	1.01	1.18
H_2O	11.26	11.13	9.77	8.69	10.92	10.21	10.99	11.18	9.61	7.78
F	0.00	0.09	0.02	0.00	0.03	0.12	0.18	0.10	0.05	0.11
Cl	0.10	0.02	0.25	0.56	0.06	0.22	0.01	0.03	0.25	0.68
Total	83.93	84.04	74.28	64.88	82.87	77.29	83.15	83.94	72.58	59.00
K	0.665	0.682	0.713	0.648	0.697	0.703	0.703	0.690	0.725	0.659
Na	0.125	0.110	0.129	0.150	0.096	0.166	0.055	0.111	0.080	0.118
A-site total	0.790	0.792	0.841	0.798	0.793	0.868	0.758	0.801	0.804	0.777
Fe	2.569	2.696	2.703	2.521	2.739	2.650	2.701	2.629	2.636	2.625
Al	0.125	0.072	0.042	0.168	0.038	0.048	0.056	0.074	0.085	0.104
As	0.001	0.001	0.002	0.001	0.001	0.001	0.002	0.001	0.001	0.001
B-site total	2.694	2.769	2.746	2.690	2.777	2.699	2.758	2.704	2.722	2.729
S	1.681	1.730	1.788	1.626	1.812	1.816	1.799	1.746	1.752	1.700
P	0.076	0.075	0.069	0.073	0.067	0.078	0.068	0.082	0.056	0.064
X-site total	1.757	1.805	1.857	1.699	1.879	1.893	1.867	1.828	1.808	1.763
Fe/Fe+Al	0.954	0.974	0.985	0.938	0.986	0.982	0.980	0.973	0.969	0.962
Na/Na+K	0.158	0.139	0.153	0.188	0.121	0.191	0.072	0.139	0.099	0.151

Sample	SWH GJG 0004 SW Hansen	SWH GJG 0004 SW Hansen	SWH GJG 0004 SW Hansen	SWH GJG 0004 SW Hansen	SWH GJG 0004 SW Hansen	SWH GJG 0004 SW Hansen	SWH GJG 0004 SW Hansen	SWH GJG 0004 SW Hansen	SWH GJG 0004 SW Hansen	SWH GJG 0004 SW Hansen
scar time in HF (min)	30	30	30	30	30	30	30	30	30	30
K_2O	6.57	5.85	6.13	6.74	6.74	7.42	6.90	6.89	6.42	6.70
Na_2O	0.75	0.53	0.44	0.52	0.51	0.45	0.51	0.71	0.62	0.30
FeO	38.89	36.01	39.63	38.80	37.57	39.55	39.85	39.66	38.88	37.45
Fe_2O_3 (calc)	43.16	39.97	43.99	43.07	41.70	43.90	44.23	44.02	43.15	41.57
Al_2O_3	0.30	0.31	0.45	0.35	0.36	0.69	0.32	0.75	0.31	0.55
As_2O_3	0.00	0.00	0.00	0.02	0.04	0.02	0.05	0.02	0.03	0.00
MoO_3	0.00	0.00	0.00	0.00	0.00	0.00	0.00	0.00	0.00	0.00
SO_2	22.98	20.03	23.42	23.08	21.55	23.67	23.59	23.03	22.74	22.38

SO_3 (calc)	28.72	25.04	29.27	28.84	26.93	29.58	29.48	28.79	28.42	27.96
P_2O_5	1.06	0.85	1.19	0.76	0.88	1.29	1.15	1.24	1.01	0.96
SiO_2	0.00	0.15	0.39	0.00	0.00	0.65	0.08	0.88	0.00	0.00
H_2O	10.71	9.58	10.99	10.64	10.17	11.30	11.01	11.20	10.61	10.39
F	0.34	0.28	0.15	0.20	0.28	0.14	0.13	0.16	0.28	0.40
Cl	0.07	0.11	0.02	0.08	0.11	0.03	0.03	0.03	0.05	0.11
Total	81.66	73.70	82.80	81.17	78.21	85.19	83.62	84.57	80.96	79.25
K	0.705	0.700	0.641	0.727	0.761	0.754	0.719	0.706	0.694	0.740
Na	0.122	0.097	0.070	0.086	0.087	0.070	0.081	0.111	0.103	0.051
A-site total	0.827	0.797	0.710	0.813	0.847	0.824	0.800	0.817	0.797	0.791
Fe	2.732	2.827	2.713	2.744	2.779	2.634	2.723	2.663	2.756	2.712
Al	0.030	0.034	0.043	0.035	0.038	0.065	0.031	0.071	0.032	0.057
As	0.000	0.000	0.000	0.001	0.002	0.001	0.003	0.001	0.002	0.000
B-site total	2.762	2.861	2.756	2.780	2.818	2.700	2.756	2.735	2.789	2.768
S	1.811	1.764	1.799	1.831	1.787	1.768	1.808	1.735	1.808	1.817
P	0.076	0.067	0.083	0.054	0.066	0.087	0.080	0.085	0.073	0.070
X-site total	1.886	1.831	1.881	1.885	1.853	1.854	1.887	1.819	1.880	1.887
Fe/Fe+Al	0.989	0.988	0.984	0.988	0.987	0.976	0.989	0.974	0.989	0.980
Na/Na+K	0.148	0.121	0.098	0.106	0.102	0.085	0.101	0.136	0.129	0.064

Sample	SWH GJG 0025 SW Hansen	SWH GJG 0025 SW Hansen	SWH GJG 0025 SW Hansen	SWH GJG 0025 SW Hansen	SWH GJG 0025 SW Hansen	SWH GJG 0025 SW Hansen	SWH GJG 0025 SW Hansen	SWH GJG 0025 SW Hansen	SWH GJG 0025 SW Hansen	SWH GJG 0025 SW Hansen
scar time in HF (min)	0	0	0	0	0	0	0	0	0	0
K_2O	6.79	6.86	6.86	6.54	6.45	4.87	5.79	5.27	5.20	4.94
Na_2O	0.69	0.62	0.59	0.68	0.46	0.44	0.74	0.65	0.30	0.26
FeO	39.94	39.70	39.36	39.75	40.09	46.16	42.08	41.69	40.44	25.45
Fe_2O_3 (calc)	44.33	44.07	43.69	44.12	44.50	51.24	46.71	46.27	44.89	28.25
Al_2O_3	0.14	0.21	0.17	1.20	0.41	1.56	0.86	1.16	0.16	0.20
As_2O_3	0.02	0.00	0.02	0.00	0.01	0.00	0.01	0.00	0.00	0.03
MoO_3	0.00	0.00	0.00	0.00	0.00	0.00	0.00	0.00	0.00	0.00
SO_2	23.42	23.54	23.46	21.63	23.21	16.85	22.08	17.89	24.60	16.12

SO_3 (calc)	29.26	29.41	29.32	27.03	29.00	21.06	27.59	22.36	30.74	20.15
P_2O_5	1.10	1.05	0.92	1.06	1.12	1.41	1.20	1.25	0.91	0.47
SiO_2	0.00	0.00	0.00	1.38	0.29	2.31	1.34	1.67	0.03	0.10
H_2O	10.91	10.91	10.81	11.02	10.96	10.81	11.28	10.34	11.03	7.26
F	0.05	0.09	0.15	0.05	0.00	0.04	0.08	0.00	0.05	0.08
Cl	0.03	0.03	0.05	0.04	0.03	0.14	0.02	0.12	0.00	0.69
Total	83.09	83.01	82.38	83.34	83.02	84.59	85.47	80.04	82.71	55.62
K	0.714	0.722	0.729	0.681	0.676	0.517	0.589	0.586	0.542	0.781
Na	0.111	0.099	0.096	0.108	0.074	0.072	0.114	0.110	0.047	0.064
A-site total	0.825	0.821	0.824	0.789	0.749	0.589	0.703	0.695	0.589	0.845
Fe	2.754	2.737	2.739	2.713	2.752	3.213	2.807	3.034	2.759	2.636
Al	0.014	0.020	0.017	0.116	0.040	0.153	0.081	0.119	0.015	0.030
As	0.001	0.000	0.001	0.000	0.001	0.000	0.001	0.000	0.000	0.003
B-site total	2.769	2.757	2.757	2.828	2.792	3.366	2.889	3.153	2.774	2.668
S	1.811	1.820	1.831	1.656	1.787	1.316	1.652	1.460	1.882	1.873
P	0.077	0.073	0.065	0.074	0.078	0.100	0.081	0.092	0.063	0.050
X-site total	1.887	1.893	1.896	1.729	1.865	1.415	1.733	1.552	1.945	1.923
Fe/Fe+Al	0.995	0.993	0.994	0.959	0.986	0.955	0.972	0.962	0.995	0.989
Na/Na+K	0.134	0.120	0.116	0.137	0.098	0.121	0.162	0.158	0.080	0.075

Sample	SWH GJG 0025 SW Hansen	SWH GJG 0025 SW Hansen	SWH GJG 0025 SW Hansen	SWH GJG 0025 SW Hansen	SWH GJG 0025 SW Hansen	SWH GJG 0025 SW Hansen	SWH GJG 0025 SW Hansen	SWH GJG 0025 SW Hansen	SWH GJG 0025 SW Hansen	SWH GJG 0025 SW Hansen
scar time in HF (min)	30	30	30	30	30	30	30	30	30	30
K_2O	6.39	7.59	5.16	5.86	6.66	6.16	6.26	5.23	6.26	5.45
Na_2O	0.89	0.47	0.73	1.13	0.66	0.83	0.79	0.53	0.88	0.78
FeO	39.78	40.53	29.55	37.51	38.45	37.10	37.82	29.73	36.74	31.81
Fe_2O_3 (calc)	44.16	44.98	32.79	41.64	42.68	41.18	41.98	33.00	40.78	35.31
Al_2O_3	0.22	0.25	0.81	0.36	0.19	0.32	0.34	0.70	0.36	0.65
As_2O_3	0.02	0.03	0.01	0.01	0.00	0.01	0.01	0.02	0.01	0.00
MoO_3	0.00	0.00	0.00	0.00	0.00	0.00	0.00	0.00	0.00	0.00
SO_2	23.80	24.22	18.07	21.73	23.03	21.79	22.89	17.19	22.14	18.93

SO_3 (calc)	29.74	30.27	22.59	27.15	28.78	27.23	28.60	21.48	27.66	23.65
P_2O_5	0.91	0.82	0.68	0.84	1.04	1.02	0.99	0.63	0.90	0.73
SiO_2	0.14	0.00	0.84	0.24	0.18	0.43	0.32	0.78	0.48	0.28
H_2O	10.98	11.16	8.63	10.26	10.69	10.31	10.62	8.37	10.36	8.94
F	0.22	0.00	0.43	0.39	0.30	0.31	0.72	0.42	0.86	0.74
Cl	0.01	0.02	0.48	0.29	0.12	0.15	0.35	0.44	0.28	0.46
Total	83.35	85.07	65.38	78.61	81.32	78.43	81.09	64.03	79.26	68.76
K	0.668	0.781	0.686	0.656	0.715	0.687	0.676	0.718	0.693	0.700
Na	0.141	0.073	0.148	0.192	0.107	0.140	0.130	0.110	0.149	0.152
A-site total	0.809	0.854	0.834	0.847	0.822	0.827	0.806	0.827	0.842	0.851
Fe	2.726	2.733	2.575	2.750	2.707	2.708	2.679	2.673	2.669	2.677
Al	0.021	0.024	0.099	0.037	0.019	0.033	0.034	0.089	0.037	0.077
As	0.001	0.002	0.001	0.001	0.000	0.001	0.001	0.002	0.001	0.000
B-site total	2.747	2.758	2.675	2.788	2.726	2.741	2.713	2.763	2.706	2.753
S	1.829	1.832	1.767	1.787	1.819	1.784	1.818	1.733	1.803	1.786
P	0.064	0.056	0.061	0.062	0.075	0.075	0.072	0.058	0.066	0.062
X-site total	1.892	1.888	1.827	1.849	1.893	1.859	1.890	1.791	1.869	1.848
Fe/Fe+Al	0.993	0.991	0.963	0.987	0.993	0.988	0.987	0.968	0.987	0.972
Na/Na+K	0.174	0.085	0.177	0.226	0.130	0.169	0.161	0.132	0.176	0.178

Sample scar	KS-JB-3 June Bug	KS-JB-3 June Bug	KS-JB-3 June Bug	KS-JB-3 June Bug	KS-JB-3 June Bug	KS-JB-3 June Bug	KS-JB-3 June Bug	KS-JB-3 June Bug	KS-JB-3 June Bug	KS-JB-3 June Bug
time in HF (min)	30	30	30	30	30	30	30	30	30	30
K_2O	6.02	7.20	6.17	6.58	6.71	6.71	6.86	7.13	6.68	6.80
Na_2O	1.06	0.47	1.09	1.03	0.81	0.76	0.96	0.63	0.63	0.62
FeO	36.13	38.96	37.32	38.29	38.82	36.65	36.44	36.03	33.89	36.12
Fe_2O_3 (calc)	40.11	43.25	41.42	42.50	43.09	40.68	40.44	39.99	37.62	40.09
Al_2O_3	0.58	1.11	0.59	1.12	0.78	0.96	0.94	1.40	0.98	1.57
As_2O_3	0.00	0.02	0.03	0.01	0.03	0.00	0.01	0.03	0.02	0.04
MoO_3	0.00	0.00	0.00	0.00	0.00	0.00	0.00	0.00	0.00	0.00
SO_2	23.32	24.62	23.19	23.73	24.38	22.98	23.05	22.95	21.92	22.87
SO_3 (calc)	29.15	30.77	28.99	29.66	30.47	28.72	28.81	28.68	27.39	28.58
P_2O_5	0.09	0.18	0.12	0.12	0.11	0.53	0.54	0.86	0.54	0.67

SiO_2	0.11	0.11	0.12	0.11	0.07	0.10	0.08	0.09	0.09	0.09
H_2O	10.31	11.10	10.44	10.82	10.93	10.51	10.54	10.64	9.95	10.60
F	0.21	0.22	0.09	0.19	0.11	0.09	0.00	0.06	0.07	0.00
Cl	0.15	0.05	0.12	0.09	0.05	0.14	0.16	0.16	0.27	0.11
Total	77.98	84.03	79.27	82.09	82.79	79.44	79.58	79.97	75.05	79.47
K	0.670	0.744	0.678	0.698	0.705	0.733	0.747	0.769	0.771	0.736
Na	0.179	0.074	0.183	0.165	0.130	0.126	0.159	0.103	0.110	0.102
A-site total	0.848	0.818	0.860	0.863	0.835	0.858	0.906	0.871	0.881	0.838
Fe	2.636	2.641	2.689	2.662	2.673	2.623	2.601	2.547	2.563	2.565
Al	0.060	0.106	0.060	0.110	0.076	0.097	0.095	0.140	0.105	0.158
As	0.000	0.001	0.002	0.001	0.001	0.000	0.001	0.002	0.001	0.002
B-site total	2.696	2.748	2.750	2.773	2.750	2.720	2.696	2.688	2.669	2.724
S	1.908	1.871	1.874	1.851	1.883	1.845	1.846	1.819	1.859	1.821
P	0.007	0.012	0.009	0.009	0.008	0.039	0.040	0.062	0.042	0.049
X-site total	1.915	1.883	1.883	1.859	1.891	1.883	1.885	1.881	1.901	1.870
Fe/Fe+Al	0.978	0.961	0.978	0.960	0.973	0.964	0.965	0.948	0.961	0.942
Na/Na+K	0.210	0.090	0.212	0.191	0.155	0.146	0.176	0.118	0.125	0.121

Sample	SWH GJG 0001 SW Hansen	SWH GJG 0001 SW Hansen	SWH GJG 0001 SW Hansen	SWH GJG 0001 SW Hansen	SWH GJG 0001 SW Hansen	SWH GJG 0001 SW Hansen	SWH GJG 0001 SW Hansen	SWH GJG 0001 SW Hansen	SWH GJG 0001 SW Hansen	SWH GJG 0001 SW Hansen	SWH GJG 0001 SW Hansen	SWH GJG 0001 SW Hansen
scar time in HF (min)	30	30	30	30	30	30	30	30	30	30	30	30
K_2O	1.35	1.25	0.48	0.48	0.75	0.88	0.85	0.37	1.17	0.99	0.63	0.63
Na_2O	3.93	3.57	5.24	1.26	1.89	2.19	3.77	1.35	3.16	3.49	4.29	4.11
FeO	33.13	32.35	38.40	13.00	14.66	17.71	30.31	7.22	29.95	28.52	37.61	34.90
Fe_2O_3 (calc)	36.77	35.91	42.62	14.42	16.27	19.66	33.64	8.02	33.24	31.66	41.74	38.74
Al_2O_3	0.30	0.43	0.25	0.43	2.06	1.16	1.06	1.13	0.94	2.66	0.39	0.50
As_2O_3	0.01	0.00	0.01	0.00	0.00	0.00	0.00	0.00	0.00	0.00	0.00	0.00
MoO_3	0.00	0.00	0.00	0.00	0.00	0.00	0.00	0.00	0.00	0.00	0.00	0.00
SO_2	20.42	20.12	23.14	9.44	9.20	11.73	18.92	4.44	18.30	16.68	22.08	21.01
SO_3 (calc)	25.52	25.14	28.92	11.79	11.49	14.66	23.65	5.55	22.88	20.85	27.59	26.25
P_2O_5	0.60	0.66	0.67	0.45	0.56	0.66	1.08	0.24	0.96	0.85	0.96	1.17
SiO_2	1.43	1.91	1.31	1.16	3.61	1.97	1.75	0.97	1.32	2.04	1.38	1.15

H_2O	9.68	9.64	10.98	4.39	5.64	6.03	9.34	2.62	8.93	8.96	10.66	10.10
F	0.65	0.59	0.28	0.37	0.72	0.31	1.33	1.75	1.39	3.55	0.51	0.72
Cl	0.34	0.52	0.34	1.22	0.84	1.01	0.46	1.30	0.47	0.47	0.22	0.24
Total	71.83	71.04	81.11	32.19	39.93	43.65	68.87	21.39	66.59	68.22	78.72	74.53
K	0.160	0.149	0.050	0.126	0.153	0.167	0.105	0.160	0.151	0.127	0.068	0.072
Na	0.708	0.646	0.833	0.500	0.584	0.635	0.704	0.899	0.617	0.679	0.703	0.710
A-site total	0.867	0.795	0.883	0.626	0.737	0.802	0.808	1.059	0.768	0.806	0.771	0.782
Fe	2.574	2.525	2.632	2.228	1.956	2.212	2.441	2.077	2.522	2.394	2.655	2.599
Al	0.033	0.048	0.024	0.105	0.388	0.204	0.120	0.459	0.112	0.315	0.039	0.053
As	0.001	0.000	0.001	0.000	0.000	0.000	0.000	0.000	0.000	0.000	0.000	0.000
B-site total	2.608	2.573	2.656	2.333	2.344	2.416	2.561	2.535	2.634	2.709	2.694	2.651
S	1.780	1.761	1.779	1.815	1.376	1.643	1.710	1.433	1.729	1.571	1.748	1.754
P	0.048	0.052	0.047	0.079	0.076	0.084	0.088	0.071	0.082	0.073	0.069	0.088
X-site total	1.827	1.813	1.826	1.894	1.452	1.726	1.798	1.504	1.811	1.643	1.817	1.842
Fe/Fe+Al	0.987	0.982	0.991	0.955	0.834	0.916	0.953	0.819	0.958	0.884	0.986	0.980
Na/Na+K	0.816	0.812	0.943	0.799	0.792	0.792	0.871	0.849	0.804	0.842	0.912	0.909

Sample	PIT VWL 0005	PIT VWL 0005	PIT VWL 0005	PIT VWL 0005	PIT VWL 0005	PIT VWL 0005	PIT VWL 0005	PIT VWL 0005	PIT VWL 0005	PIT VWL 0005	PIT VWL 0005
scar	PIT core	PIT core	PIT core	PIT core	PIT core	PIT core	PIT core	PIT core	PIT core	PIT core	PIT core
time in HF (min)	30	30	30	30	30	30	30	30	30	30	30
K_2O	7.41	6.30	7.16	5.36	6.75	6.41	6.00	6.31	5.15	6.15	5.51
Na_2O	0.13	0.12	0.10	0.11	0.16	0.05	0.11	0.13	0.32	0.17	0.30
FeO	35.43	32.13	35.20	24.03	29.91	20.77	27.53	31.69	39.19	41.23	38.77
Fe_2O_3 (calc)	39.33	35.66	39.07	26.67	33.20	23.05	30.56	35.17	43.50	45.77	43.03
Al_2O_3	0.03	0.03	0.03	3.27	0.25	8.08	0.15	0.30	1.93	0.87	1.02
As_2O_3	0.00	0.03	0.01	0.00	0.00	0.00	0.00	0.04	0.00	0.01	0.00
MoO_3	0.00	0.00	0.00	0.00	0.00	0.00	0.00	0.00	0.00	0.00	0.00
SO_2	22.13	20.01	21.61	16.13	20.53	13.61	18.13	21.92	23.26	23.17	22.17
SO_3 (calc)	27.65	25.01	27.01	20.16	25.65	17.01	22.66	27.40	29.06	28.96	27.70
P_2O_5	0.10	0.09	0.11	0.03	0.03	0.02	0.08	0.12	0.11	0.11	0.13

SiO_2	0.18	0.28	0.23	5.47	0.45	15.05	0.27	0.44	1.78	0.48	0.79
H_2O	9.84	8.92	9.69	9.08	8.92	11.76	7.96	9.44	11.21	10.89	10.47
F	0.04	0.00	0.07	0.18	0.07	0.29	0.11	0.14	2.64	3.26	1.57
Cl	0.57	0.65	0.68	0.44	0.39	1.26	0.60	0.41	0.12	0.05	0.18
Total	75.85	68.55	74.88	64.10	67.44	77.32	60.95	70.93	85.70	86.39	80.90
K	0.864	0.811	0.848	0.677	0.868	0.626	0.865	0.767	0.527	0.649	0.605
Na	0.023	0.024	0.018	0.022	0.031	0.008	0.025	0.024	0.050	0.027	0.050
A-site total	0.887	0.835	0.866	0.699	0.899	0.634	0.890	0.791	0.577	0.676	0.654
Fe	2.708	2.711	2.733	1.991	2.524	1.329	2.602	2.525	2.631	2.848	2.786
Al	0.004	0.004	0.004	0.382	0.030	0.729	0.020	0.034	0.183	0.085	0.103
As	0.000	0.002	0.001	0.000	0.000	0.000	0.001	0.002	0.000	0.001	0.000
B-site total	2.711	2.717	2.737	2.372	2.554	2.058	2.623	2.561	2.814	2.933	2.889
S	1.897	1.894	1.882	1.499	1.943	0.977	1.922	1.960	1.751	1.795	1.787
P	0.008	0.008	0.009	0.003	0.003	0.002	0.008	0.010	0.008	0.008	0.009
X-site total	1.904	1.902	1.891	1.502	1.945	0.979	1.930	1.969	1.759	1.803	1.796
Fe/Fe +Al	0.999	0.999	0.999	0.839	0.988	0.646	0.992	0.987	0.935	0.971	0.964
Na/Na +K	0.026	0.029	0.020	0.031	0.034	0.013	0.028	0.030	0.087	0.040	0.076

Table D-2. PB Jarosite Microprobe Data

Analysis	**A-0-01**	**A-0-02**	**A-0-03**	**A-0-04**	**A-0-05**	**A-0-06**	**A-0-07**	**A-0-08**	**A-0-09**	**A-0-010**
# min HF treatment	0	0	0	0	0	0	0	0	0	0
K2O	9.29	9.08	9.23	8.81	9.17	8.11	9.21	7.93	9.43	7.93
Na2O	-0.01	0.00	0.02	0.03	-0.01	0.01	0.01	0.02	0.01	-0.04
FeO (measured)	43.11	43.17	44.12	44.40	43.60	43.02	43.79	42.83	42.10	42.15
Fe2O3 (calculated)	47.85	47.91	48.97	49.29	48.40	47.75	48.60	47.54	46.74	46.78
Al2O3	0.85	1.03	0.31	0.21	0.21	0.85	0.47	0.75	1.34	1.15
As2O3	0.35	0.32	0.15	0.10	0.21	0.24	0.15	0.39	0.10	0.31
SO2	24.71	24.69	25.12	24.74	24.07	25.24	24.52	24.89	24.81	24.70
SO3 (calculated)	30.88	30.85	31.40	30.92	30.08	31.54	30.64	31.11	31.00	30.87
P2O5	0.08	0.02	0.13	0.07	0.05	0.02	0.03	0.02	0.07	0.06
MoO3	0.15	0.23	0.17	0.30	0.21	0.14	0.26	0.30	0.29	0.26
F	0.15	0.07	0.03	0.12	0.03	0.19	0.04	0.18	0.12	0.25
Cl	0.02	0.00	0.00	0.02	0.00	-0.01	0.01	0.00	0.01	0.03
H2O	10.37	10.49	9.60	10.12	11.64	11.16	10.58	11.76	10.88	12.40
Total	89.45	89.44	90.37	89.74	88.33	88.66	89.37	88.06	88.98	87.32

time (min)	0.00	0.00	0.00	0.00	0.00	0.00	0.00	0.00	0.00	0.00
K	0.92	0.89	0.90	0.87	0.93	0.80	0.92	0.79	0.93	0.79
Na	0.00	0.00	0.00	0.00	0.00	0.00	0.00	0.00	0.00	0.00
Fe	2.79	2.79	2.84	2.88	2.89	2.78	2.85	2.80	2.72	2.76
Al	0.08	0.09	0.03	0.02	0.02	0.08	0.04	0.07	0.12	0.11
As	0.02	0.02	0.01	0.00	0.01	0.01	0.01	0.02	0.00	0.02
S	1.79	1.79	1.81	1.80	1.79	1.83	1.79	1.82	1.80	1.81
P	0.01	0.00	0.01	0.00	0.00	0.00	0.00	0.00	0.00	0.00
Mo	0.01	0.01	0.01	0.01	0.01	0.00	0.01	0.01	0.01	0.01
F	0.00	0.00	0.00	0.00	0.00	0.00	0.00	0.00	0.00	0.00
Cl	0.00	0.00	0.00	0.00	0.00	0.00	0.00	0.00	0.00	0.00
OH	6.00	6.00	6.00	6.00	6.00	6.00	6.00	6.00	6.00	6.00
Total	11.60	11.59	11.60	11.60	11.64	11.51	11.62	11.51	11.58	11.50
A (Na+K)	0.92	0.89	0.91	0.88	0.93	0.80	0.92	0.79	0.93	0.79
B (Fe+Al+Mo)	2.87	2.89	2.87	2.91	2.91	2.87	2.91	2.87	2.85	2.87
X (S, P, As)	1.81	1.80	1.83	1.81	1.80	1.84	1.80	1.84	1.80	1.83

Analysis	**A-480-01**	**A-480-02**	**A-480-03**	**A-480-04**	**A-480-05**	**A-480-06**	**A-480-07**	**A-480-08**	**A-480-09**
# min HF treatment	480	480	480	480	480	480	480	480	480
K2O	9.15	9.08	9.27	8.97	9.27	8.99	9.21	7.32	9.43
Na2O	0.04	0.00	0.04	0.03	-0.02	0.01	-0.03	-0.02	0.01
FeO (measured)	42.84	42.99	42.44	42.06	42.39	42.95	42.09	42.38	43.63
Fe2O3 (calculated)	47.55	47.71	47.11	46.69	47.05	47.67	46.72	47.04	48.43
Al2O3	0.58	0.29	1.22	1.23	0.93	0.61	1.18	0.77	0.69
As2O3	0.11	0.14	0.05	0.08	0.23	0.23	0.24	0.38	0.29
SO2	24.58	25.05	25.05	25.11	25.06	24.78	24.72	24.57	24.78
SO3 (calculated)	30.72	31.31	31.30	31.38	31.32	30.97	30.90	30.70	30.97
P2O5	0.09	0.11	0.10	0.08	0.06	0.08	0.04	0.09	0.05
MoO3	0.42	0.32	0.41	0.39	0.14	0.32	0.21	0.24	0.18
F	0.11	0.10	0.19	0.17	0.01	0.03	0.21	0.02	0.09
Cl	0.01	0.02	-0.01	0.01	0.00	-0.01	0.01	-0.01	0.01
H2O	11.24	10.93	10.31	10.97	11.01	11.10	11.31	13.47	9.84
Total	88.64	88.96	89.51	88.85	88.98	88.88	88.47	86.52	90.06
time (min)	480	480	480	480	480	480	480	480	480
K	0.911	0.901	0.906	0.881	0.9145	0.892	0.913	0.7395	0.9275
Na	0.0055	0	0.006	0.004	0	0.002	0	0	0.0015
Fe	2.7975	2.796	2.7195	2.708	2.741	2.793	2.7345	2.807	2.812
Al	0.053	0.0265	0.1105	0.112	0.085	0.056	0.1075	0.072	0.063
As	0.005	0.0065	0.0025	0.0035	0.011	0.011	0.011	0.018	0.0135
S	1.8005	1.828	1.8	1.813	1.8175	1.8075	1.8015	1.825	1.7915
P	0.006	0.007	0.007	0.005	0.004	0.0055	0.003	0.006	0.0035
Mo	0.0135	0.0105	0.013	0.0125	0.0045	0.01	0.007	0.008	0.0055
F	0	0	0	0	0	0	0	0	0

Cl	0	0	0	0	0	0	0	0	0
OH	6	6	6	6	6	6	6	6	6
Total	11.5925	11.5755	11.5635	11.539	11.577	11.577	11.5775	11.475	11.618
A (Na+K)	0.92	0.90	0.91	0.89	0.91	0.89	0.91	0.74	0.93
B (Fe+Al+Mo)	2.86	2.83	2.84	2.83	2.83	2.86	2.85	2.89	2.88
X (S, P, As)	1.81	1.84	1.81	1.82	1.83	1.82	1.82	1.85	1.81

APPENDIX E: STABLE ISOTOPE CORRECTION FACTORS AND DATA

Correction factors for stable isotope analyses were based on solid standards analyzed with each sample run.

E.1. $\delta^{34}S$ Correction

$\delta^{34}S$ corrections were made by plotting known values for standards as a function of measured values, forming a line. Measured values for the samples were then put into the equation for this line. If sample peak was significantly smaller than the reference peak, the analysis was not included.

Table E-1. Standards used for $\delta^{34}S$ analysis.

Standard	Mineral	Known $\delta^{34}S_{CDT}$ Value (‰)
AJC	$BaSO_4$	-3.6
FeS	FeS	+7.8
NBS-123	ZnS	+17.3
NZ-2	Ag_2S	21
NBS-127	$BaSO_4$	20.73

Table E-2. $\delta^{34}S$ Analyses August 27, 2007.

Sample ID	Mineral	Comment	Amount	raw d34S	corrected
AJC		STD	2.78	-7.951	**-2.6**
AJC		STD	2.73	-7.725	**-2.4**
FeS	FeS	STD	1.01	2.864	**7.4**
FeS	FeS	STD	1.01	0.640	**5.3**
NBS-123	ZnS	STD	1.01	12.985	**16.7**
NBS-123	ZnS	STD	1.10	13.948	**17.6**
NBS-127	BaSO4	STD	2.73	17.090	**20.5**
NBS-127	BaSO4	STD	2.81	17.589	**20.9**
PB	BaSO4	JAR	2.67	-22.132	**-15.7**
PB (DUP)	BaSO4	JAR	2.63	-23.550	**-17.0**
HAS GJG 0001	BaSO4	JAR	2.63	-12.371	**-6.7**

GHS VWL 0007	BaSO4	JAR	2.62	-8.072	**-2.7**
SWH GJG 0025	BaSO4	JAR	2.72	-9.215	**-3.8**
PIT VWL 0007	BaSO4	JAR	2.78	-14.126	**-8.3**
SWH GJG 0001	BaSO4	JAR	2.76	-8.518	**-3.1**
SWH GJG 0001 (DUP)	BaSO4	JAR	2.95	-7.781	**-2.4**
SWH VWL 0001	BaSO4	JAR	2.72	-9.158	**-3.7**
ESS VWL 0001	BaSO4	JAR	2.98	-5.641	**-0.5**
KS-SC-1	PY		0.74	-4.540	**0.5**
KS-BC-4	PY		0.73	-3.951	**1.1**
KS-JB-5	PY		0.75	-3.886	**1.1**
KS-JB-5 (DUP)	PY		0.73	-3.597	**1.4**
KS-BC-2	PY		0.75	-3.827	**1.2**
KS-JB-2	PY		0.75	-3.553	**1.4**
PB (DUP)	BaSO4	JAR	2.85	-21.940	**-15.5**
NBS-123	ZnS	STD	0.97	12.701	**16.4**
NBS-127	BaSO4	STD	2.88	18.246	**21.5**

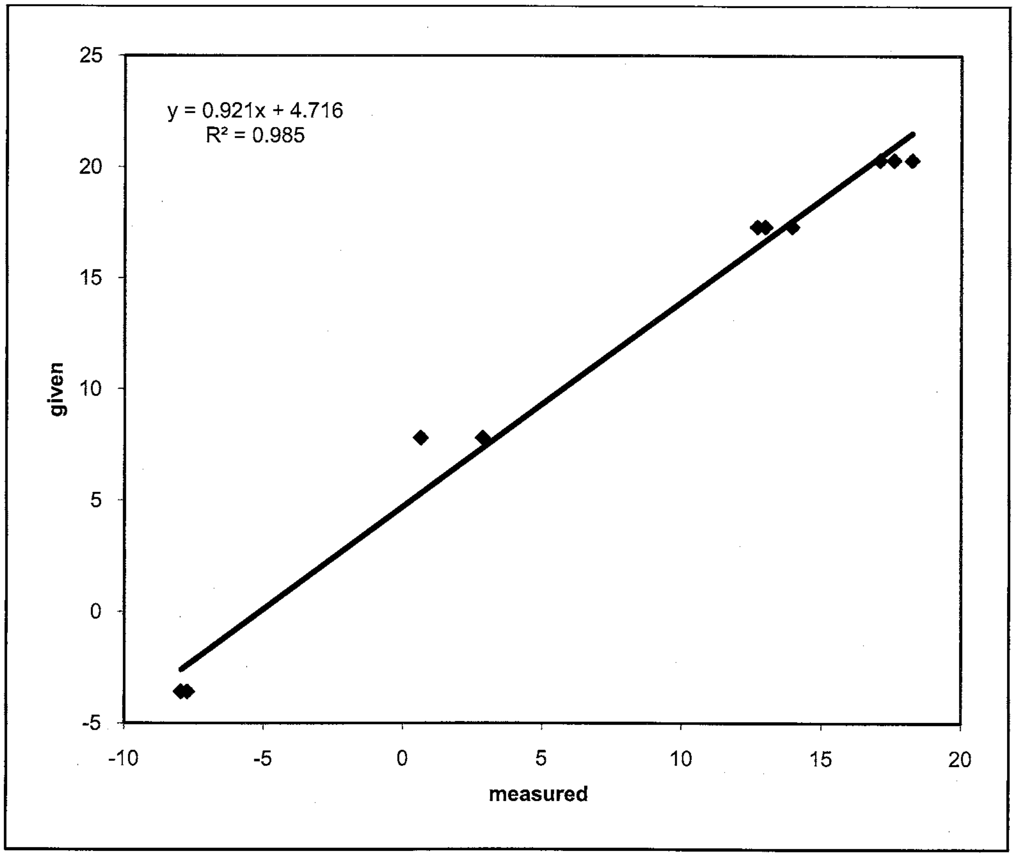

Figure E-1. Trendline for 8-27-07

Table E-3. δ^{34}S Analyses December 21, 2007.

Sample	Amount	Mineral	Comment	Amplitude	Raw Delta 34S	Final Correction

AJC	2.72	BASO4	STD	5433	-6.33	**-3.5**
AJC	2.68	BASO4	STD	5462	-6.31	**-3.5**
AJC	2.69	BASO5	STD	5649	-6.09	**-3.3**
FES	1.11	ZnS	STD	5040	6.015	**8.8**
FES	1.15	ZnS	STD	3244	3.471	**6.2**
NBS123	1.16		STD	3906	13.97	**16.7**
NBS123	1.14		STD	4781	14.769	**17.5**
NBS127	2.59	BASO4	STD	5186	18.382	**21.1**
NBS127	2.69	BASO4	STD	5160	18.193	**20.9**
KS-JB-4	2.86	BASO4		5629	-3.585	**-0.8**
PB	2.63	JAROSITE		4161	-22.186	**-19.3**
PB (DUP)	2.5	JAROSITE		4106	-22.294	**-19.4**
MM6127-03	2.59	BASO4		3874	-22.07	**-19.2**
ESS-VWL-0001	2.66	BASO4		4547	-5.03	**-2.2**

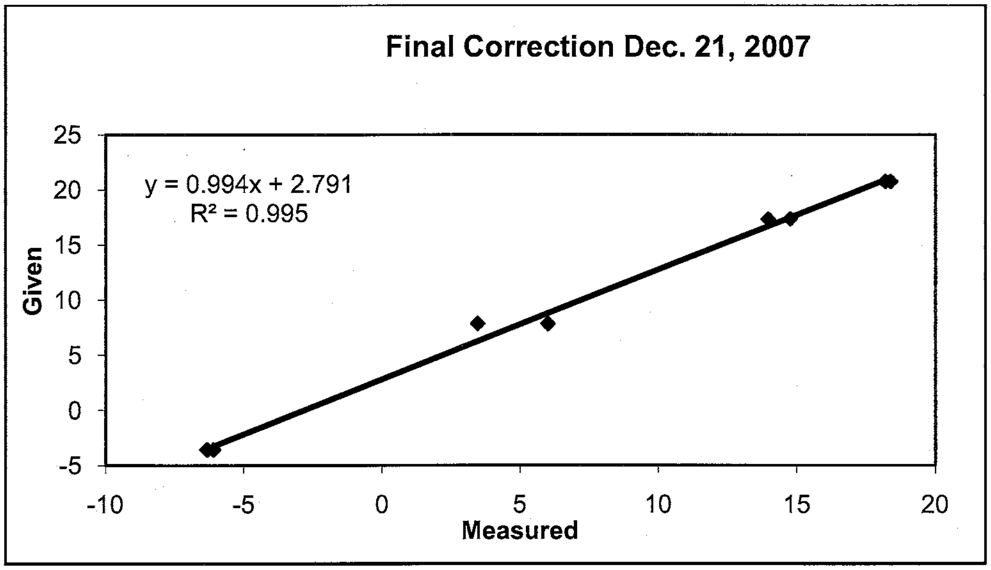

Figure E-2. Trendline for 12-21-07.

Table E-4. δ^{34}S Analyses March 13. 2008.

Sample	Identifier	comment	Amount	Sam. Amp (mV)	Delta 34S	**Corrected Delta 34 S**
HIS PY	Py	STD	0.67	2696	-0.716	**1.1**
AJC	BaSO4	STD	2.68	4115	-5.153	**-3.2**
AJC	BaSO4	STD	2.42	3103	-5.897	**-3.9**
FeS	FeS	STD	0.96	2782	6.192	**7.7**
FeS	FeS	STD	0.97	2880	6.172	**7.7**
NBS 123	ZnS	STD	1.02	3293	15.705	**16.8**
NBS 123	ZnS	STD	1.09	5368	16.700	**17.8**
NZ2	Ag2S	STD	2.91	4174	20.308	**21.3**

NZ2	Ag2S	STD	2.78	2931	19.807	**20.8**
KS-SC-2	BaSO4		2.75	2474	-4.331	**-2.4**
KS-SC-2 (DUP)	BaSO4		2.63	2145	-4.969	**-3.0**
KS-JB-3	BaSO4		2.92	2343	-2.919	**-1.0**
KS-JB-3 (DUP)	BaSO4		2.72	2073	-3.025	**-1.1**

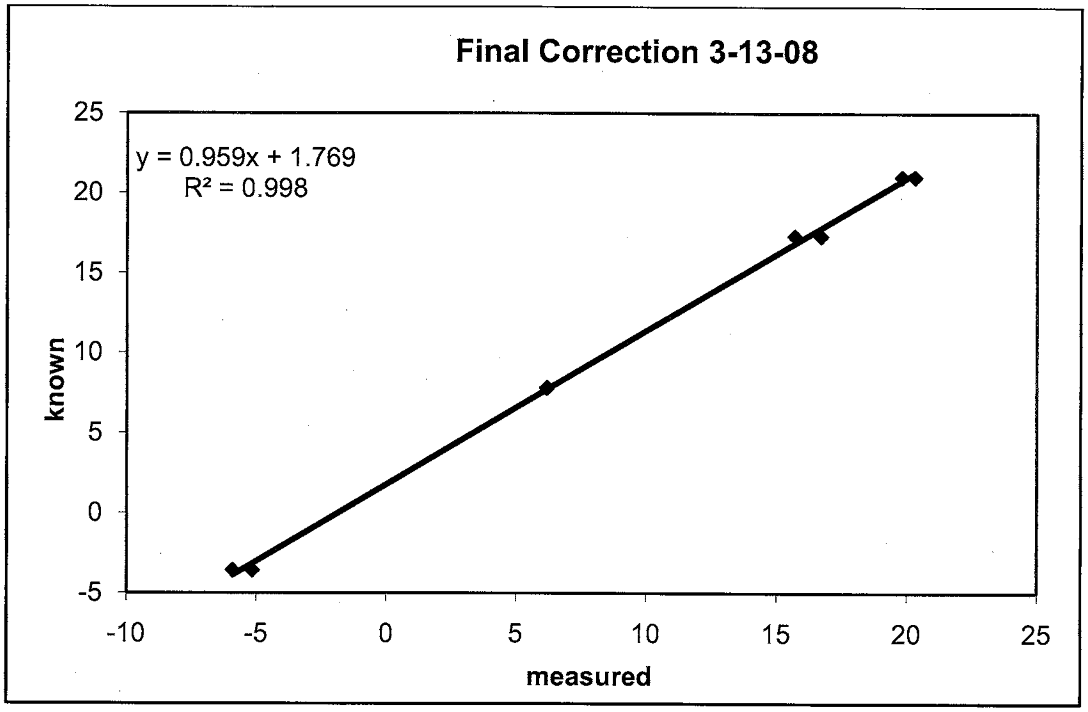

Figure E-3. Trendline for 3-13-08.

E.2. $\delta^{18}O$ Corrections

$\delta^{18}O$ corrections were also made by plotting standard known values as a function of measured values. Measured values for the samples were then put into this equation. If sample peak was significantly smaller than the reference peak, the analysis was thrown out.

Table E-5. Standards used for $\delta^{18}O$.

Standard	**Material**	**Known $\delta^{18}O_{VSMOW}$ Value (‰)**
HEKA	Benzoic Acid	25.1
NBS-127	$BaSO_4$	9.3

Table E-6. $\delta^{18}O$ analyses 1-15-08-PM-1

Sample	Identifier	comment	amount	d18O/16O	corrected value
Blank			0.00		
HEKA		STD	0.32	33.672	**25.1**
HEKA		STD	0.27	33.262	**24.6**
HEKA		STD	0.34	29.213	**20.4**
NBS-127	BaSO4	STD	0.24	18.735	**9.3**
NBS-127	BaSO4	STD	0.27	18.077	**8.6**
NBS-127	BaSO4	STD	0.21	17.861	**8.4**
PB	JAR		0.40	13.111	**3.4**
PB (DUP)	JAR		0.35	13.376	**3.7**
PB	BaSO4		0.26	20.754	**11.5**
PB (DUP)	BaSO4		0.21	21.870	**12.6**
ESS VWL 0001	JAR		0.35	6.883	**-3.1**
ESS VWL 0001 (DUP)	JAR		0.46	6.904	**-3.1**
ESS VWL 0001	BaSO4		0.21	9.003	**-0.9**
ESS VWL 0001 (DUP)	BaSO4		0.22	12.000	**2.3**
KS-SC-2	BaSO4		0.25	14.831	**5.2**
KS-SC-2 (DUP)	BaSO4		0.25	12.813	**3.1**
HEKA		STD	0.33	33.214	**24.6**
PIT VWL 0005	JAR		0.35	7.562	**-2.4**
PIT VWL 0005 (DUP)	JAR		0.35	7.273	**-2.7**
PIT VWL 0005	BaSO4		0.25	11.012	**1.2**
PIT VWL 0005 (DUP)	BaSO4		0.20	8.965	**-0.9**
HEKA		STD	0.28	34.365	**25.8**
NBS-127	BaSO4	STD	0.24	20.456	**11.1**

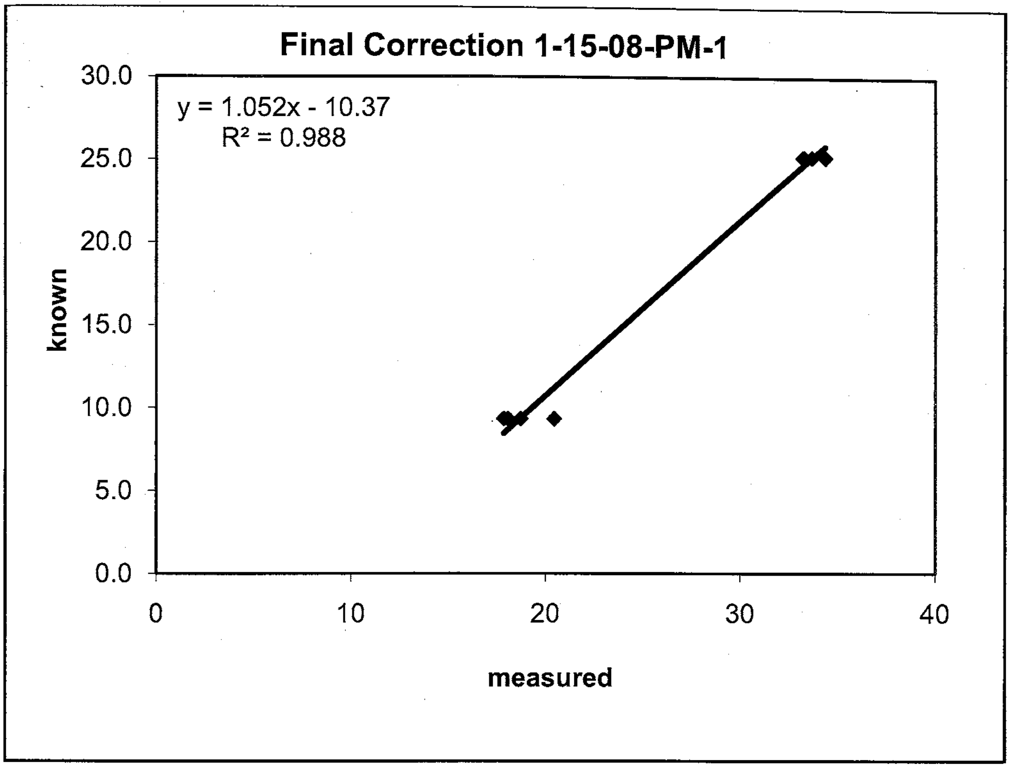

Figure E-4. Trendline for 1-15-08-PM-1

Table E-7. $\delta^{18}O$ for 1-15-08-PM-2.

Sample	Mineral	comment	amount	d18O/16O	corrected value
BLANK					
HEKA		STD	0.32	34.173	**25.3**
HEKA		STD	0.28	33.606	**24.7**
HEKA		STD	0.35	34.337	**25.5**
NBS-127	BASO4	STD	0.22	17.870	**9.0**
NBS-127	BASO4	STD	0.17	19.400	**10.5**
NBS-127	BASO4	STD	0.22	18.846	**10.0**
KS-JB-4	JAR		0.40		**-8.8**
KS-JB-4	BASO4		0.21	9.793	**0.9**
KS-JB-4 (DUP)	BASO4		0.22	10.558	**1.7**
KS-JB-3	JAR		0.46	9.744	**0.9**
KS-JB-3 (DUP)	JAR		0.35	6.851	**-2.0**
KS-JB-3	BASO4		0.24	11.092	**2.2**
KS-JB-3 (DUP)	BASO4		0.22	10.971	**2.1**
HEKA		STD	0.30	33.298	**24.4**
GHS-VWL-0004	JAR		0.40	7.153	**-1.7**
SWH-GJG-0001	JAR		0.40	6.329	**-2.5**
SWH-GJG-0001 (DUP)	JAR		0.38	5.402	**-3.4**
SWH-GJG-0001	BASO4		0.21	10.089	**1.2**
SWH-GJG-0001 (DUP)	BASO4		0.20	11.446	**2.6**
SWH-GJG-0024	JAR		0.40	10.103	**1.3**
SWH-GJG-0024 (DUP)	JAR		0.42	12.678	**3.8**

SWH-GJG-0024	BASO4		0.19	8.453	**-0.4**
SWH-GJG-0024 (DUP)	BASO4		0.21	9.632	**0.8**
HEKA		STD	0.25	34.164	**25.3**
NBS-127	BASO4	STD	0.24	16.811	**8.0**
PB	BASO4		0.22	22.758	**13.9**

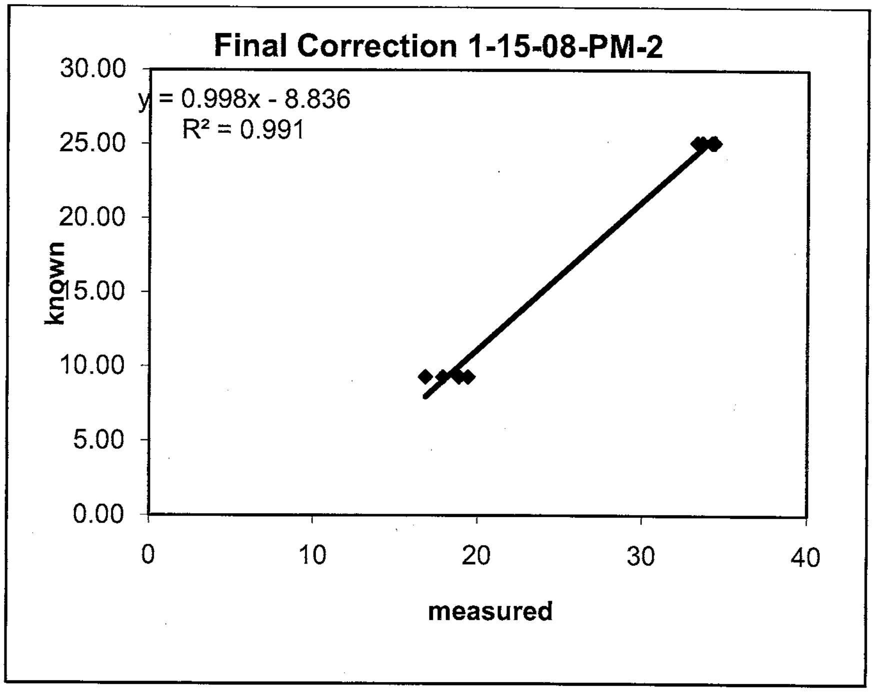

Figure E-5. Trendline for 1-15-08-PM-2.

Table E-8. $\delta^{18}O$ for 1-15-08-PM-3

Sample	mineral	comment	amount	d18O/16O	corrected value
Blank				10.509	
HEKA		STD	0.28	33.951	**26.7**
HEKA		STD	0.26	31.764	**24.2**
NBS-127	BaSO4	STD	0.25	18.088	**8.9**
NBS-127	BaSO4	STD	0.24	18.162	**9.0**
SWH-GJG-0004	JAR		0.44	6.933	**-3.6**
SWH-GJG-0025	JAR		0.43	7.806	**-2.6**
SWH-GJG-0025 (DUP)	JAR		0.40	6.509	**-4.1**
SWH-GJG-0025	BaSO4		0.27	6.013	**-4.6**
SWH-GJG-0025 (DUP)	BaSO4		0.26	8.675	**-1.7**
GHS-VWL-0007	BaSO4		0.22	14.920	**5.3**
GHS-VWL-0007 (DUP)	BaSO4		0.27	16.321	**6.9**
HEKA		STD	0.33	31.734	**24.2**
PIT-VWL-0002	BaSO4		0.17	11.554	**1.6**
PIT-VWL-0002 (DUP)	BaSO4		0.28	12.347	**2.5**
HAS-GJG-0001	BaSO4		0.28	7.163	**-3.3**
HEKA		STD	0.33	31.794	**24.2**
HEKA		STD	0.26	33.192	**25.8**

NBS-127	BaSO4		0.22	19.518	**10.5**
PB	BaSO4		0.23	24.752	**16.4**

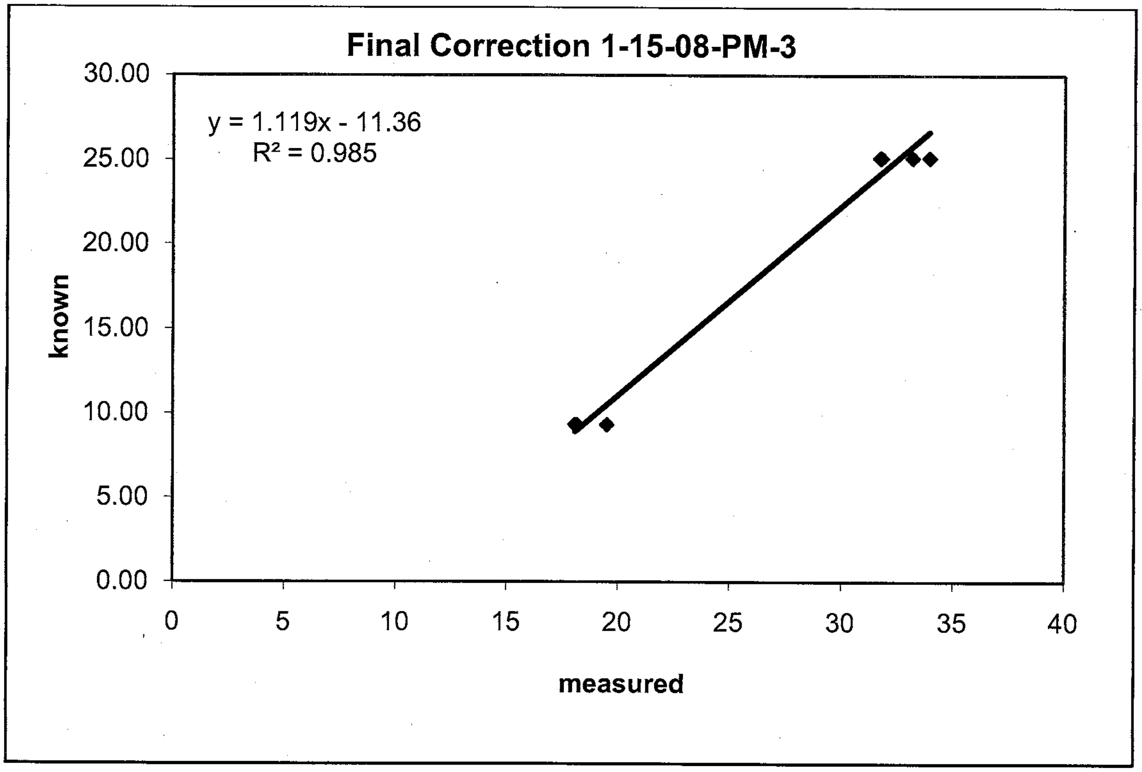

Figure E-6. Trendline for 1-15-08-PM-3.

Table E-9. $\delta^{18}O$ for 1-17-08.

Sample	mineral	Comment	amount	d18O/16O	corrected value
Blank					
HEKA		STD	0.28	41.940	**26.2**
HEKA		STD	0.29	41.377	**25.6**
NBS-127	BaSO4	STD	0.26	27.022	**9.9**
NBS-127	BaSO4	STD	0.24	26.942	**9.8**
PB	JAR		0.45	20.714	**3.0**
PB	BaSO4		0.24	26.707	**9.5**
ESS VWL 0001	BaSO4		0.25	19.871	**2.1**
KS-SC-2	BaSO4		0.23	19.266	**1.4**
KS-SC-2 (DUP)	BaSO4		0.20	19.578	**1.7**
HEKA		STD	0.26	42.196	**26.5**
PIT VWL 0005	BaSO4		0.27	18.630	**0.7**
PIT VWL 0005 (DUP)	BaSO4		0.25	19.172	**1.3**
KS-JB-3	JAR		0.36	16.182	**-2.0**
KS-JB-3 (DUP)	JAR		0.38	14.380	**-3.9**
SWH GJG 0001	JAR		0.38	17.085	**-1.0**
SWH GJG 0001 (DUP)	JAR		0.41	14.990	**-3.3**

HEKA		STD	0.35	40.341	**24.5**
SWH GJG 0001	BaSO4		0.19	19.750	**1.9**
SWH GJG 0001 (DUP)	BaSO4		0.24	17.905	**-0.1**
SWH GJG 0024	BaSO4		0.27	17.356	**-0.7**
SWH GJG 0025	JAR		0.34	15.051	**-3.2**
SWH GJG 0025 (DUP)	JAR		0.48	13.989	**-4.4**
HEKA		STD	0.31	41.895	**26.2**
SWH GJG 0025	BaSO4		0.24	14.309	**-4.0**
SWH GJG 0025 (DUP)	BaSO4		0.23	14.829	**-3.5**
HEKA			0.27	39.631	**23.7**
HEKA		STD	0.36	38.094	**22.0**

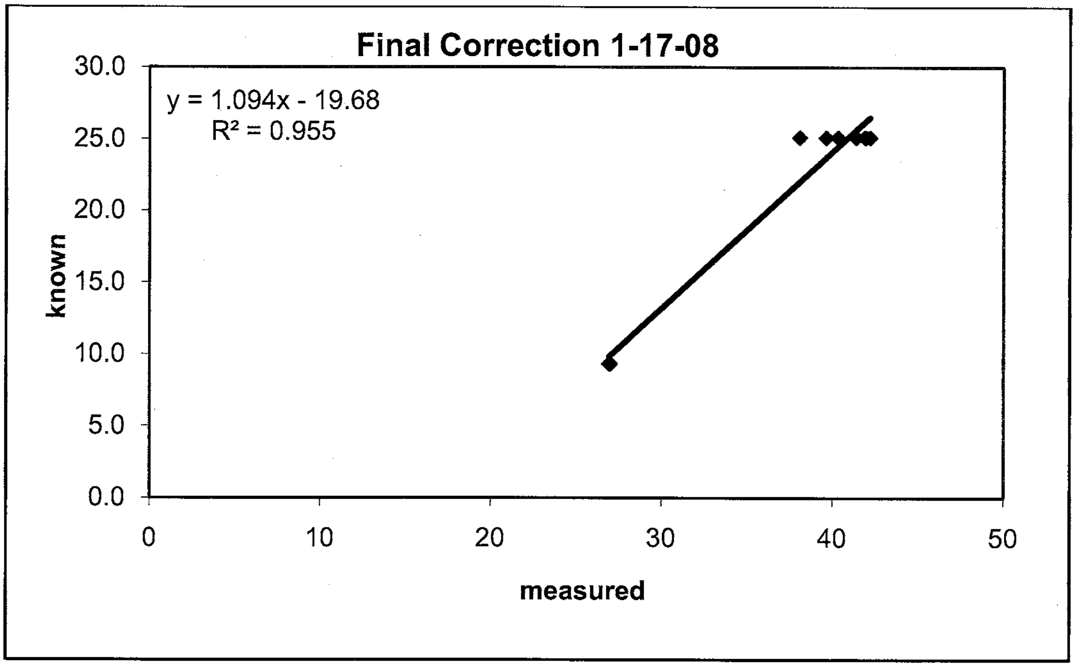

Figure E-7. Trendline for 1-17-08.

Table E-10. $\delta^{18}O$ for 1-22-08.

Sample	Mineral	Comment	amount	d18O/16O	corrected value
Blank					
HEKA		STD	0.29	29.796	24.0
HEKA		STD	0.17	31.200	25.5
HEKA		STD	0.10	31.775	26.1
NBS-127	$BaSO_4$	STD	0.18	17.192	10.5
NBS-127	$BaSO_4$	STD	0.11	16.843	10.1
NBS-127	$BaSO_4$	STD	0.29	16.013	9.2
PB	JAR		0.09	13.787	6.8
PB	JAR		0.20	13.006	6.0
PB	JAR		0.31	12.059	5.0
PB	JAR		0.49	11.821	4.7
HEKA		STD	0.19	30.159	24.4

CAS VWL 0007	JAR		0.37	5.187	-2.4
CAS VWL 0007	JAR		0.30	5.163	-2.4
HEKA*		STD	0.29	24.149	17.9
NBS-127		STD	0.28	14.890	8.0
NBS-127		STD	0.18	15.839	9.0

*Omitted

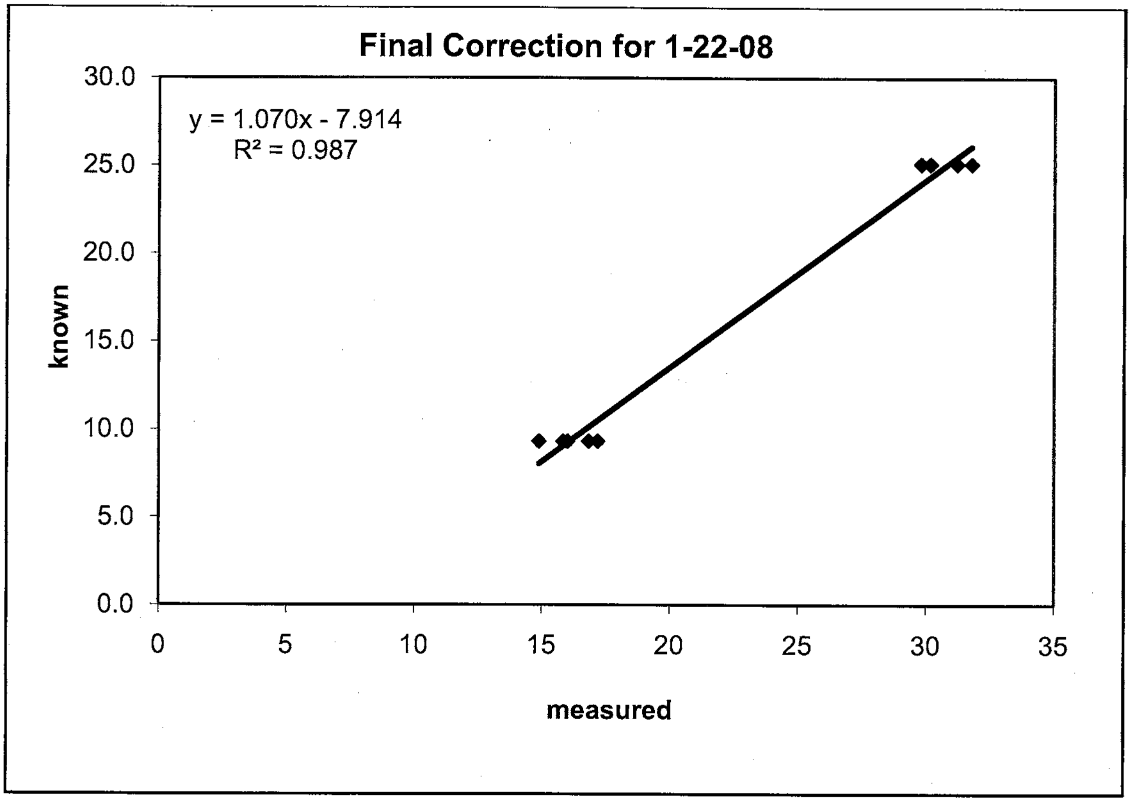

Figure E-8. Trendline for 1-22-08

Table E-11. $\delta^{18}O$ for 1-29-08

sample	mineral	for	amount	d18O/16O		**corrected value**
Blank						
HEKA		STD	0.33	54.928		**25.4**
HEKA		STD	0.29	55.340		**25.8**
HEKA		STD	0.20	54.196		**24.8**
NBS-127	BaSO4	STD	0.17	36.272		**9.5**
NBS-127	BaSO4	STD	0.25	35.916		**9.2**
NBS-127	BaSO4	STD	0.19	36.666		**9.8**
CAS VWL 0007	BaSO4		0.23	24.236		**-0.8**
CAS VWL 0007 (DUP)	BaSO4		0.22	24.047		**-1.0**
BCS VWL 0002	BaSO4		0.19	26.235		**0.9**
BCS VWL 0002 (DUP)	BaSO4		0.23	25.842		**0.6**
SWH GJG 0024	BaSO4		0.27	25.560		**0.3**
SWH GJG 0024 (DUP)	BaSO4		0.19	25.436		**0.2**
HEKA			0.31	54.538		**25.1**

CAS VWL 0007	JAR		0.28	25.417		0.2
CAS VWL 0007 (DUP)	JAR		0.22	24.933		-0.2
PIT VWL 0007	JAR		0.31	24.657		-0.4
PIT VWL 0007 (DUP)	JAR		0.35	24.241		-0.8
PIT VWL 0007	BaSO4		0.26	24.467		-0.6
PIT VWL 0007 (DUP)	BaSO4		0.27	24.649		-0.5
HEKA		STD	0.24	53.650		24.3
NBS-127	BaSO4		0.17	35.540		8.9

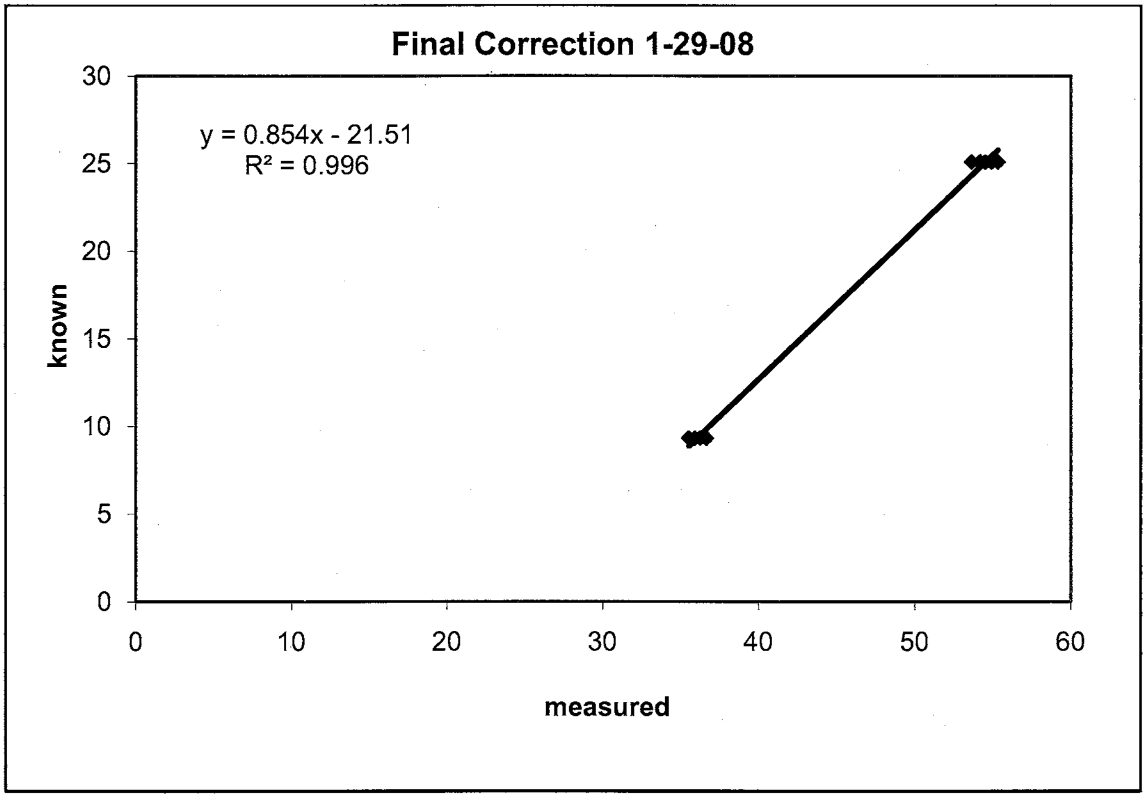

Figure E-9. Trendline for 1-29-08.

Table E-12. $\delta^{18}O$ for 3-19-08.

sample	Mineral	Comment	amount	d18O/16O measured	corrected value
blank					
HEKA		STD	0.36	30.806	24
HEKA		STD	0.29	31.709	25
HEKA		STD	0.33	31.509	25
NBS-127	BaSO4	STD	0.20	14.539	8
NBS-127	BaSO4	STD	0.21	15.478	9
NBS-127	BaSO4	STD	0.25	16.240	10
MM6127-07 (PB)	JAR		0.48	11.089	5
KS-SC-2	JAR		0.37	4.493	-1
KS-SC-2 (DUP)	JAR		0.45	5.091	-0
HEKA		STD	0.26	31.219	25

HEKA		STD	0.25	31.468	**25**
HEKA		STD	0.30	30.831	**24**

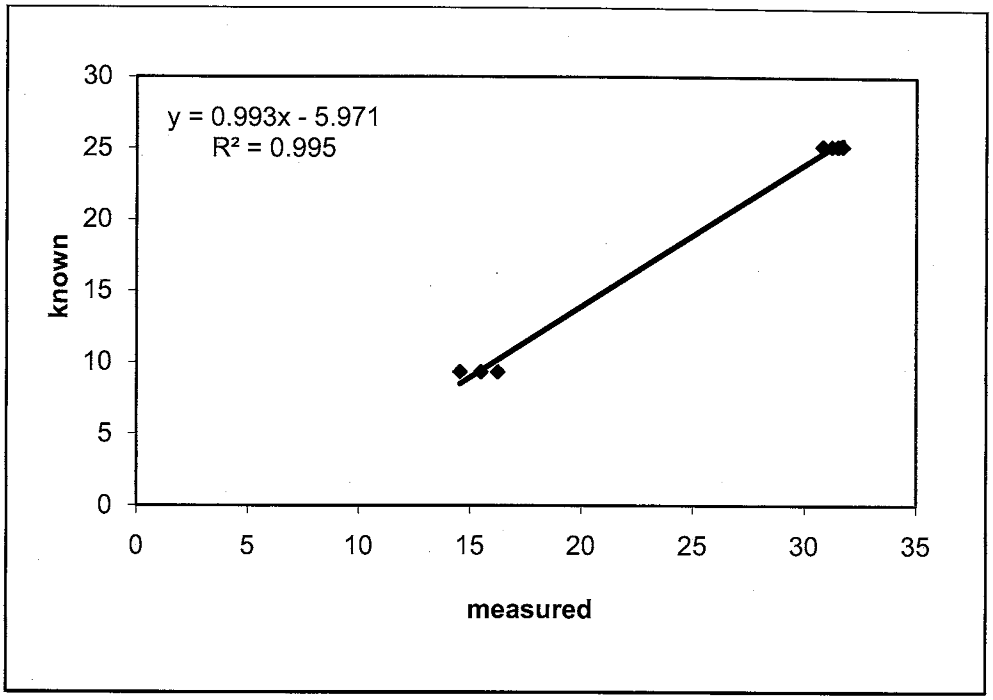

Figure E-10. Trendline for 3-19-08.

E.3. δD Corrections

Measuring hydrogen isotope ratios in hydrous minerals can be difficult, and, although each jarosite run produced reproducible duplicates, the three runs presented here required different approaches to correcting standard values. Jarosite was analyzed on August 22, 2007, November 30, 2007, and March 17, 2008, and correction factor calculations are presented in chronological order.

Table E-13. Standard δD values

Standard	Material	Known δD_{VSMOW} Value (‰)
HEKA	Benzoic Acid	-61
CH-7	Polyurethane	-100
NBS-30	Biotite	-64

E.3.1. August 22, 2007

With the exception of HEKA, measured δD values for standards run on August 22, 2007 were approximately 30‰ heavier than known values, so sample δD values were corrected by subtracting 30‰ from measured δD.

Table E-14. Measured and corrected δD 8/22/07.

Sample	Mineral	Comment	Amount	Measured δD	Corrected value
CH-7		STD	0.16	-71.253	-10
CH-7		STD	0.08	-73.857	-10
CH-7		STD	0.10	-71.576	-10
HEKA		STD	0.26	-44.720	-7
HEKA		STD	0.19	-42.063	-7
NBS30	BT	STD	0.62	-33.556	-6
NBS30	BT	STD	0.66	-34.086	-6
A-0	JAR		0.55	-79.460	-10
A-0	JAR		0.54	-86.444	-11
PIT-VWL-0007	JAR		0.50	-90.449	-12
PIT-VWL-0007 (DUP)	JAR		0.55	-99.149	-12
SWH-GJG-0001	JAR		0.53	-96.226	-12
SWH-GJG-0001 (DUP)	JAR		0.50	-90.651	-12
ESS-VWL-0001	JAR		0.55	-99.184	-12
ESS-VWL-0001 (DUP)	JAR		0.55	-98.900	-12
SWH-GJG-0025	JAR		0.51	-99.027	-12
SWH-GJG-0025 (DUP)	JAR		0.51	-99.821	-13
CH-7		STD	0.14	-71.244	-10
HEKA		STD	0.25	-46.755	-7
NBS30	BT	STD	0.64	-28.568	-5
A-0	JAR		0.50	-75.515	-10

E.3.2. November 30, 2007

On November 30, 2007, there seemed to be a relationship between the relative size of the sample peak and reference peak and measured δD. This relationship was most apparent in the HEKA standard. When the HEKA peak was bigger than the reference peak (~2000 mV), measured δD values were heavier, but when the HEKA peak was smaller than the reference peak, measured δD values were lighter (Figure E-11). The slope of the trendline was multiplied by measured δD values. The result was added to the measured δD value. These numbers were approximately 16.014‰ heavier than the known standard value, so 16.014‰ was subtracted.

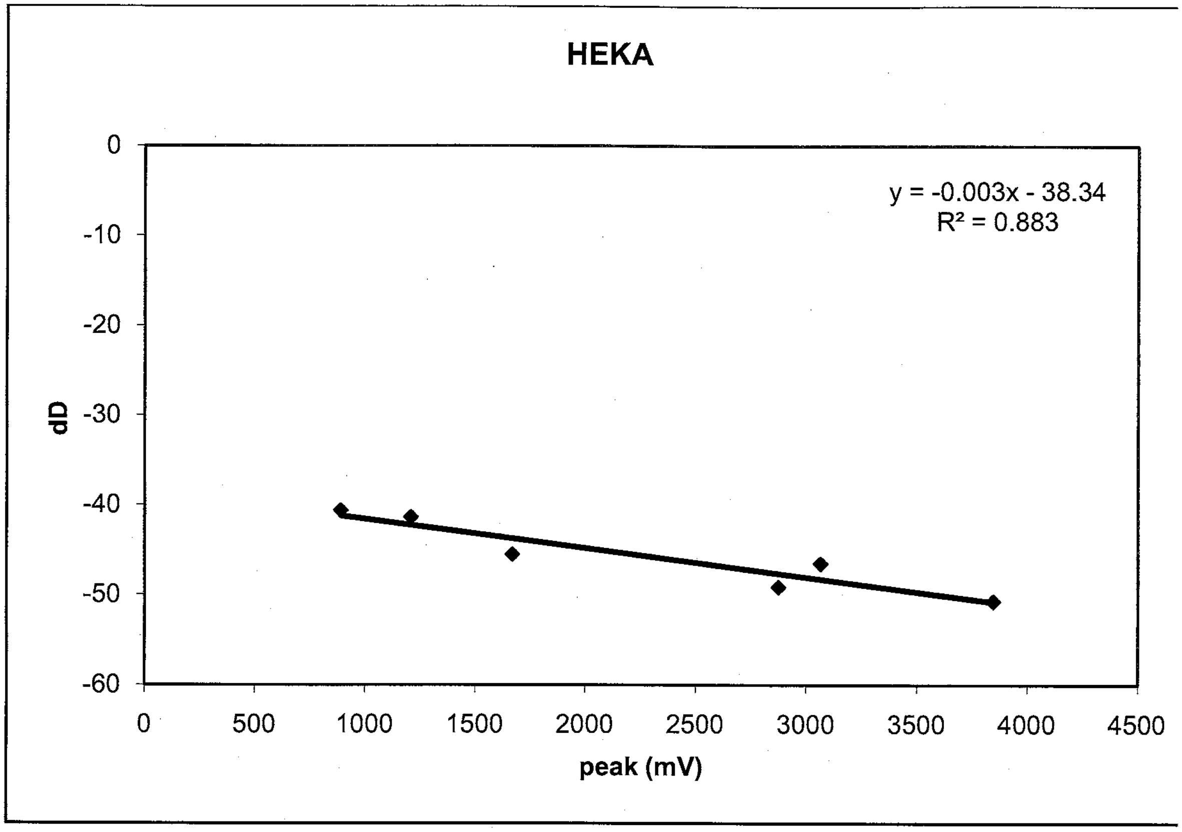

Figure E-11. Trendline for peak size vs measured δD values on November 30, 2007.

Table E-15. Measured and corrected δD 11/30/07.

A	B	C	D	E	F	G	H	I
Sample	amount (mg)	Sample peak (mV)	Measured δD	Avg ref peak (mV)	Column E-C	slope* F	Column D+G	Column H-16.013
HEKA	0.28	3848	-50.731	2053	-1795	5.744	-44.987	**-61**
HEKA	0.2	2876	-49.176	2017	-859	2.7488	-46.4272	**-62**
HEKA	0.24	1670	-45.542	1986	316	-1.0112	-46.5532	**-63**
CH-7	0.06	3043	-81.154	1958	-1085	3.472	-77.682	**-94**
CH-7	0.08	3198	-80.199	1939	-1259	4.0288	-76.1702	**-92**
CH-7	0.09	2415	-77.079	1913	-502	1.6064	-75.4726	**-91**
NBS-30	2.19	2082	-39.575	1893	-189	0.6048	-38.9702	**-55**
NBS-30	1.85	1858	-35.806	1876	18	-0.0576	-35.8636	**-52**
NBS-30	2.39	2555	-37.76	1857	-698	2.2336	-35.5264	**-52**
PB	0.72	1368	-92.756	1840	472	-1.5104	-94.2664	**-110**
PB	0.64	2258	-96.321	1824	-434	1.3888	-94.9322	**-111**
PB	0.62	1573	-92.885	1807	234	-0.7488	-93.6338	**-110**
PIT VWL 0005	0.68	1911	-111.096	1791	-120	0.384	-110.712	**-127**

PIT VWL 0005 (DUP)	0.6	1959	-112.232	1775	-184	0.5888	-111.6432	**-128**
KS-JB-3	0.76	911	-97.308	1760	849	-2.7168	-100.0248	**-116**
KS-JB-3 (DUP)	0.6	915	-97.68	1746	831	-2.6592	-100.3392	**-116**
KS-SC-2	0.43	1356	-79.074	1731	375	-1.2	-80.274	**-96**
KS-SC-2 (DUP)	0.82	2508	-87.524	1717	-791	2.5312	-84.9928	**-101**
HEKA	0.19	891	-40.662	1702	811	-2.5952	-43.2572	**-59**
KS-JB-4	0.5	1399	-84.516	1688	289	-0.9248	-85.4408	**-101**
KS-JB-4 (DUP)	0.46	1263	-88.619	1673	410	-1.312	-89.931	**-106**
GHS VWL 0004	0.55	1337	-101.427	1659	322	-1.0304	-102.4574	**-118**
ESS VWL 0001	0.51	831	-96.131	1646	815	-2.608	-98.739	**-115**
ESS VWL 0001 (DUP)	0.53	1722	-104.62	1633	-89	0.2848	-104.3352	**-120**
HEKA	0.36	3066	-46.547	1620	-1446	4.6272	-41.9198	**-58**
SWH GJG 0004	0.42	480	-91.176	1607	1127	-3.6064	-94.7824	**-111**
PB-HF	0.63	1496	-92.372	1594	98	-0.3136	-92.6856	**-109**
PB-HF	0.76	1471	-92.125	1580	109	-0.3488	-92.4738	**-108**
HEKA	0.26	1209	-41.416	1568	359	-1.1488	-42.5648	**-59**
CH-7	0.1	1919	-74.52	1555	-364	1.1648	-73.3552	**-89**

E.3.3.March 17, 2008

On March 17, 2008, the difference between measured and known δD for standards varied as a function of the absolute value of the difference between reference peak and sample peak height. As the difference between peak heights approached zero, the difference between known and measured values approached 24.04‰ (Figure E-12). The slope of the trendline for this relationship was multiplied by the absolute value of the difference between sample and reference peak height. The result was added to measured δD before subtracting 24.04‰.

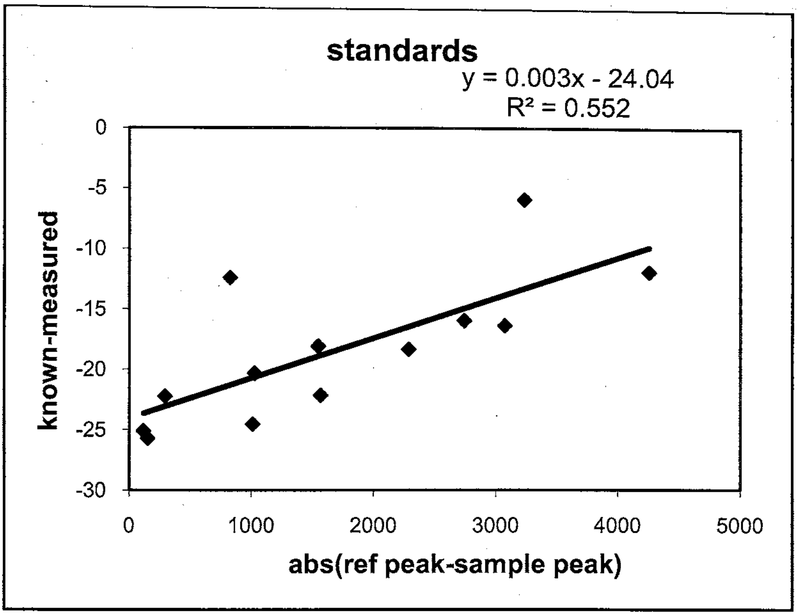

Figure E-12. Trendline for δD correction factor 3/17/08.

Table E-16. Measured and corrected δD 3/17/08.

A	B	D	E	F	G	H	I	K
sample	amount (mg)	Sample peak (mV)	measured δD	Avg ref peak (mV)	Abs(F -D)	0.0033 *G	E+H	col L-24.041
HEKA	0.22	2164	-38.762	2459	295	0.974	-37.789	**-62**
HEKA	0.15	1410	-40.658	2439	1029	3.396	-37.262	**-61**
HEKA	0.20	6674	-48.920	2419	4256	14.043	-34.877	**-59**
CH-7	0.11	4686	-81.613	2399	2288	7.549	-74.064	**-98**
CH-7	0.08	5121	-83.970	2379	2742	9.049	-74.921	**-99**
CH-7	0.08	3908	-81.879	2360	1548	5.108	-76.771	**-101**
NBS-30	1.90	2492	-38.266	2340	152	0.502	-37.764	**-62**
NBS-30	2.81	3333	-39.451	2321	1012	3.340	-36.111	**-60**
NBS-30	1.90	2420	-38.894	2302	118	0.389	-38.505	**-63**
CAS VWL 0007	0.63	3262	-118.661	2265	998	3.292	-115.369	**-139**
CAS VWL 0007 (DUP)	0.56	2227	-120.666	2231	4	0.013	-120.653	**-145**

SWH GJG 0004	0.98	3562	-132.124	2227	1335	4.406	-127.719	**-152**
SWH GJG 0004 (DUP)	0.93	3282	-133.211	2209	1073	3.541	-129.670	**-154**
HEKA	0.11	1346	-48.551	2173	827	2.727	-45.824	**-70**
HEKA	0.16	5270	-54.974	2037	3234	10.671	-44.303	**-68**
CH-7	0.10	5094	-83.559	2020	3074	10.144	-73.415	**-97**

APPENDIX F: RADIOCARBON DATING

When cosmic-ray generated thermal neutrons collide with nitrogen nuclei in the atmosphere, ^{14}C forms through an n, p reaction: $^{14}_{7}N + n \rightarrow ^{14}_{6}C + p$. Because the flux of cosmic rays is not constant, the concentration of ^{14}C in the atmosphere varies over time, and ^{14}C years do not coincide perfectly with calendar years (Dickin, 2005). There are several different calibration curves available that take latitude and environment (terrestrial or marine) into account.

OxCal 4.0 (Bronk Ramsey, 1995 and 2001) was used to convert ^{14}C years BP to calendar years based on the IntCal04 calibration curve of Reimer et al. (2004), which is calibrated for northern hemisphere ^{14}C fluctuations over the past 26,000 years based on tree ring data, corals, and foraminifera (Figure F-1). The program produces calendar ages based on a Gaussian distribution of ^{14}C years BP. The calibration curve is not completely smooth, so uncertainty on calculated calendar years can exceed uncertainty of ^{14}C age.

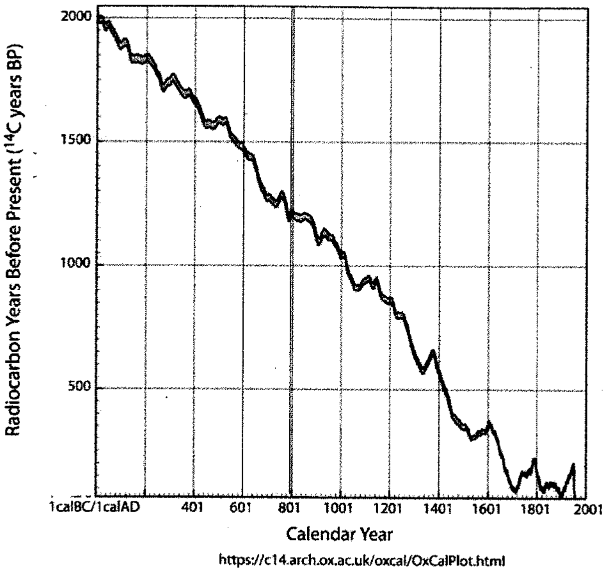

Figure F-1. IntCal04 calibration curve (Reimer et al., 2004) from the OxCal 4.0 program (Bronk Ramsey, 1991 and 2001).

REFERENCES

Alpers, C.N.; Rye, R.O.; Nordstrom, D.K.; White, L.D.; King, B.S., 1992, Chemical, crystallographic and stable isotopic properties of alunite and jarosite from acid hypersaline Australian lakes: Chemical Geology 96, no.1-2, p.203-226.

Arehart, G.B. and O'Neil, J.R., 1993, D/H ratios of supergene alunite as an indicator of paleoclimate in continental settings, in, P.K. Swart, K.C. Lohmann, J. McKenzie, and S.Savin (eds) Climate change in continental isotopic records: AGU Geophysical Monograph 78, p. 277-284.

Bachmann, O., Dungan, M.A., Lipman, P.W., 2002, The Fish Canyon magma body, San Juan volcanic field, Colorado: Rejuvenation and eruption of an upper-crustal batholiths: Journal of Petrology 43, no. 8, p. 1469-1503.

Bauer, P.W. and Kelson, K.I., 2004, Rift extension and fault slip rates in the San Luis basin, New Mexico: New Mexico Geological Society, 55th Field Conference, Guidebook, p. 172-180.

Bauer, P.W., 2008, The San Luis basin of the northern Rio Grande rift: New Mexico Geological Society Spring Meeting, Abstracts with Programs.

Bronk Ramsey, C, 1995, Radiocarbon calibration and analysis of stratigraphy: The OxCal program: Radiocarbon, 37, p. 425-430.

Bronk Ramsey, C, 2001, Development of the radiocarbon calibration program OxCal,: Radiocarbon, 43, p. 355-363.

Caine, J.S., 2006, Questa Baseline and Premining Ground-Water Quality Investigation 18. Characterization of Brittle Structures in the Questa Caldera and Their Potential Influence on Bedrock Ground-Water Flow, Red River Valley, New Mexico: USGS Professional Paper 1729, 44 p.

Campbell, A., and Lueth, V.W., 2006, Rock pile weathering stability: Final report (phase I) on the stable isotopic composition of pile and scar samples.

Campbell, A. and Lueth, V.W., 2008, Isotopic and textural discrimination between hypogene, ancient supergene and modern sulfates at the Questa mine, New Mexico: Applied Geochemistry 23, p. 308-319.

Clark, K.F., and Read, C.B., 1972, Geology and ore deposits of Eagle Nest area: New Mexico Bureau of Mines and Mineral Resources, Bulletin 94, 152 p.

Connell, S.D., 2004, Geology of the Albuquerque basin and tectonic development of the Rio Grande rift in north-central New Mexico, *in*, G.H. Mack and K.A. Giles, eds, The geology of New Mexico, a geologic history: New Mexico Geological Society, p. 359-388.

Czamanske, G.K., Foland, K.A., Kubacher, F.A., Allen, J.C., 1990, The ^{40}Ar/^{39}Ar chronology of caldera formation, intrusive activity, and molybdenum ore deposition near Questa, New Mexico: New Mexico Geological Society, 41st Field Conference, Guidebook, p. 355-358.

Dickin, A., 2005, Radiogenic Isotope Geology, 2nd Edition: New York, Cambridge University Press, 492 p.

Donohoo-Hurley, L., Geissman, J.W., Fawcett, P., Wawrzyniec, T., Goff, F., 2007, A 200 kyr Pleistocene lacustrine record from the Valles Caldera: Insight from environmental magnetism and paleomagnetism: New Mexico Geological Society, 58th Field Conference, Guidebook, p. 424-432.

Dutrizac, J.E., Jambor, J.L., 2000, Jarosites and their application in hydrometallurgy, *in*, C.N. Alpers, J.L. Jambor, D.K. Nordstrom, eds, Sulfate Minerals: Crystallography, Geochemistry, and Environmental Significance, Reviews in Mineralogy and Geochemistry, v. 40: Mineralogical Society of America, Washington, DC, p. 405-452.

Elwood Madden, M.E., Guess, J.R., Madden, A.S., Rimstidt, J.D., 2008, Measuring jarosite dissolution rates to determine jarosite lifetimes on earth and Mars (abs.): Geochimica et Cosmochimica Acta, Awards Ceremony Speeches and Abstracts of the 18th Annual V.M. Goldschmidt Conference, A243.

Enders, MS; Knickerbocker, C; Titley, SR; Southam, G., 2006, The role of bacteria in the supergene environment of the Morenci Porphyry Copper Deposit, Greenlee County, Arizona: Economic Geology, v.101, no.1, p.59-70.

Fawcett, P.J., Heikoop, J., Goff, F., Anderson, R.S., Donohoo-Hurley, L., Geissman, J.W., WoldeGabriel, G., Allen, C.D., Johnson, C.M., Smith, S.J., Fessenden-Rahn, J., 2007, Two Middle Pleistocene glacial-interglacial cycles from the Valle Grande, Jemez Mountains, northern New Mexico: New Mexico Geological Society, 58th Field Conference, Guidebook, p. 409-417.

Graf, G.J., 2008, Mineralogical and geochemical changes associated with sulfide and silicate weathering in natural alteration scars, Taos County, New Mexico: New Mexico Institute of Mining and Technology unpublished MS thesis, 193 p.

Harden, J.W., 1982, A quantitative index of soil development from field descriptions: examples from a chronosequences in central California: Geoderma, v. 28, 1-28.

Hoefs, J., 2004, Stable isotope geochemistry: Springer, 244 p.

Jaboyedoff, M. and Cosca, M.A., 1999, Dating incipient metamorphism using ^{40}Ar/^{39}Ar geochronology and XRD modeling: a case study from the Swiss Alps: Contributions to Mineralogy and Petrology, v. 135, p. 93-113.

Juliani, C., Rye, R.O., Nunes, Snee, L.W., Corrêa-Silva, R., Monteiro, L.V.S., Bettencourt, J.S., Neumann, R., Neto, A.A., 2005, Paleoproterozoic high-sulfidation mineralization in the Tapajós gold province, Amazonian Craton, Brazil: geology, mineralogy, alunite argon age, and stable isotope constraints: Chemical Geology, v. 215, 95-125.

Karlstrom, K.E.; Crow, R.S.; Peters, L.; McIntosh, W.; Raucci, J.; Crossey, L.J.; Umhoefer, P.; Dunbar, N., 2007, Ar-40/Ar-39 and field studies of Quaternary basalts in Grand Canyon and model for carving Grand Canyon: Quantifying the interaction of river incision and normal faulting across the western edge of the Colorado Plateau: Geological Society of America Bulletin, v. 119, p. 1283-1312.

Kelley, S., 2002, Excess argon in K-Ar and Ar-Ar geochronology: Chemical Geology, v. 188, p. 1-22.

Kelson, K.I. and Olig, S.S., 1995, Estimated rates of Quaternary crustal extension in the Rio Grande rift, northern New Mexico: New Mexico Geological Society, 46th Field Conference, Guidebook, p. 9-12.

Lipman, P.W., Mehnert, H.H., Naeser, C.W., 1986, Evolution of the Latir volcanic field, northern New Mexico, and its relation to the Rio Grande rift, as indicated ny Potassium-Argon and fission track dating: Journal of Geophysical Research, v. 91, p. 6329-6345.

Lipman, P.W. and Reed, J.C., Geologic map of the Latir volcanic field and adjacent areas, northern New Mexico: US Geological Survey Miscellaneous Investigations Map I-1907, scale 1:48,000.

Lo, C. and Onstott, T.C., 1989, ^{39}Ar recoil artifacts in chloritized biotite: Geochimica et Cosmochimica Acta, v. 53, p. 2697-2711.

Ludington, S., Plumlee, G., Caine, J., Bove, D., Holloway, J., Livo, E., 2004, Questa baseline and pre-mining groundwater quality investigation. 10. Geologic influences on ground and surface waters in the lower Red River watershed, New Mexico: USGS Scientific Investigations Report 2004-5245, 45 p.

Lueth, V.W., Goodell, P.C., Heizler, M.T., Peters, L., 1998, Geochemistry, geochronology, and tectonic implications of jarosite mineralization in the northern Franklin Mountains, Doña Ana County, New Mexico: New Mexico Geological Society, 49th Field Conference, Guidebook, p. 309-316.

Lueth, V.W., Chamberlin, R.M., Peters, L., 2004, Age of mineralization in the Luis Lopez manganese district, Socorro County, NM, as determined by $^{40}Ar/^{39}Ar$ dating of cryptomelane: NMBGMR Bulletin, v. 160, p. 239-249.

Lueth, V.W., Rye, R.O., Peters, L., 2004, $^{40}Ar/^{39}Ar$ data repository for *"Sour gas" hydrothermal jarosite: ancient to modern acid-sulfate mineralization in the southern Rio Grande rift*: NMBGMR Open-File Report OF-AR-22, 9 p.

Lueth, V.W., Rye, R.O., Peters, L., 2005, "Sour gas" hydrothermal jarosite: ancient to modern acid-sulfate mineralization in the southern Rio Grande rift: Chemical Geology, v. 215, p. 339-360.

Lueth, V.W., Campbell, A.R., and Peters, L.M., 2006, Final report (Phase I) on the geochronological (40Ar/39Ar) dating of jarosite and alunite samples from the Red River area alteration scars and the Questa Mine: The timing of alteration scar formation and weathering: Questa Rock Pile Weathering and Stability Project, Unpublished report, 18 p.

Lueth, V.W., Samuels, K., Peters, L., Campbell, A.R., 2008a, Data report on the geochronological ($^{40}Ar/^{39}Ar$ and ^{14}C) dating of jarosite, alunite, manganese oxide, and carbon samples from Red River area alteration scars, debris flows, and the Questa mine: New Mexico Bureau of Geology and Mineral Resources, 38 p.

Lueth, V.W., Samuels, K.E., Campbell, A., 2008b, Rock pile weathering stability: Final report on the geochronological ($^{40}Ar/^{39}Ar$) dating of Red River area alteration scars and debris flows: New Mexico Bureau of Geology and Mineral Resources, 19 p.

Mack, G.H.; McIntosh, W.C.; Leeder, M.R.; Monger, H.C., 1996, Plio-Pleistocene pumice floods in the ancestral Rio Grande, southern Rio Grande Rift, USA: Sedimentary Geology, v. 103, 1-8.

Machette, M.N., Marchetti, D.W., Thompson, R.A., 2007, Ancient Lake Alamosa and the Pliocene to Middle Pleistocene evolution of the Rio Grande: Friends of the Pleistocene, Rocky Mountain section field trip – Quaternary geology of the San Luis basin of Colorado and New Mexico, p. 157-167.

McDougall, I. and Harrison, M.T., 1988, Geochronology and Thermochronology by the $^{40}Ar/^{39}Ar$ method: New York, Oxford University Press, 212 p.

McIntosh, W.C., Sutter, J.F., Chapin, C.E., Kedzie, L.L., 1990, High-precision $^{40}Ar/^{39}Ar$ geochronology of ignimbrites in the Mogollon-Datil volcanic field, southwestern New Mexico: Bulletin of Volcanology, v. 52, p. 584-601.

Meyer, J., Foland, K.A., 1991, Magmatic-tectonic interaction during early Rio Grande rift extension at Questa, New Mexico: Geological Society of America Bulletin, v. 103, p. 993-1006.

Meyer, J. and Leonardson, R., 1990, Tectonic, hydrothermal and geomorphic controls on alteration scar formation near Questa, NM: New Mexico Geological Society, 41st Field Conference, Guidebook, p. 417-422.

Morrison, R.B., 1991, Introduction, *in*, R.B. Morrison, ed., Quaternary nonglacial geology: conterminous US: Geological Society of America, The Geology of North America v. K-2, p. 1-12.

Newell, D.L., Koning, D.J., Karlstrom, K.E., Crossey, L.J., Dillon, M., 2004, Plio-Pleistocene incision history of the Rio Ojo Caliente, northern Española basin, and overview of the Rio Grande system in northern New Mexico: New Mexico Geological Society, 55th Field Conference, Guidebook, p. 300-313.

Nordstrom, D.K., McCleskey, R.B., Hunt, A.G., Naus, C.A., 2005, Questa Baseline and Pre-Mining Ground-Water Quality Investigation. 14. Interpretation of ground-water geochemistry in catchments other than the Straight Creek catchment, Red River Valley, Taos County, New Mexico, 2002-2003: USGS Scientific Investigations Report 2005-5050, 94 p.

Ohmoto, H. and Rye, R.O., 1979, Isotope of sulfur and carbon, in H.L. Barnes, ed., Geochemistry of hydrothermal deposits: John Wiley and Sons, p. 509-567.

Papike, J.J., Karner, J.M., and Shearer, C.K., 2006, Comparative planetary mineralogy: Implications of martian and terrestrial jarosite. A crystal chemical perspective: Geochimica et Cosmochimica Acta, v. 70, p. 1309-1321.

Papike, J.J., Burger, P.V., Karner, J.M., Shearer, C.K., and Lueth, V.W., 2007, Terrestrial analogs of martian jarosite: Major, minor element systematics and Na-K zoning in selected samples: American Mineralogist, v. 92, p. 444-447.

Poage, M.A. and Chamberlain, C.P., 2001, Empirical relationships between elevation and the stable isotope composition of precipitation and surface waters: considerations for studies of paleoelevation change: American Journal of Science, v. 301, p. 1-15.

Polyak, V.J., McIntosh, W.C., Güven, N., Provencio, P., 1998, Age and origin of Carlsbad Cavern and related caves from $^{40}Ar/^{39}Ar$ of alunite: Science, v. 279, p. 1919-1922.

Polyak, V.J., McIntosh, W.C., Provencio, P.P, Güven, N, 2006, Alunite and natroalunite tell the story – the age and origin of Carlsbad Cavern, Lechuguilla Cave, and other sulfuric-acid type caves in the Guadalupe Mountains: New Mexico Geological Society 57th Field Conference Guidebook, p. 203-209.

Reimer, PJ, MGL Baillie, E Bard, A Bayliss, JW Beck, CJH Bertrand, PG Blackwell, CE Buck, GS Burr, KB Cutler, PE Damon, RL Edwards, RG Fairbanks, M Friedrich, TP Guilderson, AG Hogg, KA Hughen, B Kromer, G McCormac, S Manning, C Bronk Ramsey, RW Reimer, S Remmele, JR Southon, M Stuiver, S Talamo, FW Taylor, J van der Plicht and CE Weyhenmeyer, 2004, IntCal04 terrestrial radiocarbon age calibration, 0-26 cal kyr BP: Radiocarbon, 46, no. 3, p. 1029-1058.

Ritter, D.F., Kochel, R.C., Miller, J.R., 2002, Process Geomorphology: New York, McGraw Hill, 560 p.

Rogers, K.L., Larson, E.E., Smith, G., Katzman, D., Smith, G.R., Cerling, T., Wang, Y., Baker, R.G., Lohmann, K.C., Repenning, C.A., Patterson, P., Mackie, G., 1992, Pliocene and Pleistocene geologic and climatic evolution in the San Luis Valley of south-central Colorado: Paleogeography, Paleoclimatology, Paleoecology, v. 94, 55-86.

Rosholt, J.N., Colman, S.M., Stuiver, M., Damon, P.E., Naeser, C.W., Naeser, N.D., Szabo, B.J., Muhs, D.R., Liddicoat, J.C., Forman, S.L., Machette, M.N., Pierce, K.L., 1991, Dating methods applicable to the Quaternary, in, Morrison, R.B. (ed.), Quaternary nonglacial geology: Conterminous U.S.: Geological Society of America, 45-73.

Ross, P.S., Jébrak, M., Walker, B.M., 2002, Discharge of hydrothermal fluids from a magma chamber and concomitant formation of a stratified breccia zone at the Questa porphyry molybdenum deposit, New Mexico: Economic Geology, v. 97, p. 1679-1699.

Rye, R.O. and Stoffegren, R.E., 1995, Jarosite-water oxygen and hydrogen fractionations: Preliminary experimental data: Economic Geology, v. 90, p. 2336-2342.

Rye, R.O. and Alpers, C.N., 1997, The stable isotope geochemistry of jarosite: USGS Open File Report 97-88, 28 p.

Rye, R.O., Bethke, P.M., Lanphere, M.A., Steven, T.A., 2000, Neogene geomorphic and climatic evolution of the central San Juan Mountains, CO: K/Ar age and stable isotope data on supergene alunite and jarosite from the Creede mining district, in, P.M. Bethke and R.L. Hay (eds.), Ancient Lake Creede: Its volcano-tectonic setting, history of sedimentation and relation to mineralization in the Creede mining district: GSA Special Paper 346: 340 p.

Schilling, J.H., 1956, Geology of the Questa molybdenum (Moly) mine area, Taos County, New Mexico: New Mexico Bureau of Mines and Mineral Resources, Bulletin 51, 87 p.

Seal, R.R., 2003, Stable-isotope geochemistry of mine waters and related solids, *in*, Jambor, J.L., Blowes, D.W., and Ritchie, A.I.M. (eds), Environmental aspects of mine wastes: Mineralogical Association of Canada 430 pp.

Shaw, S., Wells, C., Robertson, A., Fortin, S., Walker, B., 2003, Background Characterisation Study of Naturally Occurring Acid Rock Drainage in the Sangre De Cristo Mountains, Taos County, New Mexico, *in* 6th ICARD: Cairns, Queensland, Australia, July 12-18, 2003, p. 605-616.

Smith, A.M.L., Hudson-Edwards, K.A., Dubbin, W.E., Wright, K., 2006, Dissolution of jarosite [$KFe_3(SO_4)_2(OH)_6$] at pH 2 and 8: Insights from batch experiments and computational modeling: Geochimica et Cosmochimica Acta, v. 70, p. 608-621.

Smith, G.A., Moore, J.D., McIntosh, W.C., 2002, Assessing roles of volcanism and basin subsidence in causing Oligocene-Lower Miocene sedimentation in the northern Rio Grande rift, New Mexico, USA: Journal of Sedimentary Research, v. 72, p. 836-848.

Smith, G.A., 2004, Middle to Late Cenozoic development of the Rio Grande rift and adjacent regions in northern New Mexico, *in*, G.H. Mack and K.A. Giles, eds, The geology of New Mexico, a geologic history: New Mexico Geological Society, p. 331-358.

Smith, P.E., Evensen, N.M., York, D., 1993, First successful $^{40}Ar/^{39}Ar$ dating of glauconies: Argon recoil in single grains of cryptocrystalline material: Geology, v. 21, p. 41-44.

Stoffregen, R.E., Alpers, C.N., Jambor, J.L., 2000, Alunite-Jarosite crystallography, thermodynamics, and geochronology, *in*, C.N. Alpers, J.L. Jambor, and D.K. Nordstrom, eds, Reviews in Mineralogy and Geochemistry: Sulfate minerals: crystallography, geochemistry, and environmental significance: Mineralogical Society of America and the Geochemical Society, p. 453-479.

Tappa, M.J., Zimmerer, M.J., Coleman, D.S., 2008, Thermal evolution of plutons in the Questa caldera, NM (abs.): Geochimica et Cosmochimica Acta, Awards Ceremony Speeches and Abstracts of the 18th Annual V.M. Goldschmidt Conference, p. A934.

Vasconcelos, P.M., Brimhall, G.H., Becker, T.A., Renne, P.R., 1994, $^{40}Ar/^{39}Ar$ analysis of supergene jarosite and alunite: Implications to the paleoweathering history of the western USA and West Africa: Geochimica et Cosmochimica Acta, v. 58, p. 401-420.

Vasconcelos, P.M., 1999, K-Ar and $^{40}Ar/^{39}Ar$ geochronology of weathering processes: Annual Review of Earth and Planetary Sciences, v. 27, p. 183-229.

Vasconcelos, P.M. and Conroy, M., 2003, Geochronology of weathering and landscape evolution, Dugald River valley, NW Queensland, Australia: Geochimica et Cosmochimica Acta, v. 67, p. 2913-2930.

Villa, I.M., 1997, Direct determination of ^{39}Ar recoil distance: Geochimica et Cosmochimica Acta, v. 61, p. 689-691.

Wasserman, M.D., Rye, R.O., Bethke, P.M., Arribas, A., 1992, Methods for separation and total stable isotope analysis of alunite: USGS Open File Report 92-9, 20 p.

Wells, S.G., Kelson, K.I., Menges, C.M., 1987, Quaternary evolution of the fluvial systems in the northern Rio Grande rift, New Mexico and Colorado – Implications for entrenchment and integration of drainage systems, *in*, C. Menges, ed., Quaternary tectonics, landform evolution, soil chronologies, and glacial deposits – Northern Rio Grande rift of New Mexico: Friends of the Pleistocene, Rocky Mountain Cell Field Trip Guidebook, Oct. 8-11, p. 55-69.

Zimmerer, M.J., 2008, The $^{40}Ar/^{39}Ar$ geochronology and thermochronology of the Latir volcanic field and associated intrusions: implications for caldera-related magmatism: New Mexico Institute of Mining and Technology unpublished master's thesis, 120 pp.